



## Mesoscale to microscale coupling for determining site conditions in complex terrain

Olsen, Bjarke Tobias

*Link to article, DOI:*  
[10.11581/00000036](https://doi.org/10.11581/00000036)

*Publication date:*  
2018

*Document Version*  
Publisher's PDF, also known as Version of record

[Link back to DTU Orbit](#)

*Citation (APA):*  
Olsen, B. T. (2018). Mesoscale to microscale coupling for determining site conditions in complex terrain. DTU Wind Energy. DOI: 10.11581/00000036

---

### General rights

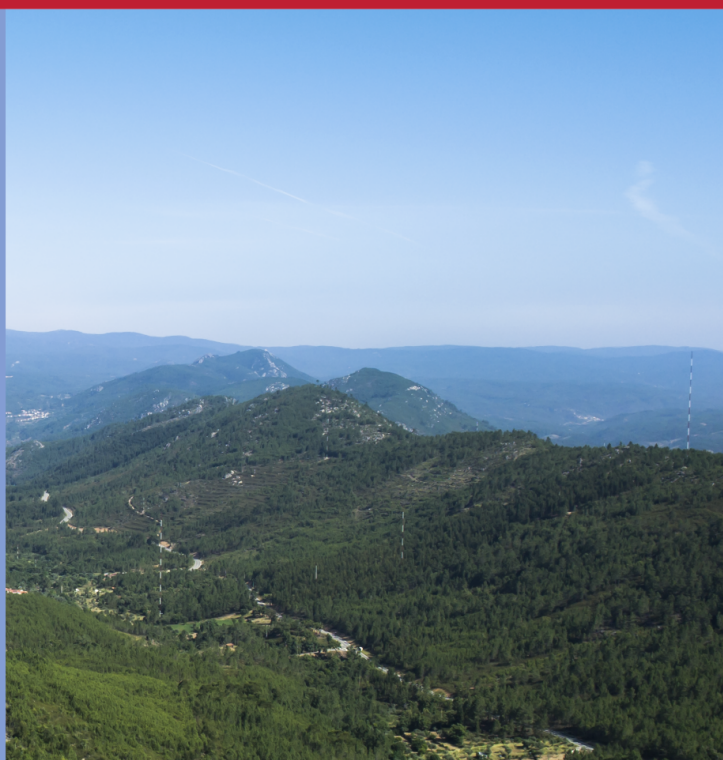
Copyright and moral rights for the publications made accessible in the public portal are retained by the authors and/or other copyright owners and it is a condition of accessing publications that users recognise and abide by the legal requirements associated with these rights.

- Users may download and print one copy of any publication from the public portal for the purpose of private study or research.
- You may not further distribute the material or use it for any profit-making activity or commercial gain
- You may freely distribute the URL identifying the publication in the public portal

If you believe that this document breaches copyright please contact us providing details, and we will remove access to the work immediately and investigate your claim.

# Mesoscale to microscale coupling for determining site conditions in complex terrain

DTU Wind Energy  
PhD Thesis



Bjarke Tobias Olsen  
DTU Wind Energy PhD-0076 (EN)  
June 2018



**Author:** Bjarke Tobias Olsen

**Title:** Mesoscale to microscale coupling for determining site conditions in complex terrain

**Division:** Department of Wind Energy

**Abstract:**

Accurate estimation of local site conditions, i.e. wind power resources and the turbulence impacting wind turbines, is an important part of wind farm planning. In complex terrain, non-linear microscale models that account for atmospheric stability effects are needed for accurate site assessment, but by themselves they are unable to account for the changing large-scale weather conditions. Therefore, coupling to a mesoscale model, which can provide these variations to the microscale models, is required.

This thesis describes, implements and validates with observed tall mast measurements a novel coupling strategy using the Weather Research and Forecasting (WRF) mesoscale model and the EllipSys3D URANS microscale model for wind downscaling. The coupling strategy is based on forcing the microscale model with momentum and temperature source terms extracted from the time-evolving mesoscale model simulation. These terms are included as source terms instead of the usual lateral boundary conditions. Two cases are presented for sites in simple and complex terrain.

First, results from simple terrain cases are presented. It is shown that a Single-Column Model (SCM) version of microscale model forced by tendencies from WRF results in long-term wind statistics of comparable statistical accuracy to results using the WRF model itself. Using different Planetary Boundary Layer and Surface Layer schemes in the WRF model simulations shows that the SCM results tend to follow the WRF model results, while maintaining a statistically similar response near the surface.

Second, the coupling method was used at the complex double hill site Perdigão. It was shown that for a simulation using 80 m grid spacing and a first-order accurate discretisation scheme, the coupled approach results in large improvements in wind statistics compared to downscaling with the WRF model with an innermost domain of 333 m grid spacing. At four masts situated on top of the two ridge tops, the mean biases in wind speed for a 32-day period were less than 3% at the top most anemometer on each mast, compared to mean errors of 8–12% and 17–25% for WRF domains of 1 km and 333 m grid spacing, respectively.

Despite the encouraging results, a clear dependence on grid spacing and numerical methods was seen in the coupled model results. Uncertainties remain about possible *double-counting* of turbulent fluxes, and its impact on the simulated wind speed, when RANS turbulence closures are used for transient atmospheric modeling at fine resolution.

*The thesis is submitted to the Danish Technical University in partial fulfillment of the requirements for the PhD degree.*

**DTU PhD-0076(EN)**

**DOI: 10.11581/DTU:00000036**

**June 2018**

**Sponsorship:**

ERA-NET Plus

*New European Wind Atlas* project  
FP7-ENERGY.2013.10.1.2

**Pages: 167**

**References: 242**

**Figures: 50**

**Tables: 22**

Wind Energy Department  
Technical University of Denmark  
P.O.Box 49  
DK-4000 Roskilde  
Denmark  
Telephone +45 46774005  
bibl@dtu.dk  
Fax +45 46774013  
www.dtu.dk









## **Declaration**

I hereby declare that except where specific reference is made to the work of others, the contents of this dissertation are original and have not been submitted in whole or in part for consideration for any other degree or qualification in this, or any other university. This dissertation is my own work and contains nothing which is the outcome of work done in collaboration with others, except as specified in the text and Acknowledgements.

Bjarke Tobias Olsen

June 2018

15 June 2018 Bjarke Tobias Olsen



## Acknowledgements

A number of people have helped to make this project possible, and I am deeply grateful for their assistance along the way.

First of all, I would like to thank my four supervisors, Jake Badger, Andrea Hahmann, Dalibor Cavar, and Jakob Mann, for their continuous support throughout the project. Secondly, to all my colleagues, and especially to Neil Davis, Rogier Floors, Patrick Volker, Robert Menke, Jacob Berg, Mark Kelly, Anna Maria Sempreviva, Xiaoli Larsen, Andreas Bechmann, Andrey Sogachev, and Poul van der Laan, for helping me with scientific and technical questions. Likewise, thank you to Javier Sanz Rodrigo and Roberto Chávez-Arroyo for fruitful discussions. Thank you to all the people who worked hard in the field collection measurements from Perdigo, and the other sites. Thank you to Eigil Kaas for inspiring me to pursue a Ph.D. in the first place, and to Hans Jørgensen for being instrumental in making it happen.

Thanks you to my fellow Ph.D. students, and office room-mates, Ásta Hannesdóttir, Julia Lange, and Jianting Du. Special thanks to Asta and Jacob Berg for giving me a ride home many times.

Thank you to Yavor Hristov and Mark Zagar for taking good care of me during my research stay at Vestas. Thank you to Lawrence Buja and family for your hospitality during my stay in Boulder. Thank you to Caroline Draxl for showing me around at NREL.

Special thanks to Nynne and the rest of my family for enduring, and supporting me throughout.

The Ph.D. project was financially supported by the NEWA ERA-NET Plus project, topic FP7-ENERGY.2013.10.1.2, and by the Technical University of Denmark, and for that I am also grateful.



## Résumé

En vigtig del af planlægning af vindfarme er præcise vindbetingelseseestimater. I komplekst terræn kræves ikke-linære mikroskalamodeller som tager højde for stabilitetseffekter for at opnå præcise estimater, men disse modeller kan i sig selv ikke tage højde for storskala vejr variationer, hvilket kræver kopling til mesoskalamodeller.

Med udgangspunkt i mesoskalamodellen *Weather Research and Forecasting* (WRF) og URANS mikroskalamodellen *EllipSys3D*, præsenterer denne afhandling en meso- til mikroskala koblingsmetode til vind nedskalering, ved at drive mikroskalamodellen med momentum og temperatur kildeled udtrukket fra mesoskalamodellen.

Metoden bliver i første omgang studeret i terræn med simpelt kompleksitet. Her vises det, at en Single-Column model (SCM) version af mikroskalamodellen drevet af tendenser fra WRF resulterer i vindstatistik som er sammenlignelig med WRFs præcision. Resultaterne viser også, at når forskellige *Planetary Boundary Layer* og *Surface Layer* skemaer anvendes i WRF, følger SCM resultaterne WRF resultater, mens en statistisk ens respons ses i den nederste del af grænselaget.

Dernæst bliver metoden brugt til at modellere *Perdigão*, en dobbelt-bakke, i komplekst terræn. Ved en simulering med 80 m celleafstande og et diskretiseringsskema med lav numerisk nøjagtighed, viste studiet at metoden resulterede i store vindstatistiske forbedringer sammenlignet med nedskalering med WRF ned til 333 m celleafstande. På toppen af bakkerne var den gennemsnitlige afvigelse for vindhastigheder mindre end 3% ved toppen af masterne, mens de var henholdsvis 8-12% og 17-25% for WRF domæner med 1 km og 333 m celleafstande.

Selvom resultaterne er lovende, ses en klar afhængighed af celleafstande og numeriske metoder. Der er fortsat usikkerheder omkring mulig *double-counting* af turbulente fluxe, og hvilken indflydelse det har når RANS *closures* anvendes til transient modelering af atmosfæren i høj opløsning.





# Table of contents

<b>List of figures</b>	<b>xvii</b>
<b>List of tables</b>	<b>xix</b>
<b>Nomenclature</b>	<b>xxi</b>
<b>1 Introduction</b>	<b>1</b>
1.1 Motivation . . . . .	1
1.2 Objectives . . . . .	4
1.3 Main contributions . . . . .	5
1.4 Outline of the thesis . . . . .	7
<b>2 Atmospheric modeling and mesoscale to microscale downscaling</b>	<b>9</b>
2.1 Atmospheric modeling . . . . .	9
2.1.1 Atmospheric flow . . . . .	9
2.1.2 Microscale modeling . . . . .	14
2.1.3 Mesoscale models . . . . .	16
2.1.4 Atmospheric <i>gray scale</i> modeling . . . . .	17
2.2 Mesoscale-microscale model coupling . . . . .	18
2.3 Wind downscaling . . . . .	20
<b>3 Microscale model</b>	<b>21</b>
3.1 Model description . . . . .	21
3.1.1 Turbulence closure . . . . .	23
3.1.2 Single column model version . . . . .	26
3.2 Temperature relaxation . . . . .	27
3.3 Rayleigh damping of gravity waves . . . . .	27

<b>4</b>	<b>Coupling via tendencies in simple terrain</b>	<b>29</b>
4.1	Methodology . . . . .	30
4.1.1	Validation sites . . . . .	30
4.1.2	Microscale model setup . . . . .	31
4.1.3	Mesoscale model setup . . . . .	31
4.1.4	Mesoscale and microscale model coupling . . . . .	37
4.2	Results . . . . .	40
4.2.1	Impact of forcing terms . . . . .	42
4.2.2	GABLS3 . . . . .	46
4.2.3	Sensitivity of wind statistics to WRF SL-PBL schemes . . . . .	51
4.2.4	Surface layer metrics at Cabauw . . . . .	56
4.2.5	Stability dependence of wind profile . . . . .	61
4.2.6	Wind shear by hour and month . . . . .	63
4.3	Summary and conclusions . . . . .	64
<b>5</b>	<b>Coupling via tendencies in complex terrain</b>	<b>67</b>
5.1	Methodology . . . . .	67
5.1.1	Validation site . . . . .	67
5.1.2	Microscale model configuration . . . . .	69
5.1.3	Mesoscale model configuration . . . . .	73
5.1.4	Mesoscale and microscale model coupling . . . . .	78
5.2	Results . . . . .	89
5.2.1	Resolved scales and sensitives . . . . .	89
5.2.2	Validation of results for one month . . . . .	95
5.3	Summary and conclusions . . . . .	124
<b>6</b>	<b>Conclusions</b>	<b>133</b>
6.1	Summary . . . . .	133
6.2	Implications and future perspectives . . . . .	136
<b>Appendix A</b>	<b>Additional resources for thesis chapters</b>	<b>139</b>
A.1	Chapter 4 . . . . .	139
A.1.1	WRF namelist.input sample . . . . .	139
A.1.2	EllipSys1D sample input file (input.dat) . . . . .	141
A.2	Chapter 5 . . . . .	143
A.2.1	WRF namelist.input sample . . . . .	143
A.2.2	EllipSys3D input file sample (input.dat) . . . . .	145

---

A.2.3	Convergence of EllipSys3D results . . . . .	147
<b>Appendix B</b>	<b>An intercomparison of mesoscale models at simple sites for wind en- ergy applications</b>	<b>155</b>
<b>References</b>		<b>175</b>



# List of figures

2.1	Characteristic scales of atmospheric modeling . . . . .	10
2.2	Idealized wavenumber-spectra of atmospheric kinetic energy . . . . .	11
2.3	Diurnal cycle of the ABL . . . . .	12
2.4	Wind profiles and stability . . . . .	13
4.1	Vertical distribution of grid levels in the SCM . . . . .	31
4.2	WRF domains . . . . .	32
4.3	land-use classes . . . . .	32
4.4	Schematic of coupling . . . . .	39
4.5	Taylor diagram: statistics for different forcing terms . . . . .	45
4.6	GABLS3: wind speed, wind direction, and temperature . . . . .	47
4.7	GABLS3: TKE and dissipation of DTKE . . . . .	48
4.8	GABLS3: vertical profiles . . . . .	50
4.9	Taylor diagram for Cabauw . . . . .	52
4.10	Taylor diagram for FINO3 . . . . .	53
4.11	Vertical mean wind speed profiles and distributions of wind speed and direction	57
4.12	Scatter plots: friction velocity, heat flux, and temperature scale . . . . .	59
4.13	Scatter plots: Obukhov length, wind shear exponent, and TKE . . . . .	60
4.14	Normalized wind speed profiles by stability . . . . .	62
4.15	Mean shear exponent by time-of-day and month-of-year . . . . .	63
5.1	The Perdigão site . . . . .	68
5.2	Locations of the masts . . . . .	70
5.3	Structure of grid cells in microscale grid . . . . .	71
5.4	Layout of microscale grid cells . . . . .	72
5.5	Surface elevation in the microscale grids . . . . .	72
5.6	WRF domains layout . . . . .	76
5.7	Land use classification . . . . .	77

5.8	Vertical profiles of relative magnitude of momentum tendency-terms . . . . .	79
5.9	Distribution of WRF grid cells around Perdigão . . . . .	80
5.10	Horizontal and vertical planes of instantaneous tendencies . . . . .	81
5.11	Distribution of tendencies . . . . .	83
5.12	Illustration of coupling method . . . . .	84
5.13	Time series of forcing . . . . .	86
5.14	Resolved topography in models . . . . .	91
5.15	Sensitivity of wind speeds to grid spacing and numerical descretization scheme	92
5.16	Sensitivity of TKE to grid spacing and numerical descretization scheme . .	94
5.17	Vertical planes of flow at 01:30 UTC 23 April 2017 . . . . .	97
5.18	Horizontal planes of flow at 01:30 UTC 23 April 2017 . . . . .	98
5.19	Vertical planes of flow at 04:00 UTC 7 May 2017 . . . . .	100
5.20	Horizontal planes of flow at 04:00 UTC 7 May 2017 . . . . .	101
5.21	Vertical planes of flow at 12:00 UTC 23 April 2017 . . . . .	102
5.22	Horizontal planes of flow at 12:00 UTC 23 April 2017 . . . . .	103
5.23	Summary of modelled and observed flow at mast 7 . . . . .	105
5.24	Summary of modelled and observed flow at mast 10 . . . . .	107
5.25	Summary of modelled and observed flow at mast 20 . . . . .	109
5.26	Summary of modelled and observed flow at mast 22 . . . . .	111
5.27	Summary of modelled and observed flow at mast 25 . . . . .	113
5.28	Summary of modelled and observed flow at mast 27 . . . . .	115
5.29	Summary of modelled and observed flow at mast 29 . . . . .	117
5.30	Summary of modelled and observed flow at mast 34 . . . . .	119
5.31	Summary of modelled and observed flow at mast 37 . . . . .	121
5.32	Power spectral density of wind speed . . . . .	125
A.1	Residuals during sensitivity study 40 m grid . . . . .	148
A.2	Residuals during sensitivity study 80 m grid . . . . .	149
A.3	Residuals during sensitivity study 40 m grid . . . . .	150
A.4	Residuals during the long G03-Q simulation . . . . .	151
A.5	Residuals during the long G03-U simulation . . . . .	152
A.6	Residuals during the long G02-U simulation . . . . .	153

# List of tables

3.1	Coefficients for the $k$ - $\varepsilon$ model . . . . .	23
4.1	WRF model configuration. . . . .	33
4.2	Range of adaptive WRF timesteps . . . . .	34
4.3	First order PBL schemes used for WRF simulations. . . . .	35
4.4	1.5 order (TKE) PBL schemes used for WRF simulations. . . . .	35
4.5	Mesoscale simulations . . . . .	41
4.6	SCM simulations . . . . .	41
4.7	Wind speed statistics at Cabauw for SCM forced by different tendency-terms	43
4.8	Wind speed statistics at FINO3 for SCM forced by different tendency-terms	44
4.9	Wind speed statistics for Cabauw . . . . .	54
4.10	Wind speed statistics for FINO3 . . . . .	55
4.11	Stability classes . . . . .	61
5.1	Computational grids for the microscale model . . . . .	71
5.2	WRF model configuration . . . . .	74
5.3	Range of adaptive time-steps observed . . . . .	77
5.4	EllipSys3D simulations . . . . .	89
5.5	Wind speed statistics for mast 7 . . . . .	106
5.6	Wind speed statistics for mast 10 . . . . .	108
5.7	Wind speed statistics for mast 20 . . . . .	110
5.8	Wind speed statistics for mast 22 . . . . .	112
5.9	Wind speed statistics for mast 25 . . . . .	114
5.10	Wind speed statistics for mast 27 . . . . .	116
5.11	Wind speed statistics for mast 29 . . . . .	118
5.12	Wind speed statistics for mast 34 . . . . .	120
5.13	Wind speed statistics for mast 37 . . . . .	122





# Nomenclature

## Roman Symbols

$C$	Mean part of generic variable: $U$ , $V$ , and $\Theta$ ...
$c$	Generic variable: $u$ , $v$ , and $\theta$ ...
$c'$	Fluctuating part of generic variable: $u'$ , $v'$ , and $\theta'$ ...
$C_\varepsilon$	Kolmogorov relation coefficient in 1.5 order PBL schemes ...
$C_{\varepsilon 1}$	$k$ - $\varepsilon$ turbulence closure coefficient ...
$C_{\varepsilon 1}^*$	$k$ - $\varepsilon$ turbulence closure coefficient ...
$C_{\varepsilon 2}$	$k$ - $\varepsilon$ turbulence closure coefficient ...
$C_{\varepsilon 2}^*$	$k$ - $\varepsilon$ turbulence closure coefficient ...
$C_{\varepsilon 3}$	$k$ - $\varepsilon$ turbulence closure coefficient ...
$C_\mu$	$k$ - $\varepsilon$ turbulence closure coefficient ...
$C_p$	Specific heat capacity for dry air at reference state $\simeq 1000 \text{ [J K}^{-1} \text{ kg}^{-1}]$ ...
$D$	Horizontal wind direction [ $^\circ$ ] ...
$F$	Forcing term for $U$ , $V$ [ $\text{m s}^{-2}$ ], and $\Theta$ [ $\text{K s}^{-1}$ ] ...
$f_c$	Coriolis parameter [ $\text{s}^{-1}$ ] ...
$G$	Geostrophic wind speed [ $\text{m s}^{-1}$ ] ...
$g$	Gravitational acceleration [ $\text{m}^2 \text{s}^{-1}$ ] ...
$H$	Sensible heat flux [ $\text{W m}^{-2} \text{s}^{-1}$ ] ...

---

$h$	Boundary layer height [m] ...
$k$	Turbulent kinetic energy [ $\text{m}^2 \text{s}^{-2}$ ] ...
$k_w$	Wavenumber [ $\text{m}^{-1}$ ] ...
$L$	Obukhov length [m] ...
$l$	Turbulent length scale [m] ...
$l_B$	Turbulent length scale in QNSE PBL scheme [m] ...
$l_b$	Turbulent length scale in MYNN PBL scheme [m] ...
$l_e$	Turbulent length scale in MYJ PBL scheme [m] ...
$l_{max}$	Global maximum turbulent length scale in $k$ - $\epsilon$ turbulence closure [m] ...
$l_N$	Turbulent length scale in QNSE PBL scheme [m] ...
$l_s$	Turbulent length scale in MYNN PBL scheme [m] ...
$l_t$	Turbulent length scale in MYNN PBL scheme [m] ...
$L_{avg}$	Averaging box size [m] ...
$M$	Molar mass of air $\simeq 29$ [ $\text{g mol}^{-1}$ ] ...
$\mathbb{B}$	Buoyant production/destruction of turbulent kinetic energy [ $\text{m}^2 \text{s}^{-3}$ ] ...
$\mathbb{P}$	Shear production term of turbulent kinetic energy [ $\text{m}^2 \text{s}^{-3}$ ] ...
$\mathbb{T}$	Averaging time [s] ...
$N$	Brunt-Väisälä frequency [ $\text{s}^{-1}$ ] ...
$n$	Number of samples in population ...
$n_x$	Number of grid cells in $x$ direction ...
$n_y$	Number of grid cells in $y$ direction ...
$n_z$	Number of grid cells in $z$ direction ...
$p$	Air pressure [Pa] ...
$q$	$\sqrt{2k}$ [ $\text{m s}^{-1}$ ] ...

---

$q_c$	Turbulent velocity scale ...
$R$	Universal gas constant $\simeq 8.313 \text{ [JK mol}^{-1}]$ ...
$r$	Correlation coefficient ...
$Re$	Reynolds number ...
$Ri_b$	Bulk Richardson number ...
$Ri_g$	Gradient Richardson number ...
$\mathbb{S}$	Scale factor in the eddy viscosity equations in the WRF 1.5 order PBL schemes ...
$S$	Horizontal wind speed $[\text{m s}^{-1}]$ ...
$T$	Air temperature $[\text{K}]$ ...
$t$	Time $[\text{s}]$ ...
$U$	Ensemble mean velocity components $[\text{m s}^{-1}]$ ...
$u$	Velocity components $[\text{m s}^{-1}]$ ...
$u'$	Fluctuating velocity components $[\text{m s}^{-1}]$ ...
$U_{LOS}$	Line-of-sight velocities from LIDAR scans $[\text{m s}^{-1}]$ ...
$U_p$	Horizontal velocities in LIDAR plane $[\text{m s}^{-1}]$ ...
$U_r$	Reference wind speed $[\text{m s}^{-1}]$ ...
$u_*$	Friction velocity $[\text{m s}^{-1}]$ ...
$V$	Ensemble mean velocity components $[\text{m s}^{-1}]$ ...
$v$	Velocity components $[\text{m s}^{-1}]$ ...
$v'$	Fluctuating velocity components $[\text{m s}^{-1}]$ ...
$W$	Ensemble mean velocity components $[\text{m s}^{-1}]$ ...
$w$	Velocity components $[\text{m s}^{-1}]$ ...
$w'$	Fluctuating velocity components $[\text{m s}^{-1}]$ ...
$x$	Cartesian coordinates $[\text{m}]$ ...

---

$y$	Cartesian coordinates [m] ...
$z$	Cartesian coordinates [m] ...
$z_0$	Roughness length [m] ...
$z_{0t}$	Thermal roughness length [m] ...

### Greek Symbols

$\alpha$	Vertical wind speed shear exponent from log-law ...
$\alpha_B$	$k$ - $\varepsilon$ model variable, scaling Bouyant dissipation of TKE ...
$\alpha_{my}$	Mellor and Yamada (1974) coefficient in turbulent length scale equation ...
$\Delta t$	Model time step [s] ...
$\Delta x$	Model grid spacing [m] ...
$\Delta y$	Model grid spacing [m] ...
$\Delta z$	Model grid spacing [m] ...
$\varepsilon$	Dissipation rate of turbulent kinetic energy [ $\text{m}^2 \text{s}^{-3}$ ] ...
$\gamma_C$	Counter gradient term in YSU PBL scheme for generic variable $C$ ...
$\kappa$	Von Kármán constant, $\simeq 0.4$ ...
$\lambda$	Latitude [ $^\circ$ ] ...
$\mu$	Dynamic molecular viscosity [ $\text{kg m}^{-1} \text{s}^{-1}$ ] ...
$\mu_t$	Dynamic turbulent eddy viscosity [ $\text{kg m}^{-1} \text{s}^{-1}$ ] ...
$\mu_\Theta$	Dynamic thermal eddy conductivity [ $\text{kg m}^{-1} \text{s}^{-1}$ ] ...
$\nu$	Kinematic molecular eddy viscosity [ $\text{m}^2 \text{s}^{-1}$ ] ...
$\nu_t$	Kinematic turbulent eddy viscosity [ $\text{m}^2 \text{s}^{-1}$ ] ...
$\nu_\Theta$	Kinematic thermal eddy conductivity [ $\text{m}^2 \text{s}^{-1}$ ] ...
$\nu_C$	Eddy diffusivity of generic variable $C$ ...
$\Omega$	Rotation rate of the earth [ $\text{rad s}^{-1}$ ] ...

$\Phi$	Model grid cell centers in fixed heights ...
$\phi$	Stability function in Monin-Obukhov similarity theory ...
$\pi$	Ratio of a circle's circumference to its diameter, $\simeq 3.14$ ...
$\psi$	Integral form of the stability function in Monin-Obukhov similarity theory ...
$\rho$	Air density [ $\text{kg m}^{-3}$ ] ...
$\sigma$	Standard deviation of wind speed [ $\text{ms}^{-1}$ ] ...
$\sigma_\varepsilon$	Schmidt number for turbulent kinetic energy dissipation ...
$\sigma_k$	Schmidt number for turbulent kinetic energy ...
$\sigma_\Theta$	Turbulent Prandtl number ...
$\tau_d$	Vertical structure of Rayleigh damping ...
$\tau_r$	Temperature nudging relaxation time-scale [s] ...
$\Theta$	Ensemble mean potential temperature [K] ...
$\theta$	Potential temperature [K] ...
$\theta'$	Fluctuating (turbulent) part of the potential temperature [K] ...
$\Theta^*$	Potential temperature corrected via nudging [K] ...
$\Theta_r$	Reference temperature [K] ...
$\Theta_v$	Virtual potential temperature [K] ...
$\Theta_*$	Temperature scale in Monin-Obukhov similarity theory ...
$\zeta$	Dimensionless height in Monin-Obukhov similarity theory ...

### Superscripts

$()^E$	EllipSys (1D or 3D) quantity ...
$()^{E\neq}$	Rest/other EllipSys (1D or 3D) results ...
$()^M$	Modelled quantity ...
$()^O$	Observed quantity ...

- $()^T$  Transpose ...
- $()^w$  WRF quantity ...
- $()^{w\neq}$  Rest/other WRF results ...

### Subscripts

- $()_{1,2,3}$  Longitudinal, lateral, and vertical directions ...
- $()_{ADV}$  Advective term ...
- $()_{agl}$  Above ground level ...
- $()_{COR}$  Coriolis term ...
- $()_{CURV}$  Curvature term ...
- $()_{DIFF}$  Horizontal diffusion term ...
- $()_g$  Geostrophic part ...
- $()_{i,j,k}$  Spatial components in tensor notation ...
- $()_{PGF}$  Pressure-gradient term ...
- $()_{PHYS}$  Physics (PBL and microphysics) term term ...
- $()_r$  Reference value ...
- $()_{RAD}$  Radiation term ...
- $()_{RAY}$  Rayleigh damping term ...
- $()_a$  Ambient value ...
- $()_s$  Surface value ...
- $()_{asl}$  Above sea level ...

### Other Symbols

- $\dot{()}$  Time derivative ...
- $\langle () \rangle$  Time average ...
- $\overline{()}$  Population average ...

**Acronyms / Abbreviations**

ABL	Atmospheric boundary layer ...
ACM	Asymmetrical convective model ...
ASL	Atmospheric surface layer ...
CBL	Convective boundary layer ...
CFD	Computational fluid dynamics ...
CNR	Carrier-to-noiseratio ...
CORINE	Coordination of information on the environment ...
DNS	Direct numerical simulation ...
DTKE	Dissipation rate of turbulent kinetic energy ...
DTU	Technical university of Denmark ...
EPSG	European petroleum survey group ...
FFT	Fast Fourier transform ...
FINO	Forschungsplattformen in Nord- und Ostsee ...
GABLS	GEWEX atmospheric boundary layer study ...
GEWEX	Global energy and water cycle experiment ...
HR SST	High resolution sea surface temperature ...
KAMM	Karlsruhe atmospheric mesoscale model ...
LBC	Lateral boundary condition ...
LES	Large eddy simulation ...
LIDAR	Light detection and ranging ...
LLJ	Low level jet ...
LOS	Line of sight ...
LRWS	Long range wind scanner ...



MAE Mean absolute error ...

ME Mean error ...

MM5 Penn. state university / NCAR numerical model 5 ...

MOST Monin-Obukhov similarity theory ...

MYJ Mellor–Yamada–Janjic ...

MYNN Mellor–Yamada and Nakanishi and Niino ...

NCAR National center for atmospheric research ...

NEWA New European wind atlas ...

NWP Numerical weather prediction ...

PANS Partially-averaged Navier-Stokes ...

PBL Planetary boundary layer ...

PGF Pressure gradient force ...

QNSE Quasi-normal scale elimination ...

QUICK Quadratic upstream interpolation for convective kinematics ...

RANS Reynolds-averaged Navier-Stokes ...

RASS Radio acoustic sounding system ...

RMSE Root-mean-square error ...

SBL Stable boundary layer ...

SCM Single-column model ...

SIMPLE Semi-implicit method for pressure linked equations ...

SODAR Sonic detection and ranging ...

SRTM Shuttle radar topography mission ...

TKE Turbulent kinetic energy ...

UDS Upwind discretization scheme ...

USGS United states geological survey ...

UTC Coordinated universal time ...

VSBL Very stable boundary layer ...

WAsP Wind analysis and application program ...

WRF Weather research and forecasting ...

WSBL Weakly stable boundary layer ...

YSU Yonsei university ...



# Chapter 1

## Introduction

### 1.1 Motivation

Over the last couple of decades, wind energy has become a central part of electricity generation in large parts of the world. As of 2016 the global installed capacity was 486GW, with annual growth rates of 17% and 12.6% in 2015 and 2016 (GWEC, 2016), and further growth is expected. In Europe, the wind energy share of electricity generation is projected to increase from 11% in 2015 to 16.5% in 2020 (Windeurope, 2017). To accommodate the demand, wind turbines need to be installed in many types of terrain, including locations characterized by complex wind flow, including sites near mountains, forests, and coastlines.

An important part of wind farm development is to accurately estimate the local wind climate for each wind turbine, as this will determine the resource for a specific turbine. Typically, the wind climate is given by a probabilistic description of the expected inflow conditions the turbine is exposed to throughout its lifetime. This includes the wind speed distribution, and flow characteristics such as turbulence and wind shear, which are important for estimating extreme loads on the turbine.

The estimation of wind climates has relied on measurements at or near the turbine site. Obtaining measurements from masts entails erecting and instrumenting one, or several, towers, collecting measurements for several years, monitoring, and maintaining the instruments. Five years of measurements, or more, are recommended to capture yearly variations (Landberg et al., 2003), making the whole endeavour expensive. Thus, in practice, much shorter periods are typically used. Point-measurements from masts are further limited by the fact that variations in the local flow, owing to inhomogeneities in the terrain and obstacles, are only valid over a limited area, spanning from meters to tens of kilometers or more, depending on the complexity of the terrain.

To reduce costs and uncertainties, numerical models are increasingly used in combination with measurements, for estimating wind climates. *Numerical Weather Prediction* (NWP) models are used to extend measurements through long-term correction methods (Vanvyve et al., 2015), or even to replace measurements entirely (Badger et al., 2014; Hahmann et al., 2014; Landberg et al., 2003). However, as discussed by Olsen et al. (2017), typical *mesoscale* (Orlanski, 1975) NWP models are operated at a grid spacing that render them unable to capture local effects of orography or surface roughness changes. This fact motivates a model-chain approach consisting of a sequence of coupled models that can capture the full range of phenomena that influence the local wind climate, essential for the accurate assessment of wind resource and site design conditions.

Flow models of varying complexity and computational cost can be used to obtain local flow corrections from the terrain and obstacles, to measurements or NWP output, generalizing the local wind climate beyond to other nearby locations in the region. Linear flow models, based on the work of Jackson and Hunt (1975), were popularized with the publication of the *European Wind Atlas* Troen and Petersen (1989) and the development of the *Wind Atlas Analysis and Application Program* (WAsP) (Mortensen et al., 2004). More recently, non-linear *Computational Fluid Dynamics* (CFD) models have gradually been incorporated in wind resource applications for steep terrain, where non-linear effects are especially important. Besides better resolving flow around steep slopes and capturing important features such as flow-separation, they also allow for a quantification of high shear and turbulence regions. The term “computational fluid dynamics” originates in engineering, and encompasses different methods of solving the Navier-Stokes equations for solving hydro- and aerodynamic problems.

The least computationally expensive way of simulating local flow effects using a non-linear model is to consider neutrally stratified flows and assume that Coriolis effects are small perturbations to the background flow. Under these assumption, the mean wind speed change relative to undisturbed flow due to terrain effects is independent of the Reynolds number. These assumptions allow for steady-state modeling of terrain effects by direction only, e.g. WAsP-CFD (Troen et al., 2014), wherein *Reynolds averaged Navier-Stokes* (RANS) type CFD models are used to solve the equations. RANS models are a subgroup of CFD models, where the (ensemble) mean part of the flow is solved and the turbulent part is parameterized in a closure model.

Assuming the *Atmospheric Boundary Layer* (ABL) to be neutrally stratified is justified in many cases (Landberg et al., 2003); either because atmospheric stability effects are rare (they happen at negligible wind speeds) or because neutral stratification represent the mean

effects of the combination of unstable and stable conditions well at the site. However, in some cases, capturing the influence of atmospheric stratification on the flow can be very important. It influences the wind resources by increasing the wind shear, and it interacts with the topography, steering the flow around hills and through gaps during stable stratification, and by increasing turbulence levels and favouring flow over hills during unstable conditions (Wallace and Hobbs, 2006). Both cases can have a large effect on the wind resource and turbine loads.

To accommodate non-neutral conditions and to resolve transient phenomena in the ABL, RANS-type CFD models are increasingly extended to include buoyancy and Coriolis forces used in combination with a transient RANS modeling approach (Koblitz et al., 2015; Rodrigues et al., 2015). These enhancements allow the models to solve much more of the ABL dynamics such as nocturnal *Low-Level Jets* (LLJ), land and sea breezes, and other transient phenomena.

CFD models used in complex terrain are typically solved on model domains with a horizontal extend of the order of ten kilometers. As such, these models are unable to account for the "larger" atmospheric modes associated with the changing weather. Integrating a transient CFD model forward in time thus requires appropriate boundary conditions that reflect the actual state of the larger-scale weather patterns. To this end, a NWP model may be coupled to the CFD model, to provide these boundary conditions.

The most common coupling methodology, i.e. methodology for feeding information from a coarse-scale model to a fine-scale model, is through *Lateral Boundary Conditions* (LBCs), where the governing variables are interpolated from the coarse-scale model onto the lateral boundaries of the fine-scale grid, constantly updating them in time, to drive the model forward. An alternative approach, which is explored in this thesis, is to couple the models via source terms, corresponding to the large-scale geostrophic forcing and advection, as discussed by e.g. Baas et al. (2010); Bosveld et al. (2014); Sanz Rodrigo et al. (2017b). The *Pressure-Gradient Force* (PGF) and advective tendencies are extracted from the NWP model and added to the CFD model as source terms in the governing equations.

Using transient CFD modeling, as opposed to steady-state modeling, can be exceedingly computationally expensive, because, just as for mast measurements, several years of simulation are required to capture the long-term wind climate. However, utilizing statistical-dynamical downscaling techniques to subset the time-period in question into climatically representative samples, or cases, can reduce the cost significantly, e.g. (Chávez-Arroyo et al., 2018; Reyers et al., 2015; Rife et al., 2013). In cases where non-neutral conditions or transient phenomena are prevalent, the benefit of better representing the wind climate, may outweigh the additional cost of computations.

Beyond resource assessment, an additional benefit of transient methodologies is that they can be used for wind power forecasting also. In this case, instead of generating a reanalysis of the wind climate, the wind field is simulated for the coming hours or days. Wind forecasting serve as an important assistance for wind farm and electricity grid operators, and electricity traders.

## 1.2 Objectives

The purpose of research described in this thesis was to develop methodologies for improving the assessment of wind resources in complex terrain. Specifically, it was to develop a model-chain based on coupling of mesoscale NWP models and *microscale* CFD models, enabling downscaling of the wind climate to turbine scales with applicability to a range of weather conditions, including non-neutral atmospheric stability. A separate objective of the thesis was to study uncertainties of mesoscale models, to evaluate the need for using a coupled meso-microscale model-chain for site assessment.

The starting point for the microscale modeling was the *EllipSys3D*  $k$ - $\epsilon$  RANS flow solver (Michelsen, 1992, 1994; Sørensen, 1995), which has been used for steady-state *Atmospheric Surface Layer* (ASL) modeling, known as WAsP-CFD. Recently, this model was modified to allow for more general atmospheric boundary layer (ABL) flow-conditions by including buoyancy and Coriolis forces (Koblitz et al., 2015). Buoyancy forces were included by adding a transport equation for temperature and allowing density variations to impact the gravitation acceleration term via the Boussinesq approximation. Furthermore, modifications were made to the  $k$ - $\epsilon$  turbulence closure to take non-neutral conditions into consideration (Sogachev et al., 2012). Previous to the work in this thesis, the model was verified for idealized transient flow cases, where the model was forced by a constant background pressure gradient and a varying surface temperature. Validation of the model with more realistic boundary conditions for modeling of real complex cases, was needed. Koblitz (2013) noted that one of the main improvements for the model would be to provide realistic boundary conditions, and pointed to using NWP models to provide them. Additionally, several unanswered questions lingered, including what methodology to use for estimating the turbulent length-scales in the turbulent closure, which relies on the non-local Mellor and Yamada (1974) length-scale limitation, and may benefit from using a local method.

The work in this thesis was supported by the *New European Wind Atlas* (NEWA) ERA-NET Plus project, which aims to create a next-generation wind atlas covering Europe. It

succeeds the European wind atlas (Troen and Petersen, 1989), which was itself a landmark for wind energy at the time it was created, and helped accelerate the methodologies used for resource assessment in wind energy ever since. To reach its goal, the NEWA project aims to advance the wind energy science, both in terms of improving models and by creating invaluable measurement datasets by carrying out large field campaigns in challenging terrain. The field campaigns in the project includes *Perdigão*, a double-hill in Portugal, *Alaiz* a highly complex site within a valley in northern Spain, and *Kassel* a forested hill in Germany. In this thesis it was not possible to include results from all sites, so the focus was on the *Perdigão* campaign, which was also the most ambitious one, in terms of instrumentation.

An important part of developing the model-chain, was to investigate coupling methodologies between the NWP and the CFD models. This involved a literature review of existing methodologies, choosing a methodology, exploring the technique, and validation at several sites, in particular complex sites, such as *Perdigão*.

## 1.3 Main contributions

### Peer-reviewed journal papers

- Olsen, B.T., Hahmann, A.N., Sempreviva, A.M., Badger, J., Jørgensen, H.E. *An intercomparison of mesoscale models at simple sites for wind energy applications*, 2017, Wind Energy Science, 2(1):211-228, DOI:10.5194/wes-2-211-2017
- Olsen, B.T., Cavar, D., Hahmann, A.N., Kelly, M., *Mesoscale to microscale coupling via momentum and temperature tendencies: validation in simple terrain*, 2018, Wind Energy Science [IN PREPARATION]
- Olsen, B.T., Cavar, D., *Mesoscale to microscale coupling via momentum and temperature tendencies in complex terrain*, 2018, Wind Energy Science [IN PREPARATION]

### Conference presentations

- Olsen, B.T., Hahmann, A.N., Sempreviva, A.M., Badger, J., Jørgensen, H.E., *Simulating wind energy resources with mesoscale models: Intercomparison of state-of-the-art models*, European Wind Energy Conference, 2015, November 17 - 20, 2015, Paris Expo – Porte de Versailles, Paris
- Olsen, B.T., Cavar, D., Hahmann, A.N., Badger, J., Mann, J., *Modelling atmospheric flow over complex terrain using an unsteady-RANS model forced by mesoscale model*,



Wind Energy Science Conference 2017, 26 June - 29 June 2017, Technical University of Denmark

### Workshop/project presentations

- Olsen, B.T., Cavar, D., Hahmann, A.N., Badger, J., Mann, J., *Generating large-scale tendencies from WRF for microscale model forcing*, Annual meeting, New European Wind Atlas project, April 24 – 26, 2017, Pamplona, Riga
- Olsen, B.T., Cavar, D., Hahmann, A.N., Badger, J., Mann, J., *Towards seamless downscaling for AEP in complex terrain*, Bi-Annual meeting, New European Wind Atlas project, October 23 – 25, 2017, Riga, Latvia

### Posters

- Olsen, B.T., Badger, J., Hahmann, A.N., Cavar, D., Mann, J., *Wind resource assessment in complex terrain using a one-way coupled meso- and microscale model approach*, 17th WRF Users' Workshop, June 27 – July 1, 2016, Boulder Colorado.
- Olsen, B.T., Badger, J., Hahmann, A.N., Cavar, D., Mann, J., *Improving wind climate estimation using one-way coupled meso- to microscale models*, 2015, EAWC PhD seminar, September 22 – 25, 2015, University of Stuttgart

### Numerical code implementation

- EllipSys3D: Implementation of several adjustments and features, such as Rayleigh-damping, temperature nudging adjustment, and more.
- WRF: modifications to include extraction of momentum and temperature tendencies to the standard output variables
- wrfinpy: Python package for running WRF in consecutive simulations, postprocessing and plotting, including treatment of the momentum and temperature tendencies to accommodate more easy generation of input for the microscale model.
- ellipsual: Python package for running EllipSys3D in consecutive simulations, including generation of the relevant mesoscale input, and for postprocessing and plotting of the EllipSys3D output.

## 1.4 Outline of the thesis

The thesis is divided into seven chapters. Chapter 1 (current chapter) contains a general introduction. A short summary of each of the chapters is given here:

Chapter 2 provides background information relevant for understanding the physical system and the complications related to modeling of ABL flow. Furthermore, a review of the state of mesoscale and microscale modeling for site assessment, and efforts to couple meso- and microscale models are given.

In chapter 3, the unsteady RANS microscale model formulation is described, including a description of a Single-Column model (SCM) version of the 3D model.

Chapter 4 presents a study of forcing the SCM, described in chapter 3, by momentum and temperature tendencies, as well as surface temperatures, derived from the WRF model, for a calendar year at two sites characterized by simple terrain. The objective was to validate the coupling technique for a range of weather conditions, and to study the long-term effects on the wind climate relative to the mesoscale model results.

Chapter 5 builds on the findings described in Chapter 4, by studying mesoscale to microscale coupling via momentum and temperature tendencies, and surface temperatures, in complex terrain at the Perdigão site. The study includes validation for a one month period with mast measurements, as well as a study of events observed by long-range WindScanner LIDARs at the site.

Chapter 6 summarizes the thesis and provides a discussion of the future work that can further advance the coupled meso-microscale methodology to improve wind climate estimation at complicated sites.



## **Chapter 2**

# **Atmospheric modeling and mesoscale to microscale downscaling**

### **2.1 Atmospheric modeling**

A range of atmospheric numerical models are used to solve atmospheric flows at many different scales. Broadly speaking they can be divided into two categories based on how they evolved: 1) NWP models historically used by meteorologists for weather and climate prediction, and 2) CFD models used by engineers to solve complex flow around buildings, bridges, and other objects. Both types of models are computational fluid dynamics models, but at this point the name is associated with the engineering lineage. NWP and CFD models used for atmospheric applications have historically been developed to operate at very different spatial scales. However, with advances in computing power, NWP models are gradually used for smaller and smaller scales, while CFD models are able to solve bigger and bigger problems, with an increased demand for more realistic boundary conditions and physics, which means that the models are converging at intermediate scales and are gradually solving overlapping problems. In the following a summary of the physical system, i.e. flow in the atmosphere and flow in the ABL in particular, is given. This is followed by a description of mesoscale and microscale models, and their utilization to wind energy applications. Finally meso- to microscale model coupling is discussed.

#### **2.1.1 Atmospheric flow**

The Earth's atmosphere is a global heat-transporting fluid in motion, seeking equilibrium from the uneven state caused by differential heating of the planet. This redistribution of heat

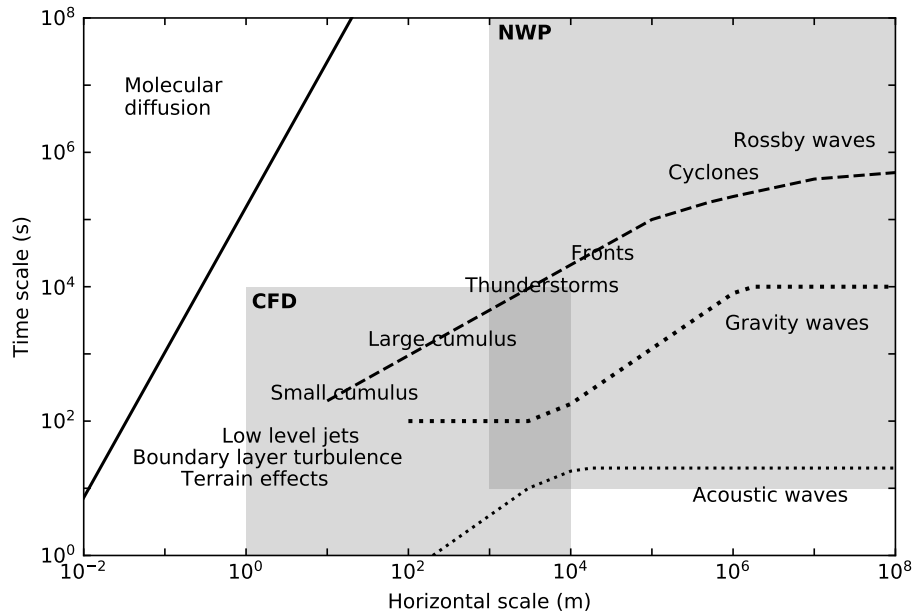


Fig. 2.1 Characteristic time and horizontal scales of different atmospheric phenomena. The shaded gray areas span the typical range of scales solved by NWP and CFD models, respectively. The figure is a modified adaption of Fig. 1.1 from (Lauritzen et al., 2011).

ultimately causes motion on a range of characteristic temporal and spatial scales, subdivided into different phenomena by e.g. Orlandi (1975).

At planetary scales  $O(\sim 10000 \text{ km})$  potential vorticity conserving *Rossby waves* govern the flow. They are associated with the *jet stream* and atmospheric pressure systems. The *synoptic* scales  $O(\sim 1000 \text{ km})$  include most high-pressure systems and extratropical cyclones, and their associated warm- and cold fronts. The “medium” scales, called *mesoscales*, span approximately from  $\sim 200 \text{ km}$  to  $\sim 1 \text{ km}$  and include single cumulus clouds up to large convective systems and frontal zones. The smallest (turbulent) scales are known as the *microscales*, they contain turbulent eddies in the PBL that vary in size from approximately the size of the depth of the PBL down to millimeters. At smaller scales molecular diffusion converts kinetic energy to heat.

Figure 2.1 shows the characteristic length and time scales of a range of atmospheric phenomena. The gray boxes indicate the approximate scales resolved by the NWP and CFD models. It should be noted that the resolvable scales for CFD models are dependent on the model formulation. Some formulations, such as RANS, assume a scale-separation and solve only for the slowly changing steady, or pseudo-steady solution, treating the smallest scales of motion by a turbulence closure model (see below). Wind turbines are situated in the ABL

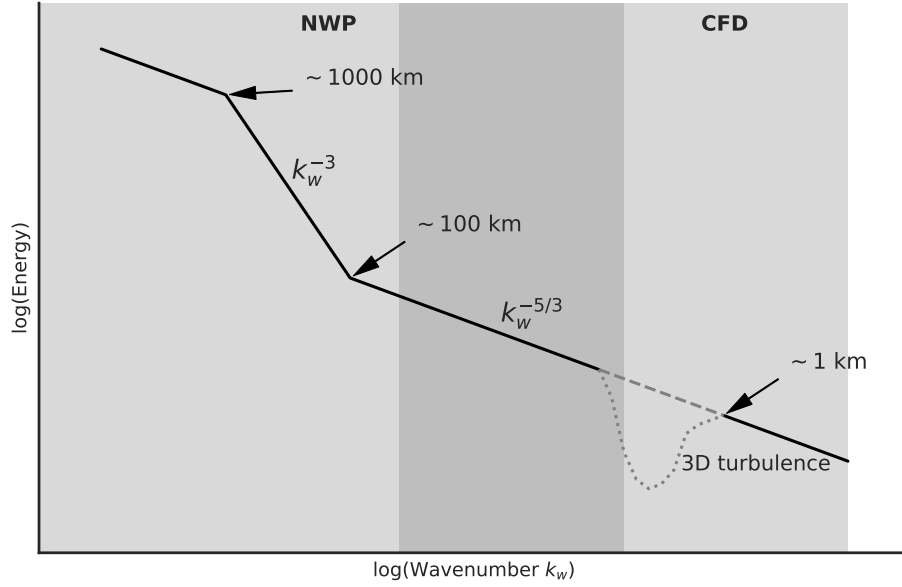


Fig. 2.2 Idealized representation of the horizontal wavenumber spectra of kinetic energy observed in the atmosphere. The dip represented by the dotted gray line indicate the *spectral gap* observed in some studies.

and experience the turbulent flow there, but the nature of the flow depends on the full range of phenomena, which is why they need to be accounted for by the models.

The distribution of kinetic energy in the atmosphere on different horizontal scales is illustrated in figure 2.2. It represents the most common interpretation from atmospheric observations (Kaimal and Finnigan, 1994; Nastrom and Gage, 1985). The presence of the  $k_w^{-3}$  range at the largest scales is subject to ongoing debate. Some interpret the range as a downscale enstrophy cascade (Lindborg, 1999), while some question the validity of the  $k_w^{-3}$  scaling itself, and argue that it is a result of analysis error (Lovejoy et al., 2009). The dynamics causing the  $k_w^{-5/3}$  scaling at intermediate scales are also a subject of ongoing debate. Possible explanations for its existence include that it is a 3D forward energy cascade from interacting gravity waves, or that it is a 2D inverse energy cascade with energy input from deep cumulus convection. The high wave-number part of the spectrum represents the 3D turbulence range. The dip in energy illustrated by the dotted line in Fig. 2.2 represent a *spectral gap*, that has been observed in some studies, under certain conditions (Babic et al., 2017; Gjerstad et al., 1995; Guo Larsén et al., 2018). The spectral gap represents a range of scales with low variability in-between the diurnal and semi-diurnal signal and turbulence. Even though the dynamics behind the observed scaling patterns is not well understood it is often used to argue for the validity of atmospheric models Skamarock (2004).

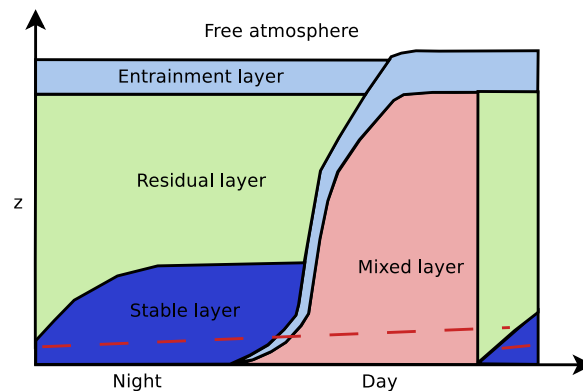


Fig. 2.3 The diurnal cycle of the ABL during fair weather conditions. It shows the growing well-mixed day-time layer, which is detached from the surface as a stable night-time layer grows underneath. The dashed red line signify the top of the surface layer. Adapted from Fig. 9.21 from Wallace and Hobbs (2006)

The gray boxes in Fig. 2.1 and 2.2 indicate scales typically solved by NWP and CFD models, respectively. It illustrates why coupling between these two types of models is important, i.e. CFD models solve terrain effects well, but lack information about the large-scale flow, which may be provided by the NWP model.

### The atmospheric boundary layer

(ABL) makes up the lowest part of the troposphere. It is the layer between the surface and the rest of the atmosphere, and is the layer where the influence of the surface is felt most, which is why the atmosphere above it is sometimes referred to as the *free atmosphere*. The thickness of the layer varies in time, between a few meters up to  $\sim 4$  km, but typical heights are  $\sim 1$  km, or 10% of the depth of the troposphere (Stull, 1988). The top of the ABL is associated with a shallow statically stable layer that separates it from the rest of the atmosphere.

The ABL can be approximately subdivided into three vertical layers: the atmospheric surface layer (ASL), the ABL core, and the entrainment or capping layer. The ASL makes up the lowest 10% of the ABL. In this layer surface friction dominates, and momentum and temperature fluxes are approximately constant with height, and Coriolis effects are small. In the ABL core region momentum and temperature fluxes start to decrease, and surface friction becomes less important, while Coriolis effects become more important.

During fair weather conditions, typically associated with high-pressure systems, the diurnal cycle of the ABL evolves in a predictable way, as illustrated by figure 2.3. During the day, as the surface heats up, shallow thermals heated by the surface, rise and cause mixing throughout the ABL, increasing the ABL depth through exchange with the air in the

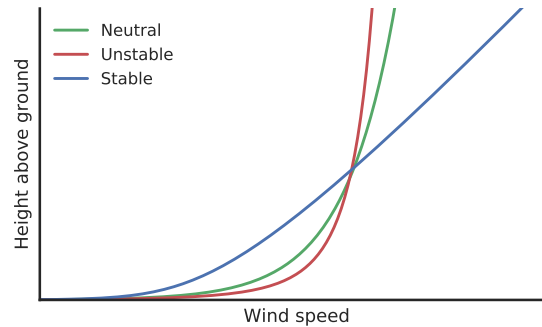


Fig. 2.4 Wind speed profiles associated with different atmospheric stability. Adapted from Fig. 9.17 from Wallace and Hobbs (2006)

free atmosphere. This process is known as *entrainment*. This daytime ABL dominated by thermals is also known as the convective boundary layer (CBL). As the sun sets, the emission of longwave radiation cools the surface, causing a gradually growing stable layer near the ground, and causing a detachment of the upper well-mixed daytime layer, known as the *residual layer*. This, stable boundary layer (SBL), may be further subdivided into the weakly stable boundary layer (WSBL), and the very stable boundary layer (VSBL) (Grachev et al., 2005). In the WSBL, turbulence is weak but persistent and mechanical mixing maintain a heat flux towards the cooling surface. In the VSBL, turbulence is intermittent and weak mechanical mixing is unable to maintain a heat flux towards the surface, causing *runaway cooling* where the surface and upper air become detached from each other (Louis, 1979). During overcast skies and strong surface winds the boundary layer may be considered near-neutral.

Atmospheric stability in the ASL is associated with different shapes of the vertical wind speed profile, illustrated in Fig. 2.4. The turbulence during unstable conditions causes more mixing of momentum downwards, causing a steep gradient of wind speed just above the surface and a more homogeneous wind speed with height higher up. During stable conditions, the friction from the ground is decoupled from the wind above, and mixing is weak, causing a less homogeneous, steeper gradient of wind speed with height.

Near coastlines, mountains, forested areas, and cities, many additional effects occur. In mountainous terrain the interplay between the topography and buoyancy forces cause a range of phenomena that influence the flow. In general, positively buoyant air will tend to rise above hills, while negatively buoyant air will tend to sink and flow around hills.



### 2.1.2 Microscale modeling

*Computational fluid dynamics* is the common name given to a range of methods used to solve the Navier-Stokes equation. Many methods exist, but the three main approaches are: *Direct Numerical Simulation* (DNS), *Large-Eddy Simulation* (LES), and *Reynolds-Averaged Navier-Stokes* (RANS).

DNS models solve the full range of scales relevant to a turbulent system. From the largest scales, including the integral length scale of turbulence, all the way to the dissipative *Kolmogorov microscales* (Landahl and Mollo-Christensen, 1992). This requires a very fine-scaled computational mesh, and it is (currently) exceedingly costly for atmospheric simulations of any significant spatial and temporal extent.

LES models (Deardoff, 1970; Smagorinsky, 1963) use a spatial (low-pass) filtering of the Navier-Stokes equations to avoid the computational cost of solving the smallest scales of the flow. The filtering involves splitting the flow into grid-scale and Subgrid-Scale (SGS) components, and parameterizing the sub-grid stresses via a grid-size-dependent SGS model. LES models have been used for many atmospheric applications, including: flow in urban environments (Letzel et al., 2008; Tseng et al., 2006; Walton et al., 2002; Xie and Castro, 2008, 2009; Xie et al., 2008), atmospheric boundary layer studies (Basu and Porté-Agel, 2006; Beare et al., 2006; Kumar et al., 2006; Stoll and Porté-Agel, 2008), flow over terrain (Bechmann, 2006; Uchida and Ohya, 2003), cumulus cloud studies (Matheou et al., 2011; Seifert and Heus, 2013; Siebesma et al., 2003), and for flow around wind turbines and wind farms (Calaf et al., 2010; Lu and Porté-Agel, 2011; Porté-Agel et al., 2013, 2011; Zhang et al., 2012).

RANS models (Reynolds, 1895) utilize time-filtered equations. They use Reynolds decomposition to separate the instantaneous flow  $u$  field into the mean  $U$  and fluctuating variables  $u' = u - U$ , solving only for the mean part. However, the evolution of the mean flow depends on the fluctuating (turbulent) part. This is known as the *closure problem*. In fact, any order of flow equations depends on higher order terms. To close the equations, the turbulent fluxes are related to known quantities via a closure model, of which there are many. The most commonly used ones for ABL flow modeling are based on the *eddy viscosity* concept, that relates gradients of the mean flow to turbulent mixing through eddy viscosity. Estimating the eddy viscosity may be done simply via the mean flow gradients themselves (first-order closure), or it may be based on higher order quantities. Commonly, a *two-equation closure* is used, which, as the name suggests, involves transport equations for two additional variables, e.g. *Turbulent Kinetic Energy* (TKE or  $k$ ) and *Dissipation rate of Turbulent Kinetic Energy*

(DTKE or  $\varepsilon$ ) (Launder and Spalding, 1974), known as the  $k$ - $\varepsilon$  model. RANS models can be used to solve either steady-state problems, in which case the time-derivative is omitted, and the flow solution gradually relaxed towards a steady-state, or it may be solved as a transient solution, keeping the time-derivative. This is known as unsteady RANS, or URANS (Nakayama and Miyashita, 2001). For URANS problems, scale-separation is assumed to be maintained because the integral timescale of the mean flow is assumed to be slower than the integral timescale of the most energetic turbulent eddies. This is discussed further in section 2.1.4. RANS models have been used for atmospheric flow including: flow over terrain (Bechmann and Sørensen, 2011; Castro et al., 2003; Huser et al., 1997; Koblitz et al., 2015; Sørensen, 1995), wind turbine wakes (Cabezón et al., 2011; El Kasmi and Masson, 2008), and around building and urban areas (Blocken et al., 2007, 2012; Franke et al., 2011; Hanna et al., 2006; Vu et al., 2002; Yang et al., 2008).

While a neutral-atmosphere incompressible fluid approach has been used for CFD modeling of atmospheric applications (Castro et al., 2003; Huser et al., 1997; Sørensen, 1995), a need for more realistic ABL physics has pushed development of CFD models. For wind energy applications, one of the top priorities has been to allow for modeling of non-neutral atmospheric stability conditions (Castro et al., 2008, 2010; Chang et al., 2018; Koblitz et al., 2015; Meissner et al., 2009; Rodrigues et al., 2015). However, with the addition of temperature transport equations and buoyancy forces, a number of considerations arise, of both numerical/technical and physical nature, that further complicate ABL modeling, including consideration of surface coupling (Basu et al., 2008; Holtslag and Svensson, 2013), and boundary layer depth limitation (Sescu and Meneveau, 2014).

A separate category, and the most simple, of microscale flow models are linearized flow models. These were the first models widely used for wind resource assessment, and remain widely used. They are derived from linearising the Navier-Stokes equation, i.e. by assuming an attached boundary layer flow with small gradients and using scaling analysis to justify omitting high-order and non-linear terms. This means that influences of orography, surface roughness changes, obstacles, and stability are treated as small perturbations to the background flow (Jackson and Hunt, 1975; Troen and Petersen, 1989; Walmsley et al., 1986). Because the models are linear, their computational cost is negligible on modern computer hardware. Linear methods lose their validity in steep terrain, but terrain-correction methods have been developed to attempt to improve the performance in steep terrain with some success Mortensen et al. (2006).

### 2.1.3 Mesoscale models

The first NWP models were used to forecast the patterns of the large-scale high-altitude Rossby waves, by integrating the 500 hPa pressure surface forward in time (Charney et al., 1950). Through the years, the range of applications and the complexity of the models have increased steadily. From coarse-resolution climate models, used to model the past and future climate (Collins et al., 2006) operated at  $O(\sim 100 \text{ km})$ , to global weather prediction models (Baldauf et al., 2011; Lin, 2004; Skamarock et al., 2008, 2010) typically operated at  $O(\sim 10 \text{ km})$  grid spacing, to regional mesoscale models that are operated at  $O(\sim 1 \text{ km})$ . Mesoscale models resolve phenomena at the mesoscales (described above), e.g. they are convection-permitting models. They are used for weather forecasting (Baldauf et al., 2011), hindcasting (Al-Yahyai et al., 2010), atmospheric research (Yair et al., 2010), and more. For wind energy, mesoscale models have become a key component for resource assessment (Hahmann et al., 2014; Jimenez et al., 2007), wind power forecasting (Foley et al., 2012; Monteiro et al., 2009), and planning (Balog et al., 2016). One of the most commonly used mesoscale model is the *Weather Research and Forecasting* (WRF) modeling system (Skamarock et al., 2008). The WRF model is easy to access, has strong community support, and it includes a multitude of configuration options that allow for vast customization.

Because NWP models are weather models, they do not just integrate the continuous equations for momentum, heat and moisture, but incorporate important physical processes, such as the transfer of radiation, surface ocean properties, soil, and land-surface properties. Also included are cloud and precipitation processes. As such, they are much more general than most CFD models, but at an additional computational cost.

Mesoscale models are operated at grid-scales  $O(\sim 1 \text{ km})$  and above, and thus do not resolve the 3D turbulence in the PBL. Instead, they rely on turbulence parameterization schemes, commonly called *Planetary Boundary Layer* (PBL) schemes, that, just like the RANS-type CFD models discussed below, rely on turbulence closure models that relate known quantities to turbulent diffusion. A range of closure models exists, but the two most common types used are: first-order non-local closures (Hong et al., 2006; Pleim, 2007) and local TKE schemes (Janjić, 1994; Nakanishi and Niino, 2006; Sukoriansky et al., 2005) that solve a transport equation for turbulent kinetic energy. A review of PBL schemes can be found in Cohen et al. (2015) and Kleczek et al. (2014) and their sensitivities in different environments are studied in e.g.: Dimitrova et al. (2016); Draxl et al. (2014); García-Díez et al. (2013); Hariprasad et al. (2014); Hu et al. (2010); Milovac et al. (2016); Muñoz-Esparza et al. (2016); Sathyanadh et al. (2017); Shin and Dudhia (2016).

During the last few decades, the WRF NWP model has been gradually enhanced to make it suitable for solving atmospheric flows at scales below  $O(\sim 1 \text{ km})$ . LES SGS models have

been implemented that allow for the model to be operated without the RANS-type PBL schemes that is normally used (Mirocha et al., 2014, 2010; Moeng et al., 2007). WRF-LES has already been used for a range of applications, including studies of: offshore CBLs (Muñoz-Esparza et al., 2014a), flow in complex terrain (Munoz-Esparza et al., 2017; Rai et al., 2017a,b; Talbot et al., 2012), SBL turbulence (Udina et al., 2016; Wang et al., 2013), cloudy boundary layers (Yamaguchi and Feingold, 2012), and wind energy applications (Liu et al., 2011; Mirocha et al., 2015).

#### 2.1.4 Atmospheric *gray scale* modeling

The length scale of the most energetic turbulent eddies in the ABL varies from centimeters to several kilometers. At grid-scales much larger than the turbulent length scale (mesoscale range), atmospheric models cannot resolve the eddies, and must rely on turbulence models, based on the RANS principles of scale separation, that account for effects of turbulent fluctuations on the mean flow. When several of the largest turbulent eddies fit inside a single model grid cell, and when the integral model time-step is larger than the integral timescale of the eddies, it is easy to see that the turbulence model accounts for the ensemble mean influence of many subgrid/sub-timescale eddies.

When the model grid spacing is much smaller than the characteristic turbulent length scale (LES range), the model resolves the largest eddies that are responsible for the bulk of the turbulent flux transport, violating the RANS assumption of a scale-separation between the resolved (mean) flow, and the turbulent fluxes, which is why LES models use an SGS model that filter by scale, not by time. At the intermediate scales, where the grid spacing and the turbulent length scales are of the same order of magnitude, both the RANS and the LES assumptions are violated. Wyngaard (2004) coined the term *terra incognita* for these scales, while others refer to them as the *gray scales*. These scales are the subject of ongoing research (Honnert et al., 2011; Poll et al., 2017; Zhou et al., 2014), for the development of scale-aware model parameterizations that work outside the inertial range of turbulence as well (Kitamura, 2016).

In the case of wind climate modeling for determining wind farm site conditions, the gradually increasing computational resources available allow for dynamical climate modeling at scales below  $O(1 \text{ km})$ , but using an LES-type model would require using a model grid spacing guaranteed to resolve scales within the inertial range of turbulence, that for the WSBL could be smaller than  $O(\sim 1 \text{ m})$ , far exceeding reasonable computational cost for climate estimation. For climate estimation purposes, using a turbulence closure model that does not have this restriction remains attractive at the gray scales .

It has been suggested that RANS closure models at the *gray scales* runs the risk of double counting turbulence effects (Baklanov et al., 2011), while others suggest that the practical implications may be limited because the explicit and modelled turbulence both feed on the same available energy, causing a competition where the earliest or strongest mixing mechanics suppress additional mixing from the other (Arnold et al., 2012; Hong and Dudhia, 2012). It remains uncertain at what scales RANS-type closures are appropriate. Arnold et al. (2012) suggests that it may be appropriate to run WRF with a PBL scheme at scales as low as 300 – 500 m grid spacing.

An alternative to spatial-filtered (LES) closures, and time-filtered (RANS) closures, is TKE-filtered *Partially-Averaged Navier-Stokes* (PANS) closures (Girimaji, 2006). The PANS closure filters the equations based on the ratio of the modelled turbulent length scales, and the grid-scale, reducing the eddy viscosity when turbulent eddies are resolved at the grid-scales, and defaulting to a RANS-closure when turbulence is subgrid-scale. However, to the authors knowledge the PANS methodology has not been applied to atmospheric flows as of now.

## 2.2 Mesoscale-microscale model coupling

For many applications, including wind energy site assessment, the region of interest for modelling spans only a limited area. CFD model-domains used for atmospheric applications typically span  $O(\sim 10 \text{ km})$  in horizontal direction. This means that, for real-time atmospheric simulations, appropriate boundary conditions that reflect the changing weather patterns must be provided to the model, e.g. from a mesoscale model. The process of continuously cascading the instantaneous flow field information from one model to another is sometimes referred to as *dynamical coupling* (Warner, 2011), and *mesoscale to microscale coupling* is understood as coupling of a mesoscale model with an LES, RANS, or other type of microscale model. Dynamical model coupling, i.e. exchanging information, may be done in a *one-way*, with no feedback from the fine domain to the coarse domain, or it may be *two-way*, with feedback and it may be *online*, where the solutions of both domains are integrated forward in time at the same time or it may be *offline*, where the solutions of the first and second domain are solved separately. The coupling can be done within the same modeling system, such as is often the case for WRF (Skamarock et al., 2008), or it can be done between different models.

For dynamical model coupling, the most common communication approach between models is through lateral boundary conditions (LBCs) (Warner, 2011). In this approach LBCs are continuously provided to the fine-scale domain, i.e. the prognostic variables are interpolated from the coarse-scale domain onto the lateral boundaries fine-scale domain.

Inconsistencies in model physics, parameterization, and numerical methods, between the two domains, means that the flow in the fine-scaled domain requires a spin-up region, a *fetch*, where the flow gradually adjusts towards balanced self-consistent state. The model solution in the fetch-region may be error prone, and should generally not be trusted (Warner, 2011). This is especially true in mountain regions where differences in resolved topography can give rise to differences in surface elevation, and where the input of LBCs can create gravity waves reflection requiring a lateral damping zone. Another challenge with using LBCs is related to model coupling across the atmospheric *gray scales*, where additional consideration must be made when dealing with the transition from ensemble-averaged (smooth) flow in the coarse-scale domain to eddy-resolving (turbulent) flow in the fine-scale domain (Mazzaro et al., 2017; Muñoz-Esparza et al., 2014b, 2015).

Another methodology for dynamical coupling explored in this thesis, is the model coupling via momentum and temperature tendencies. In this approach, the fine-scale domain (CFD domain in this case) is forced via source terms, rather than LBCs, consisting of relevant momentum and temperature tendencies extracted from the large-scale model domain. This approach was used for Single-Column Model (SCM) evaluation by e.g. (Bosveld et al., 2014; Sanz Rodrigo et al., 2017b) to investigate turbulence closure models for a diurnal cycle where geostrophic shear and advection, of both momentum and temperature, played a role in forming a nocturnal-LLJ at the Cabauw mast in the Netherlands. To the authors knowledge, coupling via tendencies, has not been used before for non-idealized cases in complex terrain. The methodology requires the use of periodic boundary conditions, and hence smoothing of topography near the domain boundaries. The methodology has several desirable properties: 1) the spin-up, or fetch region of LBCs approaches, is replaced by a smoothed region near the boundary and periodic boundary conditions, resulting in fewer issues related to model-inconsistencies and no need for Rayleigh damping at the lateral boundaries, 2) Concerns related to applying a divergent velocity field to the boundaries are avoided, 3) for LES domains the recirculation of the flow via cyclic boundary conditions reduces the need for perturbation techniques for turbulence spin-up, 4) a background pressure gradient is often used to drive CFD models, forcing the flow via body-forces, so this approach also fits well into the existing methodologies. However, the methodology of extracted tendencies from a mesoscale model and using them to drive another model is largely unexplored, so it remains a question whether it can be widely generalized.

## 2.3 Wind downscaling

Downscaling of the wind fields has many application within wind energy. Dynamical downscaling is used for planning, power production forecasting, power system simulation, in- and outflow characterization, turbine control, and studies of wakes from turbines and terrain. For complex terrain flow, dynamical downscaling has been done based on mesoscale models coupled to both URANS-type CFD models (Castro et al., 2010; Duraisamy et al., 2014; Ely et al., 2012; Gopalan et al., 2014; Rodrigues et al., 2015), and to LES (Horvath et al., 2012; Lundquist et al., 2010; Muñoz-Esparza et al., 2016, 2017; Rai et al., 2017a,b; Wang et al., 2013), all utilizing coupling via LBCs. Dynamical downscaling, although computationally costly, may also be used for wind resource assessment and estimation of fatigue and extreme loads on turbines. A cheaper alternative though is the use of statistical-dynamical techniques to reduce the required simulation time (Badger et al., 2014; Chávez-Arroyo et al., 2018; Frank et al., 2001; Rife et al., 2013).

Statistical downscaling has been used for wind resource assessment for several decades, Jackson-Hunt type downscaling methodologies (Troen and Petersen, 1989) were originally used for horizontally extrapolating mast measurements. This methodology has since advanced to allow the use of model datasets in place of measurements for input. Generally, the procedure has three steps: 1) obtaining a statistical representation of the wind climate at a location from a reanalysis dataset or through modeling, 2) generalizing the model wind climate by removing modelled mesoscale or microscale effects, and finally 3) downscaling the wind climate to the local site using Jackson-Hunt type models. This approach has been used for generating wind atlases of Ireland with the KAMM/WAsP method (Frank et al., 2001), a wind atlas of South-Africa with the WRF/WAsP method (Hahmann et al., 2014), and even the whole world with the Global Wind Atlas methodology (Badger et al., 2016). A similar approach, is the use of mass-conserving models (Brower, 1999; Scire et al., 2000) instead of Jackson-Hunt type models, likewise coupled to NWP models as for example the SiteWind method (Brower, 1999).

A separate class of downscaling methodologies are long-term correction methods that use measurements at the site to find empirical relations between a long-term model dataset and the overlapping measurement period to synthetically extent the measurements into the full period covered by the model (Vanvyve et al., 2015; Zhang et al., 2015)

For wind climate estimation in complex terrain no clear methodology has emerged as the clear dominant one, and further development of both mesoscale models, microscale models, and coupling procedure is needed. However, one promising approach seems to be dynamical coupling of meso- and microscale models, combined with statistical-dynamical downscaling methodologies. Further exploration of this is needed.

# Chapter 3

## Microscale model

### 3.1 Model description

The microscale model is based on the *Reynolds-Averaged Navier-Stokes* (RANS) equations including Bouyancy and Coriolis forces; the turbulence closure is a modified  $k-\varepsilon$  two-equation closure. The model has been implemented in the *EllipSys3D* finite-volume CFD code at the *Technical University of Denmark* (DTU). An in-depth description of the modeling system can be found in Michelsen (1992), Michelsen (1994), and Sørensen (1995). A description of the modifications that enable non-neutral atmospheric stratification is described in Koblitz (2013). In the following, a summary is given.

To arrive at the RANS equations, Reynolds decomposition is used to split the instantaneous atmospheric motion  $u_i$  into the mean  $U_i$  and the fluctuating part  $u'_i$ , such that  $u_i = U_i + u'_i$ . The subscript  $i$  refer to spatial indices in Einstein notation, implying  $x_i = (x_1, x_2, x_3) = (x, y, z)$  and  $U_i = (U, V, W)$ , where  $x, y, z$  are Cartesian coordinates and  $U, V, W$  are velocities along those coordinates. The mean part  $U_i$  refers to the ensemble mean, i.e., the mean of many realizations of the same flow. For stationary, or quasi-stationary atmospheric conditions, the ensemble-average  $U$  converges towards the time-average  $\langle u \rangle$  given a long enough averaging period  $\mathbb{T}$ ,

$$\langle u_i(t) \rangle = \frac{1}{\mathbb{T}} \int_t^{t+\mathbb{T}} u_i(t) dt \quad (3.1)$$

The length of the characteristic averaging period depends on the integral time-scale (the time-step) of the model, and the amount of variance in the flow. The underlying assumption is that the convergence is achieved such that  $\langle u_i(t) \rangle \approx U_i(t)$ .

RANS models can be solved as a steady state problem, where the time-derivative is ignored. In that case, a steady-state solution is iteratively found by solving the system of equations until changes in the field are sufficiently small. Since the model will here be used



for transient problems, the time-derivative is retained. This is referred to as unsteady-RANS (URANS) modeling. The scale-separation discussed above is often violated for URANS simulations of high Reynolds-number flows, like flow in the ABL, with fine-scaled model grids (Davidson and Peng, 2003).

The governing continuity, momentum, and temperature RANS equations for incompressible flow are given by:

$$\frac{\partial}{\partial x_i}(\rho U_i) = 0 \quad (3.2)$$

$$\frac{\partial \rho U_i}{\partial t} = \frac{\partial}{\partial x_j} \left[ -\rho U_i U_j + (\mu + \mu_t) \left( \frac{\partial U_i}{\partial x_j} + \frac{\partial U_j}{\partial x_i} \right) \right] - \frac{\partial \hat{p}}{\partial x_i} + g_i(\rho - \rho_0) + \varepsilon_{ijk} f_c \rho U_k + \rho F_{U,i} \quad (3.3)$$

$$\frac{\partial}{\partial t}(\rho \Theta) + \frac{\partial}{\partial x_i}(\rho U_i \Theta) - \frac{\partial}{\partial x_i} \left[ \left( \mu + \frac{\mu_t}{\sigma_\Theta} \right) \frac{\partial \Theta}{\partial x_i} \right] = \rho F_\Theta \quad (3.4)$$

here,  $U_i$  and  $\Theta$  are the mean velocity and the potential temperature. The mean potential temperature follows similar Reynolds decomposition principles, i.e.  $\Theta$  is equal to the fluctuating temperature subtracted from the instantaneous temperature  $\Theta = \theta - \theta'$ .

$f_c = 2\Omega \sin \lambda$  is the Coriolis parameter, where  $\varepsilon_{ijk}^T = (-1, 1, 0)$  and  $\Omega$  and  $\lambda$  are the rotational rate of Earth  $7.272 \times 10^{-5} \text{ rad s}^{-1}$  and the latitude, respectively.  $\mu$  is the molecular viscosity;  $F_{U,i}$  and  $F_\Theta$  represents additional momentum, and heat source-terms.

Buoyancy forces are implemented via the Boussinesq approximation (Boussinesq, 1897), which dictates that variations in the air density  $\rho$  should only influence the gravitational acceleration  $g_i^T = (0, 0, g)$  term. The reference air density  $\rho_0 \approx 1.225 \text{ kg m}^{-3}$ . Furthermore, the Boussinesq approximation requires that density varies linearly with temperature only, such that the ideal gas law is approximated as

$$\rho \approx \frac{M p_0}{RT}, \quad (3.5)$$

where  $p_0 = 10^5 \text{ Pa}$  is the standard atmospheric pressure,  $M = 29 \text{ g mol}^{-1}$  is molar mass of air, and  $R = 8.313 \text{ J K mol}^{-1}$  is the universal gas constant. The temperature  $T$  is replaced by the potential temperature,

$$\Theta = T \left( \frac{p_0}{p} \right)^{R/C_p}, \quad (3.6)$$

where the specific heat capacity for dry air is  $C_p \approx 1000 \text{ J K}^{-1} \text{ kg}^{-1}$ . The pressure  $\hat{p}$ , is the pressure added with the hydrostatic pressure, assuming hydrostatic balance  $\hat{p} = p + \rho_0 g z$ .

Turbulent mixing is modeled using a turbulent viscosity  $\mu_t$  determined by the two-equation turbulence closure (described below). The closure replaces the Reynolds stress term  $\overline{\rho u'_i u'_j}$  with the turbulent eddy viscosity concept based on the Boussinesq hypothesis (Schmitt,

Table 3.1 Coefficients for the  $k$ - $\varepsilon$  model. From Sogachev et al. (2012).

$\kappa$	$C_\mu$	$C_{\varepsilon 1}$	$C_{\varepsilon 2}$	$C_{\varepsilon 3}$	$\sigma_k$	$\sigma_\varepsilon$	$\sigma_\Theta$
0.4	0.03	1.52	1.83	Eq. (3.17)	2.95	2.95	Eq. (3.19)

2007). This closure relates the turbulent mixing to gradients in the mean flow through a eddy viscosity  $\mu_t$  that acts similar to molecular viscosity; except it is typically much greater than the molecular viscosity, which is why the molecular viscosity term is often omitted in high Reynolds-number flows that use this closure:

$$\rho \overline{u'_i u'_j} = -\mu_t \left( \frac{\partial U_i}{\partial x_j} + \frac{\partial U_j}{\partial x_i} \right) + \frac{2}{3} \rho k \delta_{ij}. \quad (3.7)$$

The term  $\frac{2}{3} \rho k \delta_{ij}$ , where  $k$  is turbulent kinetic energy, is absorbed into the pressure term (Sørensen, 1995). The turbulent eddy viscosity is related to the thermal conductivity  $\mu_\Theta$  via the turbulent Prandtl-number,  $\sigma_\Theta = \mu_t / \mu_\Theta$ .

### 3.1.1 Turbulence closure

The turbulence closure is a modified version of the  $k$ - $\varepsilon$  closure (Launder and Spalding, 1974). The modifications enable turbulence modeling of non-neutral atmospheric stability conditions by including buoyancy terms. The length scale determining variables are modified to relate buoyancy constants to existing model constants, and choosing appropriate constants (Sogachev et al., 2012). A description of the implementation is found in Koblitz (2013).

In kinematic terms, where  $\nu = \mu / \rho$  and  $\nu_t = \mu_t / \rho$ , the governing equations for turbulent kinetic energy,  $k$ , and dissipation of turbulent kinetic energy,  $\varepsilon$ , is given by

$$\frac{\partial k}{\partial t} + U_i \frac{\partial k}{\partial x_i} - \frac{\partial}{\partial x_i} \left[ \left( \nu + \frac{\nu_t}{\sigma_k} \right) \frac{\partial k}{\partial x_i} \right] = \mathbb{P} + \mathbb{B} - \varepsilon + \varepsilon_a \quad (3.8)$$

$$\frac{\partial \varepsilon}{\partial t} + U_i \frac{\partial \varepsilon}{\partial x_i} - \frac{\partial}{\partial x_i} \left[ \left( \nu + \frac{\nu_t}{\sigma_\varepsilon} \right) \frac{\partial \varepsilon}{\partial x_i} \right] = \frac{\varepsilon}{k} (C_{\varepsilon 1}^* \mathbb{P} + C_{\varepsilon 3} \mathbb{B} - C_{\varepsilon 2} \varepsilon) + C_{\varepsilon 2} \frac{\varepsilon_a^2}{k_a} \quad (3.9)$$

The turbulent viscosity of  $k$  and  $\varepsilon$  are related to  $\nu_t$  through the so-called Schmidt-numbers  $\sigma_k$  and  $\sigma_\varepsilon$ . They are, along with the other model coefficients  $C_{\varepsilon 1}^*$ ,  $C_{\varepsilon 2}$ , and  $C_{\varepsilon 3}$ , discussed below. Their chosen values are listed in table 3.1. Minimum (ambient) values of turbulence and dissipation of turbulence are added via  $k_a$  and  $\varepsilon_a$  to avoid numerical instabilities and runaway cooling during in VSBL cases. Values of  $k_a = 10^{-4} \text{ m}^2 \text{ s}^{-2}$  and  $\varepsilon_a = 7.208 \times 10^{-8} \text{ m}^2 \text{ s}^{-3}$  are used, following (Koblitz et al., 2015). An additional diffusion term in the  $\varepsilon$  equation

suggested by Sogachev et al. (2012) is not included. It was motivated by inconsistencies observed in Sogachev and Panferov (2006), and proposed to obtain consistent results between the  $k$ - $\varepsilon$  closure model and the  $k$ - $\omega$  closure model (Wilcox, 1998) for simulations of forest canopies, so to narrow the scope of this thesis it is disregarded. The shear production  $\mathbb{P}$  and buoyant production/destruction  $\mathbb{B}$  terms are given by

$$\mathbb{P} = \nu_t \left( \frac{\partial U_i}{\partial x_j} + \frac{\partial U_j}{\partial x_i} \right) \frac{\partial U_i}{\partial x_j}, \quad (3.10)$$

and

$$\mathbb{B} = -\frac{\nu_t}{\sigma_\Theta} \frac{g_i}{\Theta} \frac{\partial \Theta}{\partial x_i}. \quad (3.11)$$

The buoyancy term  $\mathbb{B}$  couples potential temperature to the turbulence model, causing turbulent production for negative potential temperature gradients in  $z$  (unstable conditions), and suppresses turbulence for positive gradients (stable conditions). The eddy viscosity is related to the transported turbulence variables as

$$\nu_t = C_\mu \frac{k^2}{\varepsilon} = C_\mu^{1/4} k^{1/2} l, \quad (3.12)$$

where  $l$  is the characteristic turbulent length scale, which is related to  $k$  and  $\varepsilon$  as

$$l = C_\mu^{3/4} \frac{k^{3/2}}{\varepsilon}. \quad (3.13)$$

As mentioned above, the closure was modified following Sogachev et al. (2012) to appropriately account for buoyancy effects. The classical  $k$ - $\varepsilon$  closure works well for rough-wall and shear flows, but in the atmospheric boundary layer (ABL), buoyancy plays an important role in modulating the turbulent length scale, and the classical  $k$ - $\varepsilon$  closure is known to be too diffusive (Apsley and Castro, 1997; Detering and Etling, 1985). In the VSBL the turbulent length scales can be very small  $O(\sim 1 \text{ cm})$ , or even vanish, while, during free convection in the CBL it may grow as large as several kilometers deep in a well mixed boundary layer. To accommodate both extremes, changes in  $l$  are needed based on the conditions. Following (Apsley and Castro, 1997),  $l$  is modified by defining a  $C_{\varepsilon 1}^*$  that is given by

$$C_{\varepsilon 1}^* = C_{\varepsilon 1} + (C_{\varepsilon 2} - C_{\varepsilon 1}) \frac{l}{l_{max}}, \quad (3.14)$$

where  $l_{max}$  acts as the limiting turbulent length scale (global maximum). The  $\varepsilon$  equation retains the standard behavior of the  $k$ - $\varepsilon$  when  $l$  is much smaller than  $l_{max}$ . When  $l$  approaches  $l_{max}$ ,  $C_{\varepsilon 1}^*$  becomes  $C_{\varepsilon 2}$ , resulting in a balance between destruction and production, ultimately

limiting  $l$  to  $l_{max}$ . Because  $\varepsilon$  tend to dominate near the ground, typically resulting in  $l < l_{max}$ , the model retains log-law behaviour near the ground with the modification.

Sogachev et al. (2012) determines the maximum length scale  $l_{max}$  following Mellor and Yamada (1974):

$$l_{max} = \alpha \frac{\int_0^\infty z \sqrt{k} dz}{\int_0^\infty \sqrt{k} dz}, \quad (3.15)$$

where  $\alpha$  is a constant,  $\alpha = 0.075$  such that  $l_{max}$  is in balance with the Blackadar scale (Blackadar, 1962) during neutral conditions  $l_{max} = 0.00026 G f_c^{-1}$ , where the geostrophic wind is  $G = \sqrt{U_g^2 + V_g^2}$ .

Model coefficients are adapted to the ABL flow as well.  $C_\mu$  is typically chosen to be 0.09 for industrial flows (Launder and Spalding, 1974), while a value of 0.03 is often used for atmospheric flows (Duynderke, 1988; Katul et al., 2004), and also used here. To ensure agreement with the constant-stress logarithmic wind profile near the ground, the relation

$$\sigma_\varepsilon = \frac{k^2}{C_\mu^{1/2} (C_{\varepsilon 2} - C_{\varepsilon 1})} \quad (3.16)$$

is also satisfied (Pope, 2001). The value of the coefficients  $C_{\varepsilon 1} = 1.52$  and  $C_{\varepsilon 2} = 1.83$  from Kantha et al. (2005) were chosen following Sogachev et al. (2012).

To make the modifications self-consistent, and to reduce the requirement for parameter-tuning, Sogachev et al. (2012) related  $C_{\varepsilon 3}$  to the existing model coefficients by

$$C_{\varepsilon 3} = (C_{\varepsilon 1} - C_{\varepsilon 2}) \alpha_{\mathbb{B}} + 1 \quad (3.17)$$

and determines  $\alpha_{\mathbb{B}}$  from the gradient Richardson-number  $Ri_g = \mathbb{B}/\mathbb{P}$  as

$$\alpha_{\mathbb{B}} = \begin{cases} 1 - \frac{l}{l_{max}} & \text{for } Ri_g \geq 0 \\ 1 - \left[ 1 + \frac{C_{\varepsilon 2} - 1}{C_{\varepsilon 2} - C_{\varepsilon 1}} \right] \frac{l}{l_{max}} & \text{for } Ri_g < 0 \end{cases} \quad (3.18)$$

The turbulent Prandtl-number  $\sigma_\Theta$ , which relates turbulent eddy viscosity to eddy conductivity, is likewise varied with  $Ri_g$

$$\sigma_\Theta = \begin{cases} 0.74 & \text{for } Ri_g \geq 0 \\ 0.74 \left( 1 - 15 \left[ \mathbb{B} \left( \mathbb{P} + |\frac{\alpha_{\mathbb{B}} \mathbb{B}}{\sigma_\Theta}| \right)^{-1} \right] \right)^{-1/4} & \text{for } Ri_g < 0 \end{cases} \quad (3.19)$$

The model coefficients are listed in table 3.1.

The friction velocity and sensible heat flux are calculated in the model as

$$u_*^2 = -\mu_t \left( \frac{\partial U_i}{\partial x_j} + \frac{\partial V_j}{\partial x_i} \right) \quad (3.20)$$

and

$$H = \frac{\mu_t}{\sigma_\Theta} \frac{\partial \Theta}{\partial z}. \quad (3.21)$$

### 3.1.2 Single column model version

A Single-Column Model (SCM) version of the EllipSys3D model described above was implemented (see details in van der Laan and Sørensen (2017)). It is referred to as *EllipSys1D* and has been shown to produce results consistent with the the 3D code for simulations of flow over homogeneous terrain in the Leipzig measurements case Lettau (1950), and the *GEWEX (Global Energy and Water cycle EXperiment) Atmospheric Boundary Layer Study 2 (GABLS2)* case (Svensson et al., 2011), but at a substantially lower computational cost. EllipSys1D provides a fast and easy model for implementing changes, for testing them, and for idealized simulations. A summary of how its formulation differs from the 3D code formulation, is given below.

In 1D, only the vertical coordinate  $z$  exists, and the vertical advection in  $z$  is assumed to be negligible. These two assumptions mean that all horizontal gradients  $\frac{\partial}{\partial x}$  and  $\frac{\partial}{\partial y}$ , including horizontal advection, drop out. It also means that there is no continuity equation, or vertical velocity  $W$ . The pressure gradient term also drops out and pressure becomes the hydrostatic pressure, with density variations caused by differences in temperature only. Since no vertical mean motion is assumed to exist, the buoyancy term is dropped as well, and buoyancy only impacts the eddy viscosity closure, increasing or decreasing turbulence-induced mixing. The horizontal momentum, and temperature equations become

$$\frac{\partial U}{\partial t} = -\frac{\partial}{\partial z} \left[ (\mathbf{v} + \mathbf{v}_t) \frac{\partial U}{\partial z} \right] + f_c V + F_U \quad (3.22)$$

$$\frac{\partial V}{\partial t} = -\frac{\partial}{\partial z} \left[ (\mathbf{v} + \mathbf{v}_t) \frac{\partial V}{\partial z} \right] - f_c U + F_V \quad (3.23)$$

$$\frac{\partial \Theta}{\partial t} = -\frac{\partial}{\partial z} \left[ \left( \mathbf{v} + \frac{\mathbf{v}_t}{\sigma_\Theta} \right) \frac{\partial \Theta}{\partial z} \right] + F_\Theta \quad (3.24)$$

The turbulence closure is also modified, dropping horizontal gradients and advection,

$$\frac{\partial k}{\partial t} = -\frac{\partial}{\partial z} \left[ \left( \mathbf{v} + \frac{\mathbf{v}_t}{\sigma_k} \right) \frac{\partial k}{\partial z} \right] + \mathbb{P} + \mathbb{B} - \varepsilon + \varepsilon_a \quad (3.25)$$

$$\frac{\partial \varepsilon}{\partial t} = -\frac{\partial}{\partial z} \left[ \left( v + \frac{v_t}{\sigma_\varepsilon} \right) \frac{\partial \varepsilon}{\partial z} \right] + \frac{\varepsilon}{k} (C_{\varepsilon 1}^* \mathbb{P} - C_{\varepsilon 2} \varepsilon + C_{\varepsilon 3} \mathbb{B}) + C_{\varepsilon 2} \frac{\varepsilon_a^2}{k_a} \quad (3.26)$$

The coefficients and formulation of  $l$ ,  $\alpha_{\mathbb{B}}$ , and  $\sigma_{\Theta}$  remains the same as for the 3D version.

## 3.2 Temperature relaxation

The temperature in the ABL varies due to many processes. During fair weather (associated with high pressure systems), surface heating by the sun typically dominates the daytime temperature evolution, while long-wave radiative cooling dominates the night-time. But other processes play an important role as well, i.e., large-scale heat advection associated with cold and warm fronts and phase-changes associated with precipitation.

While the microscale model is able to account for redistribution of heat during convective conditions, because the process is largely dominated by the heated surface, it lacks the ability to capture many other physical processes, since it is limited to modifying the temperature through fluxes from the surface. For example, the model lacks mechanisms to account for the capping inversion that limits the depth of the convective boundary layer (CBL), radiative cooling throughout the ABL; an important heat-sink during the night, as well as the aforementioned large-scale heat advection and phase-change effects. To incorporate these effects indirectly into the microscale model, temperature nudging is used. The temperature is gradually related towards a reference temperature  $\Theta_r(z, t)$  via the Newtonian cooling method:

$$\Theta^*(z, t) = \Theta(z, t) - \Delta t \frac{\Theta(z, t) - \Theta_r(z, t)}{\tau_r}, \quad (3.27)$$

where  $\Theta^*$  is the corrected temperature,  $\Delta t$  is the model time-step size, and  $\tau_r$  is the characteristic relaxation timescale. The reference temperature profile may be specified either as an idealized profile for more simple studies, or as is the case in this study, be provided from a mesoscale model output.

## 3.3 Rayleigh damping of gravity waves

The introduction of buoyancy into the microscale model permits vertically propagating gravity waves to form in mountainous terrain. These waves are naturally occurring internal waves caused by the vertical displacement of air moving over mountains resulting in oscillations on the lee side. Gravity waves can cause problems inside atmospheric models because they are reflected by top and lateral boundaries unless explicitly treated (Warner, 2010). In the microscale model, the well-known *Rayleigh damping* technique is used, which means a

gradual damping of the model variables towards predefined reference values in the top of the model domain. This is also known as a *sponge layer*. The damping is initialized at some height and gradually increased towards the top of the domain. It is implemented as an additional source term in the transport equations as

$$\frac{\partial C}{\partial t} = \tau_d(z)(C - C_r), \quad (3.28)$$

where  $C$  is a generic variable that represents  $U$ ,  $V$ ,  $W$ , and  $\Theta$ .  $C_r$  is the reference value, and  $\tau_d$  is the vertical structure of the damping. In the microscale model formulation  $\tau_d$  increases linearly between the height  $z_{d,0}$  and the top of the domain, and zero elsewhere.  $z_{d,0} = 1000$  m below the top of the domain. Only the vertical velocity component  $W$  is damped in the present study, and it is nudged towards a reference value of  $0 \text{ ms}^{-1}$ . For more details on gravity wave damping see Klemp and Durran (1983) and Israeli and Orszag (1981), which also includes a comparison of different techniques.

## Chapter 4

# Coupling via tendencies in simple terrain<sup>1</sup>

In this study, the Single-Column Model (SCM) described in section 3.1.2 is forced by time- and height varying momentum and temperature tendencies, as well as a varying surface temperature, extracted from the WRF mesoscale model. This was suggested and used by Bosveld et al. (2014) and Sanz Rodrigo et al. (2017b) for the *GEWEX Atmospheric Boundary Layer Studies 3* (GABLS3) test case (Bosveld et al., 2014; Holtslag, 2014; Kleczek et al., 2014). The case involved the simulation of a nocturnal low level jet (LLJ) in simple terrain spanning a single diurnal-cycle at the Cabauw meteorological mast in the Netherlands, originally used to evaluate SCM for mesoscale and climate models. Sanz Rodrigo et al. (2017b), SR17 henceforth in this Chapter, showed that for the GABLS3 test case the most appropriate forcing to provide the SCM was the sum forcing of the Pressure-Gradient Force (PGF) and advective momentum tendency, as well as advective temperature tendencies.

The coupling in this section is evaluated for one full year and validated at two sites in Northern Europe: Cabauw (land) and FINO3 (offshore). The aim of the research is first to study whether model coupling via tendencies is applicable in simple flow cases, i.e. whether the SCM retains the wind characteristics of the mesoscale model used to force it. This also serves in part as a prerequisite to applying the methodology to more complex flow cases. The second objective is to highlight the differences between the  $k$ - $\epsilon$  closure of the SCM and the WRF PBL schemes for a range of atmospheric conditions to guide further improvement of the turbulence closure used for microscale ABL modeling. The evaluation period for the Cabauw site overlaps the GABLS3 test case (Bosveld et al., 2014; Holtslag, 2014; Kleczek et al., 2014), which allows for a detailed evaluation of that particular day. The sensitivities

---

<sup>1</sup>This chapter consists of results that will be published in the journal paper Olsen et al. (2018)



of the methodology are tested for a range of parameters, including the influence of adding different forcing components, such as including momentum and temperature advection, and geostrophic shear, furthermore the sensitivity of the tendencies to the chosen WRF PBL scheme is also studied. These simple terrain cases allow for the use of a SCM rather than using a computationally expensive 3D model, while still allowing for the mesoscale and microscale model to be evaluated side-by-side in a relatively simple environment.

The study consists of the 3 sections. In section 2 the validation sites and the mesoscale setup is described, as well as the coupling procedure. The results are presented in section 3 and a summary of the study and the conclusions are presented in section 4.

## 4.1 Methodology

### 4.1.1 Validation sites

The methodology is validated for two tall meteorological masts, representing simple sites, Cabauw (Van Ulden et al., 1996) and *Forschungsplattformen in Nord- und Ostsee 3* (FINO3). The location of these masts is shown in fig 4.2.

Cabauw is a land site located near the city of Cabuaw in the Netherlands. The terrain is flat and mostly open fields, but with wind breaks and scattered inhomogeneities for southerly and northerly wind directions. For the prevailing wind direction (southwest), the surface roughness is characterized as nearly homogeneous open landscape (Verkaik and Holtslag, 2007). The mast is located at  $51.970^{\circ}\text{N}$ ,  $4.926^{\circ}\text{E}$  with a surface elevation of  $-0.7$  m and distance of approximately 50 km to the sea (to the northwest). The tower extends to 213 m, with measurements from 2 to 200 m A.G.L. In addition to the tower measurements, surface fluxes ( $u_*$  and  $H$ ) are used in this study, as well as *Radio Acoustic Sounding System* (RASS) profiler measurements from the GABLS3 test case Holtslag (2014) that go beyond 200 m. The year 2016 was chosen as the validation period for Cabauw to allow for comparison with the GABLS3 test case. The tower and surface measurements are validated and gap-filled, so availability is 100%.

FINO3 is a 120-m tall mast located in the North sea at  $55.195^{\circ}\text{N}$ ,  $7.158^{\circ}\text{E}$ . Wind speed measurements from three levels are used, 50, 70, and 90 m. Each level wind speed is made up of three anemometers with different boom orientations, allowing for selective combination of the measurements to minimize shear-distortion due to the mast. A wind vane at 60 m is used for wind direction. For FINO3, the year 2011 is chosen as the validation period, A wind farm was constructed and finalized in 2013 south-east of the FINO3 platform, so the year 2011 is

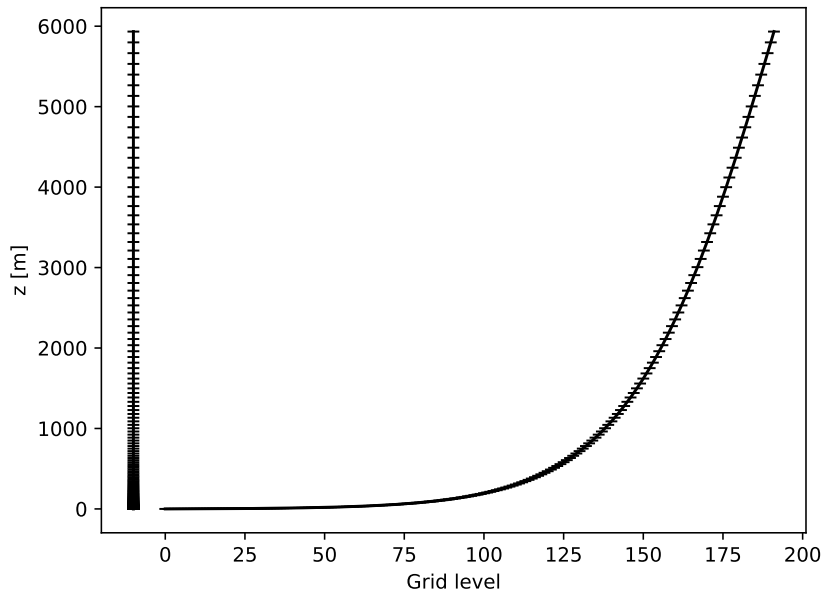


Fig. 4.1 Vertical distribution of grid levels in the Single-Column Model

chosen to have wake-free measurements. For wind speed the availability for the period is 96–100% per month, and for wind direction it is 98–100%.

#### 4.1.2 Microscale model setup

The microscale model used is the Single-Column Model version of the EllipSys3D URANS model described in Chapter 3. A computational grid similar to the one used in van der Laan and Sørensen (2017) is used. It consists of 192 grid cells extending normal to the surface up to 6000 m. The vertical distribution of grid levels are shown in Fig. 4.1. EllipSys1D uses a tridiagonal solver to quickly solve the SCM coefficient matrix. A time-step of 1 s, with 8 sub-iterations per step, was used. The surface roughness matches (numerically) that of WRF.

#### 4.1.3 Mesoscale model setup

The WRF model (Skamarock and Klemp, 2008; Skamarock et al., 2008) is the mesoscale model used in this study. A two-domain setup is used. An outer domain (d01) covers most of Europe with a horizontal grid spacing of 27 km, and an inner domain (d02), *one-way* coupled to d01, is centered on the west coast of Denmark with a horizontal grid spacing of 9 km. Figure 4.2 shows the two domains and the surface elevation in each. The two validation sites, Cabauw and FINO3, are marked by red stars.

In Fig. 4.3, the *United States Geological Survey* (USGS) land-use classes derived from the CORINE dataset (converted to USGS landuse classes) is shown near the Cabauw site

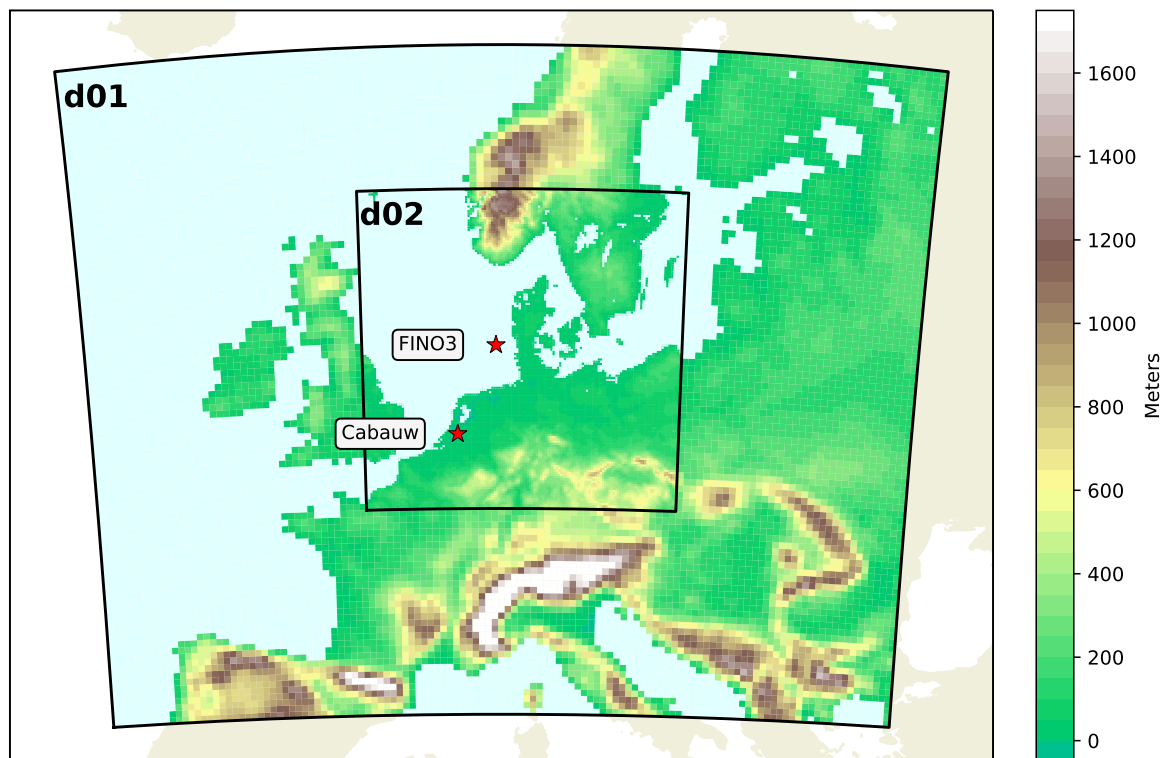


Fig. 4.2 Location of the WRF model domains (d01 and d02) and the surface elevation in each domain. The two sites (marked by a red star) are located at  $51.970^{\circ}\text{N}$ ,  $4.926^{\circ}\text{E}$  (Cabauw) and  $55.195^{\circ}\text{N}$ ,  $7.158^{\circ}\text{E}$  (FINO3).

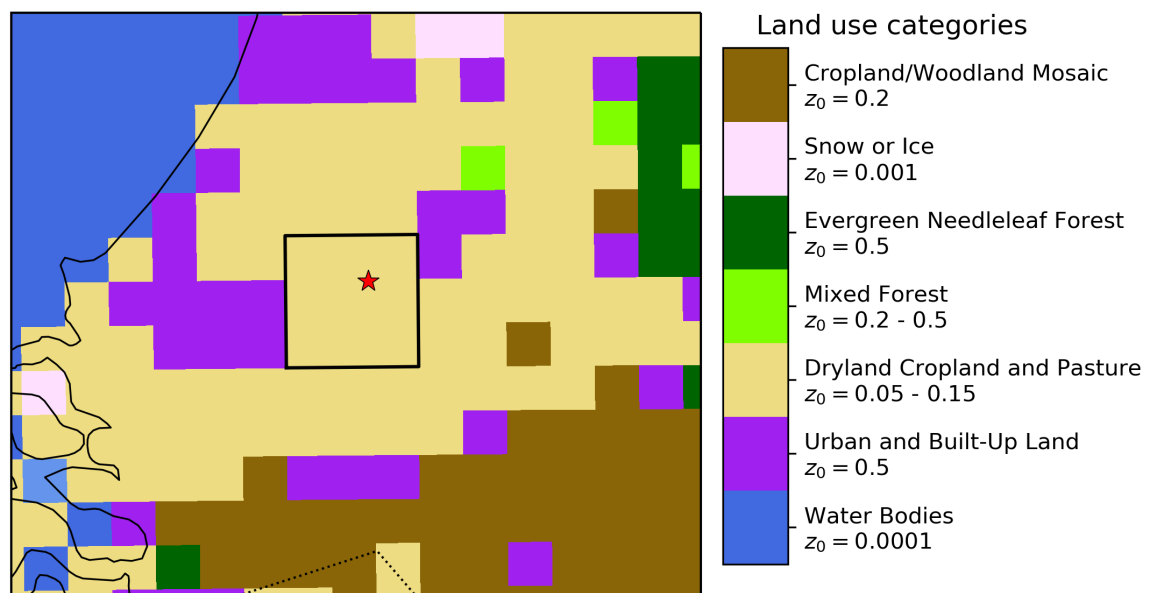


Fig. 4.3 USGS land-use classification for the WRF domain d02 grid cells near Cabauw (red star). The nine nearest cells are characterized as dryland, cropland, and pasture.

Table 4.1 WRF model configuration.

Configuration		References:
<b>Model setup</b>		
Version	ARW-WRF 3.8.1	Skamarock et al. (2008)
Initial, boundary conditions	ERA-Interim	Simmons et al. (2007)
Elevation	USGS	
land-use	CORINE	Bossard et al. (2000)
SST	HRSST	Gemmill et al. (2007)
Domains	d01, d02	
$\Delta x$ and $\Delta y$	27 km, 9 km	
Grid size ( $n_x, n_y$ )	(140, 120), (100, 100)	
Vertical levels ( $n_z$ )	61 (top at 50hPa) 21 levels below 1 km*	
$\Delta t$	Adaptive <sup>†</sup>	
<b>Model physics</b>		
Land surface model	Noah	Chen and Dudhia (2001)
Microphysics	WSM3 Micro physics	Hong et al. (2004)
Cumulus parameterization	Kain-Fritsch	Kain (2004)
Shortwave radiation	RRTM	Dudhia (1989)
Longwave radiation	RRTM	Mlawer et al. (1997)
Planetary Boundary Layer		<b>See table 4.4</b>
Surface Layer		<b>See table 4.3</b>

\*The WRF ( $\eta$ ) levels listed in Appendix A.1.1 corresponds to  $\approx 6, 22, 57, 73, 91, 114, 141, 172, 207, 246, 291, 341, 399, 463, 537, 620, 714, 820, 940 \dots$  m (cell center) at both sites.

<sup>†</sup>Target Courant–Friedrichs–Lewy (CFL) conditions:

$$\text{CFL}_{\text{total}} = 1.15, \text{CFL}_{\text{horizontal}} = 0.85$$

Table 4.2 Range of adaptive timesteps seen during the WRF simulations.

Name	Dom.	$\Delta t_{min}$	$\Delta t_{max}$
W-YSU	d01	16.01	99.99
	d02	16.01	71.62
W-ACM2	d01	27.0	99.94
	d02	21.0	71.62
W-MYJ	d01	27.0	99.96
	d02	21.0	71.62
W-MYNN2	d01	24.0	99.85
	d02	20.66	71.62
W-QNSE	d01	21.36	99.99
	d02	21.0	72.0

in the 9km (d02) WRF domain. All nine of the nearest grid cells (encircled by a black line) are characterized as dryland, cropland and pasture, which by default in WRF are given a seasonally varying roughness-length between 0.05 m during winter and 0.15 m in the summer. Verkaik and Holtslag (2007) found that the effective roughness lengths for the site varies not insignificantly for different directions, but mostly within the range 0.04–0.15 m. Looking beyond the nearest nine grid cells in the model, the site is surrounded by urban and built-up land ( $z_0 = 0.8$  m) and mixed forest ( $z_0 = 0.2 - 0.5$  m) while the sea ( $z_0 \sim 0.001$  m) is 5–6 grid cells away. Due to this, an effect of the internal boundary layer on the wind field within WRF model can not be ruled out. Table 4.1 shows the domain setup, the datasets used for initial and boundary conditions and the physics-parameterization schemes used in the simulations. The model was run in individual 72 hour chunks overlapping by a 24-hour spin-up period. Each simulation was initialized at 12:00 UTC, and radiation was updated every 30 minutes. The range of adaptive time-steps seen during the simulations are shown in Table 4.2, and were 16.01–99.99 s for domain d01 and 16.01–72.0 for domain d02.

### Planetary Boundary Layer (PBL) schemes

Numerical Weather Prediction (NWP) PBL schemes are turbulence closure schemes. However, unlike the  $k-\varepsilon$  closure in the microscale model, they also carry out the important role of estimating the PBL top. Another distinction is that the PBL schemes assume horizontal homogeneity, disregarding horizontal fluxes. This allows for the simplification that only vertical gradients are considered. This stands in contrast to typical CFD microscale closure, that makes no such assumption. But, since a SCM version of the microscale model is used

Table 4.3 First order PBL schemes used for WRF simulations.

Scheme	Used with SL scheme	Reference(s)
YSU	Revised MM5	Jiménez and Dudhia (2012)
ACM2	Revised MM5	Pleim (2007)

Table 4.4 1.5 order (TKE) PBL schemes used for WRF simulations.

Scheme	SL scheme	Turbulent length scale $l$	References
MYJ	Eta similarity	$l = l_e \frac{\kappa z}{\kappa z + l_e}$ $l_e = 0.25 \frac{\int_0^h z q dz}{\int_0^h q dz}$	Janjić (1994)
MYNN2	MYNN	$1/l = 1/l_s + 1/l_t + 1/l_b$ $l_s = \begin{cases} \kappa z / 3.7, & z/L \geq 1 \\ \kappa z (1 + 2.7z/L)^{-1}, & 0 \leq z/L < 1 \\ \kappa (1 - 100z/L)^{0.2}, & z/L < 0 \end{cases}$ $l_t = 0.23 \frac{\int_0^\infty z q dz}{\int_0^\infty q dz}$ $l_b = \begin{cases} q/N, & \frac{\partial \Theta_v}{\partial z} > 0, z/l \geq 0 \\ \left[ 1 + 5 \left( \frac{q_c}{l_t N} \right)^{1/2} \right] \frac{q}{N}, & \frac{\partial \Theta_v}{\partial z} > 0, z/l < 0 \\ \infty, & \frac{\partial \Theta_v}{\partial z} \leq 0 \end{cases}$	Nakanishi and Niino (2004)
QNSE	QNSE	$1/l = 1/l_B + 1/l_N$ $l_B = \frac{\kappa z}{158.7 \kappa z f_c / u_* + 1}$ $l_N = 0.75 \frac{k^{1/2}}{N}$	Sukoriansky et al. (2005)

$l$  turbulent length-scale,  $\kappa$  Von Kármán constant,  $z$  height above ground,  $k$  turbulent kinetic energy and  $q^2 = 2k$   
 $q_c$  turbulent velocity scale,  $L$  Obukhov length  $\Theta_v$  virtual potential temperature  
 $N$  Brunt-Väisälä frequency,  $f_c$  Coriolis parameter,  $u_*$  friction velocity

here, only vertical fluxes are considered for that as well. It should be noted that PBL schemes that include horizontal fluxes are actively being developed in the NWP community (Kosović et al., 2017; Muñoz-Esparza et al., 2016).

Five different PBL schemes are tested. Two first order schemes, Yonsei University (YSU) (Hong et al., 2006) and Asymmetric Convective Model version 2 (ACM2) scheme Pleim (2007), and three 1.5 order TKE schemes, Mellor-Yamada-Janjić (MYJ) Janjić (1994), Mellor-Yamada-Nakanishi-Niino level 2.5 scheme (MYNN2) Nakanishi and Niino (2004), and Quasi-Normal Scale Elimination (QNSE) Sukoriansky et al. (2005). In the following, a brief description of each scheme is given. For a more detailed comparison of the schemes refer to Cohen et al. (2015).

The YSU scheme is the default PBL scheme in the WRF model. It is a diffusion scheme of the form,

$$\frac{\partial C}{\partial t} = \frac{\partial}{\partial z} \left[ v_c \left( \frac{\partial C}{\partial z} - \gamma_c \right) - \overline{(w'c')}_h \left( \frac{z}{h} \right)^3 \right] \quad (4.1)$$

where  $C$  is a generic variable representing horizontal velocity components, temperature, and other scalars. The scheme builds on the ideas of Troen and Mahrt (1986) and is an extension of medium-range forecast (MRF) scheme Hong and Pan (1996). In contrast to local schemes, where mixing is influenced only by local gradients, the YSU scheme includes a counter-gradient term  $\gamma_C$  that represents the contribution from large-scale eddies to the local flux. The last term in Eq. (4.1), which separates it from the MRF scheme, represents entrainment flux from the inversion layer. The ACM2 scheme describes the total mixing as a sum of local and non-local components depending on the upward convective mixing rate. The non-local part was the basis of the ACM1 scheme (Pleim and Chang, 1992) and the local part is eddy diffusion.

The three TKE schemes have transport equation for  $k$  of the form

$$\frac{\partial k}{\partial t} = v_t \left[ \left( \frac{\partial U}{\partial z} \right)^2 + \left( \frac{\partial V}{\partial z} \right)^2 \right] + \frac{\partial}{\partial z} \left( v_t \frac{\partial k}{\partial z} \right) - v_h \frac{g}{\Theta_v} \frac{\partial \bar{\Theta}}{\partial z} - \varepsilon \quad (4.2)$$

and eddy viscosity defined as

$$v_t = S_c l k^{1/2} \quad (4.3)$$

where  $\mathbb{S}$  is a scaling parameter and  $l$  is the turbulent length-scale. The differences between the TKE schemes is their formulation of  $\mathbb{S}$  and  $l$ . Apart from using virtual potential temperature in the buoyancy term Eq. (4.2) is equal to Eq. (3.25). But unlike the microscale SCM, the one-equation (TKE) PBL schemes in WRF does not have a transport equation for  $\varepsilon$ , and instead use the Kolmogorov relation,

$$\varepsilon = C_\varepsilon \frac{k^{3/2}}{l} \quad (4.4)$$

which assumes a balance of production and dissipation. The coefficient  $C_\varepsilon$  for the three schemes are 1/11.878 (MYJ), 1/24 (MYNN2), and 1/6.0105 (QNSE) (Muñoz-Esparza et al., 2017). The MYJ and MYNN2 schemes define  $\mathbb{S}$  in terms of  $k$ ,  $l$ , and second order spatial derivatives of velocity and temperature, while the QNSE scheme defines  $\mathbb{S}$  from the gradient Richardson-number  $Ri_g$ . In table 4.4 the definitions of the turbulent length scale for the three scheme are shown. The QNSE scheme was made for stable and weakly unstable conditions, and may not perform as well during convective conditions (Sukoriansky et al., 2005). The MYJ and QNSE schemes use a background value (a value the scheme never goes below) for TKE of 0.1 and 0.005 m<sup>2</sup> s<sup>-2</sup>, respectively.

### Surface layer schemes

The surface layer schemes used are the revised MM5 Jiménez and Dudhia (2012), Eta similarity Janjić (1994), MYNN Nakanishi and Niino (2004) and QNSE Sukoriansky et al. (2005) schemes. The revised MM5 scheme uses stability functions from Cheng and Brutsaert (2005) (Fairall et al., 1996) for stable (unstable) conditions. Following Beljaars (1994), it enhances surface velocities by adding a convective velocity, and for domains where the horizontal grid spacing is larger than 5km a sub-grid velocity enhancement is also added based on Mahrt and Sun (1995). The MM5 scheme does not parameterize the thermal roughness length ( $z_{0r}$ ). In the Eta similarity scheme the stability functions are taken from Holtslag and De Bruin (1988) (Paulson, 1970) for stable (unstable) conditions. It also uses the correction from Beljaars (1994), but furthermore include a variable roughness length for temperature and humidity to account for effects of a viscous sub-layer. The QNSE surface layer formulation is similar to Eta similarity, but uses different stability functions consistent with the QNSE PBL scheme (Galperin et al., 2007). The MYNN surface layer scheme uses stability functions from Dyer and Hicks (1970), a variable roughness length for temperature and humidity, the Beljaars (1994) correction, and for grid spacing larger than 3 km also the Mahrt and Sun (1995) correction. See e.g. Liu et al. (2013) for a review of surface-layer schemes in WRF.

#### 4.1.4 Mesoscale and microscale model coupling

The meso-microscale model coupling procedure is described in the following. It follows the approach of SR17 of adding momentum and temperature tendencies as source terms into the governing equations of the microscale model.

The WRF model momentum and temperature tendencies were extracted from the model using the approach described in Lehner (2012) and used as extra forcing terms in Eq. (3.22), (3.23), and (3.24). The governing equations for momentum and heat in the WRF model are made up of many components related to dynamics, physics parameterization, and numerical stability. Here all but the PGF and advection terms are ignored.

CFD-type microscale models are often forced by a pressure gradient, representing the background large-scale geostrophic forcing. For steady-state simulations this forcing is typically constant in time and space. We use instead the forcing derived from WRF, added to the SCM as body-forces, representing a time-height varying combination of the geostrophic forcing (from the PGF) as forcing due to advection (as discussed in SR17). The forcing terms are allowed to vary in both time and height, to capture geostrophic shear, shallow layers of advection, and other important effects. Examining the tendencies also reveals that advection



and pressure terms often counter-act each other (shown in the following section), making it important to include both to avoid excessive forcing when advection is active. The forcing terms in Eq. 3.22 and 3.23 becomes

$$F_U(t, z) = \dot{U}_{\text{PGF}}^W(t, z) + \dot{U}_{\text{ADV}}^W(t, z) \quad (4.5)$$

and,

$$F_V(t, z) = \dot{V}_{\text{PGF}}^W(t, z) + \dot{V}_{\text{ADV}}^W(t, z) \quad (4.6)$$

for temperature, the advection is added to Eq. (3.24) as

$$F_{\Theta}(t, z) = \dot{\Theta}_{\text{ADV}}^W(t, z) \quad (4.7)$$

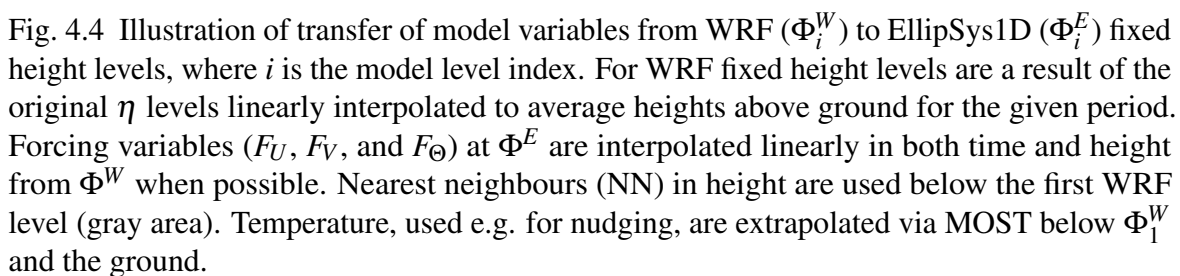
where over-dot notation denotes a time-derivative.

WRF variables are linearly interpolated from all 61 WRF model ( $\eta$ ) levels to levels of fixed heights above ground ( $\Phi^W$  in Fig. 4.4). The height of the first 21 (constant height) levels are shown in the footnotes of Table 4.5. As the SCM levels extend to just 6000 m above the ground, only the first 33 levels (up to 6427 m) WRF levels are actually used for interpolation.

Similar to SR17, the WRF tendencies are filtered both in time and in space (horizontally). The tendencies are averaged in the nearest  $3 \times 3$  grid cells of the 9 km domain surrounding the site (corresponding to a  $27 \times 27$  km averaging box), and 10 minute instantaneous values are averaged to hourly means. SR17 used tendencies from domain of 3 km wide cells and an averaging box of 9 km. However, the assumption here is that the difference is minimal in flat and relative homogeneous terrain. In the microscale model a linear interpolation in between the hourly tendency values are used. The equations above include both the PGF and advection terms, for some of the simulations discussed below the some of the these terms are not included, or they are added as time-varying terms only. The specifics are discussed below.

The transfer of WRF variables at fixed height levels ( $\Phi^W$ ) and hourly intervals to ElipSys1D model levels ( $\Phi^E$ ) at specific times are illustrated in Fig. 4.4. WRF forcing ( $F_U$ ,  $F_V$ , and  $F_{\Theta}$ ) and temperature ( $\Theta$ ), are interpolated linearly in time and height to  $\Phi^E$ , while the nearest neighbour are used below first WRF level for the forcing, and Monin-Obukhov Similarity theory (MOST) are used for temperature.

As in SR17, surface temperatures, calculated as the potential temperature at the roughness height  $z_0$ , are estimated from the diagnosed two-meter temperature in WRF, and extended



downwards to  $z_0$  using MOST

$$\Theta_{z_0} = \Theta_2 - \frac{\Theta_*}{\kappa} \left[ \ln \left( \frac{2-z_0}{z_0} \right) + \psi \left( \frac{2-z_0}{L} \right) \right], \quad (4.8)$$

where the temperature scale  $\Theta_*$  is obtained from the turbulent sensible heat flux  $H$  of units  $\text{Wm}^{-2}$  and the friction velocity  $u_*$  as

$$\Theta_* = \frac{H}{u_* \rho C_P} \quad (4.9)$$

$C_P$  is the specific heat capacity for atmospheric air  $C_P = 1005 \text{ Jkg}^{-1} \text{ K}^{-1}$  and  $\psi$  is the integral form of the stability function from MOST. The stability coefficients from Businger et al. (1971) are used

$$\psi(z/L) = \begin{cases} -4.7z/L & \text{for } z/L \geq 0 \\ 2 \ln \left[ 1/2 \left( 1 + (1 - 15z/L)^{1/2} \right) \right] & \text{for } z/L < 0 \end{cases} \quad (4.10)$$

no parameterization of the roughness length for temperature is included.

A temperature relaxation, as described in sec. 3.2, with a relaxation timescale of  $\tau_r = 10800 \text{ s}$  is also used. The temperature is relaxed towards the average vertical temperature profile in the nearest WRF grid cell, corresponding to the next following hour to the current model integration time.

## 4.2 Results

In the following the results are presented. First, results for the SCM are presented alone, to investigate the impact of forcing it with different combinations of mesoscale terms, by seeing the impact on the long-term wind statistics for the whole year and for each combination. The WRF results from the simulations using the YSU PBL scheme are used to generate the different combinations of forcing for this purpose. After that, a single combination of mesoscale terms are chosen, and studied more in-depth for the GABLS3 test case, and for the long-terms results for the year, using all five configurations of the WRF model to drive the SCM. The results for both the WRF model and the SCM are shown in that part, to allow an overview of both the WRF results and the sensitivity to PBL-SL configuration, and the sensitivity of the SCM to that choice.

Table 4.5 WRF simulations. Each simulation was run for one year at each of the two sites.

Name	Model	PBL scheme	SL scheme
W-YSU	WRF	YSU	Revised MM5
W-ACM2	WRF	ACM2	Revised MM5
W-MYJ	WRF	MYJ	Eta similarity
W-MYNN2	WRF	MYNN2	MYNN
W-QNSE	WRF	QNSE	QNSE

Table 4.6 Single-Column Model (SCM) simulations

Name	Model	Forced by	Forcing terms included
E-YSU-L1	SCM	W-YSU	$\dot{U}(t)_{\text{PGF}}$
E-YSU-L2	SCM	W-YSU	$\dot{U}(t, z)_{\text{PGF}}$
E-YSU-L3	SCM	W-YSU	$\dot{U}(t)_{\text{PGF}} + \dot{U}(t, z)_{\text{ADV}}, \dot{\Theta}(t, z)_{\text{ADV}}$
E-YSU-L4	SCM	W-YSU	$\dot{U}(t, z)_{\text{PGF}} + \dot{U}(t, z)_{\text{ADV}}$
E-YSU-L5	SCM	W-YSU	$\dot{U}(t, z)_{\text{PGF}} + \dot{U}(t, z)_{\text{ADV}}, \dot{\Theta}(t, z)_{\text{ADV}}$
E-YSU	SCM	W-YSU	$\dot{U}(t, z)_{\text{PGF}} + \dot{U}(t, z)_{\text{ADV}}, \dot{\Theta}(t, z)_{\text{ADV}}$
E-ACM2	SCM	W-ACM2	$\dot{U}(t, z)_{\text{PGF}} + \dot{U}(t, z)_{\text{ADV}}, \dot{\Theta}(t, z)_{\text{ADV}}$
E-MYJ	SCM	W-MYJ	$\dot{U}(t, z)_{\text{PGF}} + \dot{U}(t, z)_{\text{ADV}}, \dot{\Theta}(t, z)_{\text{ADV}}$
E-MYNN2	SCM	W-MYNN2	$\dot{U}(t, z)_{\text{PGF}} + \dot{U}(t, z)_{\text{ADV}}, \dot{\Theta}(t, z)_{\text{ADV}}$
E-QNSE	SCM	W-QNSE	$\dot{U}(t, z)_{\text{PGF}} + \dot{U}(t, z)_{\text{ADV}}, \dot{\Theta}(t, z)_{\text{ADV}}$

An overview of WRF simulations are shown in table 4.5, and table 4.6 shows the ten different SCM results, including what forcing was used to generate it. The “W” or “E” in the names of the SCM simulations refer to the name of the models: “WRF” and “EllipSys”.

In the following sub-sections the long-term wind statistics between the models and the observations are presented in Taylor diagrams (Taylor, 2001). Taylor diagrams allow for an easy summary of multiple statistics: correlation, ratio of standard deviations, and mean wind speed bias. The mean horizontal wind speed is given as

$$\langle S \rangle = \frac{1}{n} \sum_{i=1}^n S_i \quad (4.11)$$

where  $n$  and  $\mathbb{N}$  are individual hourly values and the total number of values (hours) respectively. The wind speed bias is the difference between the modelled and observed mean  $\langle S \rangle^m - \langle S \rangle^o$ . The standard deviation of the wind speed is given by

$$\sigma = \frac{1}{n} \sum_{i=1}^n (S_i - \langle S \rangle) \quad (4.12)$$

. In the Taylor diagrams the ratio between the modelled and observed variances  $\sigma^m / \sigma^o$  is used to show the degree to which the models under- or overestimate the variations. The correlation used is the *Pearson correlation*. All statistics are calculated on the basis of the hourly-averaged model output and measurements. The black star in the Taylor diagram represents the measurements, i.e. the perfect match where the correlation coefficient and normalized standard deviation equals one. The filled color and width of the edge-lines of the symbols represents the mean bias and the height above the surface respectively.

### 4.2.1 Impact of forcing terms

SR17 showed the importance of including both geostrophic shear and momentum and temperature advection in the forcing for a SCM to accurately capture the Low Level Jet (LLJ) in the GABLS3 test case (Sanz Rodrigo et al., 2017a,b). In Fig. 4.5, table 4.7 and table 4.8, the importance of including these effects for capturing the long-term statistics is shown at Cabauw and FINO3 for the SCM forced by W-YSU. Five different combinations of forcing are shown. 1) PGF varying only in time ( $\dot{U}_{PGF}(t)$ ), the lowest level of WRF is used. 2) PGF varying with time and height ( $\dot{U}_{PGF}(t, z)$ ). 3) PGF varying only in time, but temperature and momentum advection included, and varying in both time and height ( $\dot{U}_{PGF}(t) + \dot{U}_{ADV}(t, z), \dot{\Theta}_{ADV}(t, z)$ ). 4) PGF varying with time and height and momentum

Table 4.7 Wind speed statistics for mast Cabauw: Mean wind speed (Mean), standard deviation of wind speed (St.d.), Bias of the mean wind speed (Bias), Mean Absolute Error (MAE), Root-Mean-Square Error (RMSE), and Pearson correlation coefficient (C.C.). The best performing SCM results are highlighted in bold text. The five SCM results are: PGF varying only in time (E-YSU-L1), PGF varying with time and height (E-YSU-L2), PGF varying only in time, but temperature and momentum advection included, and varying in both time and height (E-YSU-L3), PGF varying with time and height and momentum advection included (E-YSU-L4), and PGF varying with time and height, and both momentum and temperature advection included (E-YSU-L5).

Height	Name	$\langle S \rangle$	$\sigma_S$	Bias	MAE	RSME	C.C.
200 m	Obs	8.66	4.03	-	-	-	-
	W-YSU	9.26	4.18	7.0	1.85	2.42	0.84
	E-YSU-L1	10.74	4.86	24.1	3.39	4.40	0.63
	E-YSU-L2	10.19	4.85	17.7	2.84	3.76	0.71
	E-YSU-L3	9.82	4.28	13.4	2.57	3.35	0.72
	E-YSU-L4	<b>9.26</b>	<b>4.11</b>	<b>7.0</b>	<b>1.86</b>	<b>2.46</b>	<b>0.83</b>
	E-YSU-L5	9.32	4.15	7.7	1.87	<b>2.46</b>	<b>0.83</b>
140 m	Obs	8.02	3.55	-	-	-	-
	W-YSU	8.66	3.68	7.9	1.71	2.23	0.83
	E-YSU-L1	9.78	4.21	22.0	2.87	3.74	0.65
	E-YSU-L2	9.38	4.20	16.9	2.46	3.27	0.72
	E-YSU-L3	9.00	3.71	12.2	2.21	2.90	0.72
	E-YSU-L4	<b>8.57</b>	<b>3.57</b>	<b>6.8</b>	<b>1.69</b>	2.24	0.81
	E-YSU-L5	8.63	3.60	7.6	1.70	<b>2.23</b>	<b>0.82</b>
80 m	Obs	6.97	3.00	-	-	-	-
	W-YSU	7.57	3.02	8.6	1.50	1.95	0.81
	E-YSU-L1	8.38	3.51	20.2	2.30	3.04	0.67
	E-YSU-L2	8.08	3.44	15.9	2.01	2.69	0.72
	E-YSU-L3	7.78	<b>3.05</b>	11.7	1.84	2.43	0.71
	E-YSU-L4	<b>7.42</b>	2.90	<b>6.4</b>	<b>1.48</b>	<b>1.95</b>	0.79
	E-YSU-L5	7.51	2.92	7.7	1.50	1.96	<b>0.80</b>
		[ms <sup>-1</sup> ]	[ms <sup>-1</sup> ]	[%]	[ms <sup>-1</sup> ]	[ms <sup>-1</sup> ]	[-]

Table 4.8 Wind speed statistics for mast FINO3: Mean wind speed (Mean), standard deviation of wind speed (St.d.), Bias of the mean wind speed (Bias), Mean Absolute Error (MAE), Root-Mean-Square Error (RMSE), and Pearson correlation coefficient (C.C.). The best performing SCM results are highlighted in bold text. The five SCM results are: PGF varying only in time (E-YSU-L1), PGF varying with time and height (E-YSU-L2), PGF varying only in time, but temperature and momentum advection included, and varying in both time and height (E-YSU-L3), PGF varying with time and height and momentum advection included (E-YSU-L4), and PGF varying with time and height, and both momentum and temperature advection included (E-YSU-L5).

Height	Name	$\langle S \rangle$	$\sigma_S$	Bias	MAE	RSME	C.C.
90 m	Obs	10.45	4.73	-	-	-	-
	W-YSU	10.05	4.72	-3.8	1.72	2.31	0.88
	E-YSU-L1	10.92	5.91	4.5	2.80	3.95	0.75
	E-YSU-L2	<b>10.57</b>	5.68	<b>1.1</b>	2.56	3.59	0.78
	E-YSU-L3	10.21	<b>4.82</b>	-2.3	2.00	2.72	0.84
	E-YSU-L4	9.84	4.49	-5.9	1.76	2.33	<b>0.88</b>
	E-YSU-L5	9.92	4.52	-5.1	<b>1.74</b>	<b>2.31</b>	<b>0.88</b>
70 m	Obs	10.26	4.59	-	-	-	-
	W-YSU	9.81	4.59	-4.3	1.68	2.25	0.88
	E-YSU-L1	10.57	5.70	3.0	2.70	3.79	0.75
	E-YSU-L2	<b>10.24</b>	5.49	<b>-0.2</b>	2.48	3.47	0.78
	E-YSU-L3	9.88	<b>4.65</b>	-3.7	1.95	2.64	0.84
	E-YSU-L4	9.52	4.32	-7.2	1.75	2.29	<b>0.88</b>
	E-YSU-L5	9.60	4.34	-6.4	<b>1.73</b>	<b>2.27</b>	<b>0.88</b>
50 m	Obs	9.93	4.42	-	-	-	-
	W-YSU	9.51	4.43	-4.3	1.60	2.13	0.89
	E-YSU-L1	10.18	5.48	2.5	2.57	3.62	0.75
	E-YSU-L2	<b>9.86</b>	5.27	<b>-0.7</b>	2.37	3.32	0.78
	E-YSU-L3	9.51	<b>4.46</b>	-4.2	1.86	2.53	0.84
	E-YSU-L4	9.17	4.14	-7.7	1.69	2.20	<b>0.89</b>
	E-YSU-L5	9.24	4.16	-7.0	<b>1.67</b>	<b>2.19</b>	0.88
		[ms <sup>-1</sup> ]	[ms <sup>-1</sup> ]	[%]	[ms <sup>-1</sup> ]	[ms <sup>-1</sup> ]	[-]

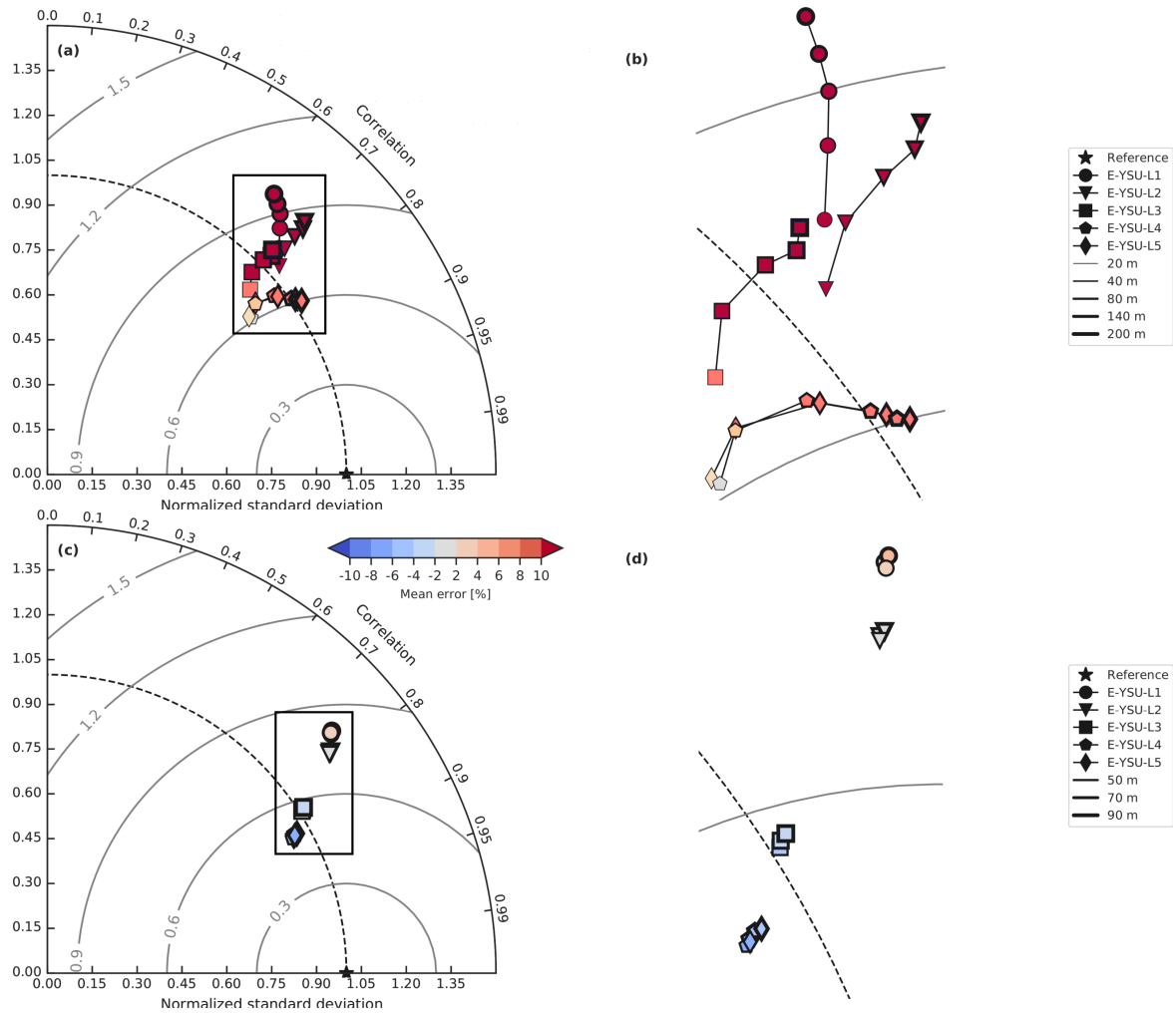


Fig. 4.5 Taylor diagram showing wind speed correlation (angle), relative annual wind speed variance ratio (radii), and annual mean wind speed biases (color) of the (hourly averaged) results from the SCM forced by the WRF tendencies, using the YSU PBL scheme, for different combinations of forcing terms included (marker symbols) at different heights (marked by the thickness of the edge line) relative to the observations (star) at Cabauw (top) and FINO3 (bottom).



advection is included ( $\dot{U}_{PGF}(t, z) + \dot{U}_{ADV}(t, z)$ ). 5) PGF varying with time and height, and both momentum and temperature advection included ( $\dot{U}_{PGF}(t, z) + \dot{U}_{ADV}(t, z), \dot{\Theta}_{ADV}(t, z)$ ).

It is clear that using just a time-dependant geostrophic wind results in a large overestimation of the mean wind speed at Cabauw (24% at 200 m), while only a small overestimation is seen at FINO3 (4.5% at 90 m). For both sites, low correlation coefficients and an overestimation of the standard deviation are seen. Adding vertical variations of PGF (akin to geostrophic shear), substantially improves the results, showing maximum errors of 17.7% at Cabauw, and 1.1% at FINO3, and an improved correlation and variance. However, the correlation is still low and the standard deviation of wind speed large relative to the other options. Further improvements are made by adding advective tendencies, especially momentum advection has a large impact at Cabauw. At FINO3 it results in an underestimation of the mean wind speed and standard deviation, but a clear improvement for correlation, MAE, and RMSE is seen.

The reduced overestimation of the wind speed, improved correlation, MAE, and RMSE, at Cabauw resulting from including the momentum advection term, points to the balancing effect that often happens between the pressure gradient force and advection, resulting in a smaller total forcing by including both together. The smallest impact is seen from adding temperature advection. However, an impact is still seen, e.g. a slightly reduced underestimation of the mean wind speed at FINO3 when temperature advection is included. At Cabauw, it does seem to increase the overestimation, but across all metrics the change is minimal. Because temperature nudging is used, part of the effects of temperature advection are already added to the model indirectly, which may partly explain the relative low impact, compared to momentum advection.

### 4.2.2 GABLS3

Figures 4.6 and 4.7 show time-height plots of horizontal wind speed ( $S = \sqrt{U^2 + V^2}$ ), wind direction ( $D$ ), potential temperature ( $\Theta$ ), turbulent kinetic energy ( $k$ ), and dissipation of turbulent kinetic energy ( $\epsilon$ ), during the diurnal cycle between 12:00 UTC 1 July 12:00 UTC 2 July 2016, corresponding to the GABLS3 test-case.

Generally, the occurrence of a LLJ is captured by all the models, but some variations in the timing, intensity and the duration are observed. The results are consistent with Fig. 9 in SR17, which is based on model configurations similar to W-YSU and E-YSU. During the weakening phase of the jet (lowering of wind speed), there is a strong turning of the wind, which is not well captured by the models. The SCM results follow the mesoscale forcing well, but tend to slightly weaken the jet and displace it downwards compared to the corresponding mesoscale model. All the models overestimate the near-surface wind speeds.

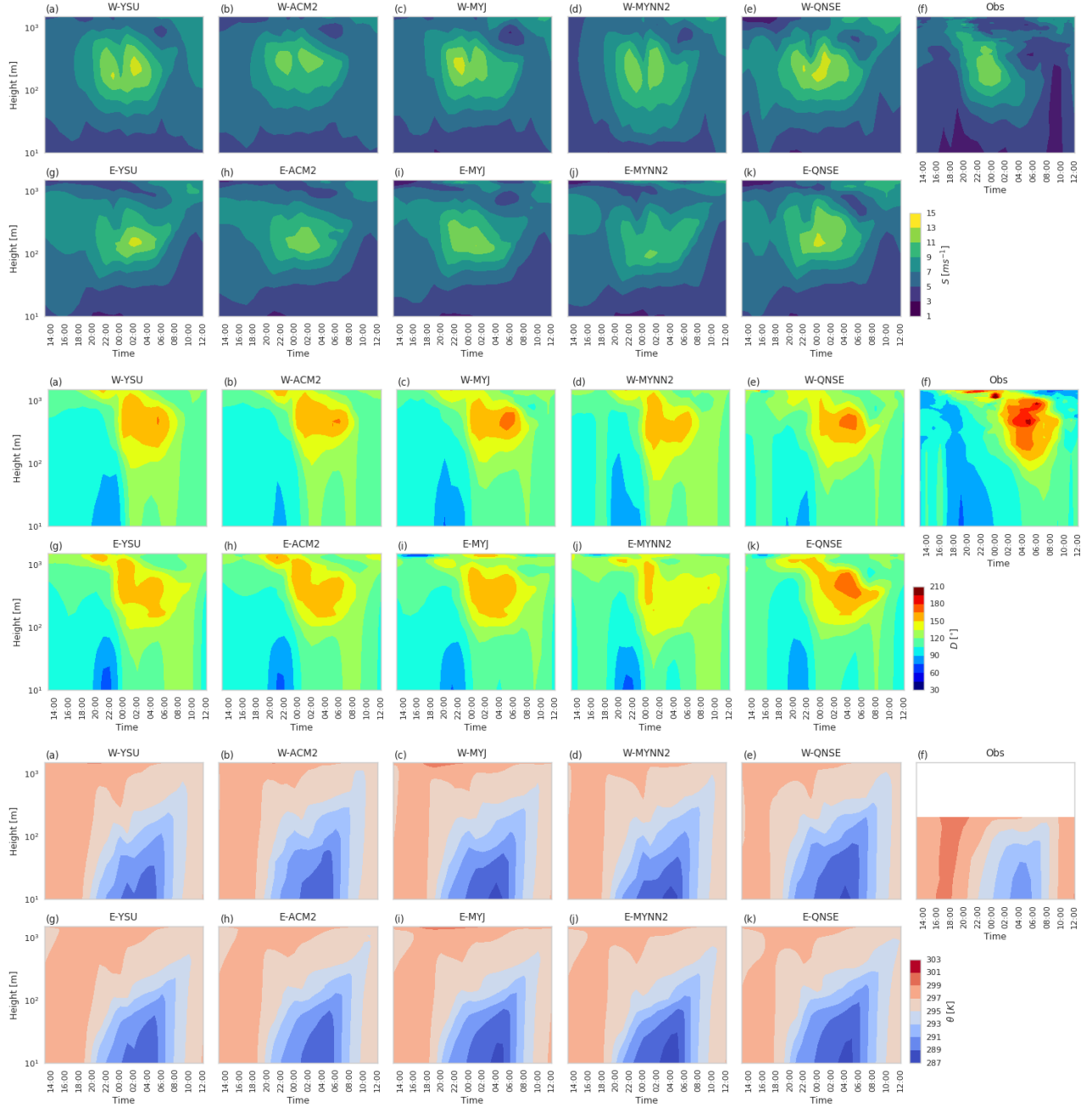


Fig. 4.6 Hourly-averaged time-height contours of: (top) horizontal wind speeds ( $S$ ), (middle) horizontal wind directions ( $D$ ), and (bottom) potential temperature ( $\Theta$ ), during the GABLS3 test case period for the five WRF model configurations (a-e), the observations (f), and the SCM runs (g-k).

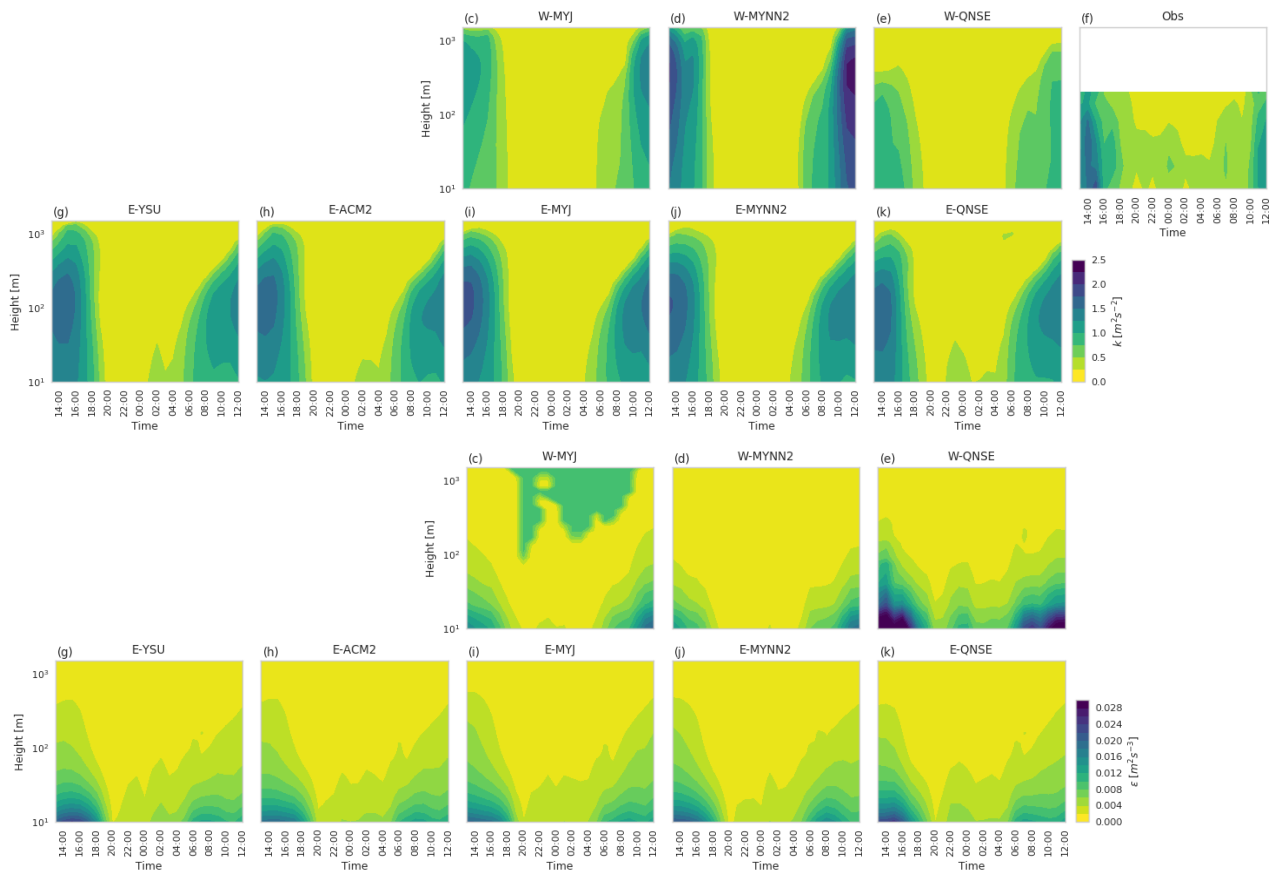


Fig. 4.7 Hourly-averaged time-height contours of: (top) turbulent kinetic energy ( $k$ ), and (bottom) dissipation of turbulent kinetic energy ( $\epsilon$ ), during the GABLS3 test case period for the five WRF model configurations (a-e), the observations (f), and the SCM runs (g-k).

The best agreement between the meso- and corresponding SCM run is seen for W-QNSE and E-QNSE, while W-MYNN2 and E-MYNN2 show the largest discrepancies. A negative temperature bias in the models is observed throughout the diurnal cycle. The mesoscale models with local PBL schemes (MYJ, MYNN, QNSE) show a larger cold bias of the near-surface temperature compared to the non-local schemes (YSU, ACM2). This is consistent with findings in e.g. Hu et al. (2010). The temperatures in the SCM results are tightly connected to the mesoscale model due to the passing of surface temperatures from WRF to the SCM and the temperature nudging, but some variations are seen e.g. colder night-time near-surface temperature and a sharper temperature gradient aloft for E-MYNN2 compared to W-MYNN2. For the modelled TKE and DTKE (Fig. 4.7), large variations are seen for the different WRF PBL schemes. W-MYNN2 have the most turbulent kinetic energy and least dissipation, while W-QNSE have much larger DTKE and lowest TKE values. Interestingly, W-MYJ show dissipation high above the surface (100+ m) during night-time. The SCM results have minor variations of TKE for the different forcing model configurations.

Figure 4.8 shows vertical profiles of hourly-averaged values of wind speed, wind direction, and potential temperature at 18:00, 00:00, 06:00, and 12:00 UTC during the GABLS3 diurnal cycle.

At all four times a clear underestimation of the temperature, of about 2 K, is seen. During the night-time transition at 18:00 the surface cooling causes the mesoscale temperature profiles to adjust more quickly than the SCM, where the surface air cools rapidly, but not the air further aloft. The wind speed and direction profiles shows good agreement between W-YSU and E-YSU, W-ACM2 and E-ACM2, and W-MYJ and E-MYJ, but W-QNSE shows larger wind speeds than E-QNSE and W-MYNN2 shows lower wind speed than E-MYNN2.

At midnight (00:00), the SCM temperature profiles follow well the profile of its forcing mesoscale model near the surface, but are warmer than it up to  $\approx 200$  m, where the profiles convergence again. The peak difference between the SCM and WRF temperatures are at 100–150 m. The jet seen in the wind speed profiles varies by a few m/s between the models. The SCM results follows the general trends of the forcing model, but the wind speed peak is located at lower heights. W-MYJ and W-QNSE captures the magnitude of the jet better than the other mesoscale models.

During the morning transition (06:00), a layer of colder air is seen in the SCM results compared to the corresponding mesoscale model up to  $\approx 125$  m, and a layer of air warmer than the mesoscale model above. All the models overestimate the wind speed above 80 m, and the inter-model variability is low below  $\sim 125$  m. The SCM results show more veering of wind with height up to  $\approx 200$  m.

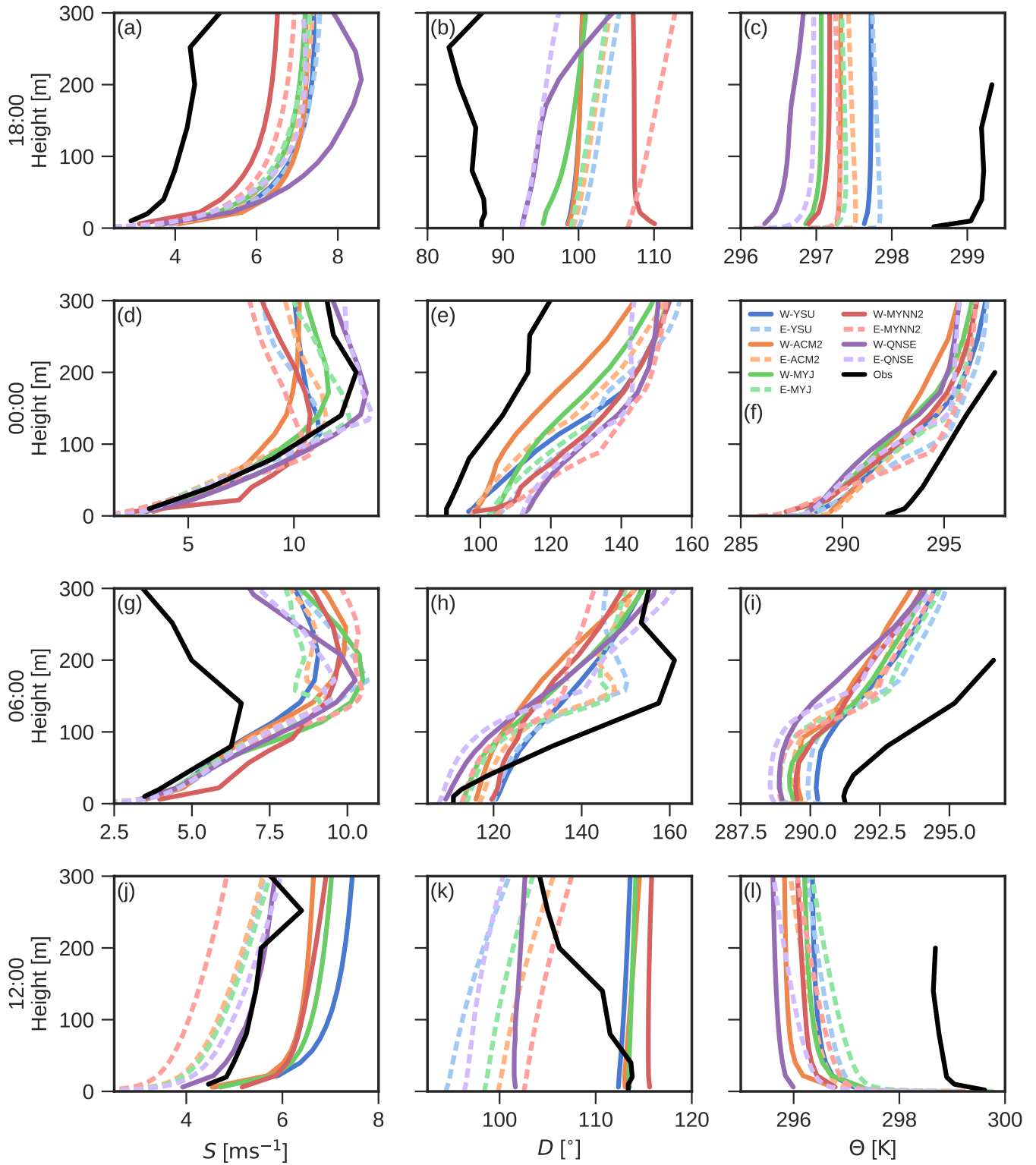


Fig. 4.8 Vertical profiles of wind speed (a-d), wind direction (e-h), and potential temperature (i-l) for the models and measurements at 18:00, 00:00, 06:00, and 12:00 UTC during the GABLS3 test case.

At 12:00, the SCM results and W-QNSE show much lower and steeper sloping wind speed profiles than the other mesoscale models. Likewise the wind directions show an angle  $\approx 15^\circ$  lower for the SCM and W-QNSE results compared to the other WRF results. The SCM results also show more veering of the wind with altitude. The temperature profiles for the SCM results show a much greater vertical gradient than the mesoscale results and the observations, pointing to more sensitivity to the day-time surface heating.

### 4.2.3 Sensitivity of wind statistics to WRF SL-PBL schemes

In Fig. 4.9 the long-term wind statistics at Cabauw is shown for WRF and for the SCM in Taylor diagrams. The exact values of the statistics are shown in tables 4.9 and 4.10. The mean wind speed profiles, wind speed distributions, and wind direction distributions (wind roses) are shown in 4.11.

At Cabauw, the WRF results overestimate the mean wind by 2.8–23.1%. But interestingly, the overestimation varies considerably for the different WRF PBL/SL scheme configurations and for different heights above ground. The W-QNSE overestimates the mean wind speed by just 2.7% at 20 m, but overestimates by 13.0% at 200 m, while the W-MYNN2 overestimates the mean wind speed by 23.1% at 20 m, decreasing aloft to 9.4% at 200 m. The W-MYNN2 also overestimates the wind speed variation more than the other configurations (Fig. 4.9). The W-MYJ and W-YSU have the smallest mean errors across heights: 8.0% at 40 m for W-MYJ and 8.6% at 80 m for W-YSU. The mean wind speed errors decrease with height for 4 of 5 configurations (W-QNSE excluded) and the correlation increases for all 5.

At Cabauw the best performing configuration is W-ACM2/E-ACM2. The E-ACM2 has the smallest mean errors, MAE, RMSE, and greatest correlation across heights. At the 140 and 200 m the W-ACM2 performed best for all metrics, and the E-ACM2 largely maintained these properties, although increased overestimation of the means and standard deviations are seen. The W-QNSE and E-QNSE are the WRF+SCM pair that deviates the least, while the W-MYNN2 and E-MYNN2 deviates the most, particularly closer to the surface where the respective turbulence closures and surface layer schemes have most effect.

In most cases the SCM results are worse than their respective forcing model results for FINO3 and aloft for Cabauw, although the deterioration is small when compared to the inter-model variation of results. Closer to the surface at Cabauw no clear pattern can be seen.

At FINO3 all five WRF simulations underestimate the annual mean wind speed by  $-1.0$  to  $-7.8$  % (Table 4.10) across the three heights. The SCM simulations results in lower annual mean wind speeds showing underestimations from  $-1.4$  to  $-10.7$  %. W-ACM2 has the lowest MAE and RMSE of the WRF results, and E-ACM2 has the lowest for the SCM results.

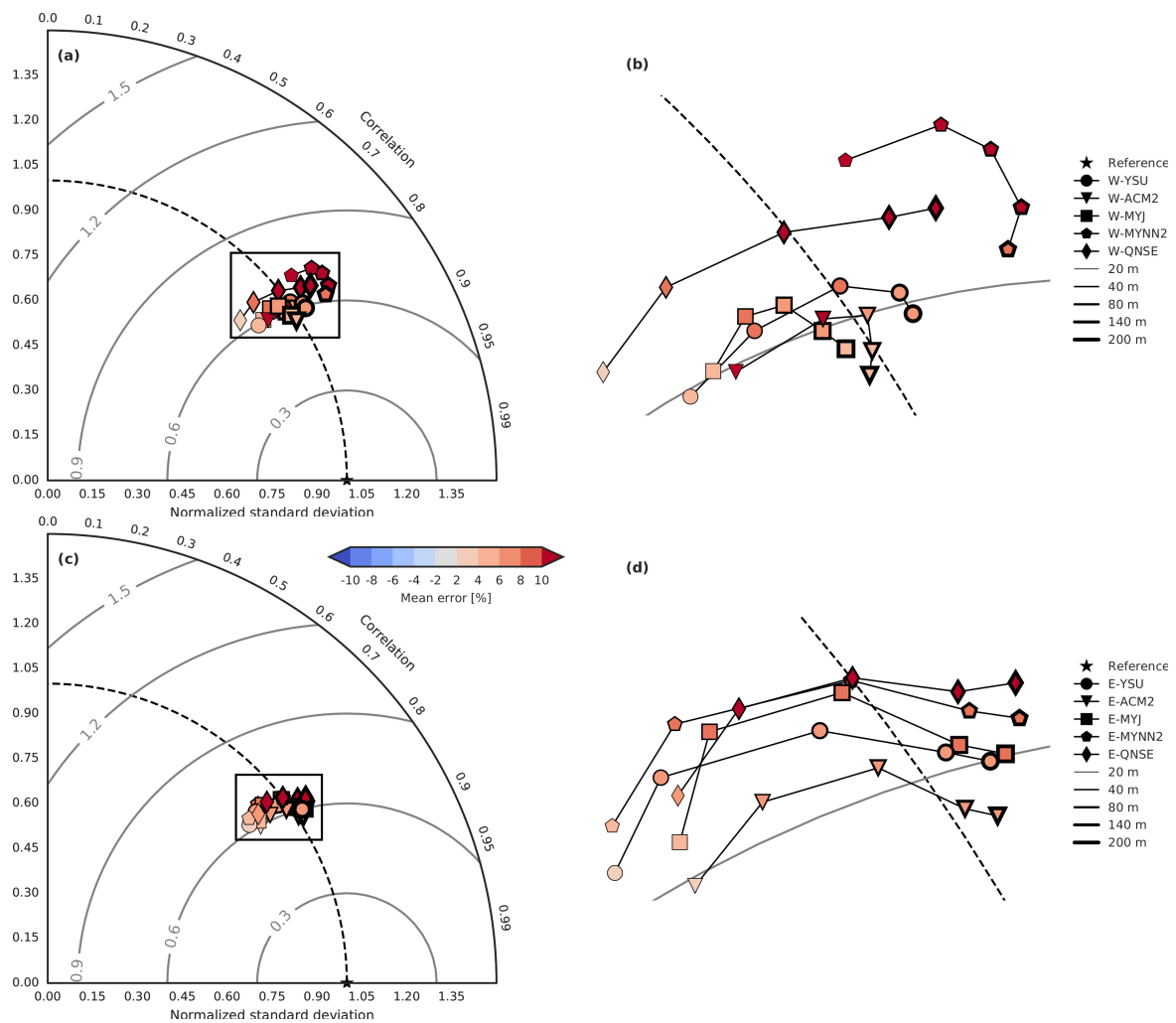


Fig. 4.9 Taylor diagram showing wind speed correlation (angle), relative annual wind speed variance ratio (radius), and annual mean wind speed biases (color) of the (hourly averaged) results from WRF (top) and the SCM (bottom) for the five WRF configurations (marker symbols) at different heights (marked by the thickness of the edge line) relative to the observations (star) at Cabauw.

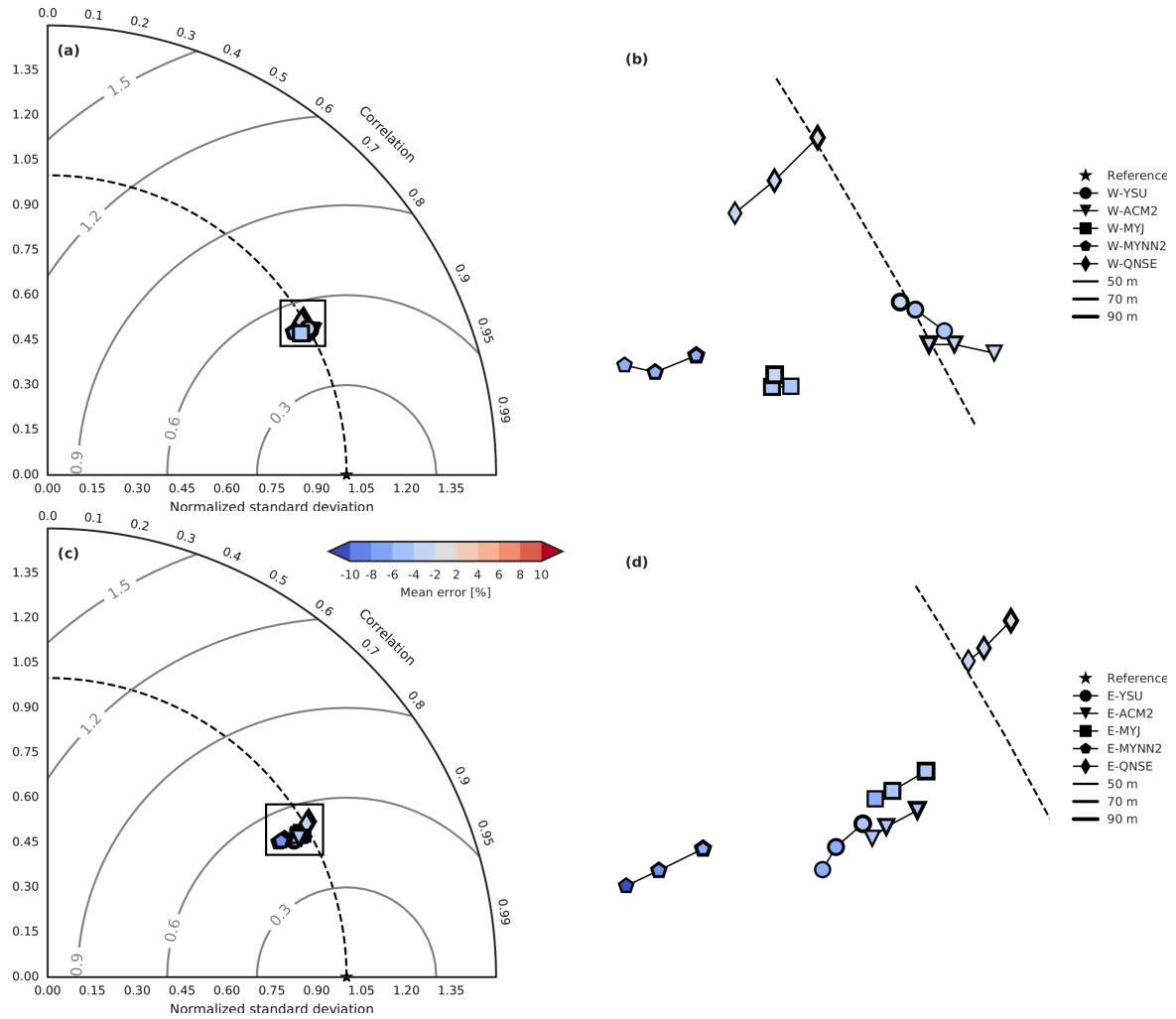


Fig. 4.10 Taylor diagram showing wind speed correlation (angle), relative annual wind speed variance ratio (radius), and annual mean wind speed biases (color) of the (hourly averaged) results from WRF (top) and the SCM (bottom) for the five WRF configurations (marker symbols) at different heights (marked by the thickness of the edge line) relative to the observations (star) at FINO3.



Table 4.9 Wind speed statistics for Cabauw: Mean wind speed (Mean), standard deviation of wind speed (St.d.), Bias of the mean wind speed (Bias), mean absolute error (MAE), root-mean-square error (RMSE), and Pearson correlation coefficient (C.C.). The best performing model is highlighted in bold text.

Height	Name	$\langle S \rangle$	$\sigma_S$	Bias	MAE	RSME	C.C.
200 m	Obs	8.66	4.03	-	-	-	-
	W-YSU	9.26	4.18	7.0	1.85	2.42	0.84
	E-YSU	9.32	4.15	7.7	1.87	2.46	0.83
	W-ACM2	<b>9.02</b>	<b>3.98</b>	<b>4.3</b>	<b>1.68</b>	<b>2.22</b>	<b>0.85</b>
	E-ACM2	9.21	4.10	6.4	1.76	2.32	<b>0.85</b>
	W-MYJ	9.14	3.96	5.6	1.80	2.37	0.83
	E-MYJ	9.39	4.18	8.5	1.90	2.48	0.83
	W-MYNN2	9.47	4.50	9.4	1.98	2.58	0.84
	E-MYNN2	9.48	4.24	9.5	1.98	2.57	0.83
	W-QNSE	9.78	4.40	13.0	2.21	2.84	0.81
	E-QNSE	9.74	4.27	12.6	2.11	2.74	0.82
140 m	Obs	8.02	3.55	-	-	-	-
	W-YSU	8.66	3.68	7.9	1.71	2.23	0.83
	E-YSU	8.63	3.60	7.6	1.70	2.23	0.82
	W-ACM2	<b>8.42</b>	<b>3.54</b>	<b>5.0</b>	<b>1.54</b>	<b>2.03</b>	<b>0.84</b>
	E-ACM2	8.52	3.57	6.2	1.58	2.09	<b>0.84</b>
	W-MYJ	8.51	3.47	6.1	1.64	2.18	0.82
	E-MYJ	8.70	3.63	8.5	1.71	2.26	0.82
	W-MYNN2	8.95	4.05	11.5	1.90	2.45	0.83
	E-MYNN2	8.79	3.67	9.6	1.78	2.33	0.81
	W-QNSE	9.02	3.77	12.5	1.96	2.53	0.80
	E-QNSE	8.97	3.68	11.8	1.85	2.43	0.81
80 m	Obs	6.97	3.00	-	-	-	-
	W-YSU	7.57	3.02	8.6	1.50	1.95	0.81
	E-YSU	7.51	2.92	7.7	1.50	1.96	0.80
	W-ACM2	7.49	3.03	7.4	1.39	<b>1.81</b>	<b>0.83</b>
	E-ACM2	<b>7.40</b>	2.96	<b>6.2</b>	<b>1.38</b>	1.83	0.82
	W-MYJ	7.47	2.90	7.1	1.46	1.92	0.80
	E-MYJ	7.58	2.98	8.7	1.52	2.02	0.79
	W-MYNN2	8.03	3.44	15.2	1.81	2.30	0.81
	E-MYNN2	7.66	<b>3.00</b>	9.9	1.57	2.06	0.79
	W-QNSE	7.74	2.99	11.0	1.65	2.12	0.78
	E-QNSE	7.73	<b>3.00</b>	10.9	1.56	2.08	0.79
		[ms <sup>-1</sup> ]	[ms <sup>-1</sup> ]	[%]	[ms <sup>-1</sup> ]	[ms <sup>-1</sup> ]	[-]

Table 4.10 Wind speed statistics for FINO3: Mean wind speed (Mean), standard deviation of wind speed (St.d.), Bias of the mean wind speed (Bias), mean absolute error (MAE), root-mean-square error (RMSE), and Pearson correlation coefficient (C.C.). The best performing model is highlighted in bold text.

Height	Name	$\langle S \rangle$	$\sigma_S$	Bias	MAE	RSME	C.C.
90 m	Obs	10.45	4.73	-	-	-	-
	W-YSU	10.05	4.72	-3.8	1.72	2.31	0.88
	E-YSU	9.92	4.52	-5.1	1.74	2.31	0.88
	W-ACM2	10.17	4.72	-2.7	<b>1.68</b>	<b>2.27</b>	<b>0.89</b>
	E-ACM2	10.03	4.59	-4.0	1.70	2.29	0.88
	W-MYJ	10.10	4.59	-3.4	1.70	2.32	0.88
	E-MYJ	9.99	4.62	-4.4	1.72	2.34	0.88
	W-MYNN2	9.74	4.54	-6.8	1.79	2.40	0.88
	E-MYNN2	9.63	4.33	-7.8	1.86	2.43	0.88
	W-QNSE	<b>10.34</b>	<b>4.73</b>	<b>-1.0</b>	1.80	2.48	0.86
	E-QNSE	10.31	4.80	-1.4	1.78	2.44	0.87
70 m	Obs	10.26	4.59	-	-	-	-
	W-YSU	9.81	<b>4.59</b>	-4.3	1.68	2.25	0.88
	E-YSU	9.60	4.34	-6.4	1.73	2.27	0.88
	W-ACM2	9.95	4.60	-3.0	<b>1.63</b>	<b>2.21</b>	<b>0.89</b>
	E-ACM2	9.72	4.41	-5.3	1.69	2.25	0.88
	W-MYJ	9.85	4.45	-4.0	1.66	2.26	0.88
	E-MYJ	9.68	4.44	-5.7	1.71	2.30	0.88
	W-MYNN2	9.47	4.37	-7.7	1.78	2.36	0.88
	E-MYNN2	9.28	4.15	-9.5	1.87	2.42	0.88
	W-QNSE	<b>10.03</b>	4.54	<b>-2.3</b>	1.75	2.39	0.86
	E-QNSE	9.98	4.62	-2.8	1.74	2.35	0.87
50 m	Obs	9.93	4.42	-	-	-	-
	W-YSU	9.51	4.43	-4.3	1.60	2.13	<b>0.89</b>
	E-YSU	9.24	4.16	-7.0	1.67	2.19	0.88
	W-ACM2	<b>9.66</b>	4.46	<b>-2.7</b>	<b>1.55</b>	<b>2.10</b>	<b>0.89</b>
	E-ACM2	9.35	4.22	-5.9	1.64	2.17	0.88
	W-MYJ	9.51	4.30	-4.3	1.59	2.16	0.88
	E-MYJ	9.32	4.25	-6.2	1.66	2.22	0.88
	W-MYNN2	9.16	4.19	-7.8	1.73	2.28	0.88
	E-MYNN2	8.87	3.95	-10.7	1.85	2.38	0.88
	W-QNSE	9.62	4.33	-3.1	1.68	2.29	0.87
	E-QNSE	9.60	<b>4.42</b>	-3.4	1.67	2.26	0.87
		[ms <sup>-1</sup> ]	[ms <sup>-1</sup> ]	[%]	[ms <sup>-1</sup> ]	[ms <sup>-1</sup> ]	[-]

Generally, the SCM errors are very similar to its forcing (WRF) simulation. At both sites the average deviation between the WRF simulation and its child SCM simulation was less than e.g. the inter-model deviation of WRF for different PBL schemes. The W-QNSE and E-QNSE are the WRF+SCM pair that deviated the least, while W-MYNN2 and E-MYNN2 deviated the most.

At Cabauw, a clear convergence of the SCM results is seen, compared to the mesoscale (convergence of the markers in Fig. 4.9 compared to Fig. 4.9), pointing to a degree of forcing-independence of the surface response in the  $k$ - $\epsilon$  closure, where “bottom-up” effects dominate. However, at FINO3 the SCM results seem to diverge.

The wind speed distribution at 80 m at Cabauw (Fig. 4.11 b) confirms that the observed mean wind speed errors correspond to a shift distributions. The wind direction distributions (wind roses) at 80 m (Fig. 4.11 c) are quite similar for the different PBL schemes, a slight misalignment (counter clockwise rotation) exists between the WRF results and the measurements, possibly resulting from a difference in veering. At FINO3, the wind speed distribution at 90 m and the wind direction distribution at 60 m are generally both well captured, but especially the 5–10  $\text{ms}^{-1}$  range seems to be over-represented in the models, while the larger wind speeds are underrepresented, pointing to an inability to capture periods of peak wind speed.

#### 4.2.4 Surface layer metrics at Cabauw

To further examine the WRF and SCM results, the surface friction velocity ( $u_*$ ), surface heat-flux ( $H$ ), surface temperature scale ( $\Theta_*$ ), surface Obukhov length, wind shear exponent aloft ( $\alpha$ ), and near-surface turbulent kinetic energy ( $k$  or TKE) was plotted against the observations from the Cabauw mast, shown in Fig. 4.12 and 4.13. Because four different surface layer (SL) schemes are used for the five different WRF configurations it is not obvious if the SL or PBL scheme contributes most to the results. So, this should be considered a study of the combined effects of the SL-PBL pairs. The wind shear exponent is calculated between  $z_1 = 80$  and  $z_2 = 140$  m using (Kelly et al., 2014)

$$\alpha = \frac{\ln(S_2/S_1)}{\ln(z_2/z_1)} \quad (4.13)$$

from the wind profile power law

$$\frac{S(z)}{S_r} = \left( \frac{z}{z_r} \right)^\alpha, \quad (4.14)$$

where  $S_r$  is the wind speed at reference height  $z_r$ .

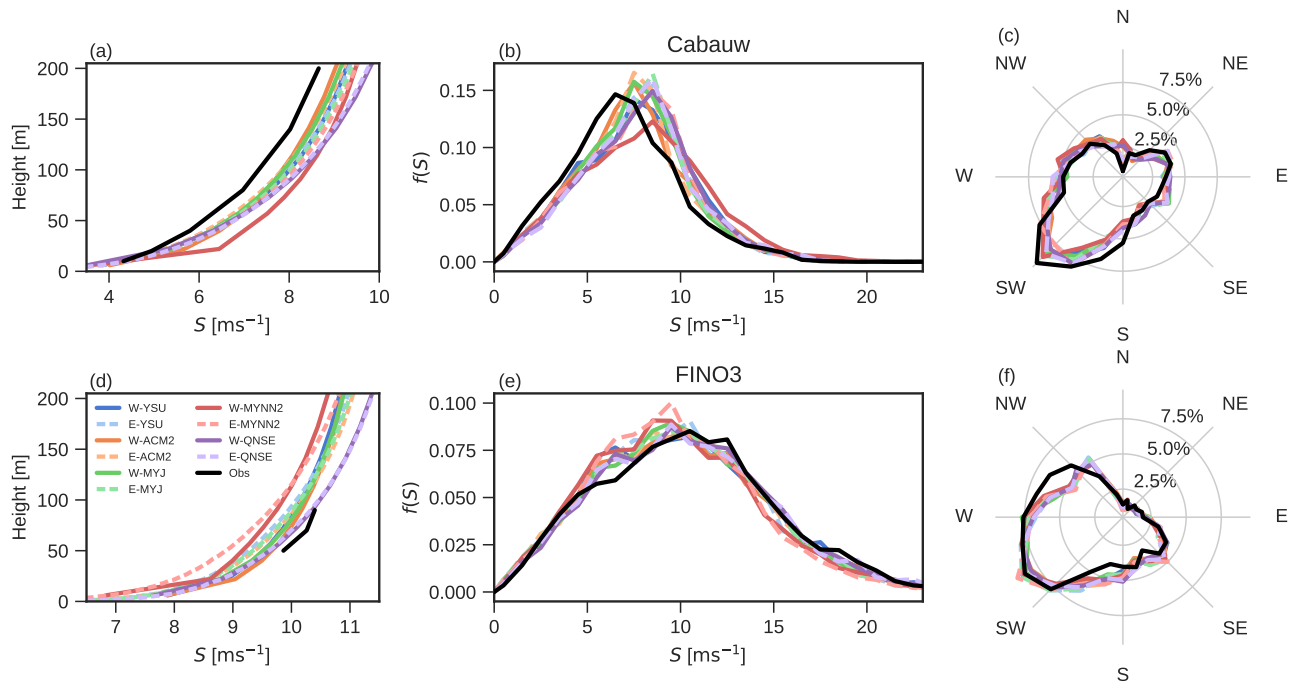


Fig. 4.11 Mean horizontal wind speed profiles **(a, d)** horizontal wind speed distribution **(b, e)**, and wind direction distribution **(c, f)** for the models and measurements at Cabauw (top) and FINO3 (bottom). Distributions are calculated at 80 (80) m at Cabauw and 90 (60) m at FINO3 for wind speed (direction). WRF are shown in full lines and the lines representing the SCM results are dashed.

Figure 4.13 shows scatter-plots of the modelled and observed TKE at 20 m. TKE is modelled in all three 1.5 order WRF PBL schemes (MYJ, MYNN2, and QNSE), and in the SCM. The measured TKE is calculated at 20 m above the ground from the standard deviation of the wind speed ( $\sigma$ ) during 10 min averaging periods, by assuming isotropic turbulence and using  $k = 3/2\sigma^2$ .

The friction velocities are generally overestimated in both the mesoscale and SCM results. This was also seen in SR17 during GABLS3. All the mesoscale and SCM results have similar mean errors (ME), mean absolute errors (MAE), and correlation coefficients. The positive biases indicate a misrepresentation of the surface roughness, overestimating the true friction.

For all WRF results, excess sensible heat fluxes (positive bias) are observed for situations of surface heating (Fig. 4.12), as well as a tendency for excess negative heat flux (negative bias) for situations of surface cooling. The SCM results show a similar pattern for surface heating conditions, but exaggerate the cooling even further during surface cooling conditions. This indicates a over-sensitivity to the prescribed varying surface temperatures. In each case the MAE is lower for WRF than the corresponding SCM. The MEs are lower for the SCM results, but this is caused by a balancing of positive and negative biases, seen by the larger MAEs. The temperature scale  $\Theta_* = H/u_*$  (Fig. 4.12) shows a similar pattern as heat flux, the SCM model tend to produce temperature scale values way below the observed during situations of surface cooling.

The Obukhov lengths generally seems well captured by both the WRF and SCM, for the bins chosen here (Fig. 4.13), but a weak signal is also seen along the primary diagonal, associated with negative correlation, especially in the unstable quadrant (upper left). This may be explained by timing-issues during night-day transition.

The correlation of the modelled and observed wind shear exponent between 80 and 140 m, shown in Fig. 4.13, shows much lower correlation than for the other metrics. This is expected because it is a result of many combined effects, including the surface roughness effects, stability related effects, and unsteadiness. Low shear situations (which are typical for unstable stability conditions) are well captured by the WRF runs except for the W-QNSE, while high shear situations show large inter-model (model-to-model) variations; the W-MYNN2 and W-ACM2 tend to have lower  $\alpha$  values. The SCM show a tendency of overestimating the shear for low shear situations, and have larger MAEs. This will be explored more below.

For TKE (Fig. 4.13), the three WRF configurations that models the TKE tend to underestimate it, especially the W-MYJ and W-QNSE, while the SCM results generally capture the TKE well. The W-MYJ often fall back to the background  $10^{-1} [m^2s^{-2}]$  level of turbulence (Fig. 4.13 b). The figure indicates that the  $k$ - $\epsilon$  closure is able to account for the turbulence quite well close to the surface.

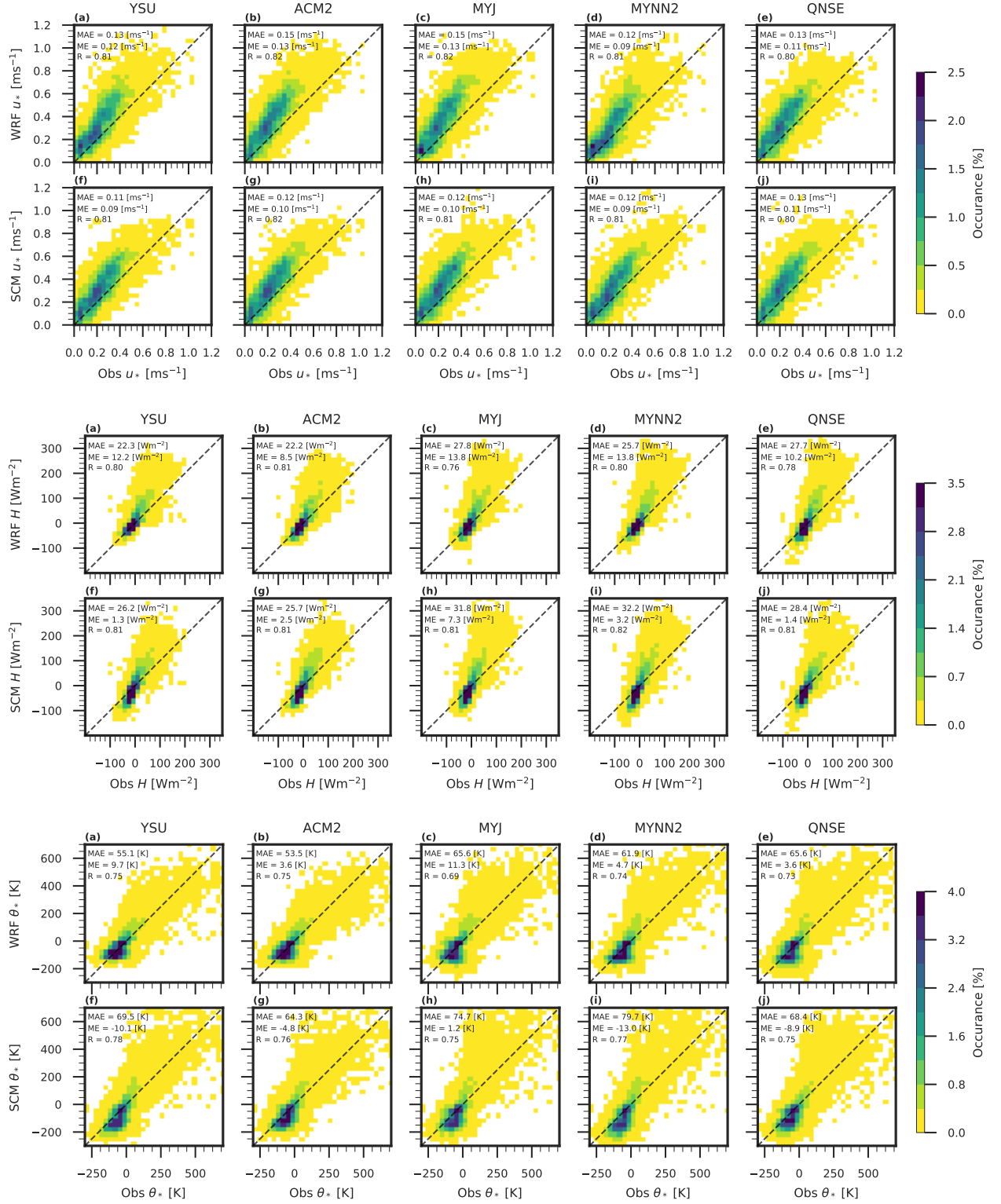


Fig. 4.12 Scatter-plots of observations vs model results of friction velocity ( $u_*$ ) at Cabauw for each of the WRF configurations (a-e) and SCM results (f-j).

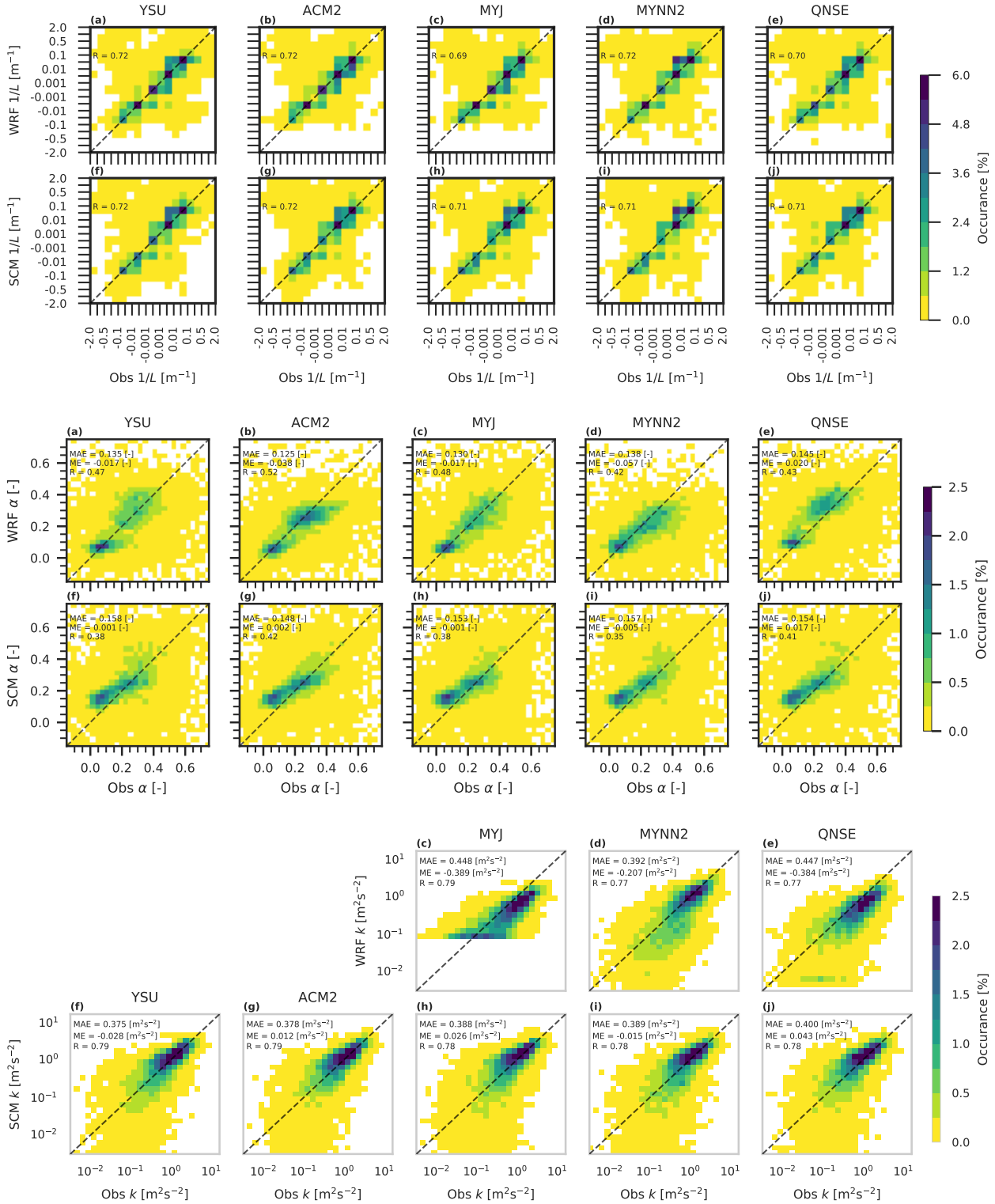


Fig. 4.13 Scatter-plots of observations vs model results of turbulent kinetic energy ( $k$ ) at Cabauw for each of the WRF configurations (a-e) and SCM results (f-j).

Table 4.11 Stability classes, similar to Draxl et al. (2014)

Stability class	Obukhov length [m]
Unstable (U)	$-500 \leq L < -50$
Neutral (N)	$ L  > 500$
Near stable (NS)	$200 < L \leq 500$
Stable (S)	$50 < L \leq 200$
Very stable (VS)	$10 < L \leq 50$

The surface layer metrics indicate that the  $k$ - $\epsilon$  closure is only weakly sensitive to the PBL and SL scheme used by the forcing mesoscale model, since these SCM results for the different configurations of WRF only varies to a lesser degree, pointing to bottom-up effects being the main driver here.

#### 4.2.5 Stability dependence of wind profile

To investigate the response of each model to different atmospheric stability conditions, wind speed profiles were constructed for five stability regimes, normalized by friction velocities (Fig. 4.14). See table 4.11) for the range of stabilities for each group. The minimum number of samples (hours) across both measurements and model results was 758 for W-YSU at Cabauw, and 299 for W-ACM2 at FINO3, but in most cases 1000+ samples (hours) were available. Measurements of friction velocity was not available for FINO3, so only model results are shown there.

At Cabauw, all the models underestimate the normalized wind speed for the unstable (U) conditions, but the SCM is slightly closer to the measurements than the mesoscale results. Neutral conditions (N) are well captured by the models, although they do underestimate the observed normalized profile. For near stable and stable conditions (NS and S) the SCM results shows lower normalized wind speeds compared to WRF (the same is true for FINO3). The WRF profiles are closer to the measured. In particular the W-MYNN2 are quite close to the measured at low heights (20 and 40 m). For very stable (VS) conditions the models generally do not capture the normalized wind speed profile well. Highly stable conditions is a well known problem for atmospheric models (Holtslag and Svensson, 2013). The normalized wind speed for the W-MYNN2 is greater than the rest of the models (also at FINO3), and it is closer to the observed profile. The E-MYNN2 does not follow the W-MYNN2.



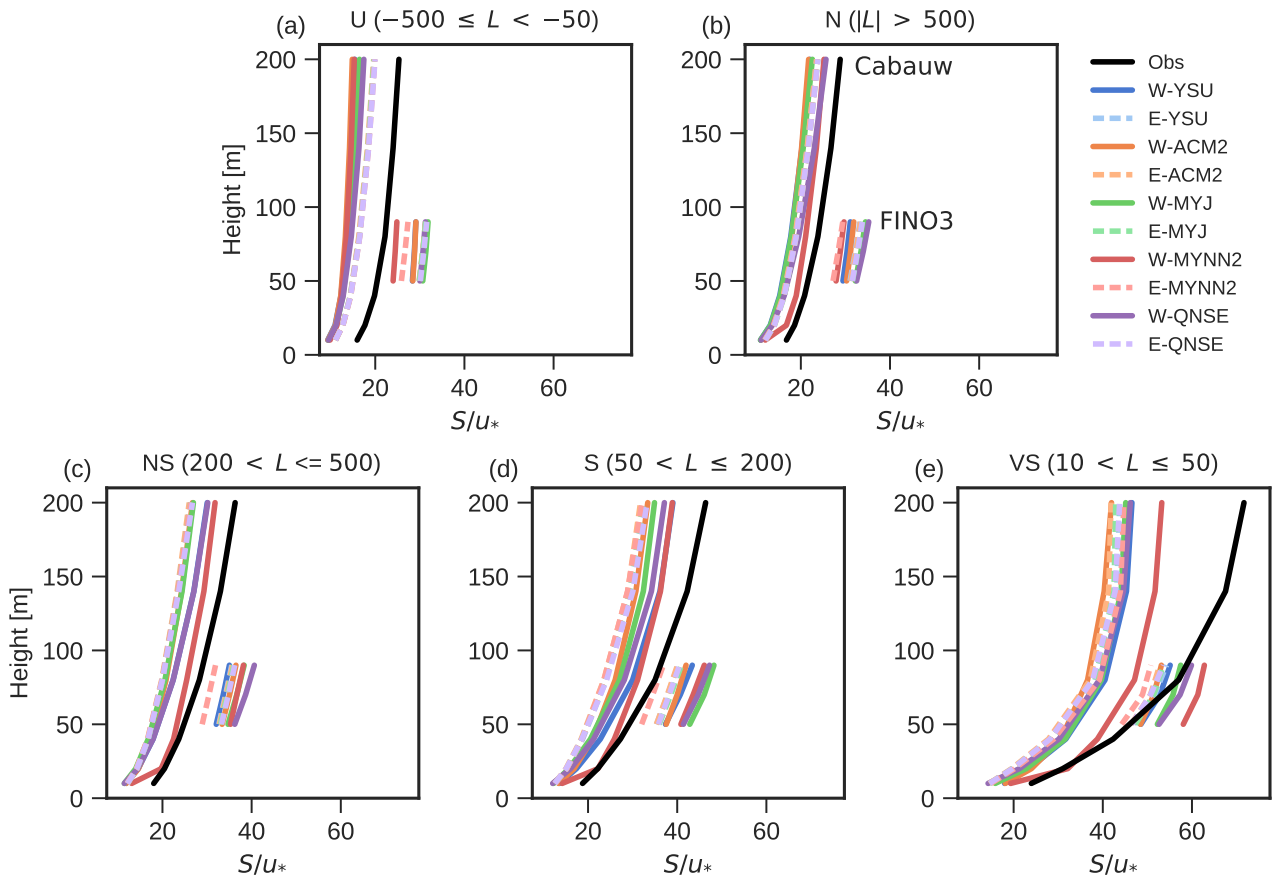


Fig. 4.14 Horizontal wind speed profiles normalized by friction velocity for five stability classes defined by Obukhov lengths ( $L$ ); (a) unstable (U), (b) neutral (N), (c) near stable (NS), (d) stable (S), and (e) very stable (VS). The classes are similar to Draxl et al. (2014).

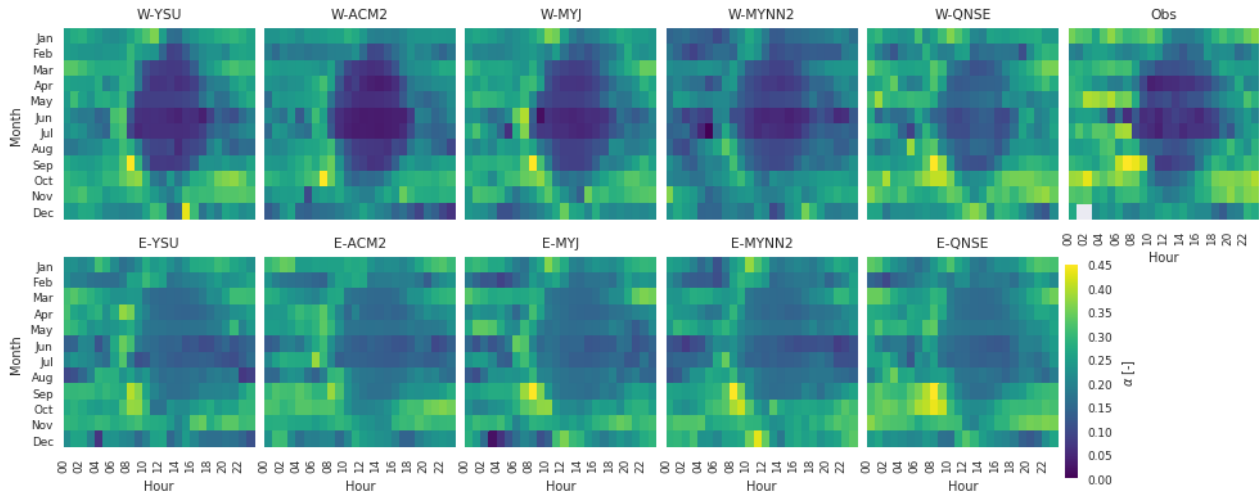


Fig. 4.15 Mean wind shear exponents at Cabauw by month of year (y axis) and hour of day (x axis) for the five WRF model configurations (a-e), the observations (f), and the SCM (g-k). The shear exponent is calculated between 80 and 140 m.

#### 4.2.6 Wind shear by hour and month

As Fig. 4.13 shows, the SCM tends to overestimate wind shear at Cabauw between 80 and 140 m when observations point to a small shear exponent (associated with unstable conditions). An explanation for this can be partly found in Fig. 4.8 at 12:00, which shows a larger temperature gradient and weaker wind speeds with a steeper slope (shear) during convective conditions for the SCM results between 80 and 140 m. Selecting heights at lower levels, e.g. 20 and 40 m show better agreement between the SCM and WRF results (not shown). However, for wind energy applications the shear at hub heights are more relevant to highlight.

To further examine the observed patterns of  $\alpha$ , in particular the temporal dependencies, mean values of shear exponent are shown in Fig. 4.15 for every month of the year and every hour of the day. The figure shows that the overestimation of wind shear for the SCM is associated with summertime-daytime conditions where unstable stability conditions are common. The WRF results generally capture the mean shear better for these conditions, apart from the W-QNSE that, just as the SCM results, show larger mean shear values. The figure also shows that during summertime night-time conditions (where rapid surface cooling is common) the E-MYNN2 tends to underestimate the mean shear.

### 4.3 Summary and conclusions

In this study a mesoscale to microscale coupling methodology was evaluated for a LLJ test case (GABLS3), for long-term surface layer characteristics, and long-term wind statistics. The coupling methodology involves forcing the microscale model with momentum and temperature tendencies extracted from a mesoscale model, as discussed by e.g. (Sanz Rodrigo et al., 2017b). The mesoscale tendencies extracted in this study from the WRF model, accounts for large-scale flow effects required by the microscale model to accurately capture the unsteady flow patterns of real-world ABL flow.

The microscale model in this study consists of Single-Column Model, based on the RANS equations combined with  $k$ - $\epsilon$  turbulence closure modified to accommodate non-neutral stability conditions. It is a simplified 1D version of the in-house CFD code EllipSys3D at DTU Wind Energy. The SCM was used in this study in order to make year-long simulations affordable. For this reason the evaluation was done at simple sites; Cabauw, a flat site with some surface roughness inhomogeneities, and FINO3, an offshore site. The evaluation period at Cabauw was the year 2006, which allowed for comparison with the GABLS3 test case (from noon 1 July to noon 2 July UTC). These simple site study cases serve as a prerequisite to using the methodology for modelling complex terrain flow. Furthermore, to study the sensitivity of the tendencies to the choice of PBL and SL scheme in WRF, five different WRF configurations were used, based on the YSU, ACM2, MYJ, MYNN2, and QNSE PBL schemes.

The results for one PBL scheme (YSU) showed that both the PGF and momentum advection are important to accurately capture the long-term wind statistics, and to a smaller degree also temperature advection, although the temperature nudging used capture some of the same effects. In many situations advection and pressure gradient forces are, to some degree, in balance. Meaning that the magnitude of the total tendency are much smaller than each of the two components alone. This means that using just geostrophic forcing leads to a large overestimation of the wind speed. It was also clear that letting the PGF vary in height (geostrophic shear) is important, not least to get the correct balance of advection tendency and pressure-gradient tendency across heights. It was chosen to use a combination of time and height varying PGF, momentum advection, temperature advection, and varying surface temperature to investigate results for all the different PBL schemes to further study the methodology.

The results for GABLS3 showed that all five WRF model simulations capture the LLJ that appears during the diurnal-cycle. However, they overestimate the strength and duration of the jet. They also show a negative temperature bias, especially for the local PBL schemes

(MYJ, MYNN2, and QNSE). The SCM driven by the WRF tendencies also capture the LLJ, but tend to smoother out the jet and lower its maximum value slightly.

The long-term wind statistic showed that WRF underestimates the mean wind speed at FINO3 by  $-1.0$  to  $-7.8 \text{ ms}^{-1}$ , depending on height and configuration. Distributions of wind speeds (Fig. 4.11) indicate that this underestimation is due to an underestimation of strong wind occurrences. At Cabauw, the WRF simulations overestimated the mean wind speed, for the W-MYNN2 configuration by as much as 23% at 20 m. But, mostly the overestimation was in the range 6 – 8%. The over-estimations are likely due to unresolved terrain effects coming from a misinterpretation of the surface roughness, and inability to capture internal boundary-layer effects coming from local-scale roughness-changes. In each case the SCM results are very similar to the results of its forcing model results. This suggests that the coupling methodology of forcing the SCM by a sum of PGF and momentum advection, as well as temperature advection, works well in these simple terrain cases. It also suggests that the  $k$ - $\epsilon$ , in general, adequately captures the turbulent effects for a range of weather conditions, at a level comparable to the WRF PBL schemes, although a slight deterioration of results was seen aloft at Cabauw and at FINO3, but this deterioration was less than the inter-model variation. Surface cooling was overestimated by the SCM by as much as 50% in some cases, indicating too strong sensitivity to the varying surface temperature derived from WRF. This should be further investigated. It could possibly be alleviated by directly using heat flux as the boundary condition for temperature in the SCM. As Rodrigues et al. (2015) remarks, this would also be better suited to complex terrain where the temperature vary differently with height depending on location, whereas heat fluxes can be assumed to vary constantly with height in the surface layer, if one neglects differential heating/cooling effects. However, as Basu et al. (2008) and others have pointed out, using heat flux carries its own limitations for highly stable conditions, depending on the implementation .

During convective conditions, both W-QNSE and the five SCM results overestimated the wind shear at Cabauw. The QNSE scheme was made for stable and weakly unstable conditions and may be less appropriate for very unstable condition (Sukoriansky et al., 2005). Likewise, the  $k$ - $\epsilon$  model may need further modifications to account for strongly unstable conditions more accurately.

While this study showed that the coupling methodology works well in simple terrain, it remains to be determined whether it also works in highly complex terrain. Terrain heterogeneities induce larger variance in the momentum and temperature tendency terms in the mesoscale model, potentially making it difficult to balance several concerns: 1) extracted tendencies should not contain resolved microscale effects, that the microscale model will also solve, i.e. double-counting of local flow effects should be avoided, and 2) the tendencies

should still capture important mesoscale effects, such as large scale channeling, gap-flow, and sloping effects that are important for steering the inflow, such that the forcing direction in the terms used in the coupling reflect the correct flow directions. Misalignment of the tendencies can cause drastically different results in complex terrain.

In summary, this study showed encouraging results that indicate that the tendencies-based coupling-technique can be used for model coupling for wind downscaling, and that the tendencies combined with the  $k$ - $\epsilon$  closure results in comparable wind statistics to the WRF results. The coupling methodology was also shown to be a useful tool for testing turbulence closures without having to implement it in a developmentally and computationally costly 3D model.

# Chapter 5

## Coupling via tendencies in complex terrain<sup>2</sup>

This study presents results of a coupled mesoscale-microscale model system in complex terrain. The URANS microscale model described in Chapter 3 is dynamically coupled via momentum and temperature tendencies to the WRF mesoscale model. The coupling methodology is studied at the Perdigão site, a forested double hill in Portugal, where an extensive measurement-campaign was carried out during the *New European Wind Atlas* (NEWA) ERA-NET Plus project.

Many considerations were made before using the meso-micro coupling. Those are first discussed extensively, and sensitivities to grid spacing and numerical methods are shown and discussed as well. Finally, the methodology is evaluated for a 32-day period at nine meteorological masts distributed across the double-hill site, in order to show statistically the performance of the methodology. Several snapshots of the flow behavior during the 32-day period are studied, comparing vertical *light detection and ranging* (LIDAR) scans to the model results, to highlight the qualities and shortcomings of the tendency-driven microscale model.

### 5.1 Methodology

#### 5.1.1 Validation site

The validation site is *Perdigão* (Fig. 5.1), a site in central Portugal named after a nearby village. It was the subject of an intense measurement campaign in the spring and summer

---

<sup>2</sup>This chapter consists of results that will be published in the journal paper Olsen and Cavar (2018)



Fig. 5.1 The Perdigão site seen from the central valley southeast of the nine masts looking towards northwest from inside the valley. Picture kindly made available by the NEWA project.

months of 2017 carried out as a part of several European and American projects, among them the New European Wind Atlas (NEWA) ERA-NET Plus project. Before and after the intense campaign, a longer period of continuous measurements was conducted during 2017 and 2018 (Fernando et al., 2018), and a shorter precampaign took place in 2015 (Vasiljevia et al., 2017). The topography of the site is characterized by two  $\approx 4$  km long parallel mountain ridges separated by a valley (*Vale Cobrão*) with a distance of  $\approx 1400$  m from ridge-top to ridge-top. The slopes on each side of the ridges have an inclination of about  $35^\circ$  (Vasiljevia et al., 2017). The bottom of the central valley is located  $\approx 200 - 250$  m below the ridge tops. The vegetation is characterized by patches of bare land, roads, or very low-height vegetation, patches of Eucalyptus and Pine trees, as shown in Fig. 5.1. Not far from the center of the southwest ridge, an Enercon E-82 2MW wind turbine is located and operated throughout most of the measurement period (Fernando et al., 2018). The site was densely instrumented with meteorological masts, an array of short-range and scanning-LIDARs, SODARs, ceilometers, weather balloons carrying radiosondes.

### Measurements from meteorological masts

For this study, only measurements from nine tall masts (Fig. 5.2) are used. The nine masts consists of three 100 m masts (20, 25, and 29) and six 60 m masts (7, 10, 22, 27, 34, and 37) instrumented with sonic anemometers and thermometers at several heights. Anemometer measurements were averaged in 10 min averaging periods, checked for obvious errors/inconsistencies, and filtered based automated error flags, but apart from that, left as is.

### Long-range LIDAR measurements

Scans from four long-range WindScanner (LRWS) LIDARs (Vasiljevic, 2014) located on a single transect perpendicular to the two ridges, going through meteorological mast 20, 22, 25, 27, and 29 as shown in Fig. 5.2. Vertical scan planes from the LRWS are used to compare with vertical cross sections from the model simulations at concurrent instances. The LIDAR line-of-sight (LOS) scans were filtered only by carrier-to-noise-ratio (CNR), removing scans below  $-24$  dB, and then time-averaged in 10 min individual periods. When presented (Fig. 5.17, 5.19, and 5.21), the scan planes from each of the four LRWS are simply layed out as a composite of the individual scans. No averaging of the scans in the overlap, or anything similar, is done. However, priority is given to laying lower scan planes on top of elevated scan planes.

### Study period

A 32-day period between 13 April and 15 May 2017, was used as the primary study-period. During that period, the weather conditions were characterized by mostly fair weather, scattered clouds, and occasional rain showers. No major frontal passages were observed, but days of strong synoptic forcing resulting elevated wind speeds occurred. The dominant wind directions were from the northeast and from the southwest, as it is typical of the site (Vasiljevia et al., 2017).

## 5.1.2 Microscale model configuration

### Computational grids

Three computational grids were generated for the microscale model, listed in table 5.1. The only difference between the three is the horizontal spacing between grid cells. The grids span  $12 \times 12$  km and extend to an elevation of 4 km above sea-level. Periodic boundary conditions are used, so outflow becomes inflow in the opposite end. In the area of interest (the center), the grid cells have a fixed width and length, and towards the domain edges they are stretched.



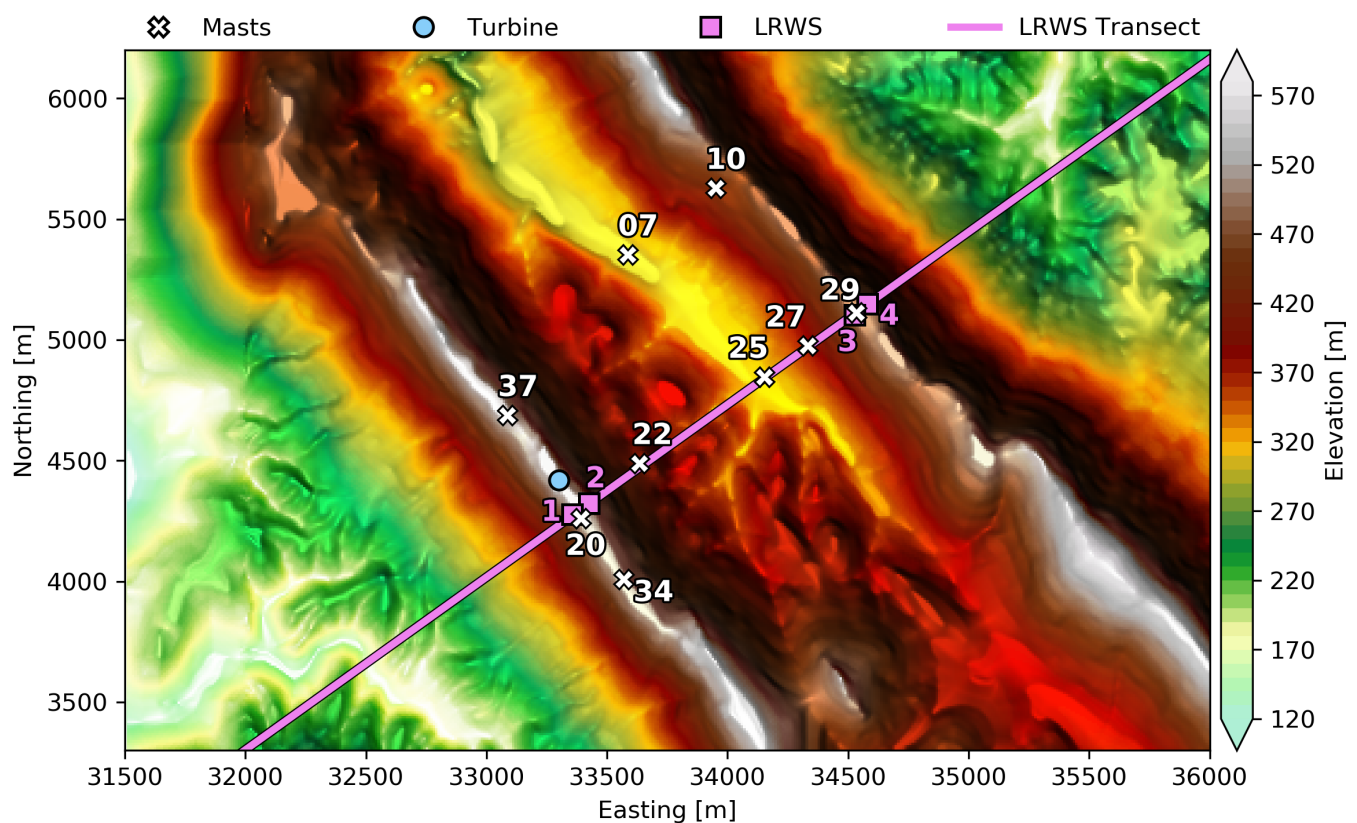


Fig. 5.2 Locations of the nine tall masts (white crosses), the wind turbine (blue circle), and the location and approximate transect (pink line) of the scan planes for the four LRWS systems (pink squares).

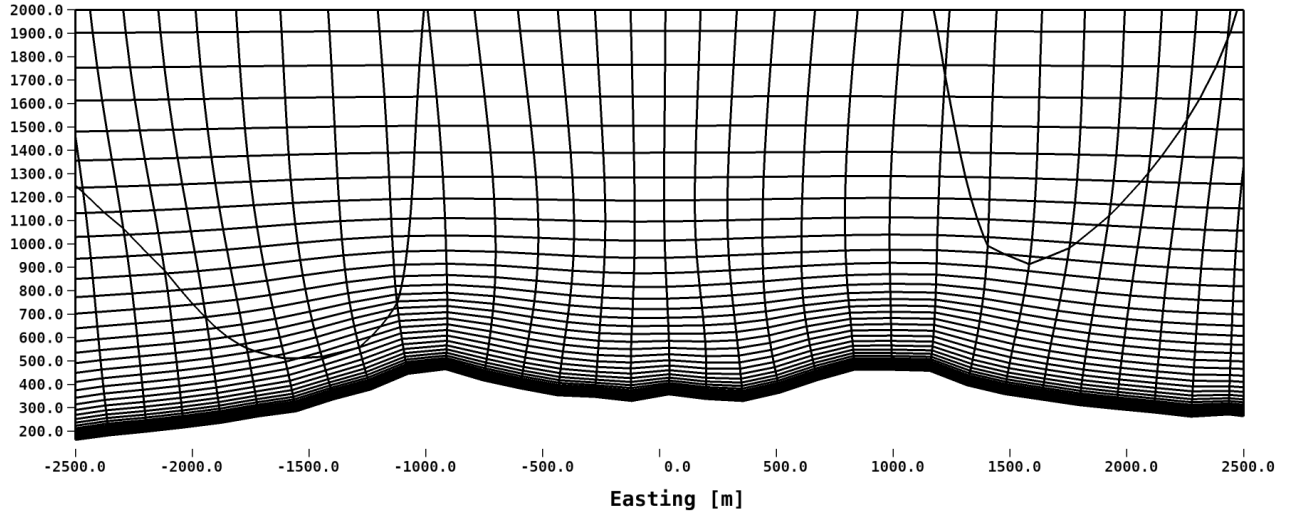


Fig. 5.3 Vertical layout of the G02 grid cells near the Perdigão double ridge region for  $y = 0$ . The y-axis is meters above sea-level. For visual purposes only every second increment, vertically and horizontally, are shown. The two seemingly random curves are plotting-artifacts.

Table 5.1 Computational grids for the microscale model: Reference names, horizontal grid spacing in center and edge regions ( $\Delta x, \Delta y$ ) and number of cells along each coordinate ( $n_x, n_y, n_z$ ).

Name	$\Delta x, \Delta y$ Center	$\Delta x, \Delta y$ Edge	$n_x, n_y, n_z$
G01	40	70	256, 256, 128
G02	80	140	128, 128, 128
G03	120	170	96, 96, 128

Figure 5.5 shows the surface elevation in one of the grids (G02). The surface elevation is based on a high-resolution elevation dataset constructed from overflight LIDAR-scans. 128 vertically stretched cells are used that increase hyperbolically towards the top of the domain. Near the surface, the grid cells are orthogonal to the surface and follow the terrain, while they gradually become rectangular and constant-height towards the top (fig 5.3). Figure 5.4 shows the approximate vertical extend and elevation of each level, revealing the high density of vertical levels close to the surface. The first cell is placed on top of the surface roughness length  $z_0$ . The center of the domains are located at  $(x, y) = (34200, 4500)$  in the Portuguese TM06 (EPSG:3763) projection.

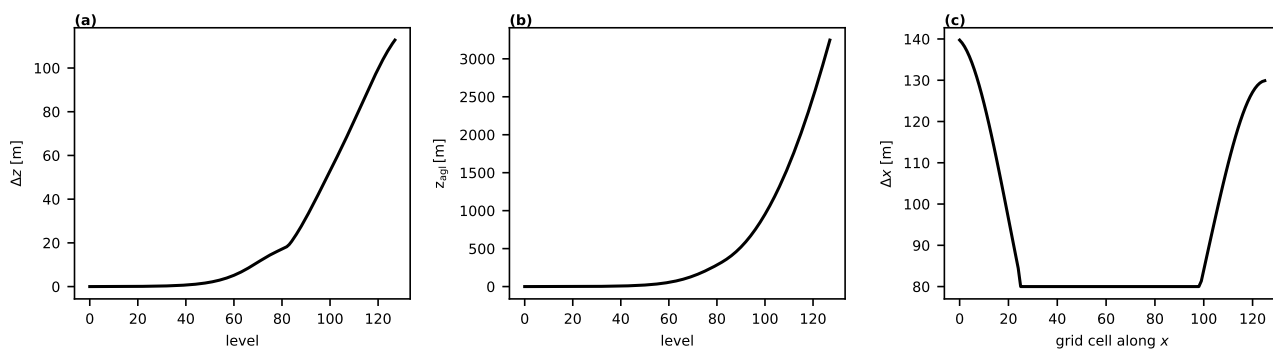


Fig. 5.4 (a) Spacing of each of the 128 levels from bottom to top, (b) approximate height above terrain for each of the vertical levels. (c) approximate grid size in  $x$  ( $\Delta x$ ) across the G02 domain.

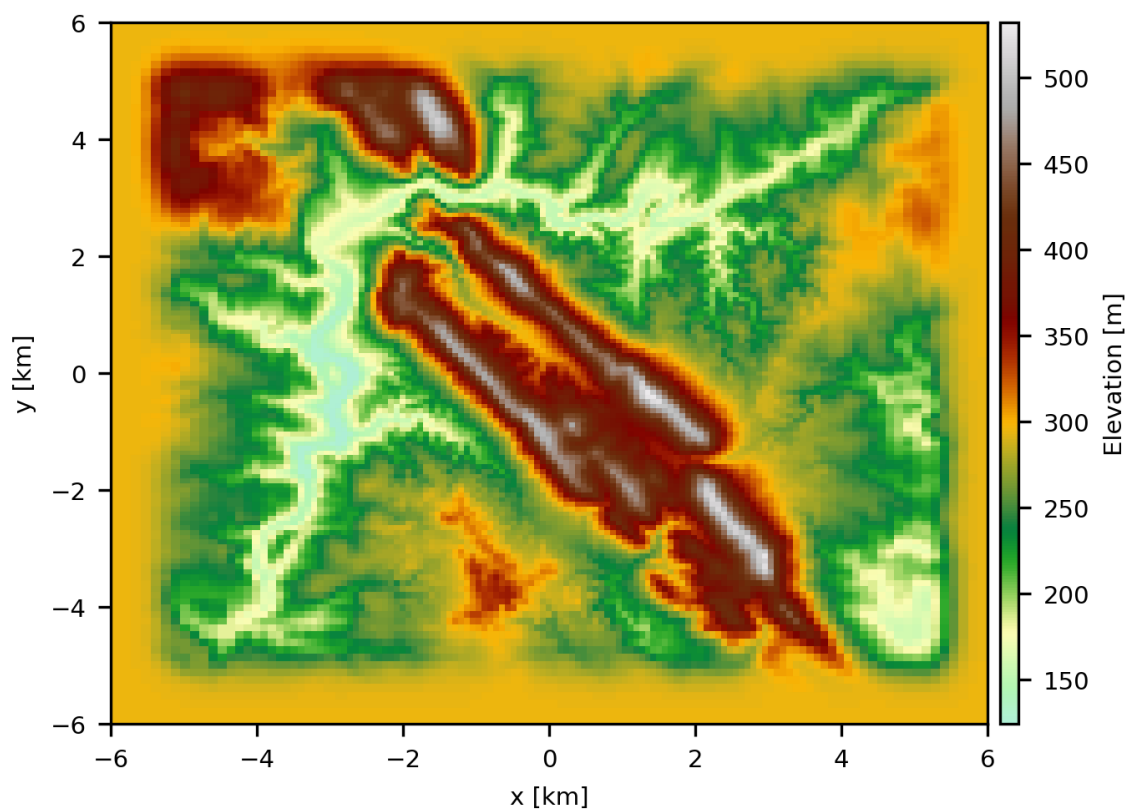


Fig. 5.5 Elevation of the surface in the microscale domain G02. Near the edges the elevation has been relaxed towards a constant height. The coordinates system is relative to (34200, 4500) in the EPSG:3763 projection.

### Numerical methods

A Finite-volume discretization with collocated variable arrangement is used to solve the transport equations in general curvilinear coordinates. The pressure is solved using the SIMPLE algorithm (Patankar and Spalding, 1972), with the Rhie-Chow correction method (Rhie and Chow, 1983). Advection is solved using either the third-order accurate upstream interpolation for convective kinematics (QUICK) scheme (Leonard, 1979), or the first-order accurate upwind scheme (Courant et al., 1952) (see section 5.2 for details). The upwind scheme is highly damping, effectively reducing the resolvable scales due to poorly resolving sharp gradients. Therefore, a low-order scheme is generally undesirable, and should be avoided. However, these same characteristics may sometimes be desirable for experimental purposes. In the context of atmospheric *gray scale* modeling where turbulence is solved by a closure model, and explicitly resolved eddy-structures of temporal and spatial scales similar to atmospheric turbulence, the reduction of effective resolution may maintain scale-separation at smaller grid-scale than high-accuracy solvers. However, it still involves multiple negative consequences due to the low order of accuracy, including a suppression of desirable flow-structures, underestimation of extremes, and excessive numerical mixing.

#### 5.1.3 Mesoscale model configuration

The Weather Research and Forecasting (WRF) model (Skamarock et al., 2008) is used to provide forcing for the microscale model, and used as a reference in the validation of the microscale model with observations. The WRF model solves the fully compressible non-hydrostatic Euler equations in Cartesian horizontal coordinates, and uses terrain-following vertical coordinates. In this study a third-order Runge-Kutta time-stepping scheme is used, including a time-step splitting (semi-implicit) scheme for acoustic modes. Third- and fifth-order differencing is used in the vertical and horizontal directions, respectively. The prognostic variables are placed on a grid that is horizontally and vertically staggered, using the Arakawa C grid layout (Arakawa and Lamb, 1977).

A five-domain setup of one-way coupled zooming grids was used with equal horizontal grid spacing in  $x$  and  $y$  of 27, 9, 3, 1, and 1/3 km. The domains are labeled by their index, from the most course one: d01 to the most fine one: d05. All five domains have 61 vertical levels, and are made up of  $100 \times 100$  grid cells in the horizontal, centered on the Perdigão site at  $39.705^\circ\text{N}$ ,  $7.731^\circ\text{W}$ . The ERA-Interim reanalysis dataset (Dee et al., 2011) is used for initial and lateral boundary conditions (LBCs) for the outermost domain, while LBCs for the four inner domains are provided by its parent domain. Table 5.2 shows the configuration and

Table 5.2 WRF model configuration for the five WRF domains. A sample WRF input file (“namelist.input”) is available in Appendix A.2.1.

Configuration		References:
<b>Model setup</b>		
Version	ARW-WRF 3.8.1	Skamarock et al. (2008)
Init. and LBCs	ERA-Interim	Simmons et al. (2007)
Elevation	Viewfinder <sup>◇</sup>	
Land use	CORINE	Bossard et al. (2000)
SST	HRSST	Gemmill et al. (2007)
Domains	d01, d02, d03, d04, d05	
$\Delta x$ and $\Delta y$	27, 9, 3, 1, 1/3 km	
Grid size(s) ( $n_x, n_y$ )	(100, 100), . . . , (100, 100)	
Vertical levels ( $n_z$ )	61 (top at 50 hPa) 21 levels below 1 km*	
$\Delta t$	Adaptive <sup>†</sup>	
<b>Model physics</b>		
Land surface model	Noah	Chen and Dudhia (2001)
Microphysics	WSM3 Micro physics	Hong et al. (2004)
Cumulus parameterization	Kain-Fritsch	Kain (2004)
Shortwave radiation	Dudhia	Dudhia (1989)
Longwave radiation	RRTM	Mlawer et al. (1997)
Planetary Boundary Layer	YSU	Hong et al. (2006)
Surface Layer	Revised-MM5	Jiménez and Dudhia (2012)

\*The WRF ( $\eta$ ) levels listed in Appendix A.2.1 correspond to  $\approx 6, 22, 41, 57, 73, 92, 114, 141, 172, 207, 247, 292, 343, 400, 466, 539, 623, 718, 825, 946 \dots$  m (cell centers in d02 at TW20)

<sup>†</sup>Target Courant–Friedrichs–Lewy (CFL) conditions:  $CFL_{\text{total}} = 1.15$ ,  $CFL_{\text{horizontal}} = 0.85$

<sup>◇</sup> Gapfilled SRTM

datasets used for setting up the WRF simulations. The cumulus scheme was only active for domains d01 and d02.

The simulations use the Yonsei University Planetary Boundary Layer (YSU) scheme (Hong et al., 2006). The scheme models turbulent diffusion as a vertical (column) process, with diffusion related to the vertical gradients of the mean flow by an eddy viscosity following a prescribed normalized vertical profile. As indicated by Olsen et al. (2018), the choice of PBL scheme in the WRF model only influences the momentum and temperature tendencies in the model to a relatively small degree in simple terrain. In complex terrain, this may not be true, but to reduce the scope of the study only a single PBL scheme was tested.

It is common practice to use mesoscale models that utilizes a PBL scheme to model turbulence, to progressively downscale the atmospheric flow via gradual nesting to grid cell

widths of about 1–3 km. Beyond that point, extra considerations must be taken of how to treat turbulence when the model may explicitly resolve the most energetic eddies in the PBL. Here, domain d05 has a grid spacing of  $333 \times 333$  m, that is a scale where this consideration should be made. In this study, no extra care is taken, and the PBL scheme is kept active in all grids. The results from d05 should be considered experimental, and serve as a reference, since it has become more common for modelers to use very fine grid spacing (Horvath et al., 2012), and some have suggested that using PBL schemes may be appropriate even down to 300 – 500 m (Arnold et al., 2012; Hong and Dudhia, 2012).

The surface layer scheme, which models the vertical structure of the atmosphere below the lowest model level and provides lower boundary conditions for governing temperature and momentum equations, is the revised MM5 scheme (Jiménez and Dudhia, 2012). This scheme uses modified similarity functions relative to the original MM5 scheme (Beljaars, 1994; Dyer, 1974; Grell et al., 1994; Paulson, 1970; Webb, 1970; Zhang and Anthes, 1982) for highly stable and unstable conditions, replacing them with those of Fairall et al. (1996) and Cheng and Brutsaert (2005). Furthermore, hard limits on the possible values of the stability function have been removed with this revision, and the lower limit imposed on friction velocity has been reduced from  $0.1$  to  $0.001 \text{ m s}^{-1}$ . The lower limit is maintained to avoid runaway cooling (Louis, 1979) where, during rapid radiative cooling and low wind speeds, the surface may be completely decoupled from the surface, ultimately reducing the heat flux to zero.

The land use classes were provided by the Coordination of Information on the Environment (CORINE) dataset, and the United States Geological Survey (USGS) land use classification was used to convert them to surface roughness lengths. Figure 5.7 shows the CORINE land use classification around the site in d05. Most of the land is classified as “Mixed Shrubland/Grassland” across the ridges and in the central valley, as well as most of the land just east of the site, but patches of “Cropland/Woodland Mosaic” are also prevalent in the central valley and on the slopes. The “Mixed Shrubland/Grassland” class is converted via the classification to a seasonally-varying surface roughness length between 1 and 6 cm, which is very low when considering the actual vegetation of the site, with many Eucalyptus and Pine trees. To the west of the site, the land is classified mostly as “Cropland/Woodland Mosaic” and “Evergreen Needleleaf Forest” that corresponds to higher roughness lengths between 20 and 50 cm.

The Viewfinder dataset was used to generate topographical heights for the WRF domains. The dataset consists of mainly SRTM data gap-filled with local elevation maps, and are provided in a resolution of  $\approx 2$  arc-seconds. The extent, and surface elevation, of each domain is shown in figure 5.6.

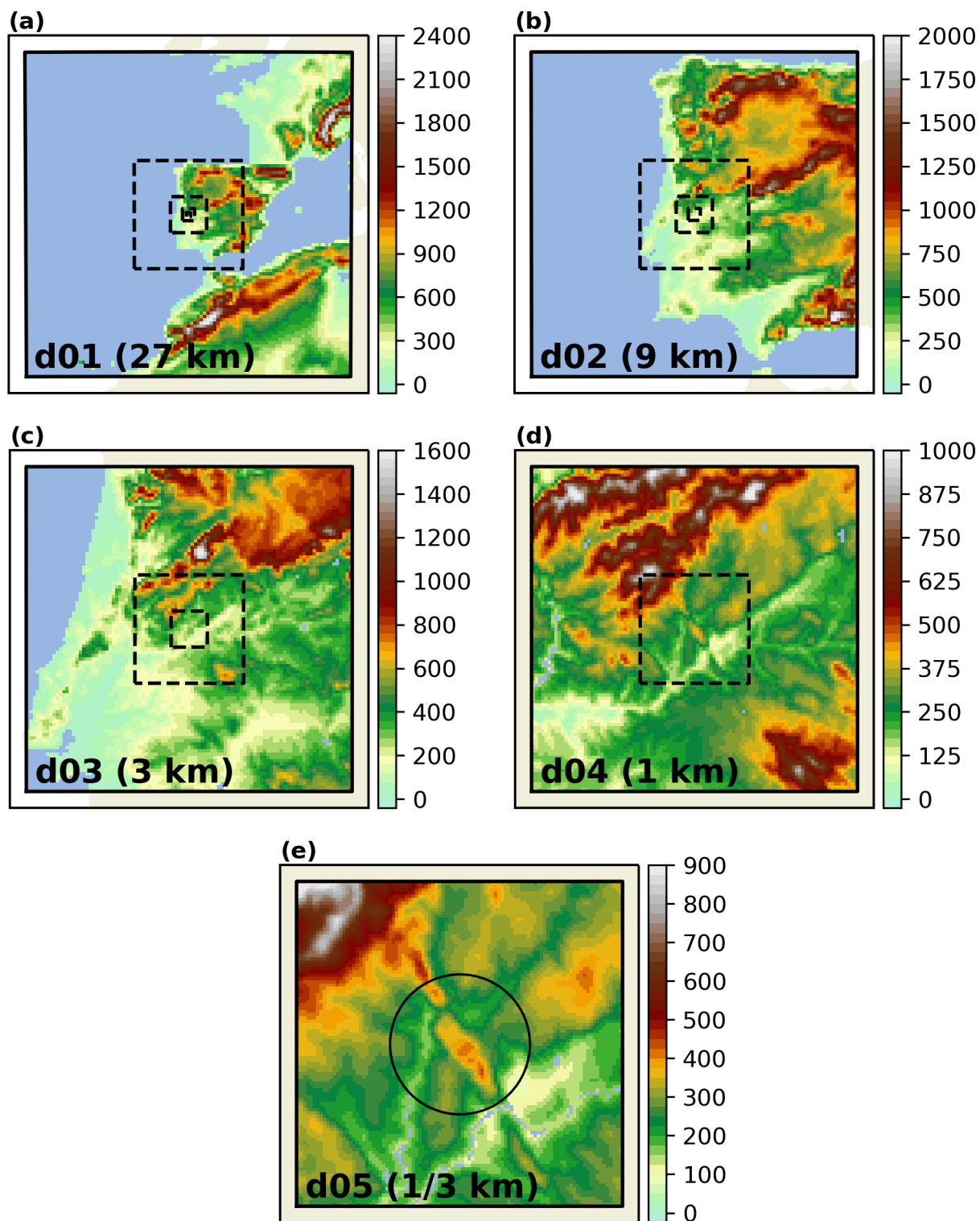


Fig. 5.6 The extent and surface elevation in meters of each of the five WRF domains (d01-d05), with each domains horizontal grid spacing ( $\Delta x, \Delta y$ ; 27-1/3 km) in parenthesis. The footprint of the inner domains is shown in dashed lines in each domain, and the Perdigão site is highlighted with a circle in the innermost domain.

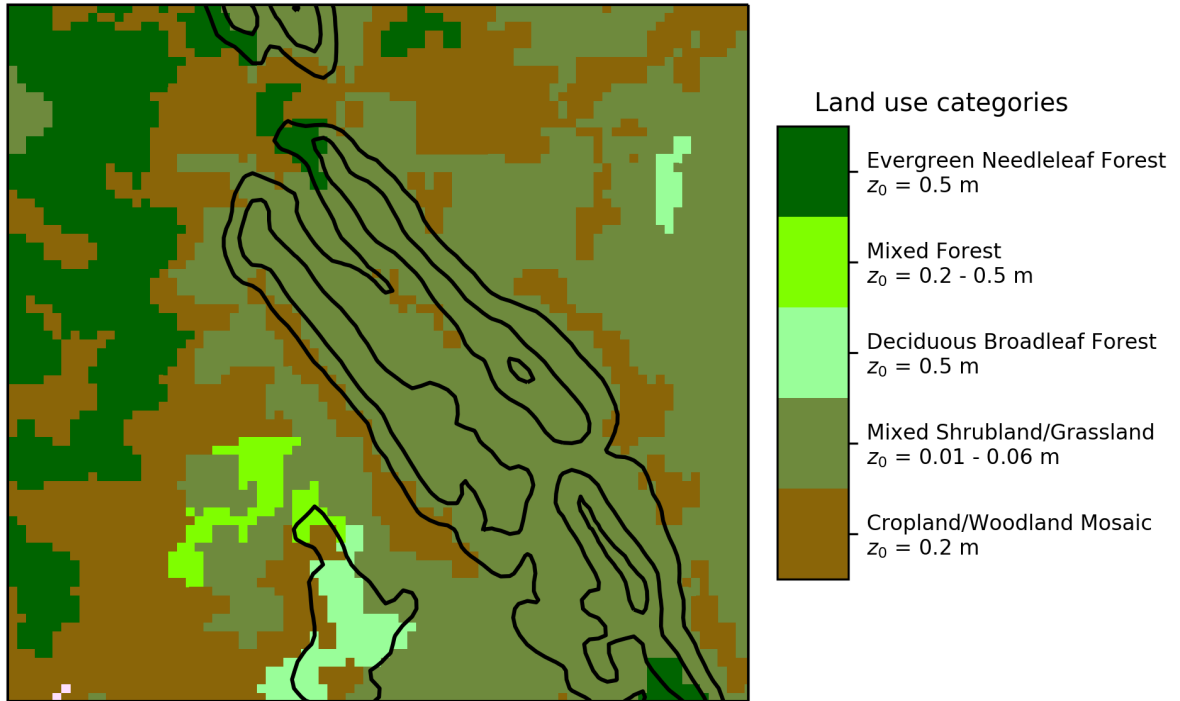


Fig. 5.7 USGS land use classes from the CORINE dataset near the Perdigão site in d05. Black contour lines show the topographical height at 300, 400, and 500 m revealing the site layout. Most of the land use classes near the site are characterized as “Mixed Shrubland/Grassland” and “Cropland/Woodland Mosaic”.

Table 5.3 Grid spacing and range of adaptive time-steps observed during the WRF simulations for each domain.

Domain	$\Delta x, \Delta y$	$\Delta t_{min}$	$\Delta t_{max}$
d01	27	27.0	68.56
d02	9	27.0	71.62
d03	3	7.5	24.0
d04	1	2.5	8.0
d05	1/3	0.83	3.0
	[km]	[s]	[s]



The WRF model was run in individual 72 hour chunks, overlapping by 24 hours corresponding to the initial spin-up time that is discarded. Each chunk was initialized anew from the ERA-Interim analysis (cold start). The maximum and minimum sizes of the adaptive time-steps seen during the WRF simulations are shown in Table 5.3.

#### 5.1.4 Mesoscale and microscale model coupling

Coupling of the microscale and mesoscale model is done one-way and offline, i.e. the WRF simulations are completed, then the output is post-processed and used as input for the microscale model. The coupling is based on the methodology described in Sanz Rodrigo et al. (2017b), and involves coupling via source terms in the transport equations, i.e. body-forces across the entire microscale domain, in combination with surface boundary conditions for temperature provided by the mesoscale model.

The tendencies are extracted at run-time from the WRF model as additional output variables. They are calculated during the many sub-steps involved in solving the transport equations in WRF, as was described by Lehner (2012). Additional post-processing and averaging is done to prepare the tendencies for ingestion into the microscale model. The momentum variables are solved in a mass-coupled state in WRF, and must be decoupled from mass to be applicable. Velocity vectors in the WRF model are solved in grid-relative coordinates and must be turned to earth-relative components. Model levels are sigma-levels (pressure levels), so linear-interpolation in height is used to get them to fixed heights. The tendencies, especially the pressure-gradient term, can be quite noisy, so WRF output is written every 10 minutes and averaged to hourly values.

In idealized terms, the horizontal momentum (exemplified here with  $U$ ), and temperature ( $\Theta$ ) tendencies in WRF are given by the sums

$$\dot{U}^w = \dot{U}_{\text{ADV}} + \dot{U}_{\text{PGF}}^w + \dot{U}_{\text{PHYS}}^w + \dot{U}_{\text{COR}}^w + \dot{U}_{\text{CURV}}^w + \dot{U}_{\text{DIFF}}^w + \dot{U}_{\text{RAY}}^w \quad (5.1)$$

$$\dot{\Theta}^w = \dot{\Theta}_{\text{ADV}}^w + \dot{\Theta}_{\text{RAD}}^w + \dot{\Theta}_{\text{PHYS}}^w + \dot{\Theta}_{\text{DIFF}}^w + \dot{\Theta}_{\text{RAY}}^w \quad (5.2)$$

where the dot notation denotes time-derivatives. The different terms are: advection (ADV), Pressure-Gradient Force (PGF), the contribution from physical parameterization, including the PBL and micro-physics schemes (PHYS/PBL), Coriolis force (COR), Curvature correction (CURV), horizontal diffusion (DIFF), and Rayleigh damping (RAY). In WRF the terms are solved separately, which allows the extraction of each of them as a separate output variables. Figure 5.8 shows vertical profiles over the Perdigão site of the mean relative magnitudes of the different momentum tendency-components for the complete year 2017

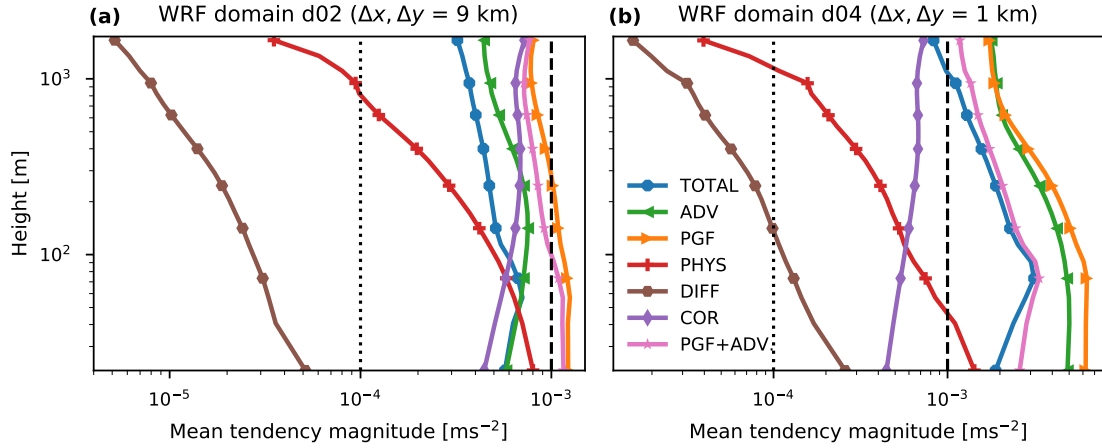


Fig. 5.8 Vertical profiles of the magnitude of the momentum tendencies averaged for all of 2017. The different tendencies are: The total tendency (blue), Advection tendency (green), Pressure-Gradient-Force (Orange), PBL and micro-physics tendencies combined (red), Horizontal diffusion (brown), Coriolis force (purple), and the pressure-gradient force term added with the advection term (pink). The profiles are computed in the grid column nearest to the Perdigão site at 39.70597°N, 7.74373°W (mast 20) for the respective WRF domain: for d02 (a) and d04 (b).

(ignoring curvature). The relative magnitude of the vector-sum of the pressure-gradient and advection terms are shown as well. To no great surprise, the largest relative forcing comes from the pressure tendency. The mean magnitude of all the tendencies peak in the lower part of the ABL, either at the surface or tens of meters aloft. On average, the total tendency (sum of everything) is smaller than the pressure and advection tendencies, pointing to a counter-balancing effect of the terms. This is also clear from the PGF+ADV tendency, that it is smaller than the pressure-term itself. This would indicate that using the pressure-gradient term as microscale forcing alone might lead to excessive forcing, except for idealized situations of perfect geostrophic balance.

Figure 5.9 shows outlines of WRF model grid cells around the site. As Fig. 5.6 also suggests, the d02 grid cells are too large to resolve the Perdigão double ridge complex, d03 captures a slight bump in the terrain, and d04 resolves the site as a single mountain ridge. The Perdigão region fits well inside domain d02, without averaging out too much of the surrounding large-scale terrain features, as for example the large mountain range to the northwest of Perdigão, which is averaged together with the Perdigão area in WRF domain d01.

All but the pressure and advection terms relate to effects that are either: 1) not directly relevant to the microscale model, such as the curvature correction, 2) solved by the microscale model itself, or 3) corrections and/or filters that are used to maintain numerical stability within

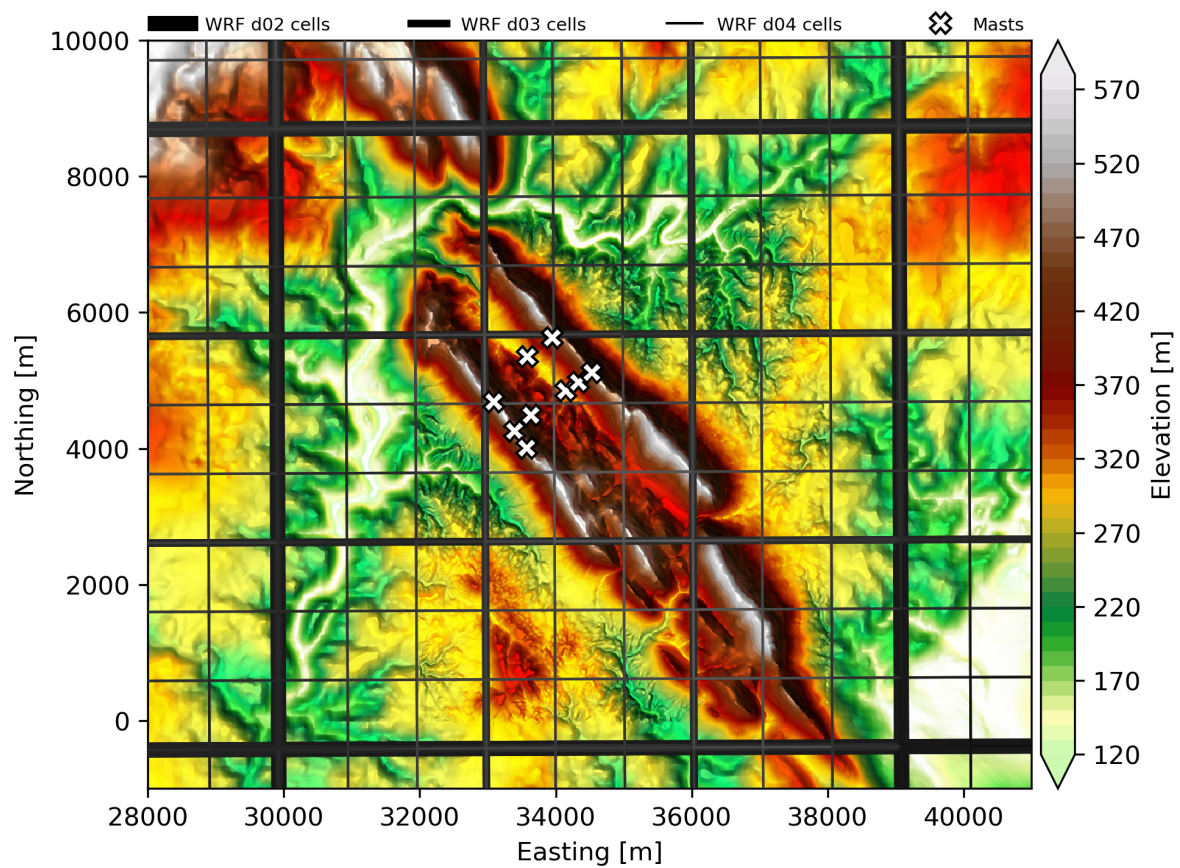


Fig. 5.9 Surface elevation around the Perdigão site and WRF grid cell-outlines for domains d02 (thick lines), d03 (medium lines), and d04 (thin lines) overlaid the Perdigão site. Masts are shown with white crosses. Projection: EPSG:3763.

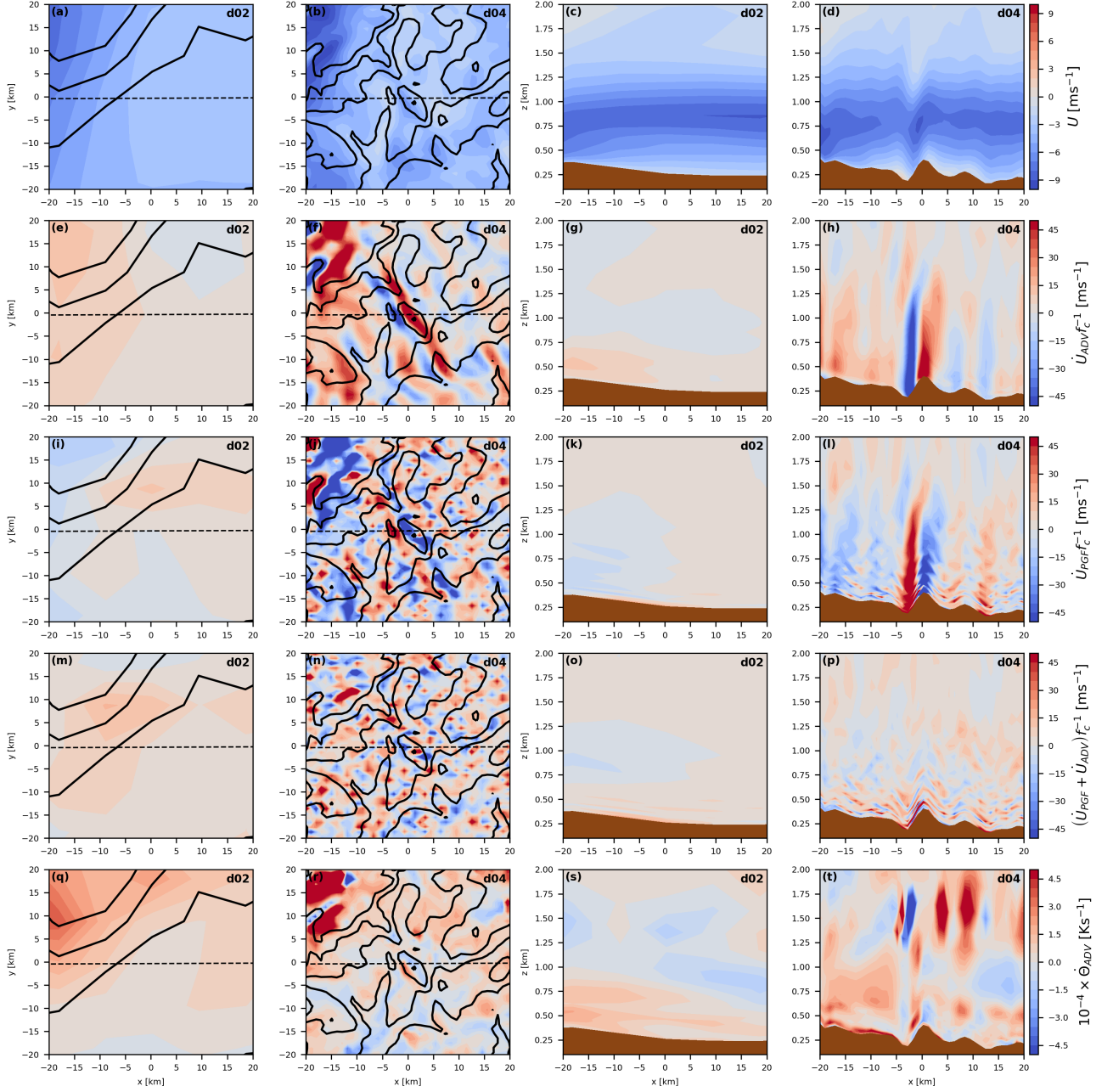


Fig. 5.10 Instantaneous  $U$  velocities (**a-d**), advective tendencies of  $U$  (**e-h**), pressure-gradient tendencies of  $U$  (**i-l**), sum of advective and pressure tendencies of  $U$  (**m-p**), and temperature tendencies (**q-t**) at 01:30 UTC 23 April 2017 around the Perdigão site for WRF domains d02 and d04. The two left columns shows horizontal planes at 100 m above the surface, with topographical height contours in black for every 100 m of elevation. The two columns on the right shows vertical planes along the dashed line in the horizontal-plane plots. Momentum tendencies are shown in terms of the Coriolis frequency  $f_c$ . Horizontal Coordinates are relative to (34200, 4500) in the EPSG:3763 projection.

WRF. Therefore, the natural terms to look at for the coupling are the pressure-gradient term and advection of momentum and heat. These terms carry the main “top-down” information about the large-scale evolution of the atmospheric state that the microscale model is missing.

Near the surface, and especially in mountainous terrain, the pressure gradient and advection tendencies vary greatly due to the blocking, counter-circulations and other terrain-induced flow effects. These local effects will be solved by the microscale model, so it is desirable that this local signal is absent in the forcing passed on from the mesoscale model. This begs the questions: “What is the right mesoscale resolution and spatio-temporal filter to use to generate the microscale model-input?”. For reference, the studies by Sanz Rodrigo et al. (2017b) and Olsen et al. (2018), where the tendency-approach is used in simple terrain, both use spatial and temporal averaging of the tendencies. Sanz Rodrigo et al. (2017b) averages tendencies from a 3 km WRF domain in  $9 \times 9$  km averaging boxes and re-samples to hourly averages. Olsen et al. (2018) takes a similar approach, but use a 9 km domain and  $27 \times 27$  km averaging boxes, and hourly averages.

Figure 5.10 shows snapshots in horizontal and vertical planes at 01:30 UTC on 23 April 2017 for horizontal and vertical planes of  $U$  velocity and momentum and temperature tendencies for WRF domains d02 and d04. The black lines in the horizontal planes indicate topographical height contours. The figure shows that a low-level jet (LLJ) is present in both of the domains. The flow direction is from northeast, hence the easterly flow in  $U$ . The impact of the resolved terrain is seen clearly in the pressure-gradient and advection tendencies (Fig. 5.10 h and i), especially near the Perdigão “hill”. The pressure gradient and advection terms largely counter-balance each-other near the hill, which is clear in their sum (Fig. 5.10 (p)). The same can be seen in d02, especially in the east side of the terrain, although it is not as clear as for d04. The pressure tendency shows significant levels of high-frequency variance that appear as “noise”, especially in d04. This variance is also apparent in the pressure-advection summed tendency. These high-frequency signals are not the kind of spatio-temporal variance that is desirable to bring to the microscale mode, so filtering them out seems appropriate. To no great surprise, the temperature-advection tendencies also show greater variance in domain d04 than d02. Curiously, the greatest variance is found above the peak momentum tendencies, and close to the surface.

It seems clear that the mesoscale input passed on to the microscale model should be well-adjusted to the large-scale topography, i.e. it should force the flow towards the correct general direction of the flow at the scales of the microscale domain, accounting for the steering-effect of the topography at larger scale; from mountain-ranges and the like. On the other hand, it should not include flow features from the local topography that will be captured

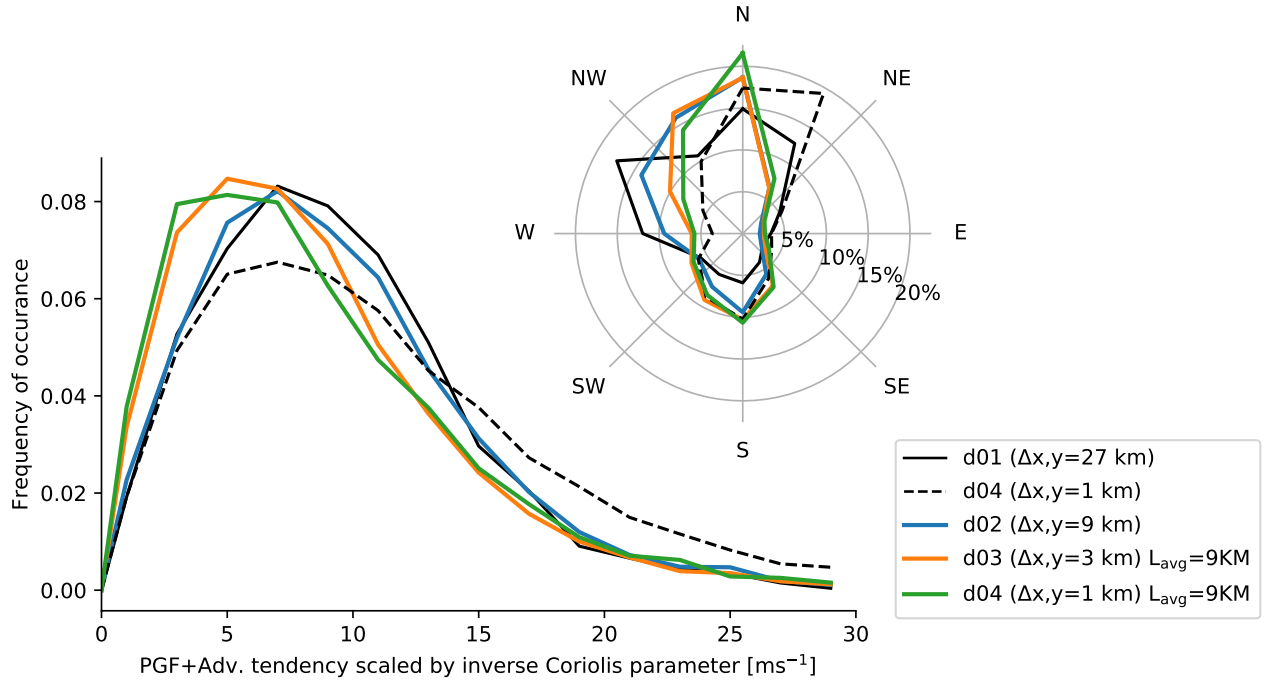


Fig. 5.11 Wind speed and wind direction distributions of the combined pressure-gradient force and advection momentum tendencies averaged across the first 300 m above the surface for WRF grid cells centered on 39.70597°N, 7.74373°W (mast TW20) and for spatial averages ( $L_{avg}$ ) around that location for different WRF domains.

within the microscale domain. As described above, most of the Perdigão mountain complex and the surrounding area fit inside one WRF d02 grid cell (Fig. 5.9).

Figure 5.11 shows the distributions of the magnitude and direction of the pressure-plus-advection tendency scaled by the inverse Coriolis frequency for all of 2017. It indicates that up-scaling the results from d03 or d04 in a  $9 \times 9$  kilometer averaging box results in weaker forcing compared to using results directly from the 9-km domain. It also shows that the direction distribution is quite different between d01 and d02, indicating steering from more resolved surrounding topography. It is an open question what the “correct” combination of domain and filtering is, and should be further investigated. Validating the tendencies against measured quantities is difficult, especially in highly complex terrain, where no direct physical equivalent metric exists to the coarse mesoscale tendencies. For now, the mesoscale tendencies from d02 ( $\Delta x, \Delta y = 9$  km) are used in the following. The approach taken in the following is to force the microscale model by a time- and height-varying forcing, mimicking the geostrophic wind. But, using the WRF pressure-gradient tendency alone would not work well when advection is prevalent, so the combined pressure-advection tendency is used as a pseudo-geostrophic wind. The assumption is that the advection is just a linear correction to



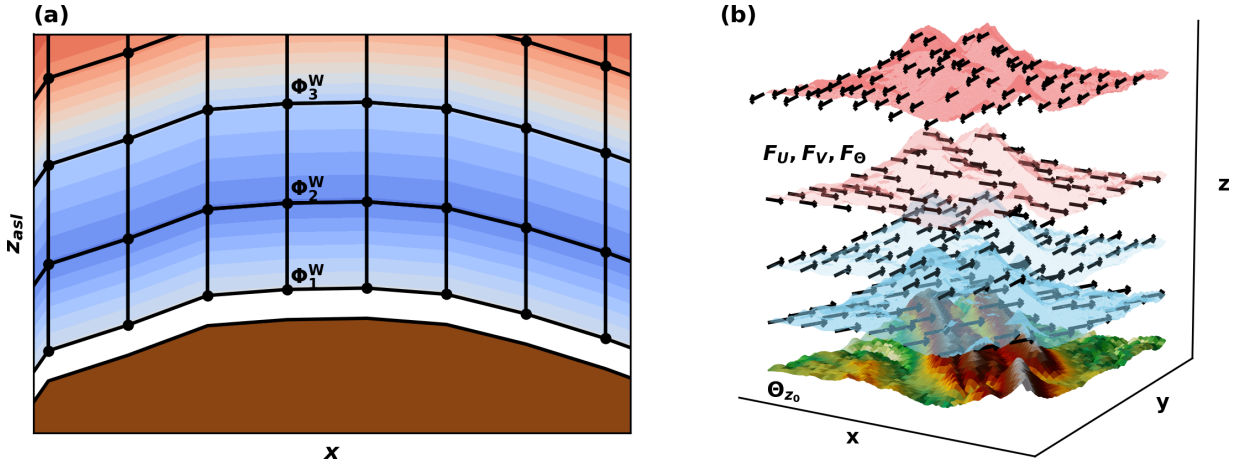


Fig. 5.12 Transfer of forcing and temperatures:  $F_U$ ,  $F_V$ ,  $F_\Theta$ , and  $\Theta$  from WRF to EllipSys3D follows the approach outlined in Fig. 4.4 with both forcing and temperature constant in constant height above ground ( $z_{agl}$ ) (a and b).

the geostrophic flow, whether this is a good assumption should be further investigated. The horizontally homogeneous tendencies from the d02 grid cell are added as additional forcing terms into equation (3.3) and (3.24) by defining the  $F$  terms for  $U$ ,  $V$ , and  $\Theta$  as

$$F_U(t, x, y, z) = \dot{U}_{PGF}^W(t, z) + \dot{U}_{ADV}^W(t, z), \quad (5.3)$$

$$F_V(t, x, y, z) = \dot{V}_{PGF}^W(t, z) + \dot{V}_{ADV}^W(t, z), \quad (5.4)$$

where  $z$  is height above terrain, and

$$F_\Theta(t, x, y, z) = \dot{\Theta}_{ADV}^W(t, z). \quad (5.5)$$

Unlike the approach used in Chapter 4, no spatial averaging was done for the Perdigão case, but the tendencies were averaged in time to hourly intervals. Linear interpolation in time was used inside the microscale model in-between each hour to get the appropriate forcing, as illustrated by Fig. 4.4. The time- and height-dependent tendencies was applied at the corresponding time and height above terrain in the microscale model, i.e. the forcing is homogeneous in constant height above terrain, as illustrated in Fig. 5.12. The 61 WRF levels extend to  $\approx 20$  km, but only the first 29 levels (up to 4465 m) are used by the microscale model (as the top of the grid extends only to 4000 m).

Figure 5.13 shows the time-series of the vertically-averaged momentum and temperature tendencies for the first 300 m of the atmosphere. The period covers the first 14 days of the 32-day period used for validation in the section below. Most of the time the pressure

gradient is driving the total forcing (pressure-advection sum), but in a few instances spikes of advection-driven forcing also occur. The pressure-gradient and advection compensate each other during most of the period, and only rarely is the sum of the two larger than both of them.

### Surface roughness

The microscale surface roughness is modelled as a single homogeneous roughness, by assigning the roughness length in the WRF d02 grid cell to the microscale model surface. As Fig. 5.7 shows, most of the land near Perdigão is characterized as “Mixed Shrubland/Grassland” in the CORINE dataset. As described in section 5.1.3, the dominant land use class is used to up-scale the land use from the native resolution to the coarse model grid cells. This results in the d02 grid cell being characterized as “Mixed Shrubland/Grassland” as well. The corresponding surface roughness for the validation period is  $\approx 5$  cm, which is therefore used as the microscale surface roughness.

The Perdigão site and its surroundings are covered with many patches of eucalyptus and pine trees, which would objectively correspond to much larger surface roughnesses than 5 cm. If, as here, a single roughness is used for the site, it may be more appropriate to use the USGS “Cropland/Woodland Mosaic” or “Mixed forest” class, which correspond to roughness lengths of 20–50 cm, or even using higher surface roughnesses. Ultimately, treating the inhomogeneities and canopy effects of the surface roughness and vegetation by more sophisticated methods would be more desirable. Unpublished work by *Deutsches Zentrum für Luft- und Raumfahrt* (DLR), and the Technical University of Denmark (DTU), indicates that using the roughness normally associated with the CORINE dataset over Perdigão results in too low surface roughness, which inhibits the ability of the WRF model from capturing the observed wavelength of the nocturnal standing lee-wave behind the southwest ridge, showing that better results are had by adding additional friction.

Despite the indications that the CORINE surface roughness is too low, it is still used in the microscale model for a number of reasons: 1) to simplify the scope of the study, emphasizing the impact of better resolving the orography, not the surface roughness, 2) to allow for a more direct comparison between the meso- and microscale models, 3) to eliminate any sensitivity to differences in the surface roughness in the effective response to the mesoscale tendencies used to force the microscale model.



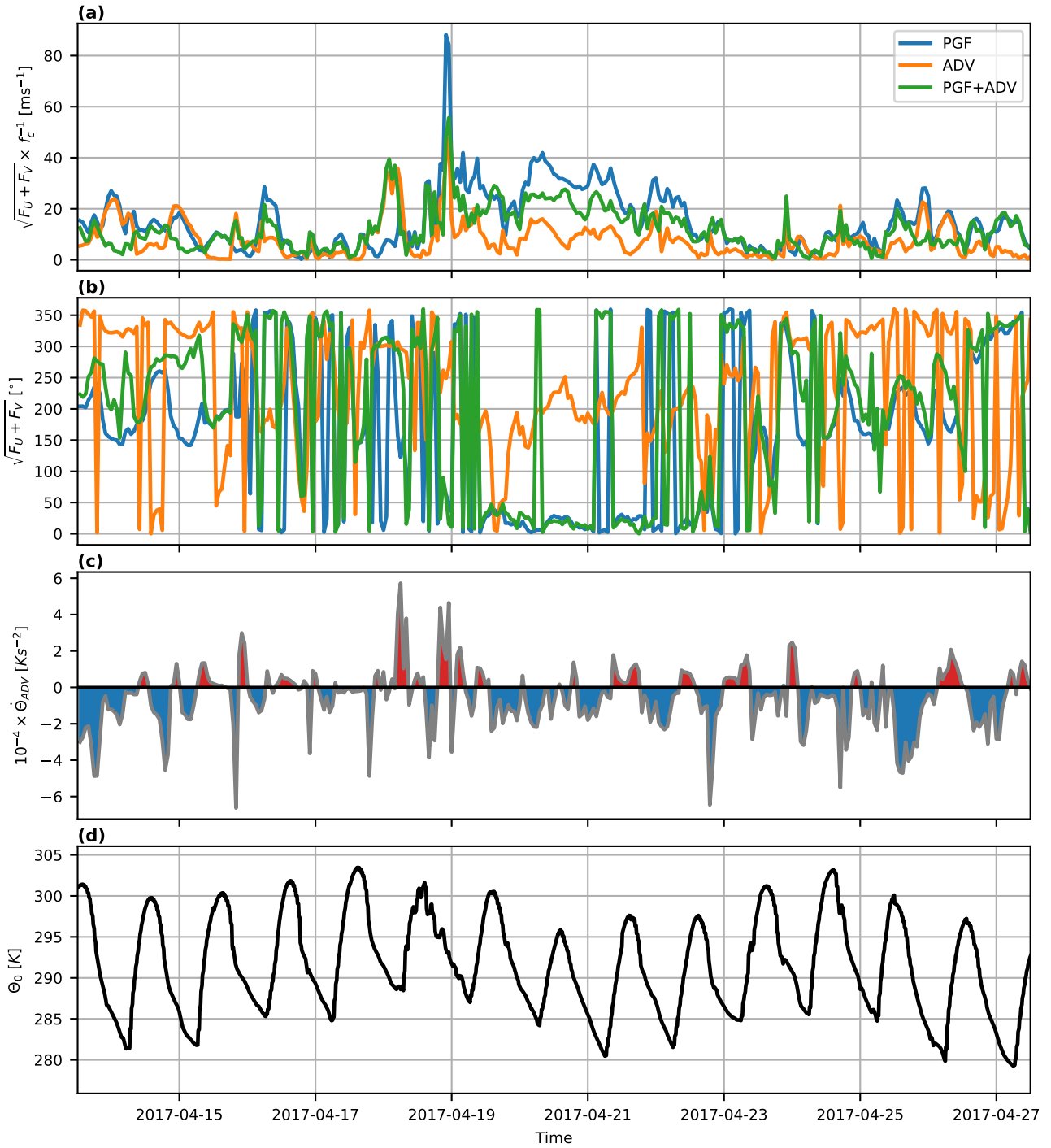


Fig. 5.13 Time-series of the magnitude and direction of the vertical average momentum-tendencies **(a-b)**, and temperature advection tendency **(c)** of the lower 300 m of the atmosphere. **(d)** derived surface temperature for the microscale model. All of the above are derived from the WRF domain d02.

### Surface boundary condition for temperature

A varying surface temperature makes up the boundary condition for the temperature equation of the microscale model (Eq. 3.24). It plays a vital role in modulating the surface fluxes, and favouring or suppressing vertical motion and turbulent mixing. In the present coupled meso-microscale system, the surface temperature is calculated from the WRF 2 m temperature and extrapolated to the surface, defined as the height of the surface roughness length  $z_0$ . The extrapolation to the surface is based on Monin-Obukhov Similarity Theory (MOST) (Monin and Obukhov, 1954) as

$$\Theta_{z_0} = \Theta_2 - \frac{\Theta_*}{\kappa} \left[ \ln \left( \frac{2 - z_0}{z_0} \right) + \psi \left( \frac{2 - z_0}{L} \right) \right], \quad (5.6)$$

where  $L$  is the Obukhov length. The stability functions  $\psi$  follow the Businger-Dyer relationships (Businger et al., 1971; Dyer and Hicks, 1970). No distinction is made between the thermal roughness length and the momentum roughness length. Likewise, no distinction is made between the surface temperature and the surface aerodynamic temperature, even though the surface aerodynamic temperature is not strictly-speaking equivalent to any observable surface temperature, due to the breakdown of MOST in the viscous sub-layer near the surface (Mahrt, 1998).

The derived surface temperature used for the study of Perdigão is shown in Fig. 5.13, for the first 14 days of the 32 day study-period. The limited number of occurrences of tooth-saw-like shape of the temperature curve, indicates mostly fair-weather conditions with few clouds in the d02 domain, resulting in both rapid heating and cooling during the day-night-day transitions, changing by 15–20 K during the diurnal cycle.

### Additional considerations for temperature modeling

As discussed in section 3.2, many physical processes in the ABL cannot be modelled by the simplified model formulation of the microscale model. Some processes are not driven by surface interactions (bottom-up processes); such as large-scale advection and subsidence, and some processes cannot be captured due to the finite vertical resolution of the model, such as very stable boundary layer flow. To allow the microscale model to either capture these processes indirectly, or to limit the problems related to its shortcomings, several mechanisms have been implemented: temperature nudging, and (lower) limiters on some variables. Below, the motivation and some details of the implementation are described below in the context of the convective boundary layer (CBL) and the stable boundary layer (SBL).

During free-convection in the PBL (CBL), turbulent eddies (thermals) rise from the heated surface to the capping inversion, causing a non-symmetrical mixing with the free-atmosphere air (i.e., *entrainment*). This results in a deepening of the PBL depth (Wyngaard, 2010). The PBL growth is limited by the finite length of the day, and large-scale subsidence. To restrain the PBL growth in a similar way in the microscale model, mechanisms akin to night-time radiative cooling and subsidence are needed. In this study, the microscale temperature is nudged towards the temperature profile of WRF ( $\Theta_r$  in Eq. 3.27), effectively limiting the depth of the PBL to the depth in the WRF model. Processes related to radiation, moisture, phase-changes, and precipitation are ignored in the microscale model, but their influence may be partly accounted for by the nudging as well. The characteristic relaxation time  $\tau_r$  is chosen to be 3600 s, which is a relatively strong nudging. For reference, Koblitz et al. (2015) uses  $\tau_r = 86400$  s, and only nudges towards the reference if it is colder than the temperature in the microscale model, mimicking night-time radiative cooling. The motivation for using a stronger nudging, and for nudging in all situations, are: 1) to keep the depth of the PBL relatively close to the WRF level, 2) to allow for effective radiative-like cooling of the ABL, especially during night-time, 3) to keep the temperature vertical temperature distributions in sync with WRF, avoiding errors caused by adding the temperature advection tendency to a mismatched vertical temperature distribution.

The stable boundary layer (SBL), may be roughly divided into two types: the weakly stable boundary layer (WSBL), and the very stable boundary layer (VSBL) (Mahrt, 1998). The WSBL is characterized by strong winds, and/or cloudy conditions, resulting in a slowly cooling surface. In this type of boundary-layer the log-linear form of the MOST Businger-Dyer stability functions have proven to work well. The VSBL corresponds to situations with weak winds and clear-sky conditions, resulting in rapid cooling of the surface. This situation can lead to a negative feedback, where turbulent mixing is inhibited by increasing stratification, in a process known as *runaway cooling* (Paulson, 1970). Heat transported towards the surface, is limited by the mechanical forcing, weak winds results in weak mechanical heat transport, and gives rise to increased stability, further suppressing the turbulent heat transport. In effect, this puts a lower limit on the wind speed and/or maximum heat flux for sustaining turbulence (Van de Wiel et al., 2012). The VSBL is widely regarded as a major challenge for atmospheric models (Basu et al., 2008; Holtslag and Svensson, 2013; Mahrt, 1998; Malhi, 1995). Taking measurements in the VSBL is very difficult, due to the long averaging times needed. As a result, no solid theoretical framework exists, and the validity of the frequently-used MOST log-linear stability functions come into question Mahrt (1998). Many modelers choose to avoid the complications of the VSBL by limiting the surface layer variables to predefined bounds; for example the friction velocity, stability

Table 5.4 EllipSys3D simulations used for modeling of Perdigão. The names refer to the grid and advection scheme used.  $\Delta t$  and  $n_{sub}$  are the model time-step and number of sub-iterations used. The same forcing from WRF was used for all of the six setups.

Name	Grid	Advection scheme	$\Delta t$	$n_{sub}$
G01-Q	G01	QUICK	1.0	5
G01-U	G01	UDS	1.0	5
G02-Q	G02	QUICK	2.0	5
G02-U	G02	UDS	2.0	5
G03-Q	G03	QUICK	3.0	5
G03-U	G03	UDS	3.0	5

[s]

functions, and turbulence (Grell et al., 1994; Janjić, 1994; Jiménez et al., 2012). In the present microscale simulations, limiters are only put on  $k$  and  $\epsilon$ . Their lower limits are set to  $10^{-4} \text{ m}^2 \text{ s}^{-2}$  and  $7.208 \times 10^{-8} \text{ m}^2 \text{ s}^{-3}$  following Koblitz et al. (2015), corresponding to a minimum turbulent length scale of 1 m for  $C_\mu = 0.03$  using Eq. (3.13). It is questionable whether this is enough to avoid runaway cooling in the VSBL, also limiting the friction velocity may be desirable.

## 5.2 Results

In the following section the results from the WRF-forced EllipSys3D simulations are presented. In Table 5.4 the six different model setups used are shown. All six of them receive exactly the same forcing from WRF, but differ by the grid, advection scheme, and time-step. Additional information about the model setup is described in Sec. 5.1.2. The level of convergence of the EllipSys3D results (a measure of the stability of the transient solution) are shown in Appendix A.2.3.

### 5.2.1 Resolved scales and sensitives

As discussed in Sec. 2.1.4, ABL modeling at intermediate scales between the small, where the most energetic turbulent eddies are well resolved by the grid, and the large, where many such eddies are fully contained within a single grid cell, is challenging. The LES assumption of a well resolved inertial range, and the RANS assumption of complete scale separation is both violated to some degree and/or at different times throughout the day as the size of the most energetic eddies evolve. Although the added viscosity of eddy-viscosity based RANS closures will tend to dampen small scale structures, larger eddies may still evolve if

grid spacing is fine enough, especially during convective conditions where their formation is favoured by increased buoyancy. Another consideration related to the grid spacing, is how the solution changes with increased resolution of the orography; is the flow around the orography well resolved, or will additional flow features arise due to better resolved orography as grid spacing is lowered?

In the following two sub-sections, the degree to which the terrain is resolved in the different model domains, and to what degree scale-dependant eddy-behavior is present in the uRANS solution for different grid spacing, are explored.

## **Terrain**

For any model to accurately capture the flow-patterns around a complex site, like Perdigão, the primary features of the terrain must be captured, both the orography and friction from the surface and vegetation. Three of the meteorological masts used for validation are located on top of the two ridges, and six are located at different positions within the central valley, so resolving the sloping ridges and the depth and details of the valley are important for a good validation for the different masts. Figure 5.14 shows a vertical cross-section through the point (34200, 4200) in the TM06 projection at a 45° angle (northeast across ridges). It shows that the WRF d05 domain does not resolve the ridges well, and it indicates a misalignment between the Viewfinder/SRTM topographical map and the one derived from LIDAR scans of the area (southwesterly shift of the orange lines). WRF domain d04 just sees a single averaged-out representation of the ridges, and the other coarser domains sees no resemblance of the site. The microscale domains resolve the features of the site quite well. However, the most coarse microscale domain (G03), at 120×120 m horizontal grid spacing, barely captures the plateau at the top of the ridges, and misses some of the fine-scale features of the central valley.

Capturing the effective drag on the wind, and the impact on mass and heat fluxes, due to vegetation and surface characteristics are also crucially important for accurately modeling the flow (Finnigan, 2000). However, in this study, to narrow the scope, all of these effects are largely ignored, and (crudely) assumed to be captured within the surface friction.

## **Grid spacing and numerical accuracy**

To investigate the differences in the microscale solution due to horizontal grid spacing and numerical accuracy, six simulations were carried out. Two for each grid in table 5.1, one using the first-order order accurate upwind discretization scheme (UDS), and one using the third-order accurate QUICK scheme. The simulations will be referred to by their grid

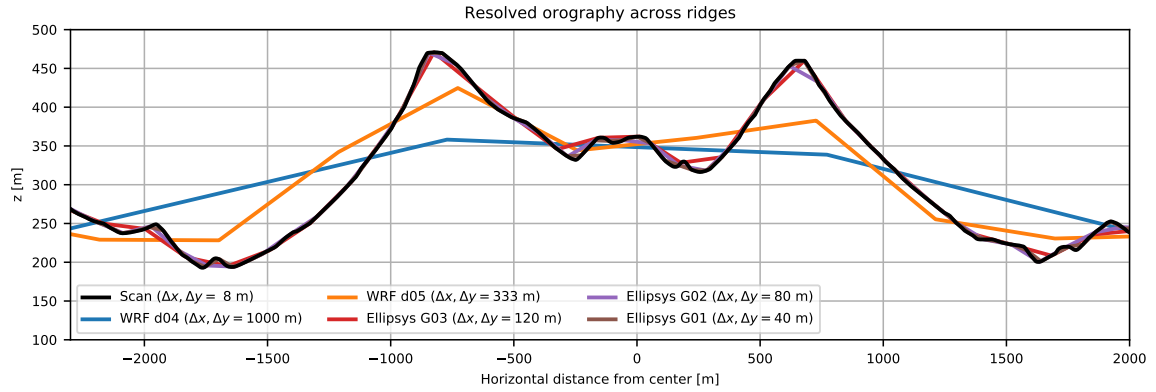


Fig. 5.14 Resolved features of the Perdigão double-ridge complex from LIDAR scans of the area (black line), and in the WRF domains d04 and d05 (blue and orange), and the microscale domains G01-G03 (brown, purple, red). The transect follows a  $45^\circ$  angle (northeastward) from the central point of the microscale domains at (34200, 4200) in the TM06 projection.

name and the first letter of the discretization scheme: G01-Q for grid G01 and QUICK, and G03-U for grid G03 and UDS. The motivation for comparing the two discretization schemes was to study the influence of effective flow resolution on the solution. In general terms, a combination of the flow-truncation due to the finite grid spacing, and the numerical dissipation, sets a finite scale of motion that can reasonably be represented by the model. For WRF, Skamarock (2004) estimated the effective resolution to be  $\approx 7\Delta x/\Delta y$ . The UDS scheme is more diffusive than the QUICK scheme, reducing the effective resolution of the model. It means that the resolved scales may be kept separate (in wavenumber space) from the turbulent scales, even at fine grid spacing, allowing more orographic features to be resolved, while maintaining turbulent effects a feature of the closure only. However, the numerical diffusion impacts a range of scales, so it is not clear how exactly the effective resolution is reduced. Another, and in many respects more appropriate approach to take, would have been to lower the flow-resolution by increasing the eddy-viscosity, dampening turbulent structures even more.

Two days, starting at 12:00 UTC 20 April 2017, were chosen as the period for the sensitivity study. Since differences between the six simulations are expected to be larger closer to the surface, the flow is evaluated at 30 m above the ground, rather than higher up. The three 100 m masts were chosen as the subjects of the study. Horizontal wind speed  $S = \sqrt{U^2 + V^2}$  and direction  $D$  are used to study the overall differences in the flow patterns, and ten-minute wind speed variance is used to estimate turbulent kinetic energy (TKE) content by assuming isotropic turbulence  $k = 3/2\sigma^2$ , and used as a metric for how much explicit/resolved turbulence is in the flow during the simulations.

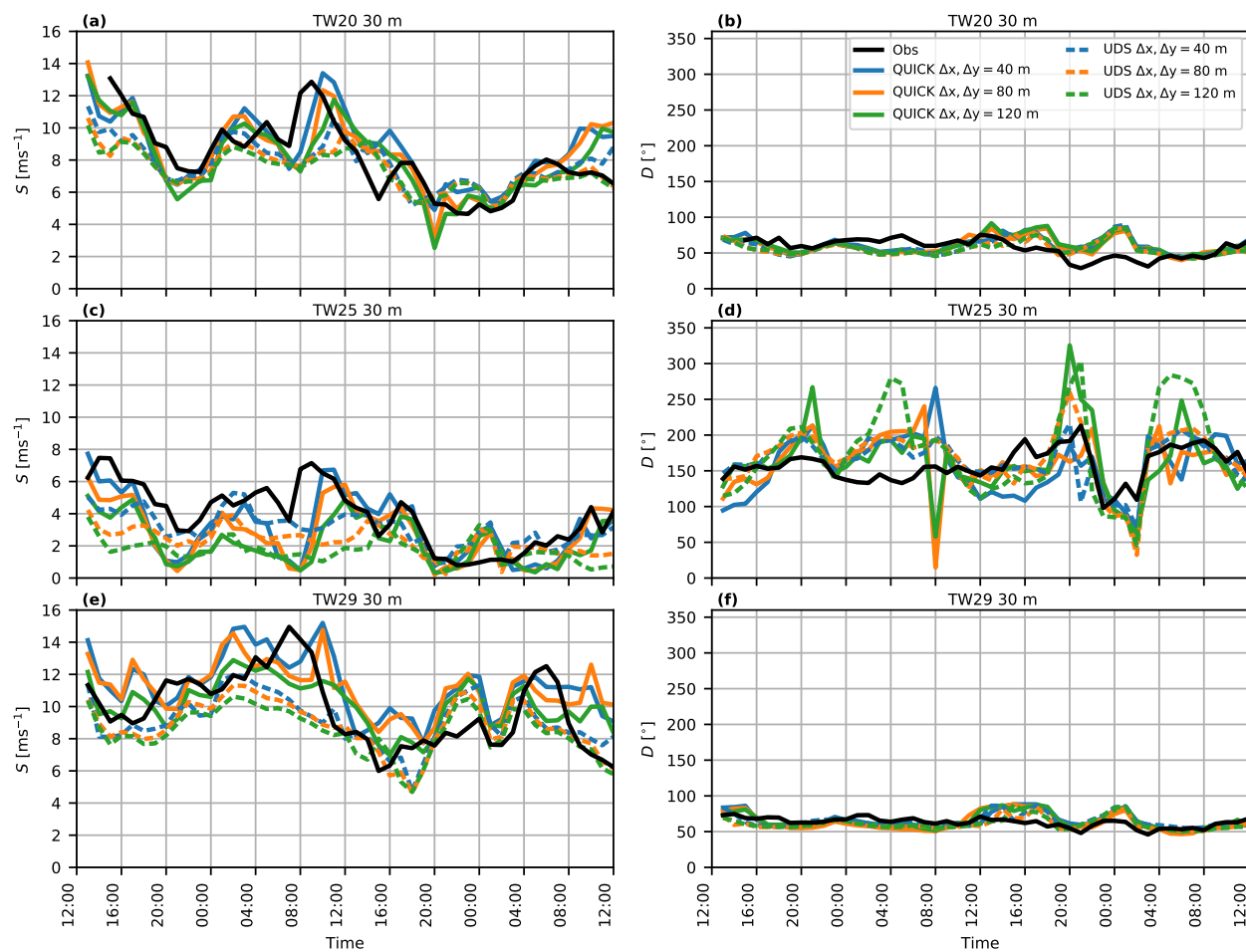


Fig. 5.15 Hourly average horizontal wind speeds ( $S = \sqrt{U^2 + V^2}$ ) and direction ( $D$ ) 30 m above the ground for mast 20 (a-b), 25 (c-d), and 29 (e-f), for the period between 12:00 April 20, and 12:00 April 22, 2017.

The convergence of the six simulations are shown in the Appendix (A.2.3; Fig. A.1, A.2, and A.3). The simulations that rely on the UDS advection scheme reaches residuals of at least one order of magnitude smaller than the corresponding simulation relying on the QUICK scheme, and in many cases a difference of several orders of magnitude is seen for the same grid. Likewise, the most course grid reaches residuals much lower than the fine grids, in some cases of one order of magnitude or more. The smallest residuals are seen during the night time, while residuals are orders of magnitude larger during convective day-time conditions. High-frequency variations are seen for both advection schemes. For G01-U this is especially true during the day-time, while G01-Q show large-amplitude high-frequency variations throughout the simulation. The residuals for G01-Q remains fairly large throughout the simulation, and one may question if the results can be considered “converged” for the used time-step and number of sub-iterations.

Figure 5.15 shows that the general pattern of the evolving wind speed is captured by the six simulations, but large variations between both the different grids, and especially between the schemes, are seen. Wind speeds are generally larger for the QUICK scheme, with higher peaks, which is especially pronounced for grids G01 and G02. The UDS scheme shows less variance and weaker peaks, but like QUICK the fine-scaled grids G01 and G02 have greater mean wind speeds and higher peaks. The results for QUICK are closer to the observations, and seem to catch more of the variance. The spike in wind speed before 12:00 UTC 21 April is captured by G01-Q and G02-Q, and only barely so in G03-Q and G01-U, and not at all in the other two.

Figure 5.16 shows the TKE modelled by the closure, the explicitly resolved, and their sum (total content) at 30 m for mast 25. A clear difference in the amount of explicitly resolved turbulence in the six simulations is seen; the two extremes being G03-U and G01-Q as expected. The modelled TKE underestimate the observed TKE; it is unclear though, how much is due to underestimation of the surface drag. For G03-U the turbulence is almost exclusively in the turbulence model, apart from a short initial period that should be considered the model spin-up (simulations start at mid-day UTC time). G01-Q has much more explicit turbulence than the other simulations, it is even larger than what is modelled by the closure most of the time. Even during the night, in the absence of the buoyant forcing that favour eddy generation during the day, explicit turbulence persists. For some of the period G01-Q also shows more modelled turbulence, with higher variance, which could indicate that interactions between the explicit and modeled turbulence are taking place. The four other simulations show some degree of resolved turbulence, in particular during the afternoon hours. A clear grid-sensitivity of the TKE is seen, which is especially clear for the QUICK scheme simulations, pointing to grid-dependant structures developing in the flow.



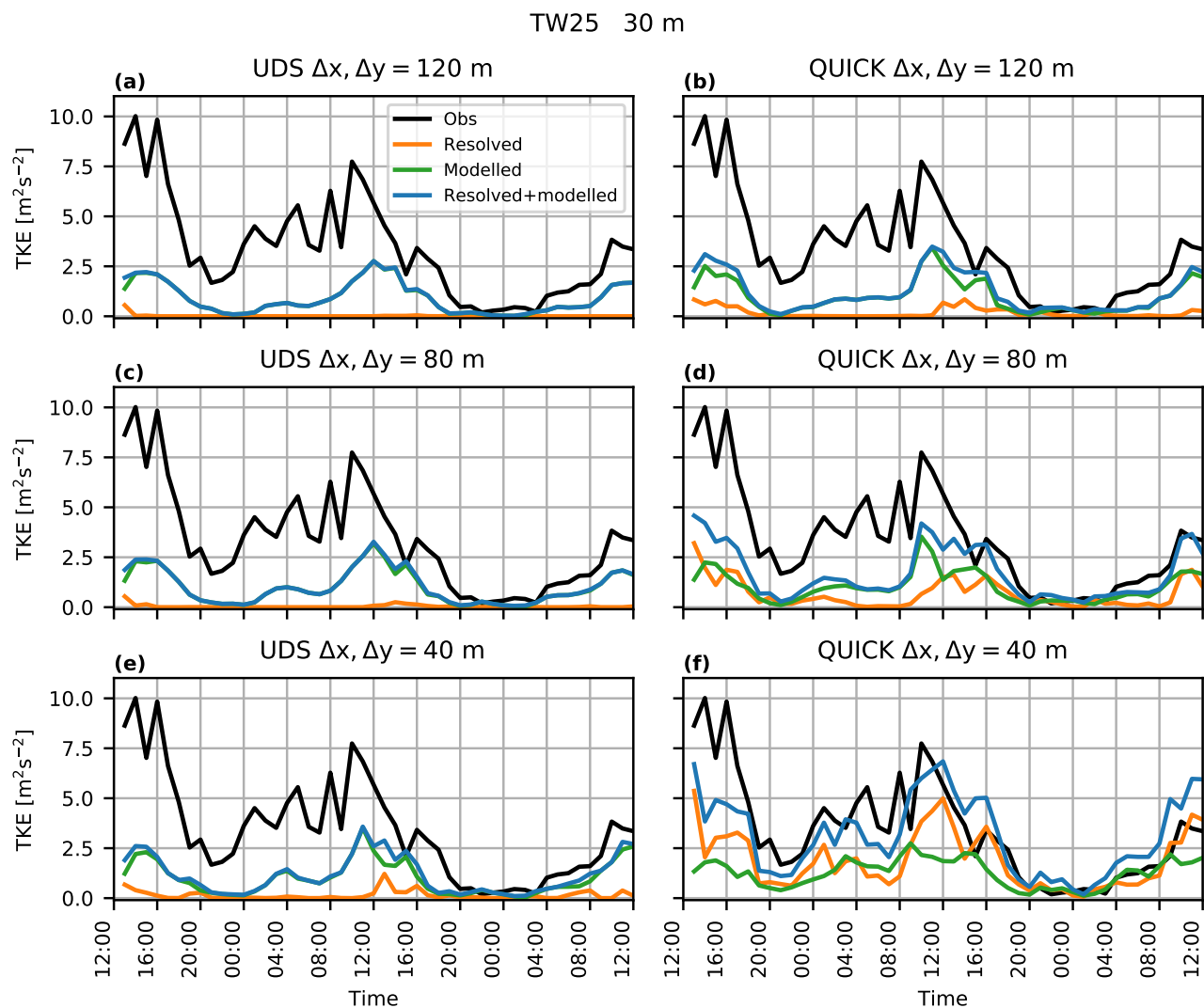


Fig. 5.16 Modelled and explicit turbulent kinetic energy (TKE) for the six microscale simulations at 30 m for mast 25.

The results indicate a clear sensitivity to both grid spacing and numerical accuracy. Using the UDS scheme seems to lead to lower wind speeds and reduced variance, possible not capturing or misrepresenting some flow behavior. On the other hand, using the QUICK scheme results in grid dependent eddy-like structures that seems to cause interactions with the turbulence model. It is unclear whether the differences observed between the simulations using the same discretization schemes are primarily caused by resolving additional features of the orography, or if they are caused by differences in the effective flow resolution, but a combination of the two is likely. For simulations of the same grid spacing, the impact of the differences in numerical diffusiveness is more clear. In the following, the G02-U and G03-Q setup is further investigated in the next section.

### 5.2.2 Validation of results for one month

While the previous section showed both encouraging and discouraging results, the overall flow patterns are captured by the tendency-driven microscale model, but on the discouraging side, grid-dependant behavior is seen. With the grid-dependent behavior comes uncertainties related to the resolved eddy-structures that interact with the turbulence closure model in an unknown way, and potentially cause double counting of turbulence. To investigate the behavior further, three of the six setups investigated above were chosen, and run for 32 days, to compile enough data to validate the statistical properties of a longer period with the mast measurements. The 32 days consisted of a consecutive period between 13 April and 15 May 2017, coinciding with the initial part of the 2017 intensive field campaign.

The three setups chosen are: G02-U, G03-U, and G03-Q, described in 5.2.1. G03-Q was chosen because it is the most coarse domain but with high numerical accuracy. It should suffer least from double-counting turbulence of the three QUICK based options. G02-U was chosen for its slighter smaller grid spacing and lower effective resolution, and G03-U is expected to have the lowest effective resolution, and it also serves as a reference for G03-Q. The microscale simulations were validated against the different WRF domains, with an emphasis on the most fine-scaled domains: d04 and d05. They represent the typical mesoscale model, and serve as a baseline/reference for the microscale model.

To avoid inconsistencies in the mesoscale forcing data arising between individual mesoscale simulations (chunks), the microscale simulations were performed in chunks overlapping with the mesoscale. To allow the flow to adjust from the initial horizontally homogeneous WRF flow to the microscale flow with terrain, two hours of initial spin-up were used. For consistency, the last two hours of the 24 hour mesoscale spin-up was used.

To study the observed flow patterns around the Perdigão site in more detail, three cases/snapshots are highlighted and discussed using LRWS measurements to compare with the microscale model simulations. Comparing planes of the instantaneous flow field, rather than time-series in points, allows both quantitatively and qualitative comparison of the vertical planes across the two Perdigão ridges. The chosen cases are: two nocturnal events with a pronounced low level jet (LLJ), forming a pronounced lee-side wave down-wind from the southwest ridge during northeasterly flow conditions, and the last one is a daytime snapshot around noon, showing how positively buoyant air near the surface impact the flow. To supplement the vertical planes, horizontal planes at 50 m above the ground from the microscale model is also presented at the same instances. Only planes for G02-U and G03-Q are shown, because even though G02-U and G03-U show differences, they are much smaller than those between G02-U and G03-Q.

### **01:30 UTC 23 April 2017**

On the night of 23 April 2017 at 01:30 (Fig. 5.17), the general flow direction came from the northeast, and a LLJ with a depth of  $\approx 300$  m, with a jet core of  $\approx 10$  m/s was present. Down slope from the southwest ridge, a standing wave in the LLJ persisted for several hours, oscillating slightly with varying wave-length and amplitude of the wave. Slower wind speeds and veering of the flow is observed behind and in front of the northeast ridge, and likewise below the crest of the lee wave.

Both G02-U and G03-Q captures a LLJ, but it is much deeper than the observed one. Figure (5.10) shows the  $U$  velocity in the WRF d02 domain for the same instance as here. It shows that the deep LLJ is also present in the mesoscale model, and hence the tendencies should have this pattern as well. Overestimation of the height, and underestimation of the speed, of the LLJ core is a well known issue for mesoscale models (Gevorgyan, 2018; Hu et al., 2013; Storm et al., 2009). Therefore, it seems likely that the ability of the microscale model to capture many of the features of the LLJ is constrained by the mesoscale tendencies. G02-U and G03-Q also capture the speed-ups above the two ridges, the slow-down and veering in front of and behind the ridges, as well as a slight dip of the LLJ on the lee side of the southwest ridge. It is, however, far from the observed shallowness, wavelength and amplitude. The G03-Q flow is qualitatively similar to G02-U; LLJ depths and features are similar, but the wind speeds are much greater, and a greater vertical wind speed gradient is present. G02-U and G03-Q both show a dip of the LLJ behind the southwest ridge, corresponding to a wave of much larger wave-length than the observed LLJ wave.

Figure 5.18 shows horizontal planes of the modelled flow 50 m above the ground. It shows the northeasterly flow across the ridges and the central valley, orographic speed-ups

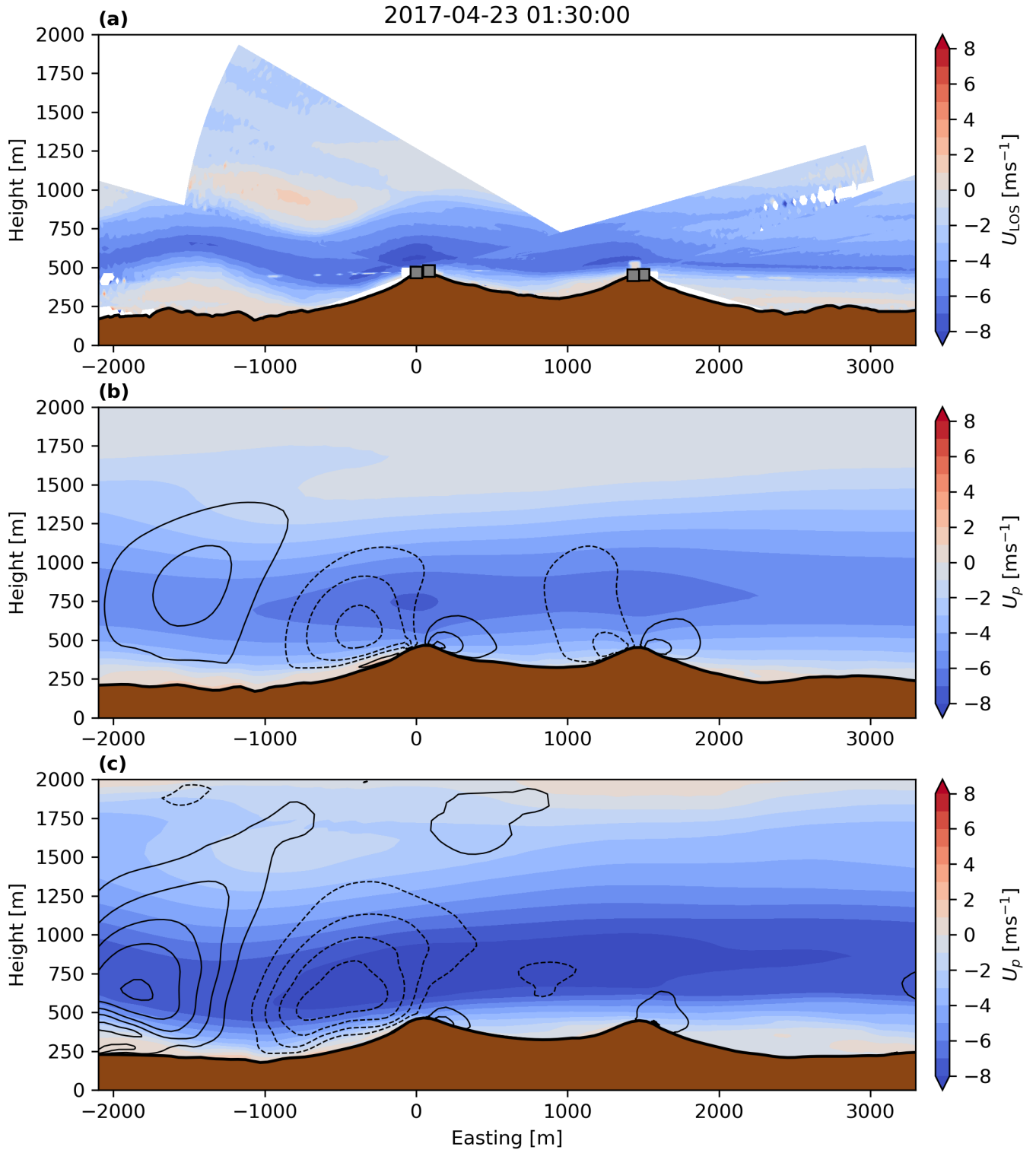


Fig. 5.17 01:30 UTC 23 April 2017. **(a)** Composite of the line-of-sight velocities ( $U_{LOS}$ ) observed by the four LRWS (gray squares). **(b)** G02-U and **(c)** G03-Q horizontal velocities in the plane along the scanner transect ( $U_p$ ), as well as negative (dashed) and positive (full) vertical velocities in contours of 0.3 m/s. The zero vertical velocity contour is not shown. Horizontal distances (Easting) are in meters along the scanner transect relative to the position of LRWS 1 (first one from the left).

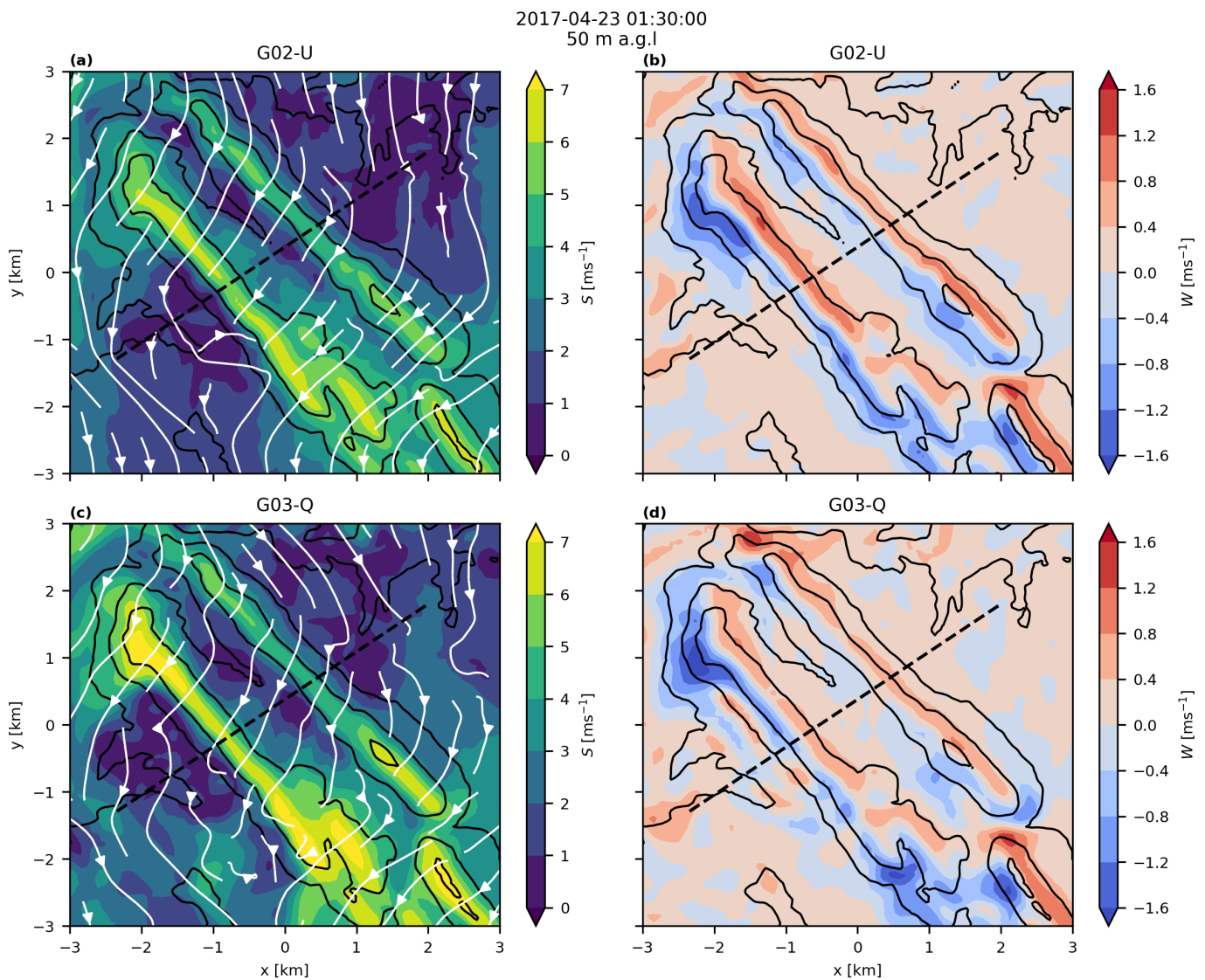


Fig. 5.18 01:30 UTC 23 April 2017. Horizontal planes of the modelled flow 50 m above the surface at the Perdigão site. The LRWS scan-planes are shown by the dashed black line, and elevation contours is shown in black for every 100 m. **(a,c)** horizontal wind speed (color) and streamlines (white lines). **(b,d)** vertical velocities.

above the ridges, rising flow before the ridges, and sinking below. It also shows the relative low wind speeds in front of and behind both ridges, indicating blocking and lee effects. Similar to the vertical planes, the horizontal planes show that the largest speed-up is at the southwest ridge, second ridge downstream from the general flow direction, and that G02-U have lower wind speeds above the ridges than G03-Q. Interestingly, the wind speed in the central valley is, in some places, lower for G03-Q than G02-U, pointing to more variance in the simulation using the high-order scheme.

#### **04:00 UTC 7 May 7 2017**

Similarly to the event described above, the flow at 04:00 UT 7 May 2017 is characterized by a nocturnal LLJ in northeasterly flow. However, wind speeds are generally lower and the LLJ more shallow ( $\approx 200$  m), than the one discussed above. The lee side wave in the LLJ also has a larger amplitude and shorter wavelength, and in the central valley the LLJ shows a clear dip into the valley. Interestingly, the jet core, i.e. the location of peak wind speed intensity, is down-slope from the southwest ridge, not at the top of the ridge. Further downslope from the peak wind speed, a re-circulation zone is present below the crest of the vertically swirling LLJ wave.

G02-U has a deep and weak LLJ with a jet core located  $\approx 500 - 750$  m above the terrain, and as such the shallow and near-surface LLJ observed is not captured, but some of the general flow patterns are captured, such as the LLJ wave behind the southwest ridge, including the strong winds on the top part of the downslope, and the re-circulation zone further down. This is also captured by G03-Q, which also show greater wind speeds in the LLJ, and greater vertical wind-shear.

The horizontal planes (Fig. 5.20) shows more sinking of the flow below the southwest ridge than the first case, owing to more pronounced and lower located wave motion of the LLJ. The general flow characteristics are quite similar to the first one described above: northeasterly flow across the ridges and central valley, weaker more circulating winds in the valleys, and wind speed-up on top of the two ridges. Likewise, the wind is stronger with more spatial variance in G03-Q than G02-U.

#### **12:00 UTC 23 April 2017.**

Case three shows a snapshot of the flow during daytime conditions. Generally, wind speeds were low during the day on 23 April, but increased levels of turbulence intensity in the measurements during the day reveals the presence of thermally driven turbulent eddies. Just like the night of 23 April, the main flow direction was from the northeast. The LRWS LIDAR

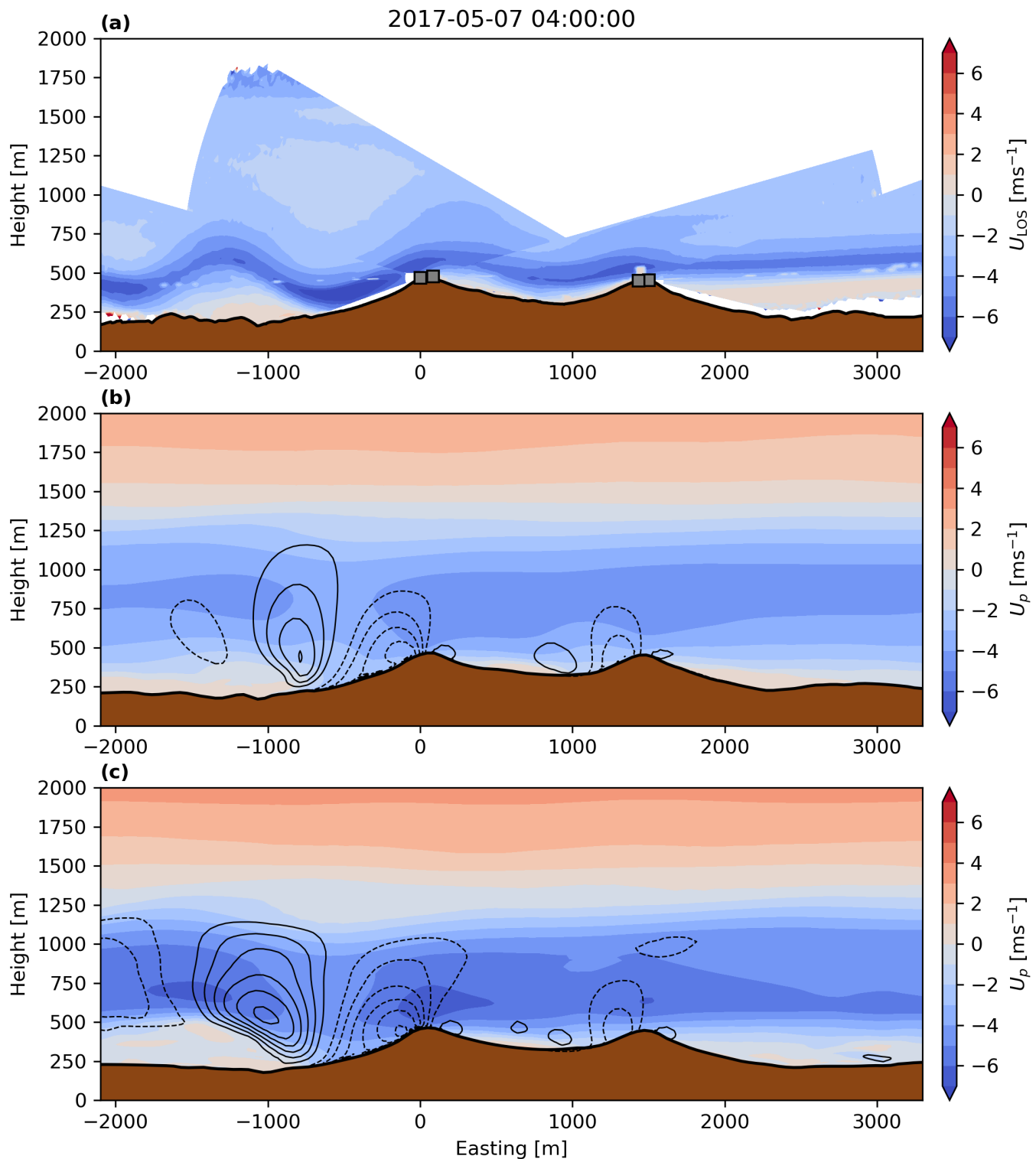


Fig. 5.19 04:00 UTC 7 May 2017. **(a)** Composite of the line-of-sight velocities ( $U_{LOS}$ ) observed by the four LRWS (gray squares). **(b)** G02-U and **(c)** G03-Q horizontal velocities in the plane along the scanner transect ( $U_p$ ), as well as negative (dashed) and positive (full) vertical velocities in contours of 0.3 m/s. The zero vertical velocity contour is not shown. Horizontal distances (Easting) are in meters along the scanner transect relative to the position of LRWS 1 (first one from the left).



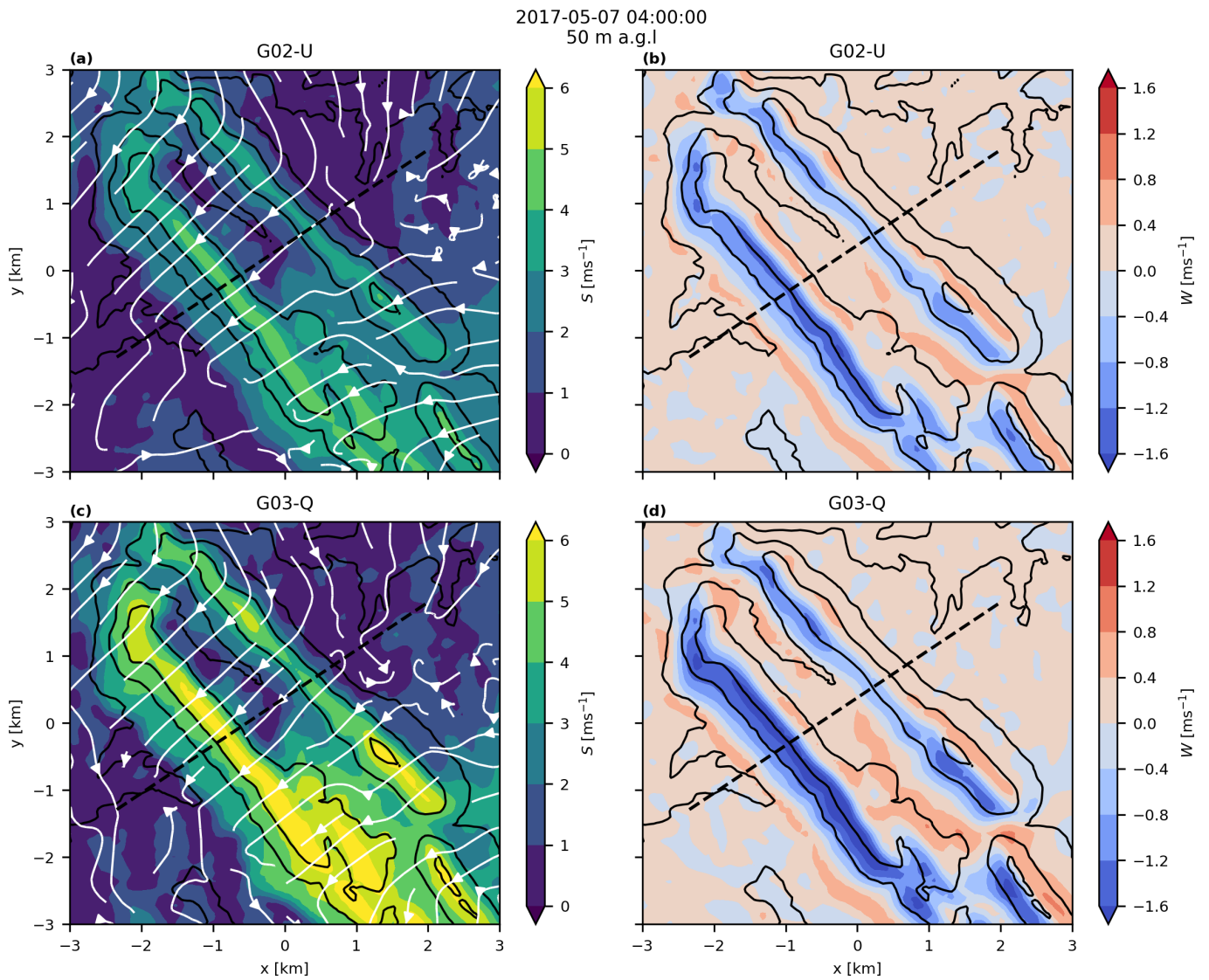


Fig. 5.20 04:00 UTC 7 May 2017. Horizontal planes of the modelled flow 50 m above the surface at the Perdigão site. The LRWS scan-planes are shown by the dashed black line, and elevation contours is shown in black for every 100 m. **(a,c)** horizontal wind speed (color) and streamlines (white lines). **(b,d)** vertical velocities.



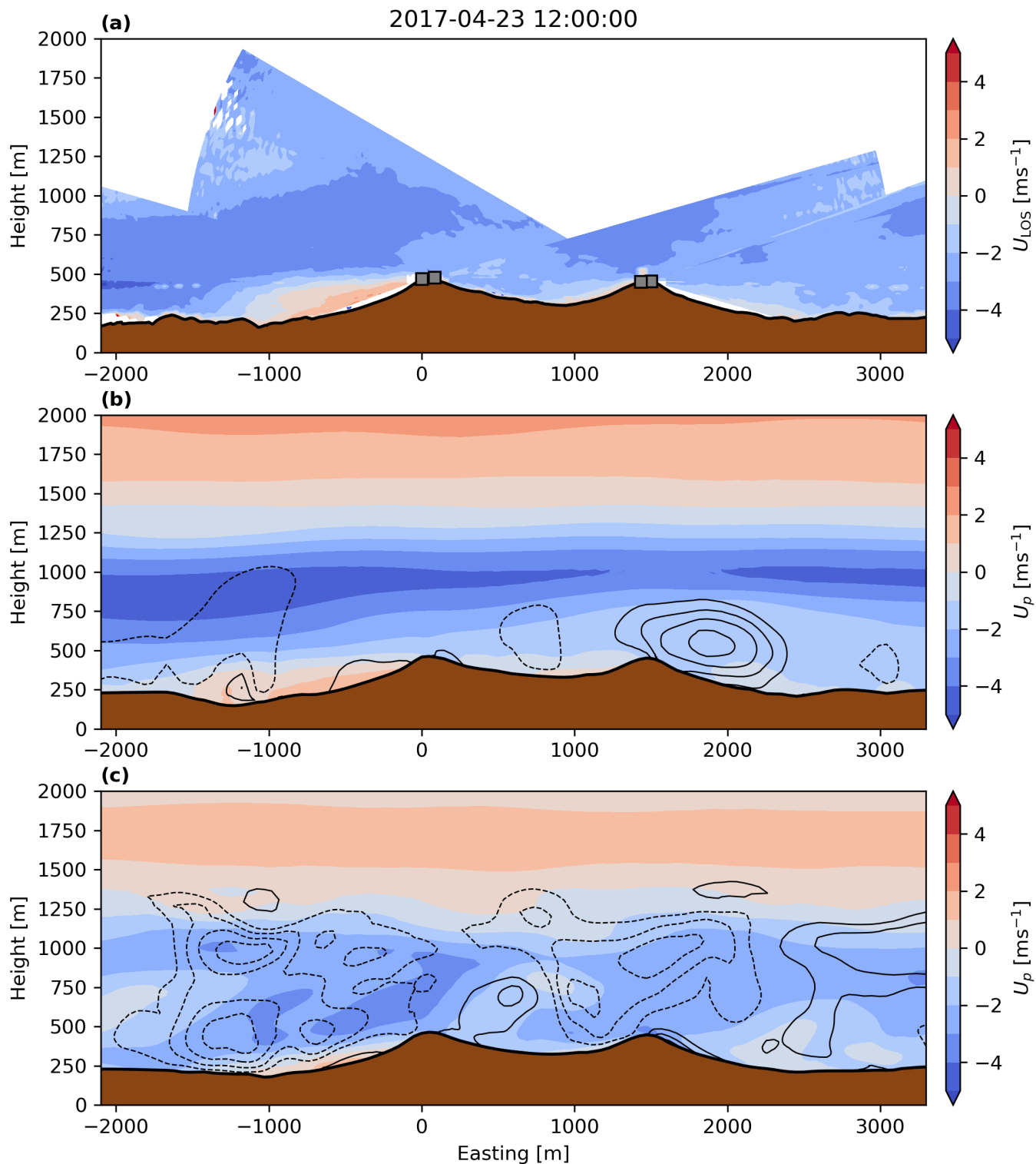


Fig. 5.21 12:00 UTC 23 April 2017. **(a)** Composite of the line-of-sight velocities ( $U_r$ ) observed by the four LRWS (gray squares). **(b)** G02-U and **(c)** G03-Q horizontal velocities in the plane along the scanner transect ( $U_p$ ), as well as negative (dashed) and positive (full) vertical velocities in contours of 0.3 m/s. The zero vertical velocity contour is not shown. Horizontal distances (Easting) are in meters along the scanner transect relative to the position of LRWS 1 (first one from the left).

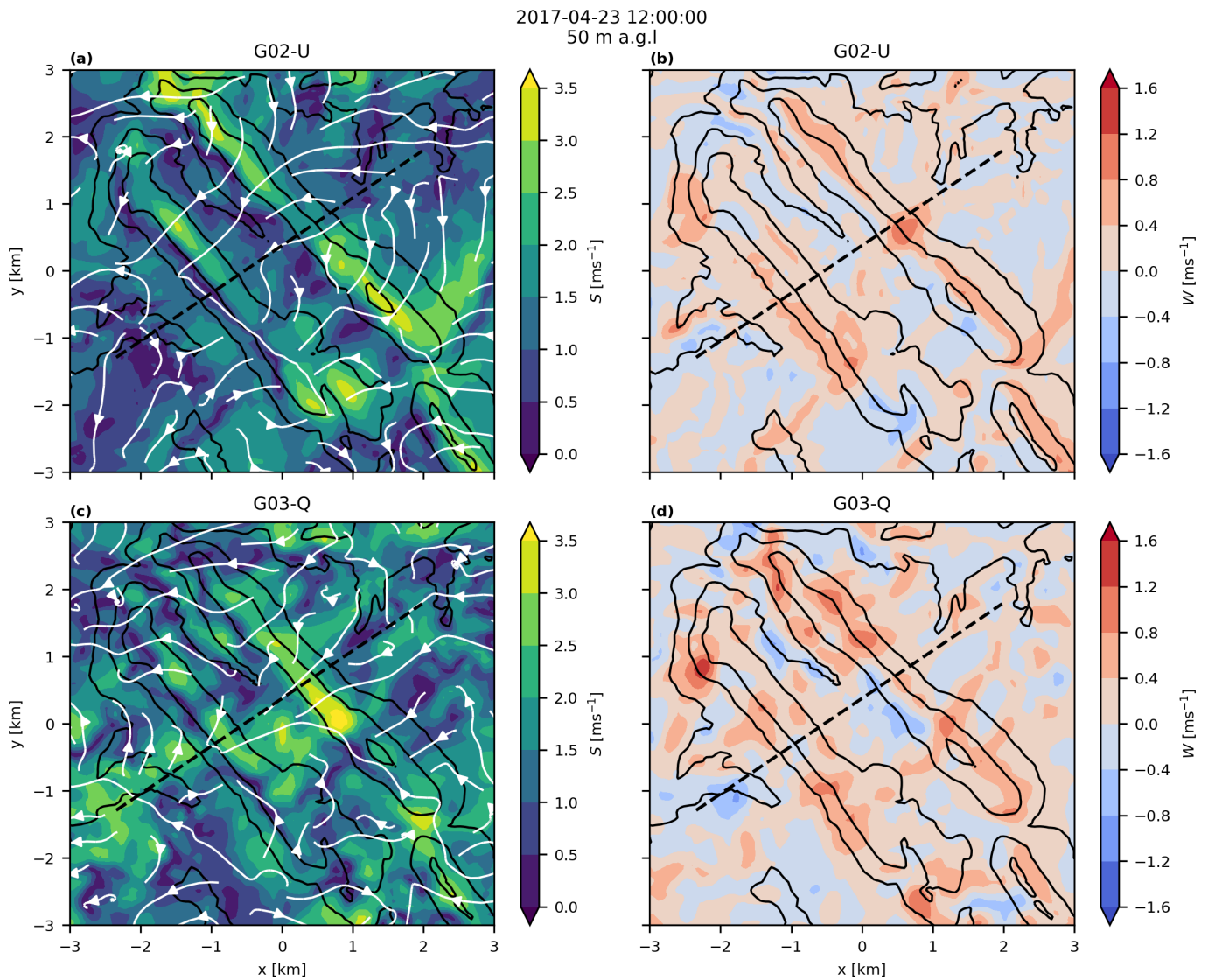


Fig. 5.22 12:00 UTC 23 April 2017. Horizontal planes of the modelled flow 50 m above the surface at the Perdigão site. The LRWS scan-planes are shown by the dashed black line, and elevation contours is shown in black for every 100 m. **(a,c)** horizontal wind speed (color) and streamlines (white lines). **(b,d)**

scans show decreased/reversed wind speeds behind the southwest ridge. In front of, and behind the northeast ridge, the blocking and lee effects seen during the stable conditions are less pronounced in the observations. The two model simulations appear qualitatively quite different. G03-Q shows lower wind speeds and signs of more vertical structures in the flow. On the other hand, G02-U shows a more stratified flow, especially aloft, and a clearer lee-side slowdown/re-circulation zone behind both ridges, compared to G03-Q. In front of the northeast ridge, G02-U show vertical velocities of approximately the same magnitude of the horizontal velocities, indicating that G02-U too are developing more vertical structures.

The horizontal flow planes (Fig. 5.22) also reveal more cell-like structures in G03-Q than G02-U. Especially visible in the vertical velocities, showing cells especially along up-slope regions, but also in the more smoothly sloping terrain. For G02-U, local peaks in wind speed found mostly around the elevation peaks, while peaks in G03-Q are also seen away from elevation peaks, e.g. in the middle of the central valley. This is another indication of the eddy-like structures being more pronounced in G03-Q.

### Time-series and statistics

Ultimately for the coupled meso- microscale model-chain to be appropriate for wind resource assessment, it must improve upon the predicted wind climate, compared to state-of-the-art methodologies. In the following, the statistical properties of G02-U, G03-U, G03-Q, and the WRF results, are validated against measurements from the nine masts for the 32 days.

Figures 5.23–5.31 show, for each of the nine masts: time series of the wind speed and direction at the top of the mast, distributions of wind speeds and wind directions (wind roses), and vertical wind speed profile. In tables 5.5–5.13 wind speed statistics for each measurement height are provided, excluding results from the most coarse WRF domain (d01). The vertical mean wind speed profiles in the figures are consistent across height, meaning that instances of missing data for any height are removed from the other heights of both the measurements and model results. In the tables, each height is treated separately so values are not consistent across heights, so missing values for each height is only removed from the corresponding model results, not for the other heights. A short summary of the results for groups of masts with similar type of placement is given below.

It is clear that on the top of the ridges: mast 29 (Fig. 5.29) on the north-east, and mast 20, 34, and 37 (fig 5.25, 5.30, and 5.31) on the south-west, both WRF d05, and EllipSys G03-Q overestimate the mean wind speed; most of all, G03-Q. Counter to that, G02-U and G03-U gives similar results, shows much smaller mean wind speed errors, and captures the shape of the vertical wind speed profiles well, except near the ground where canopy/vegetation has the most influence. At the top of the ridges, where turning of the flow due to topographic

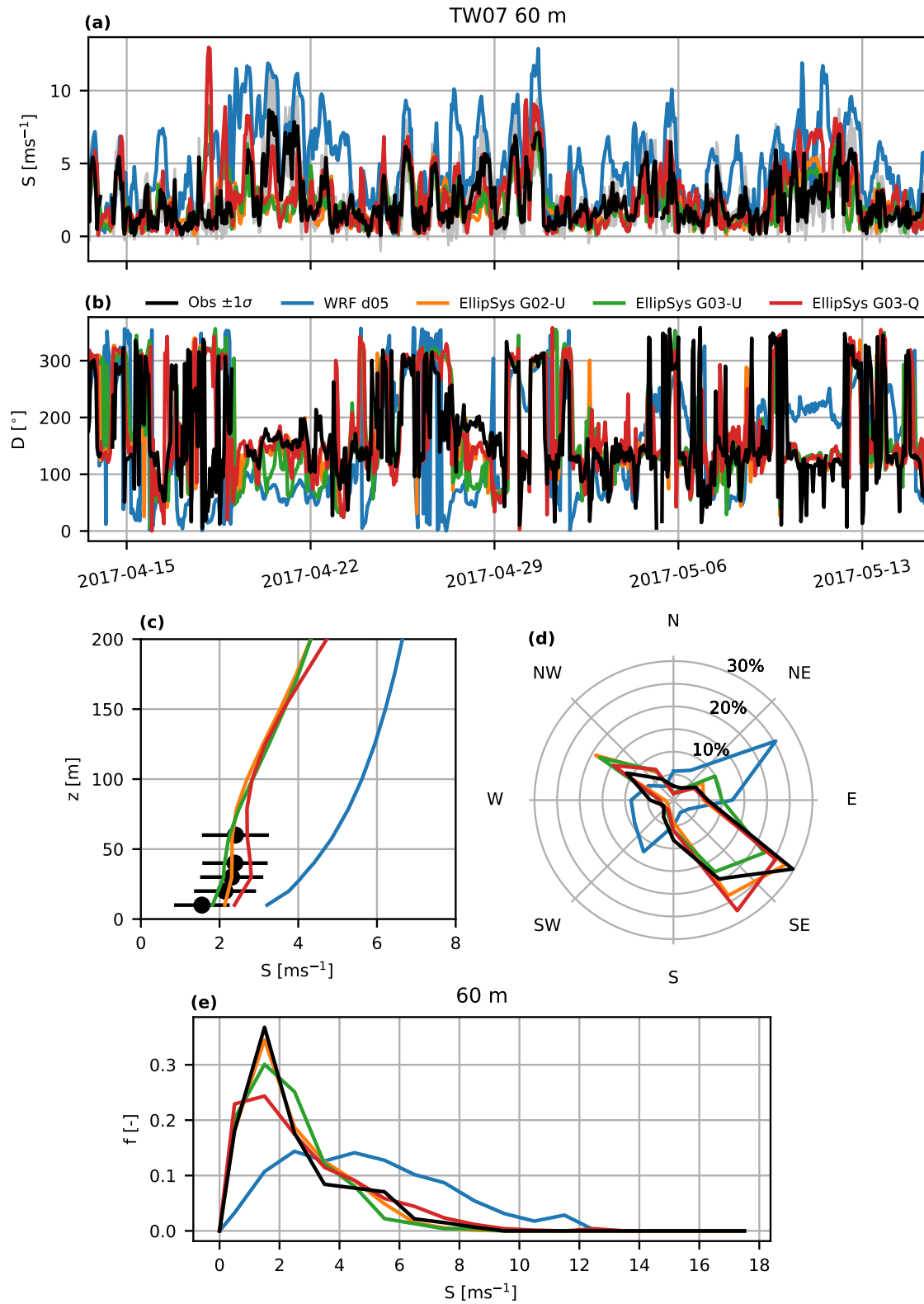


Fig. 5.23 Mast 7: **(a)** Wind speed and **(b)** wind direction at 60 m. For the wind speed the mean ten-minute standard-deviation of wind speed is shown as the gray outline. **(c)** Mean wind speed profiles. The mean ten-minute standard-deviation of wind speed is shown by the error bars. Wind direction **(d)** and wind speed **(e)** distributions at 60 m.

Table 5.5 Wind speed statistics for mast 7: Mean wind speed ( $\langle S \rangle$ ), standard deviation of wind speed ( $\sigma_S$ ), Bias of the mean wind speed (Bias), mean absolute error (MAE), root-mean-square error (RMSE), and Pearson correlation coefficient (C.C.). The best performing model is highlighted in bold text. The availability for the period is listed in the **Avail.** column.

Height	Avail.	Name	$\langle S \rangle$	$\sigma_S$	Bias	MAE	RSME	C.C.
60m	96.0	Obs	2.42	1.73	-	-	-	-
		WRF d02	5.99	3.13	147.7	3.70	4.51	0.48
		WRF d03	5.59	3.04	131.0	3.29	4.09	0.53
		WRF d04	6.11	3.31	152.5	3.75	4.59	0.56
		WRF d05	4.91	2.67	103.2	2.66	3.28	<b>0.61</b>
		EllipSys G02-U	<b>2.33</b>	<b>1.51</b>	<b>-3.8</b>	1.33	1.80	0.39
		EllipSys G03-U	2.25	1.45	-6.8	<b>1.29</b>	<b>1.78</b>	0.38
		EllipSys G03-Q	2.71	2.12	12.0	1.36	1.97	0.50
40m	96.1	Obs	2.41	1.65	-	-	-	-
		WRF d02	5.55	2.87	130.3	3.26	3.97	0.53
		WRF d03	5.17	2.81	114.7	2.88	3.60	0.57
		WRF d04	5.78	3.12	139.7	3.42	4.21	<b>0.59</b>
		WRF d05	4.42	2.48	83.5	2.28	2.84	<b>0.59</b>
		EllipSys G02-U	<b>2.32</b>	<b>1.46</b>	<b>-3.8</b>	<b>1.27</b>	<b>1.71</b>	0.40
		EllipSys G03-U	2.13	1.37	-11.6	1.30	1.79	0.32
		EllipSys G03-Q	2.79	2.21	15.9	1.44	2.06	0.48
30m	96.0	Obs	2.32	1.51	-	-	-	-
		WRF d02	5.22	2.71	125.1	3.01	3.66	0.56
		WRF d03	4.86	2.65	109.5	2.66	3.33	<b>0.59</b>
		WRF d04	5.51	2.98	137.3	3.24	4.00	<b>0.59</b>
		WRF d05	4.10	2.33	76.7	2.10	2.63	0.56
		EllipSys G02-U	<b>2.31</b>	<b>1.45</b>	<b>-0.3</b>	<b>1.20</b>	<b>1.60</b>	0.41
		EllipSys G03-U	2.11	1.32	-9.3	1.23	1.66	0.33
		EllipSys G03-Q	2.81	2.22	21.1	1.45	2.08	0.47
20m	96.0	Obs	2.15	1.38	-	-	-	-
		WRF d02	4.83	2.50	124.8	2.77	3.36	0.59
		WRF d03	4.48	2.46	108.6	2.43	3.05	<b>0.61</b>
		WRF d04	5.17	2.81	140.7	3.07	3.79	0.59
		WRF d05	3.77	2.13	75.6	1.93	2.41	0.55
		EllipSys G02-U	<b>2.22</b>	<b>1.39</b>	<b>3.5</b>	1.11	1.48	0.43
		EllipSys G03-U	1.96	1.18	-8.6	<b>1.07</b>	<b>1.46</b>	0.37
		EllipSys G03-Q	2.60	2.04	20.9	1.32	1.88	0.48
[%]		[ms <sup>-1</sup> ]	[ms <sup>-1</sup> ]	[%]	[ms <sup>-1</sup> ]	[ms <sup>-1</sup> ]		

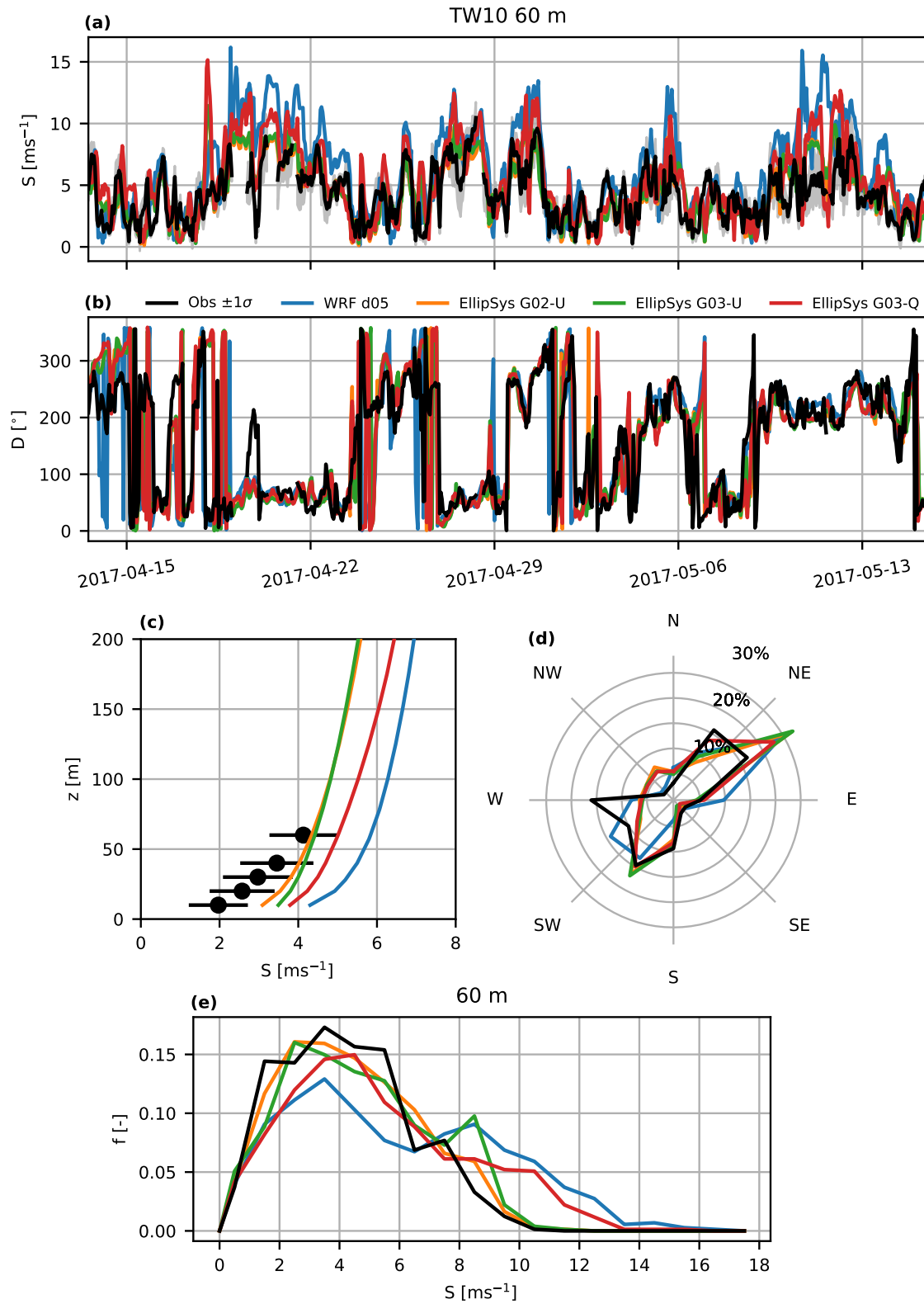


Fig. 5.24 Mast 10: (a) Wind speed and (b) wind direction at 60 m. For the wind speed the mean ten-minute standard-deviation of wind speed is shown as the gray outline. (c) Mean wind speed profiles. The mean ten-minute standard-deviation of wind speed is shown by the error bars. Wind direction (d) and wind speed (e) distributions at 60 m.

Table 5.6 Wind speed statistics for mast 10: Mean wind speed ( $\langle S \rangle$ ), standard deviation of wind speed ( $\sigma_S$ ), Bias of the mean wind speed (Bias), mean absolute error (MAE), root-mean-square error (RMSE), and Pearson correlation coefficient (C.C.). The best performing model is highlighted in bold text. The availability for the period is listed in the **Avail.** column.

Height	Avail.	Name	$\langle S \rangle$	$\sigma_S$	Bias	MAE	RSME	C.C.
60m	94.8	Obs	4.17	2.11	-	-	-	-
		WRF d02	5.81	3.03	39.3	2.23	2.91	0.61
		WRF d03	5.36	2.95	28.6	1.87	2.48	<b>0.68</b>
		WRF d04	5.55	3.16	33.1	1.99	2.70	<b>0.68</b>
		WRF d05	5.89	3.41	41.2	2.29	3.03	<b>0.68</b>
		EllipSys G02-U	<b>4.37</b>	<b>2.24</b>	<b>4.8</b>	<b>1.47</b>	<b>1.85</b>	0.64
		EllipSys G03-U	4.45	2.31	6.7	1.48	1.87	0.65
		EllipSys G03-Q	5.06	2.84	21.3	1.81	2.40	0.63
40m	96.5	Obs	3.50	1.75	-	-	-	-
		WRF d02	5.45	2.83	56.0	2.46	3.20	0.47
		WRF d03	5.05	2.79	44.4	2.12	2.83	0.54
		WRF d04	5.30	3.05	51.5	2.30	3.07	<b>0.58</b>
		WRF d05	5.66	3.28	61.9	2.64	3.44	<b>0.58</b>
		EllipSys G02-U	<b>4.12</b>	<b>2.10</b>	<b>17.7</b>	<b>1.63</b>	<b>2.02</b>	0.51
		EllipSys G03-U	4.26	2.20	21.8	1.72	2.14	0.51
		EllipSys G03-Q	4.82	2.77	37.9	2.08	2.71	0.53
30m	96.6	Obs	2.98	1.62	-	-	-	-
		WRF d02	5.15	2.69	72.8	2.62	3.42	0.33
		WRF d03	4.77	2.66	60.0	2.30	3.07	0.40
		WRF d04	5.05	2.94	69.3	2.50	3.31	<b>0.48</b>
		WRF d05	5.42	3.15	81.9	2.85	3.70	0.47
		EllipSys G02-U	<b>3.91</b>	<b>1.97</b>	<b>31.2</b>	<b>1.75</b>	<b>2.19</b>	0.41
		EllipSys G03-U	4.11	2.12	37.8	1.89	2.39	0.39
		EllipSys G03-Q	4.62	2.66	54.9	2.27	2.92	0.44
20m	97.4	Obs	2.61	1.56	-	-	-	-
		WRF d02	4.80	2.52	84.2	2.57	3.33	0.32
		WRF d03	4.44	2.49	70.4	2.26	3.01	0.38
		WRF d04	4.76	2.79	82.5	2.49	3.28	0.47
		WRF d05	5.14	2.99	97.1	2.86	3.67	0.46
		EllipSys G02-U	<b>3.64</b>	<b>1.80</b>	<b>39.8</b>	<b>1.69</b>	<b>2.10</b>	0.42
		EllipSys G03-U	3.93	2.01	50.6	1.90	2.42	0.38
		EllipSys G03-Q	4.36	2.53	67.4	2.24	2.84	<b>0.49</b>
[%]		[ms <sup>-1</sup> ]	[ms <sup>-1</sup> ]	[%]	[ms <sup>-1</sup> ]	[ms <sup>-1</sup> ]		

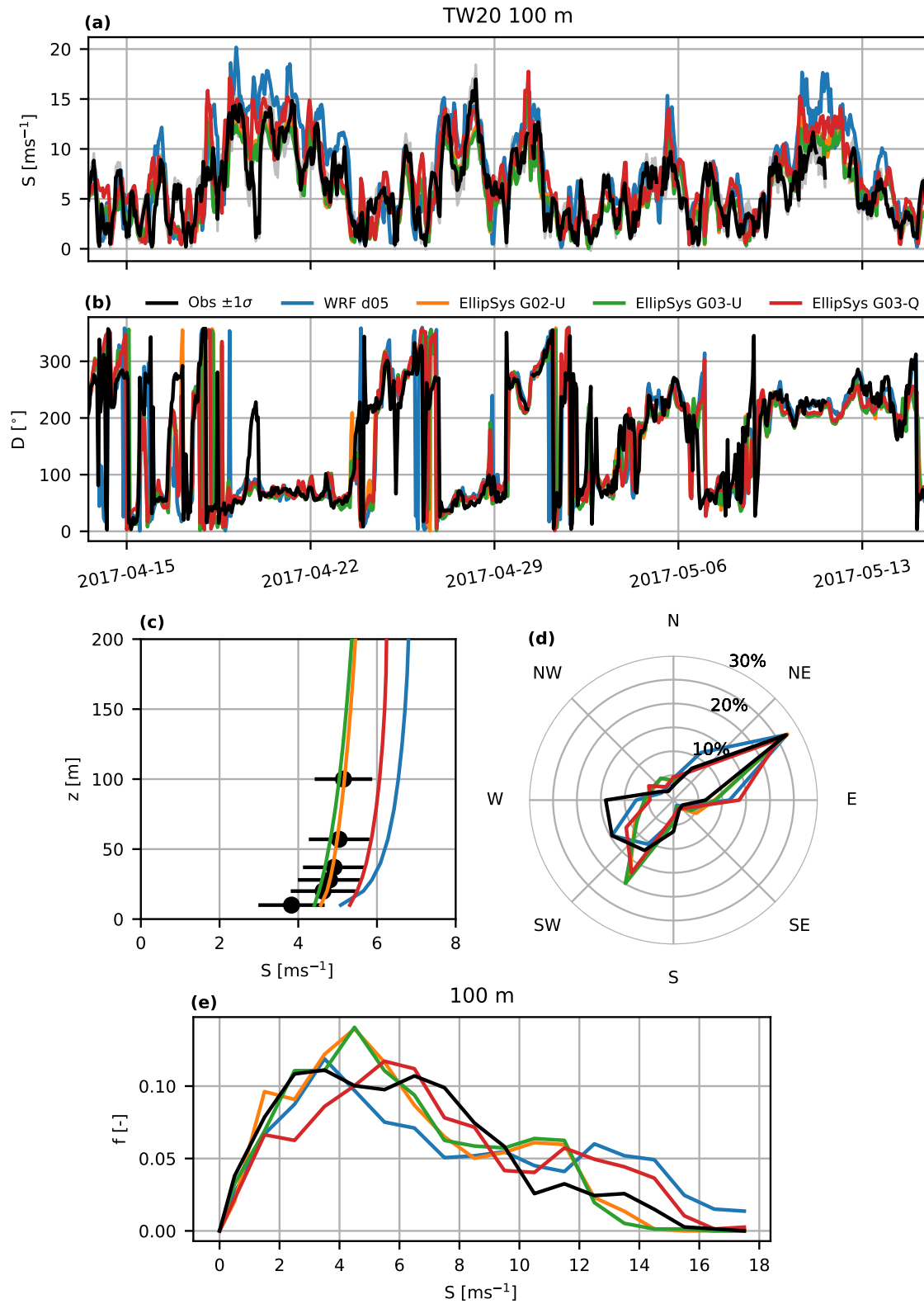


Fig. 5.25 Mast 20: **(a)** Wind speed and **(b)** wind direction at 100 m. For the wind speed the mean ten-minute standard-deviation of wind speed is shown as the gray outline. **(c)** Mean wind speed profiles. The mean ten-minute standard-deviation of wind speed is shown by the error bars. Wind direction **(d)** and wind speed **(e)** distributions at 100 m.



Table 5.7 Wind speed statistics for mast 20: Mean wind speed ( $\langle S \rangle$ ), standard deviation of wind speed ( $\sigma_S$ ), Bias of the mean wind speed (Bias), mean absolute error (MAE), root-mean-square error (RMSE), and Pearson correlation coefficient (C.C.). The best performing model is highlighted in bold text. The availability for the period is listed in the **Avail.** column.

Height	Avail.	Name	$\langle S \rangle$	$\sigma_S$	Bias	MAE	RSME	C.C.
100m	96.1	Obs	5.97	3.45	-	-	-	-
		WRF d02	6.50	3.56	8.8	1.96	2.64	0.73
		WRF d03	6.12	3.50	2.5	1.78	2.35	0.77
		WRF d04	6.71	3.82	12.4	1.93	2.60	0.77
		WRF d05	7.46	4.57	25.0	2.41	3.21	0.78
		EllipSys G02-U	<b>5.89</b>	<b>3.27</b>	<b>-1.3</b>	<b>1.72</b>	2.19	<b>0.79</b>
		EllipSys G03-U	5.74	3.17	-3.9	<b>1.72</b>	<b>2.18</b>	0.79
		EllipSys G03-Q	6.86	3.78	14.9	2.04	2.66	0.76
78m	13.8	Obs	6.54	2.99	-	-	-	-
		WRF d02	6.18	<b>3.56</b>	-5.5	<b>1.70</b>	<b>2.12</b>	<b>0.81</b>
		WRF d03	6.39	3.59	-2.3	1.82	2.29	0.77
		WRF d04	7.03	3.89	7.6	1.98	2.56	0.76
		WRF d05	8.42	4.73	28.7	2.82	3.63	0.77
		EllipSys G02-U	6.92	3.61	5.8	1.88	2.28	0.78
		EllipSys G03-U	<b>6.68</b>	3.48	<b>2.2</b>	1.85	2.22	0.78
		EllipSys G03-Q	7.64	4.16	16.9	2.36	2.96	0.75
57m	96.6	Obs	5.84	3.30	-	-	-	-
		WRF d02	<b>5.88</b>	<b>3.13</b>	<b>0.8</b>	1.85	2.37	0.73
		WRF d03	5.53	3.11	-5.2	1.72	2.21	0.77
		WRF d04	6.29	<b>3.47</b>	7.8	1.79	2.37	0.76
		WRF d05	7.17	4.40	23.0	2.30	3.06	<b>0.78</b>
		EllipSys G02-U	5.67	3.07	-2.9	<b>1.70</b>	<b>2.17</b>	0.77
		EllipSys G03-U	5.46	2.96	-6.3	1.73	2.17	0.77
		EllipSys G03-Q	6.60	3.59	13.2	1.98	2.59	0.74
37m	96.6	Obs	5.71	3.25	-	-	-	-
		WRF d02	5.38	2.86	-5.7	1.83	2.28	0.73
		WRF d03	5.08	2.85	-11.0	1.74	2.23	0.76
		WRF d04	5.94	<b>3.24</b>	4.2	1.72	2.27	0.76
		WRF d05	6.90	4.27	21.0	2.19	2.92	<b>0.78</b>
		EllipSys G02-U	<b>5.52</b>	2.96	<b>-3.3</b>	<b>1.68</b>	<b>2.14</b>	0.77
		EllipSys G03-U	5.29	2.84	-7.3	1.72	2.16	0.77
		EllipSys G03-Q	6.41	3.47	12.3	1.93	2.54	0.74
28m	94.1	Obs	5.50	3.17	-	-	-	-
		WRF d02	5.03	2.69	-8.5	1.85	2.30	0.72
		WRF d03	4.75	2.69	-13.7	1.78	2.28	0.74
		WRF d04	5.67	<b>3.08</b>	3.0	1.73	2.26	0.74
		WRF d05	6.64	4.16	20.7	2.17	2.89	<b>0.77</b>
		EllipSys G02-U	<b>5.35</b>	2.86	<b>-2.8</b>	<b>1.66</b>	<b>2.13</b>	0.76
		EllipSys G03-U	5.12	2.76	-6.9	1.69	2.14	0.76
		EllipSys G03-Q	6.20	3.36	12.7	1.92	2.54	0.72
[%]		[ms <sup>-1</sup> ]	[ms <sup>-1</sup> ]	[%]	[ms <sup>-1</sup> ]	[ms <sup>-1</sup> ]		

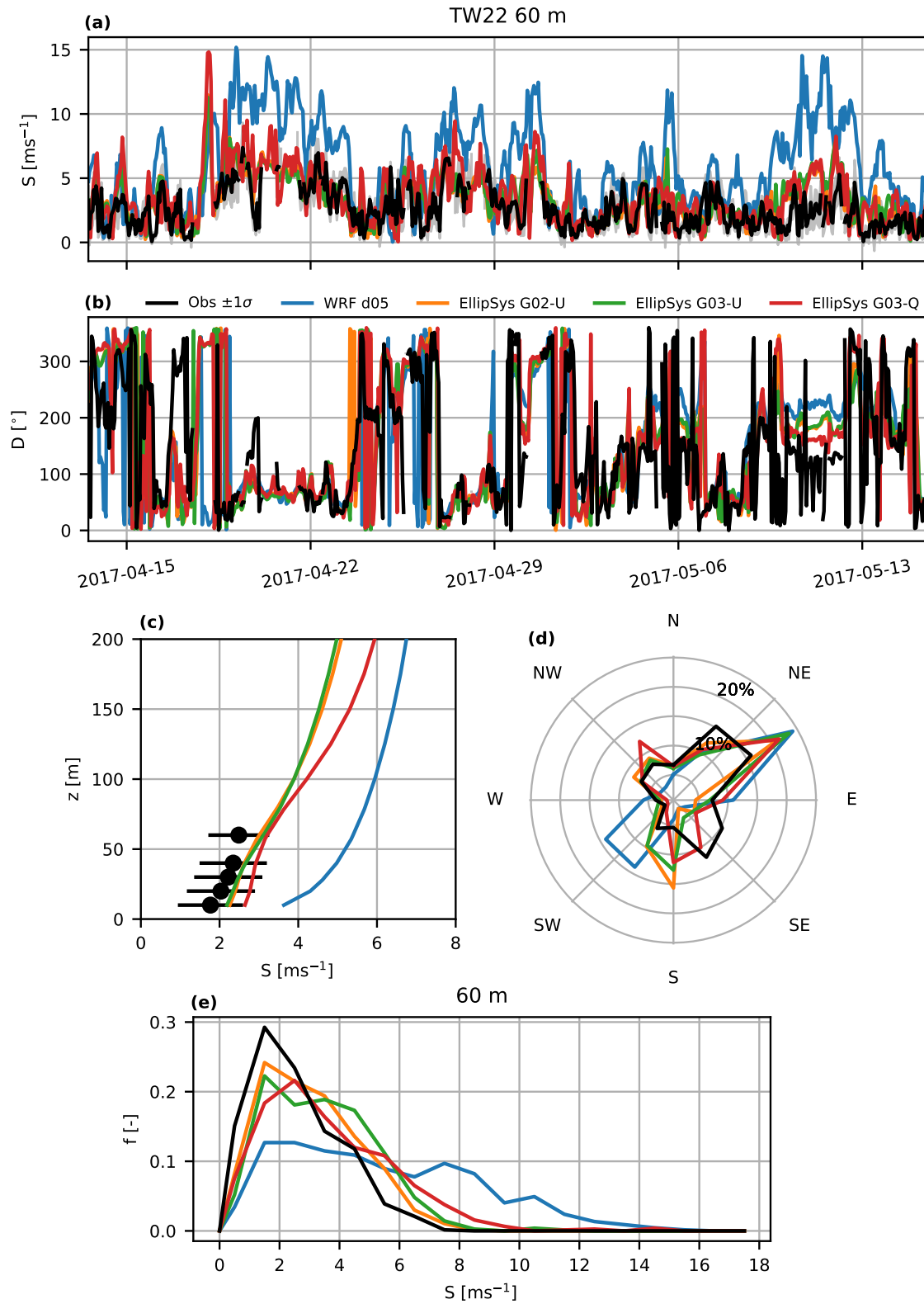


Fig. 5.26 Mast 22: (a) Wind speed and (b) wind direction at 60 m. For the wind speed the mean ten-minute standard-deviation of wind speed is shown as the gray outline. (c) Mean wind speed profiles. The mean ten-minute standard-deviation of wind speed is shown by the error bars. Wind direction (d) and wind speed (e) distributions at 60 m.

Table 5.8 Wind speed statistics for mast 22: Mean wind speed ( $\langle S \rangle$ ), standard deviation of wind speed ( $\sigma_S$ ), Bias of the mean wind speed (Bias), mean absolute error (MAE), root-mean-square error (RMSE), and Pearson correlation coefficient (C.C.). The best performing model is highlighted in bold text. The availability for the period is listed in the **Avail.** column.

Height	Avail.	Name	$\langle S \rangle$	$\sigma_S$	Bias	MAE	RSME	C.C.
60m	87.2	Obs	2.49	1.49	-	-	-	-
		WRF d02	5.47	2.82	119.3	3.21	3.89	0.46
		WRF d03	5.20	2.89	108.5	2.97	3.74	0.45
		WRF d04	5.88	3.20	136.1	3.58	4.43	0.45
		WRF d05	5.39	3.20	116.3	3.18	4.04	0.47
		EllipSys G02-U	<b>3.01</b>	1.60	<b>21.0</b>	<b>1.24</b>	<b>1.58</b>	<b>0.53</b>
		EllipSys G03-U	3.12	<b>1.59</b>	25.3	1.28	1.65	0.51
		EllipSys G03-Q	3.21	1.85	29.0	1.44	1.83	0.51
40m	96.1	Obs	2.71	1.86	-	-	-	-
		WRF d02	5.50	2.85	102.6	2.99	3.57	<b>0.62</b>
		WRF d03	5.27	2.92	94.1	2.79	3.46	0.60
		WRF d04	6.08	3.26	124.0	3.51	4.27	0.59
		WRF d05	5.47	3.25	101.7	3.00	3.76	<b>0.62</b>
		EllipSys G02-U	<b>2.81</b>	1.49	<b>3.5</b>	<b>1.17</b>	<b>1.52</b>	0.61
		EllipSys G03-U	2.83	1.46	4.3	1.20	1.55	0.59
		EllipSys G03-Q	3.14	<b>1.89</b>	15.7	1.40	1.82	0.55
30m	96.7	Obs	2.56	1.74	-	-	-	-
		WRF d02	5.18	2.70	102.2	2.81	3.36	<b>0.63</b>
		WRF d03	4.97	2.76	94.2	2.64	3.26	0.61
		WRF d04	5.83	3.12	127.5	3.41	4.12	0.60
		WRF d05	5.15	3.08	100.9	2.82	3.52	<b>0.63</b>
		EllipSys G02-U	2.67	1.42	4.2	<b>1.14</b>	<b>1.49</b>	0.58
		EllipSys G03-U	<b>2.63</b>	1.37	<b>2.7</b>	1.15	<b>1.49</b>	0.57
		EllipSys G03-Q	3.05	<b>1.89</b>	19.0	1.41	1.87	0.51
20m	96.7	Obs	2.34	1.58	-	-	-	-
		WRF d02	4.79	2.50	104.5	2.62	3.12	0.63
		WRF d03	4.60	2.56	96.6	2.46	3.04	0.61
		WRF d04	5.50	2.93	134.8	3.28	3.94	0.59
		WRF d05	4.75	2.88	102.7	2.62	3.27	<b>0.64</b>
		EllipSys G02-U	2.54	<b>1.38</b>	8.7	1.12	1.47	0.52
		EllipSys G03-U	<b>2.47</b>	1.28	<b>5.4</b>	<b>1.10</b>	<b>1.42</b>	0.53
		EllipSys G03-Q	2.95	1.90	26.2	1.41	1.93	0.46
[%]		[ms <sup>-1</sup> ]	[ms <sup>-1</sup> ]	[%]	[ms <sup>-1</sup> ]	[ms <sup>-1</sup> ]		

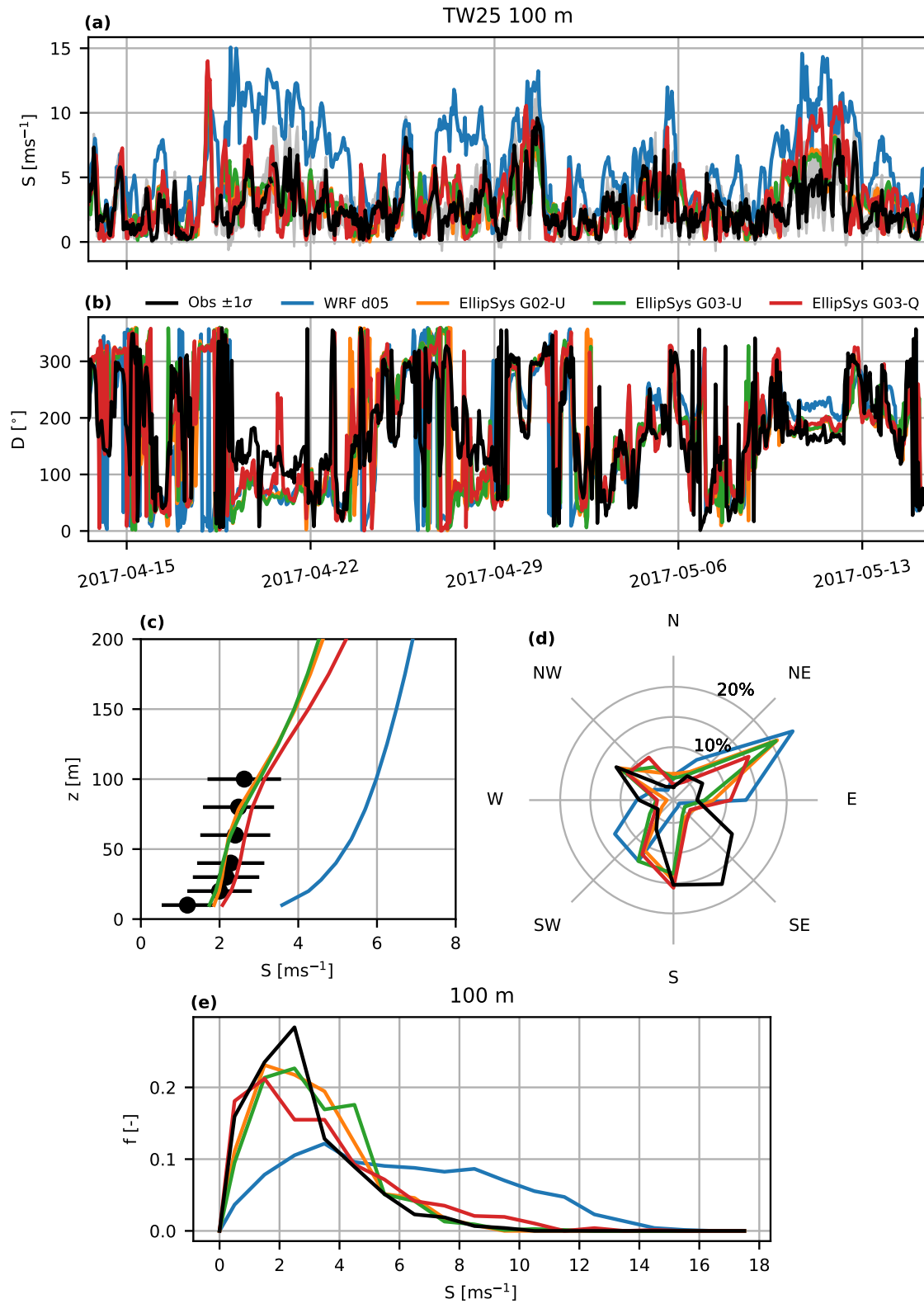


Fig. 5.27 Mast 25: (a) Wind speed and (b) wind direction at 60 m. For the wind speed the mean ten-minute standard-deviation of wind speed is shown as the gray outline. (c) Mean wind speed profiles. The mean ten-minute standard-deviation of wind speed is shown by the error bars. Wind direction (d) and wind speed (e) distributions at 60 m.

Table 5.9 Wind speed statistics for mast 25: Mean wind speed ( $\langle S \rangle$ ), standard deviation of wind speed ( $\sigma_S$ ), Bias of the mean wind speed (Bias), mean absolute error (MAE), root-mean-square error (RMSE), and Pearson correlation coefficient (C.C.). The best performing model is highlighted in bold text. The availability for the period is listed in the **Avail.** column.

Height	Avail.	Name	$\langle S \rangle$	$\sigma_S$	Bias	MAE	RSME	C.C.
100m	96.4	Obs	2.64	1.75	-	-	-	-
		WRF d02	6.51	3.45	146.2	4.04	5.00	0.41
		WRF d03	6.25	3.48	136.3	3.75	4.77	0.45
		WRF d04	6.61	3.70	150.1	4.08	5.11	0.49
		WRF d05	6.02	3.35	127.8	3.56	4.43	0.52
		EllipSys G02-U	<b>2.95</b>	<b>1.73</b>	<b>11.7</b>	<b>1.34</b>	<b>1.71</b>	0.53
		EllipSys G03-U	3.03	1.69	14.5	1.36	1.73	0.52
		EllipSys G03-Q	3.15	2.36	19.2	1.56	2.07	<b>0.56</b>
80m	96.2	Obs	2.50	1.74	-	-	-	-
		WRF d02	6.24	3.26	149.3	3.89	4.74	0.45
		WRF d03	5.98	3.30	138.8	3.61	4.51	0.49
		WRF d04	6.39	3.54	154.9	3.98	4.90	0.54
		WRF d05	5.75	3.16	129.7	3.42	4.18	<b>0.56</b>
		EllipSys G02-U	<b>2.51</b>	<b>1.69</b>	<b>0.3</b>	1.36	1.72	0.50
		EllipSys G03-U	2.62	1.61	4.8	<b>1.32</b>	<b>1.68</b>	0.50
		EllipSys G03-Q	2.84	2.27	13.4	1.49	1.99	0.55
60m	96.6	Obs	2.44	1.76	-	-	-	-
		WRF d02	5.94	3.07	143.4	3.63	4.37	0.53
		WRF d03	5.69	3.13	133.4	3.39	4.16	0.56
		WRF d04	6.14	3.40	152.0	3.79	4.61	<b>0.60</b>
		WRF d05	5.46	2.98	123.7	3.17	3.84	<b>0.60</b>
		EllipSys G02-U	2.24	<b>1.58</b>	-8.2	<b>1.30</b>	<b>1.69</b>	0.50
		EllipSys G03-U	<b>2.28</b>	1.51	<b>-6.4</b>	1.31	1.71	0.47
		EllipSys G03-Q	2.66	2.16	8.9	1.41	1.90	0.55
40m	96.2	Obs	2.31	1.66	-	-	-	-
		WRF d02	5.46	2.82	136.8	3.27	3.90	0.58
		WRF d03	5.27	2.89	128.2	3.07	3.75	0.60
		WRF d04	5.77	3.19	150.1	3.53	4.27	<b>0.64</b>
		WRF d05	4.99	2.71	116.3	2.81	3.43	0.62
		EllipSys G02-U	<b>2.12</b>	<b>1.39</b>	<b>-8.1</b>	<b>1.13</b>	<b>1.48</b>	0.55
		EllipSys G03-U	2.08	1.33	-10.0	1.19	1.59	0.47
		EllipSys G03-Q	2.52	2.01	9.1	1.29	1.76	0.56
30m	96.5	Obs	2.20	1.60	-	-	-	-
		WRF d02	5.16	2.68	134.3	3.06	3.63	0.62
		WRF d03	4.99	2.75	126.6	2.88	3.51	0.64
		WRF d04	5.52	3.07	150.6	3.37	4.05	<b>0.66</b>
		WRF d05	4.69	2.55	112.8	2.60	3.18	0.63
		EllipSys G02-U	<b>2.07</b>	<b>1.31</b>	<b>-6.2</b>	<b>1.05</b>	<b>1.38</b>	0.57
		EllipSys G03-U	1.99	1.23	-9.4	1.11	1.51	0.47
		EllipSys G03-Q	2.43	1.89	10.4	1.22	1.69	0.55
[%]		[ms <sup>-1</sup> ]	[ms <sup>-1</sup> ]	[%]	[ms <sup>-1</sup> ]	[ms <sup>-1</sup> ]		

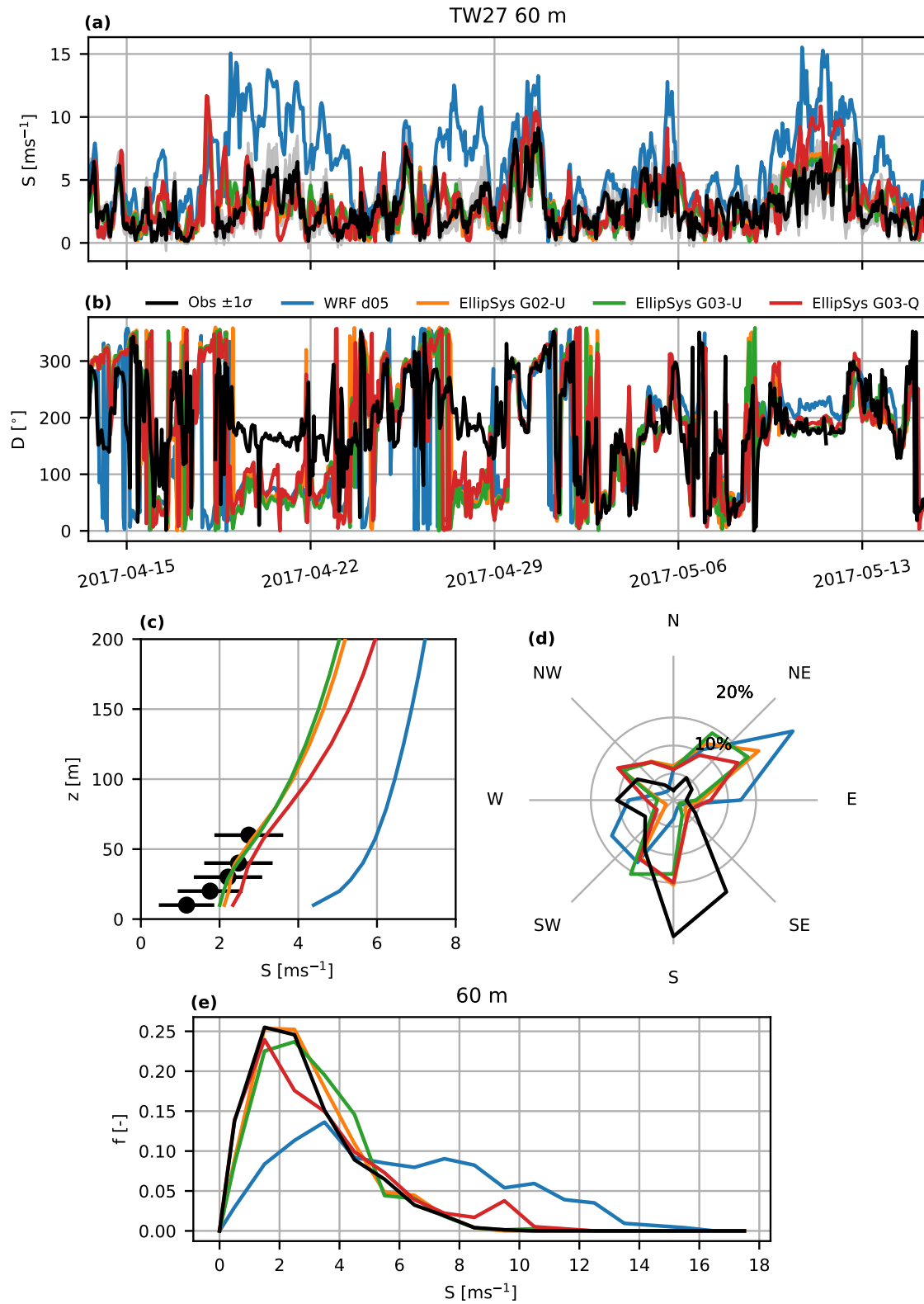


Fig. 5.28 Mast 27: (a) Wind speed and (b) wind direction at 60 m. For the wind speed the mean ten-minute standard-deviation of wind speed is shown as the gray outline. (c) Mean wind speed profiles. The mean ten-minute standard-deviation of wind speed is shown by the error bars. Wind direction (d) and wind speed (e) distributions at 60 m.

Table 5.10 Wind speed statistics for mast 27: Mean wind speed ( $\langle S \rangle$ ), standard deviation of wind speed ( $\sigma_S$ ), Bias of the mean wind speed (Bias), mean absolute error (MAE), root-mean-square error (RMSE), and Pearson correlation coefficient (C.C.). The best performing model is highlighted in bold text. The availability for the period is listed in the **Avail.** column.

Height	Avail.	Name	$\langle S \rangle$	$\sigma_S$	Bias	MAE	RSME	C.C.
60m	96.5	Obs	2.74	1.75	-	-	-	-
		WRF d02	5.93	3.06	116.0	3.41	4.25	0.42
		WRF d03	5.67	3.13	106.9	3.13	4.02	0.48
		WRF d04	5.95	3.37	116.9	3.37	4.27	0.55
		WRF d05	5.99	3.40	118.4	3.44	4.32	0.55
		EllipSys G02-U	<b>2.91</b>	<b>1.67</b>	<b>5.9</b>	1.27	1.58	0.58
		EllipSys G03-U	2.98	1.62	8.7	<b>1.25</b>	<b>1.56</b>	0.58
		EllipSys G03-Q	3.19	2.30	16.1	1.47	1.92	<b>0.61</b>
40m	96.6	Obs	2.48	1.63	-	-	-	-
		WRF d02	5.49	2.84	120.8	3.18	3.93	0.46
		WRF d03	5.28	2.91	112.5	2.97	3.75	0.51
		WRF d04	5.60	3.19	125.3	3.24	4.05	<b>0.59</b>
		WRF d05	5.65	3.21	127.4	3.32	4.11	0.58
		EllipSys G02-U	2.40	<b>1.61</b>	-3.4	1.28	1.62	0.50
		EllipSys G03-U	<b>2.46</b>	1.54	<b>-1.1</b>	<b>1.21</b>	<b>1.52</b>	0.54
		EllipSys G03-Q	2.76	2.17	11.1	1.39	1.80	<b>0.59</b>
30m	96.6	Obs	2.22	1.46	-	-	-	-
		WRF d02	5.17	2.69	132.8	3.10	3.78	0.48
		WRF d03	4.99	2.77	124.9	2.91	3.63	0.53
		WRF d04	5.32	3.06	139.9	3.20	3.96	<b>0.61</b>
		WRF d05	5.39	3.06	142.8	3.28	4.03	0.60
		EllipSys G02-U	2.29	<b>1.51</b>	3.1	<b>1.15</b>	<b>1.46</b>	0.52
		EllipSys G03-U	<b>2.24</b>	1.48	<b>0.7</b>	1.16	<b>1.46</b>	0.51
		EllipSys G03-Q	2.64	2.04	19.1	1.29	1.69	<b>0.61</b>
20m	96.6	Obs	1.76	1.17	-	-	-	-
		WRF d02	4.78	2.50	170.9	3.11	3.72	0.49
		WRF d03	4.64	2.58	162.7	2.94	3.60	0.54
		WRF d04	4.98	2.88	182.0	3.25	3.97	0.63
		WRF d05	5.06	2.86	186.5	3.35	4.04	0.61
		EllipSys G02-U	2.23	<b>1.37</b>	26.6	<b>1.01</b>	<b>1.28</b>	0.57
		EllipSys G03-U	<b>2.10</b>	<b>1.37</b>	<b>19.1</b>	1.02	1.29	0.53
		EllipSys G03-Q	2.54	1.87	44.1	1.23	1.63	<b>0.64</b>
[%]		[ms <sup>-1</sup> ]	[ms <sup>-1</sup> ]	[%]	[ms <sup>-1</sup> ]	[ms <sup>-1</sup> ]		

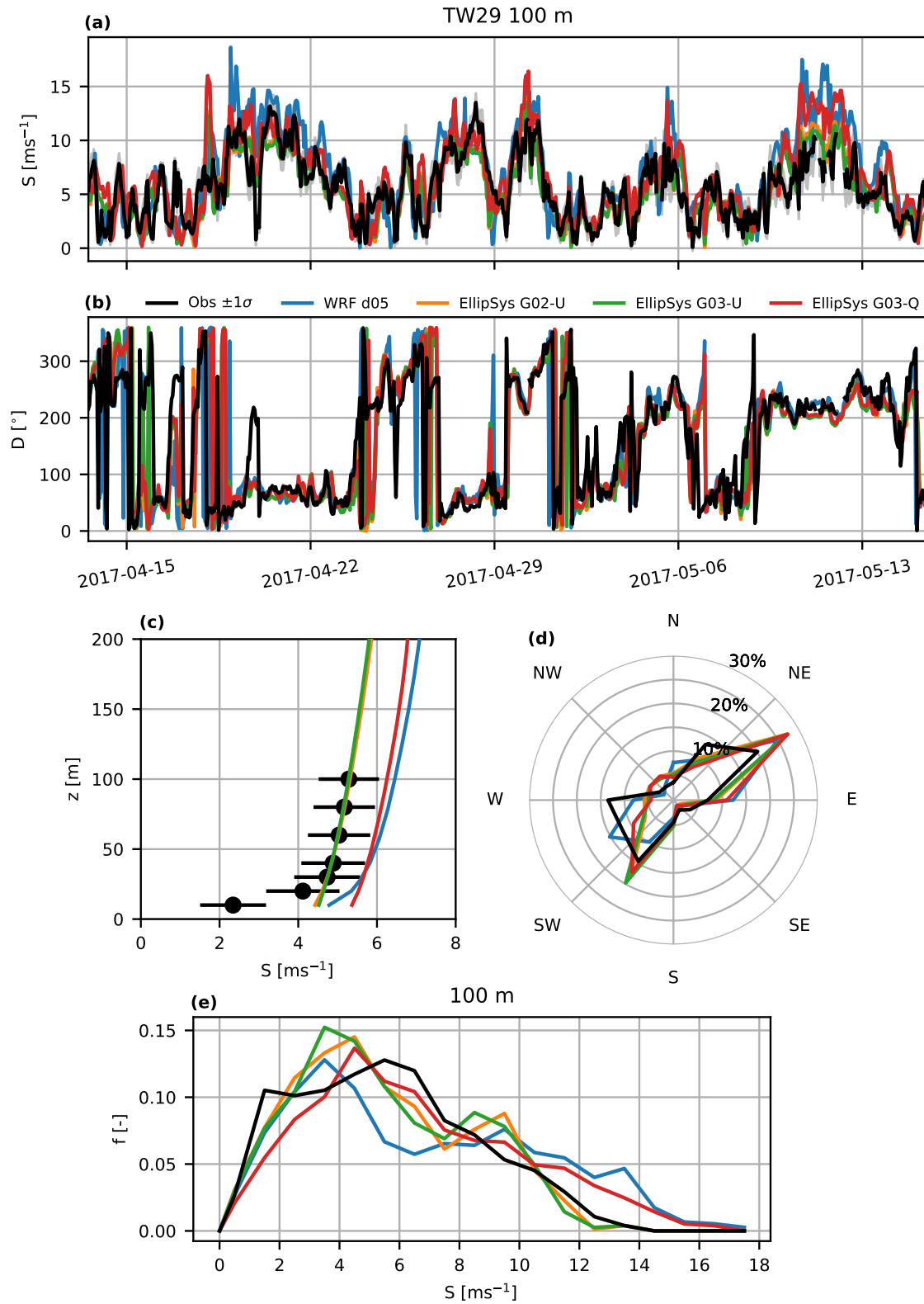


Fig. 5.29 Mast 29: **(a)** Wind speed and **(b)** wind direction at 100 m. For the wind speed the mean ten-minute standard-deviation of wind speed is shown as the gray outline. **(c)** Mean wind speed profiles. The mean ten-minute standard-deviation of wind speed is shown by the error bars. Wind direction **(d)** and wind speed **(e)** distributions at 100 m.



Table 5.11 Wind speed statistics for mast 29: Mean wind speed ( $\langle S \rangle$ ), standard deviation of wind speed ( $\sigma_S$ ), Bias of the mean wind speed (Bias), mean absolute error (MAE), root-mean-square error (RMSE), and Pearson correlation coefficient (C.C.). The best performing model is highlighted in bold text. The availability for the period is listed in the **Avail.** column.

Height	Avail.	Name	$\langle S \rangle$	$\sigma_S$	Bias	MAE	RSME	C.C.
100m	97.8	Obs	5.53	2.95	-	-	-	-
		WRF d02	6.53	3.54	18.1	1.98	2.69	0.72
		WRF d03	6.21	3.48	12.2	1.72	2.34	<b>0.77</b>
		WRF d04	6.18	3.57	11.7	1.77	2.39	<b>0.77</b>
		WRF d05	6.70	3.97	21.1	2.09	2.80	<b>0.77</b>
		EllipSys G02-U	<b>5.48</b>	<b>2.88</b>	<b>-0.9</b>	1.62	2.04	0.76
		EllipSys G03-U	5.44	2.84	-1.7	<b>1.59</b>	<b>2.01</b>	0.76
		EllipSys G03-Q	6.44	3.40	16.5	1.93	2.53	0.73
80m	98.4	Obs	5.43	2.88	-	-	-	-
		WRF d02	6.30	3.35	15.9	1.87	2.54	0.72
		WRF d03	5.98	3.31	10.0	1.64	2.21	<b>0.77</b>
		WRF d04	5.98	3.46	10.1	1.72	2.30	<b>0.77</b>
		WRF d05	6.58	3.92	21.2	2.07	2.76	<b>0.77</b>
		EllipSys G02-U	<b>5.37</b>	<b>2.82</b>	<b>-1.1</b>	1.61	2.02	0.75
		EllipSys G03-U	5.34	2.77	-1.8	<b>1.59</b>	<b>2.00</b>	0.75
		EllipSys G03-Q	6.34	3.37	16.6	1.93	2.55	0.72
60m	98.4	Obs	5.31	2.80	-	-	-	-
		WRF d02	5.96	3.13	12.3	1.73	2.33	0.72
		WRF d03	5.65	3.12	6.5	<b>1.55</b>	2.06	<b>0.77</b>
		WRF d04	5.69	3.31	7.2	1.63	2.16	<b>0.77</b>
		WRF d05	6.38	3.83	20.3	2.00	2.67	<b>0.77</b>
		EllipSys G02-U	<b>5.22</b>	<b>2.73</b>	<b>-1.6</b>	1.58	1.98	0.74
		EllipSys G03-U	5.19	2.69	-2.2	1.56	<b>1.96</b>	0.75
		EllipSys G03-Q	6.18	3.34	16.5	1.91	2.54	0.71
40m	99.1	Obs	5.19	2.75	-	-	-	-
		WRF d02	5.52	2.88	6.3	1.59	2.11	0.73
		WRF d03	<b>5.26</b>	2.90	<b>1.3</b>	<b>1.48</b>	1.93	0.77
		WRF d04	5.34	3.14	2.7	1.54	2.02	0.77
		WRF d05	6.15	3.73	18.4	1.89	2.53	<b>0.78</b>
		EllipSys G02-U	5.07	<b>2.64</b>	-2.4	1.53	1.94	0.74
		EllipSys G03-U	5.05	2.62	-2.7	1.52	<b>1.92</b>	0.75
		EllipSys G03-Q	6.05	3.36	16.5	1.88	2.53	0.71
30m	98.2	Obs	4.97	2.60	-	-	-	-
		WRF d02	5.15	2.69	3.6	1.56	2.02	0.71
		WRF d03	4.92	2.71	-1.1	<b>1.46</b>	1.89	0.75
		WRF d04	<b>5.00</b>	2.97	<b>0.5</b>	1.53	1.98	0.75
		WRF d05	5.87	3.58	18.1	1.86	2.48	<b>0.77</b>
		EllipSys G02-U	4.92	<b>2.56</b>	-1.1	1.48	<b>1.88</b>	0.74
		EllipSys G03-U	4.92	2.55	-1.1	<b>1.46</b>	1.87	0.74
		EllipSys G03-Q	5.90	3.32	18.7	1.90	2.57	0.70
[%]		[ms <sup>-1</sup> ]	[ms <sup>-1</sup> ]	[%]	[ms <sup>-1</sup> ]	[ms <sup>-1</sup> ]		

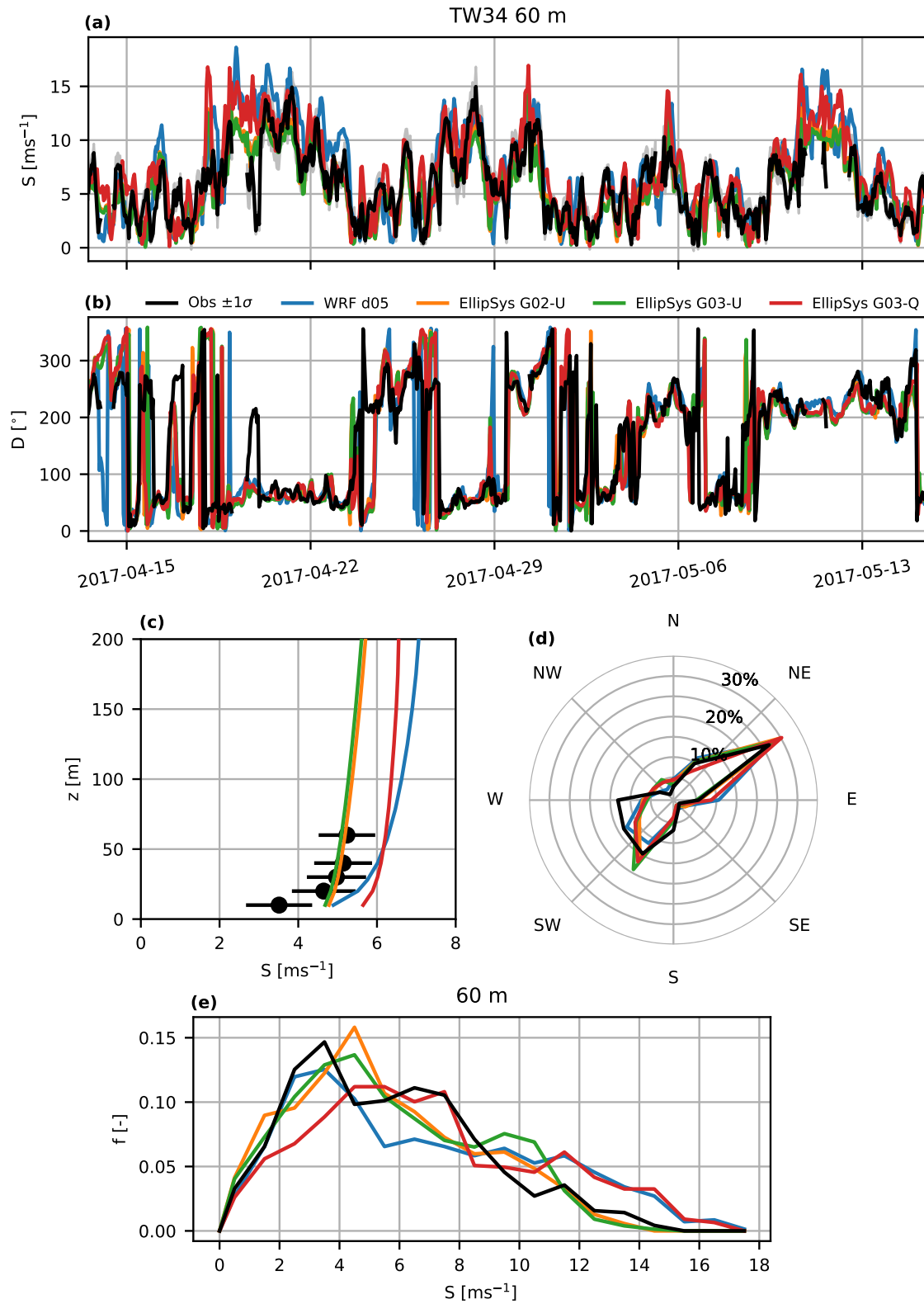


Fig. 5.30 Mast 34: **(a)** Wind speed and **(b)** wind direction at 60 m. For the wind speed the mean ten-minute standard-deviation of wind speed is shown as the gray outline. **(c)** Mean wind speed profiles. The mean ten-minute standard-deviation of wind speed is shown by the error bars. Wind direction **(d)** and wind speed **(e)** distributions at 60 m.

Table 5.12 Wind speed statistics for mast 34: Mean wind speed ( $\langle S \rangle$ ), standard deviation of wind speed ( $\sigma_S$ ), Bias of the mean wind speed (Bias), mean absolute error (MAE), root-mean-square error (RMSE), and Pearson correlation coefficient (C.C.). The best performing model is highlighted in bold text. The availability for the period is listed in the **Avail.** column.

Height	Avail.	Name	$\langle S \rangle$	$\sigma_S$	Bias	MAE	RSME	C.C.
60m	91.4	Obs	5.63	3.08	-	-	-	-
		WRF d02	5.83	3.12	3.4	1.84	2.38	0.71
		WRF d03	<b>5.51</b>	3.05	<b>-2.2</b>	1.68	2.19	<b>0.75</b>
		WRF d04	6.19	3.38	9.9	1.82	2.42	0.74
		WRF d05	6.67	3.98	18.4	2.11	2.83	<b>0.75</b>
		EllipSys G02-U	5.48	<b>3.06</b>	-2.7	<b>1.70</b>	2.17	<b>0.75</b>
		EllipSys G03-U	5.37	2.94	-4.6	1.71	<b>2.16</b>	0.75
		EllipSys G03-Q	6.56	3.57	16.5	2.00	2.68	0.72
40m	91.3	Obs	5.54	3.05	-	-	-	-
		WRF d02	<b>5.38</b>	2.86	<b>-2.9</b>	1.79	2.25	0.71
		WRF d03	5.11	2.83	-7.8	<b>1.67</b>	2.16	0.74
		WRF d04	5.88	3.17	6.2	1.75	2.29	0.73
		WRF d05	6.38	3.82	15.2	2.00	2.67	<b>0.75</b>
		EllipSys G02-U	5.35	<b>2.96</b>	-3.3	1.68	<b>2.14</b>	<b>0.75</b>
		EllipSys G03-U	5.24	2.84	-5.4	1.70	<b>2.14</b>	0.74
		EllipSys G03-Q	6.43	3.51	16.1	1.98	2.65	0.72
30m	91.4	Obs	5.36	2.98	-	-	-	-
		WRF d02	5.06	2.70	-5.6	1.75	2.20	0.71
		WRF d03	4.81	2.68	-10.2	1.66	2.16	0.73
		WRF d04	5.64	3.02	5.2	1.72	2.24	0.73
		WRF d05	6.14	3.69	14.6	1.97	2.61	0.74
		EllipSys G02-U	<b>5.28</b>	<b>2.91</b>	<b>-1.5</b>	<b>1.64</b>	<b>2.09</b>	<b>0.75</b>
		EllipSys G03-U	5.16	2.78	-3.7	1.65	<b>2.09</b>	0.74
		EllipSys G03-Q	6.34	3.47	18.2	1.97	2.65	0.72
20m	90.6	Obs	4.97	2.80	-	-	-	-
		WRF d02	4.63	2.46	-6.8	1.67	2.13	0.69
		WRF d03	4.41	2.45	-11.2	1.61	2.14	0.70
		WRF d04	5.28	<b>2.81</b>	6.3	1.68	2.20	0.70
		WRF d05	5.78	3.48	16.3	1.94	2.58	0.72
		EllipSys G02-U	<b>5.15</b>	2.85	3.7	1.59	2.06	0.74
		EllipSys G03-U	<b>5.04</b>	2.72	<b>1.3</b>	<b>1.58</b>	<b>2.03</b>	0.73
		EllipSys G03-Q	6.16	3.39	24.0	2.02	2.72	0.70
[%]		[ms <sup>-1</sup> ]	[ms <sup>-1</sup> ]	[%]	[ms <sup>-1</sup> ]	[ms <sup>-1</sup> ]		

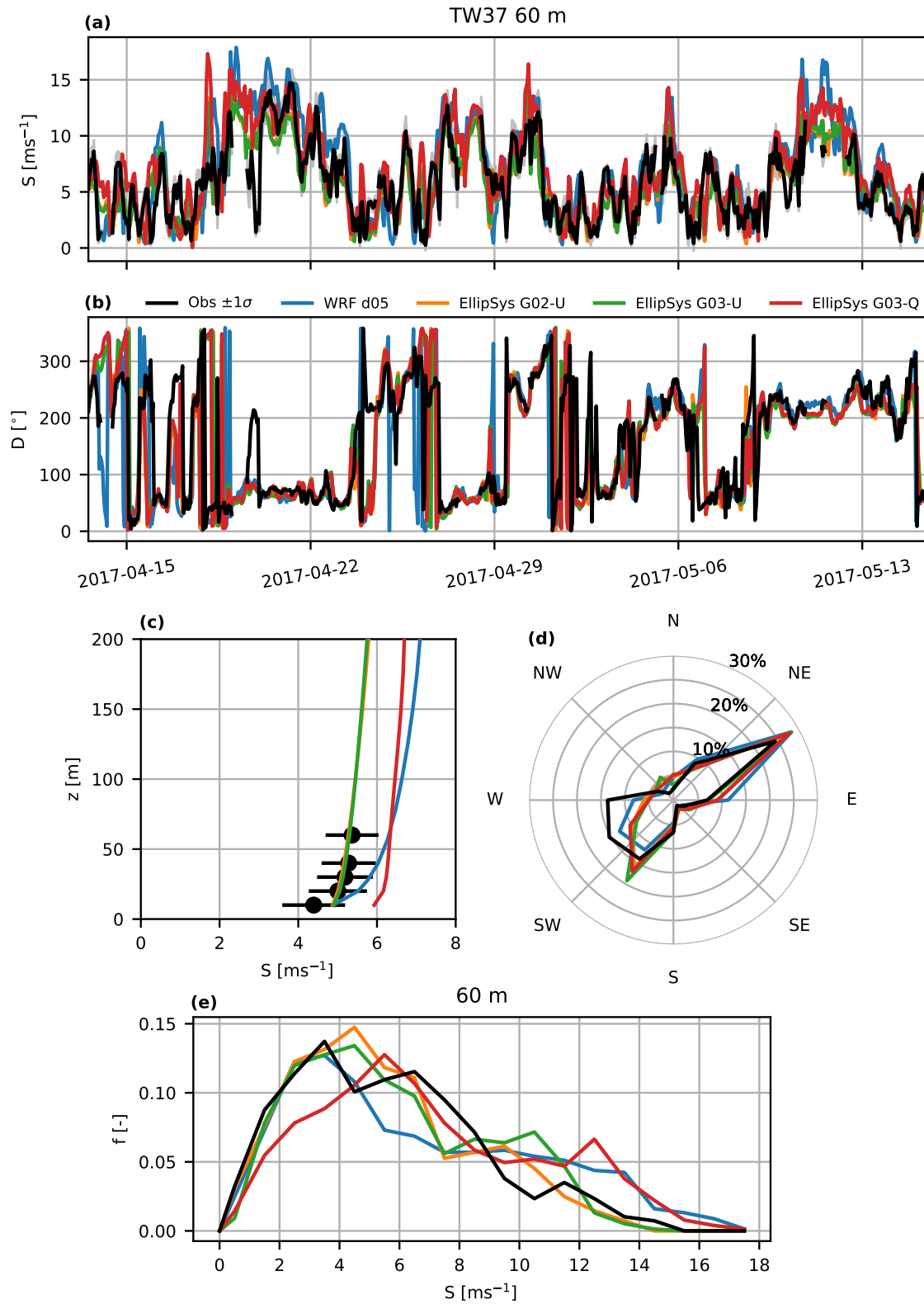


Fig. 5.31 Mast 37: **(a)** Wind speed and **(b)** wind direction at 60 m. For the wind speed the mean ten-minute standard-deviation of wind speed is shown as the gray outline. **(c)** Mean wind speed profiles. The mean ten-minute standard-deviation of wind speed is shown by the error bars. Wind direction **(d)** and wind speed **(e)** distributions at 60 m.

Table 5.13 Wind speed statistics for mast 37: Mean wind speed ( $\langle S \rangle$ ), standard deviation of wind speed ( $\sigma_S$ ), Bias of the mean wind speed (Bias), mean absolute error (MAE), root-mean-square error (RMSE), and Pearson correlation coefficient (C.C.). The best performing model is highlighted in bold text. The availability for the period is listed in the **Avail.** column.

Height	Avail.	Name	$\langle S \rangle$	$\sigma_S$	Bias	MAE	RSME	C.C.
60m	89.2	Obs	5.60	3.12	-	-	-	-
		WRF d02	5.80	<b>3.12</b>	3.6	1.85	2.42	0.70
		WRF d03	5.37	3.03	-4.0	<b>1.67</b>	2.15	0.76
		WRF d04	6.03	3.32	7.7	1.74	2.33	0.75
		WRF d05	6.56	4.01	17.3	2.06	2.76	<b>0.77</b>
		EllipSys G02-U	5.45	2.95	-2.7	1.71	2.17	0.75
		EllipSys G03-U	<b>5.47</b>	2.90	<b>-2.2</b>	1.68	<b>2.13</b>	0.75
		EllipSys G03-Q	6.55	3.52	17.1	2.00	2.68	0.72
40m	88.8	Obs	5.49	3.05	-	-	-	-
		WRF d02	<b>5.35</b>	2.87	<b>-2.5</b>	1.80	2.27	0.71
		WRF d03	4.95	2.78	-9.8	<b>1.66</b>	2.11	0.76
		WRF d04	5.71	<b>3.10</b>	4.0	1.66	2.19	0.75
		WRF d05	6.25	3.84	14.0	1.94	2.58	<b>0.77</b>
		EllipSys G02-U	5.31	2.85	-3.3	1.69	2.14	0.74
		EllipSys G03-U	5.34	2.81	-2.7	<b>1.66</b>	<b>2.10</b>	0.75
		EllipSys G03-Q	6.47	3.51	17.8	2.01	2.68	0.72
30m	89.1	Obs	5.40	3.01	-	-	-	-
		WRF d02	5.06	2.71	-6.3	1.76	2.21	0.71
		WRF d03	4.68	2.65	-13.4	1.68	2.13	0.76
		WRF d04	5.51	<b>2.99</b>	2.0	1.64	2.14	0.75
		WRF d05	6.06	3.77	12.2	1.88	2.51	<b>0.77</b>
		EllipSys G02-U	5.25	2.82	-2.7	1.66	2.10	0.74
		EllipSys G03-U	<b>5.30</b>	2.80	<b>-1.9</b>	<b>1.63</b>	<b>2.06</b>	0.75
		EllipSys G03-Q	6.45	3.55	19.6	2.04	2.72	0.72
20m	88.7	Obs	5.17	2.86	-	-	-	-
		WRF d02	4.65	2.49	-10.1	1.72	2.17	0.70
		WRF d03	4.28	2.43	-17.2	1.67	2.16	0.74
		WRF d04	<b>5.18</b>	<b>2.78</b>	<b>0.1</b>	1.60	2.09	0.73
		WRF d05	5.72	3.58	10.5	1.82	2.41	<b>0.76</b>
		EllipSys G02-U	5.14	2.76	-0.6	1.58	2.02	0.74
		EllipSys G03-U	5.19	2.75	0.4	<b>1.56</b>	<b>1.98</b>	0.75
		EllipSys G03-Q	6.36	3.53	22.9	2.08	2.75	0.72
[%]		[ms <sup>-1</sup> ]	[ms <sup>-1</sup> ]	[%]	[ms <sup>-1</sup> ]	[ms <sup>-1</sup> ]		

effects are felt the least, both the instantaneous and the distribution of wind directions are well captured by the models.

Mast 7 (Fig. 5.23) and 25 (Fig. 5.27), are located deep in the valley (Fig. 5.2). While the general flow direction above the Perdigão complex show a bi-modal nature of wind across the ridges from southwest or northeast. In the valley the flow is remarkably perpendicular to this, showing a turning of the wind along the ridges, mostly in the down-slope direction (southeasterly flow). This turning of the flow is captured by both of the microscale model simulations, most clearly seen for mast 7, but also visible closer to the surface for mast 25. The topography in the WRF domains does not resolve the central valley, so it cannot resolve this phenomena. The mean wind speed is captured well at both mast 07 and 25 by the microscale runs, but a slight overestimation is made by G03-Q at both locations. Only the wind speed at the lowest height (10 m) at both masts is overestimated by both simulations, most likely owing to the unresolved drag from the vegetation.

Mast 10 (Fig. 5.24) are located on the valley-side slope of the northeast ridge close to, but not at, the top. As the dominant wind direction is from north-east, this is a location where the lower part of the mast is in the lee of the ridge top, while the top reaches above the top of the ridge, so effects of recirculating and/or other lee effects is expected at this location. This is indeed reflected in the wind profile, revealing stronger mean shear than most of the other locations. This feature is captured by the microscale model, although they overestimate the mean wind speeds, with G02-U and G03-U again showing the smallest mean errors.

Masts 22 (Fig. 5.26) and 27 (Fig. 5.26) are located near the bottom part of the down-slope reaching into the central valley from the southwest and the northeast ridge respectively. The wind roses reveal that the relative turning (veering) of the wind in the central valley, compared to the wind aloft, is more pronounced closer to the northeast ridge. The observed wind rose at mast 27 show a dominant wind direction from the south and south-southeast, a turning that is only to some degree captured by the microscale model at 60 m. The wind rose at mast 22 is dominated by the northeasterly flow, but also shows that flow from southeast is prevalent. The mean wind speed is overestimated by the microscale models, but both simulations capture much of the reduction in wind speed, relative to WRF wherein the central valley is not resolved.

For wind resource assessment the most relevant measurements for validation are naturally the top of the four masts on the ridges, closest to where the wind turbines would, in all likelihood, be positioned. At the top of the four masts on the ridges, the G02-U microscale simulation show very low mean wind speed biases ( $-1.3\%$  at 100 m for mast 20,  $-0.9\%$  at 100 m for mast 29,  $-2.7\%$  at 60 m for mast 34, and  $-2.7\%$  at 60 m for mast 37), and the same is true for G03-U ( $-3.9\%$  at 100 m for mast 20,  $-1.7\%$  at 100 m for mast 29,  $-4.6\%$

at 60 m for mast 34, and  $-2.2\%$  at 60 m for mast 37). These are the lowest mean biases of any of the models, except for mast 34 where WRF domain d03 has a mean wind speed bias of  $-2.2\%$  at 60 m. G03-Q shows an overestimation of  $\approx 15 - 17\%$  in all four cases, while WRF d04 and d05 overestimate by  $\approx 8 - 12\%$  and  $\approx 17 - 25\%$ . The mean absolute error (MAE), and root-mean-square error (RMSE) (tables 5.5–5.13), are also lowest for G02-U and G03-U at the top of each of the nine masts, except for mast 37, where WRF d02 errors are slightly smaller.

### Spectral properties

As seen in Fig. 5.16 and 5.21, clear differences in the amount of eddy-structures and resulting variance exist between G02-U and G03-Q. This obviously points to different levels of energy at different wave-modes in the flow. To visualize that, the time-spectral density of horizontal wind speed is investigated at 100 m for mast 29 (Fig. 5.32). Each spectra was computed from the 32-day time-signal FFT at the location and averaged in 50 log-spaced (geometric progression) averaging bins. An artificial signal is expected near  $\approx 2$  days due to the chunking of individual simulations. The figure shows a near  $-5/3$  slope of the energy spectral density of the measured wind speed. Curiously, the typical diurnal-cycle signal is strong in the (coarse) WRF model results, but not pronounced in the measurements. Increased density is observed at the high-frequency modes with increasing grid spacing of the WRF domains, pointing to increased effective resolution. The diffusive nature of G02-U and G03-U is revealed from the lower densities across most scales, compared to both the measurements and G03-Q. At the sub 20-minute frequencies (spectral tail) a clear accumulation of variance is seen for G03-Q, much greater than G03-U, with a slope much more flat than the  $-5/3$  slope.

## 5.3 Summary and conclusions

To improve modeling capabilities for wind resource assessment in complex terrain, a mesoscale to microscale coupling methodology for dynamical downscaling was proposed. The methodology, based on the work of Sanz Rodrigo et al. (2017b) and others, and involves coupling of mesoscale NWP models with microscale CFD-type models via momentum and temperature tendencies. Momentum tendencies resulting from a sum of the advection and pressure gradient forces, as well as temperature advection tendencies, are extracted from a single grid column from the Weather Research and Forecasting (WRF) mesoscale model, utilizing a horizontal grid spacing that is coarse enough to ensure that the model cannot resolve local terrain effects resulting from the complex site in question. The resulting tendencies are

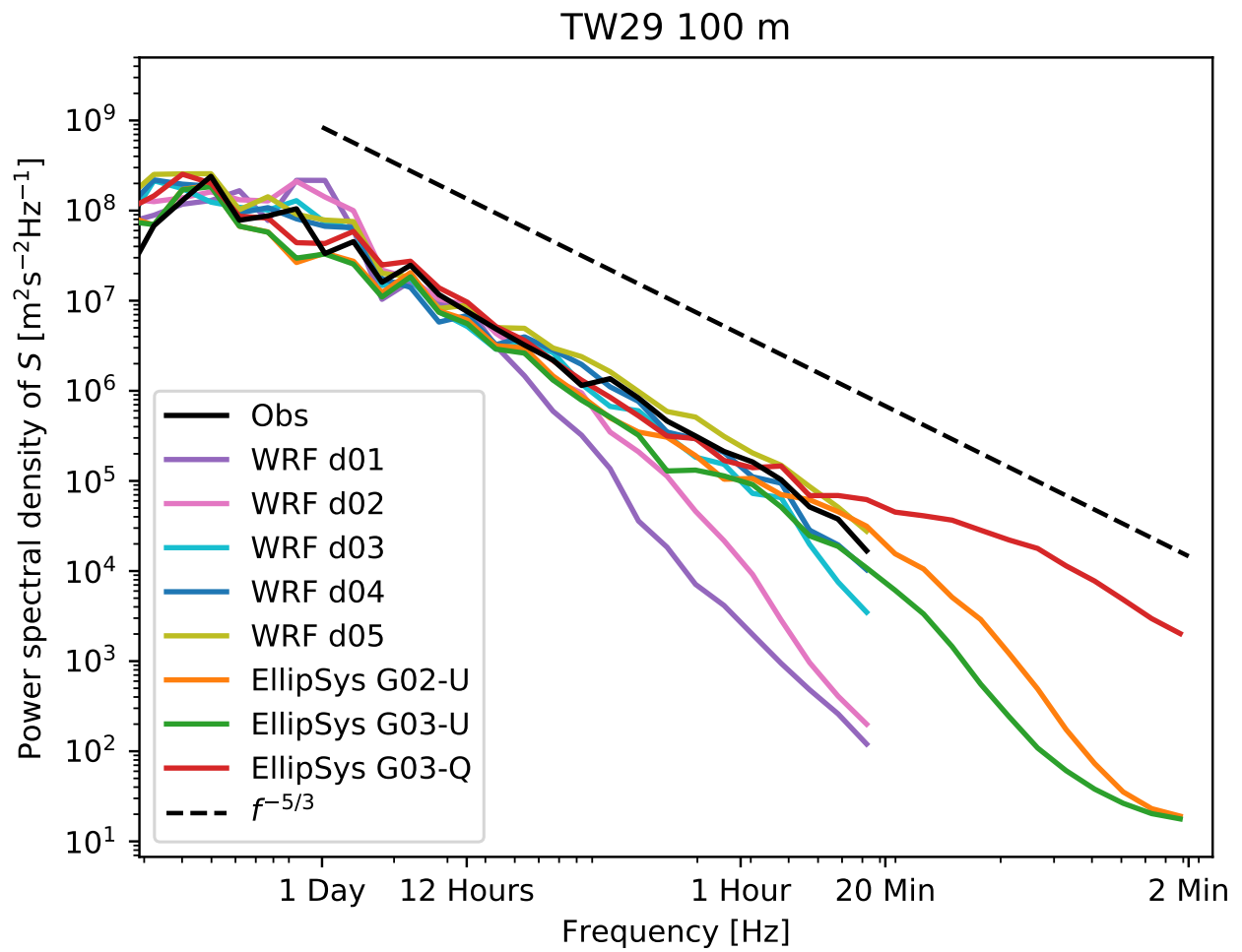


Fig. 5.32 Power spectral density of  $S = \sqrt{U^2 + V^2}$  at 100 m for mast 29.



assumed to carry information about the large-scale (synoptic and mesoscale) variations, i.e. the changing weather patterns, but not the local variations due to orographic forcing. The tendencies are applied as horizontally homogeneous body-forces to the microscale model domain, as height- and time-dependent source terms in the momentum equations. Surface boundary conditions for temperature were extracted from the mesoscale model by extrapolating the varying 2-m temperature to the microscale model surface. To accommodate the use of forcing by body-forces, as opposed to the more common approach of forcing via LBCs, the microscale lateral boundaries used periodic conditions, allowing the flow to recirculate. The terrain in the microscale domain was thus smoothed along the edges towards a singular smooth elevation in order to avoid discontinuities near the edges.

The methodology was validated at the Perdigão site using measurements from the Perdigão field campaign taken during the new European wind atlas (NEWA) project in the spring months of 2017. The measurements used for this study included vertical radial wind speed scans taken with LRWS lidars, and wind speed and direction measured from nine tall meteorological masts placed around the site, reaching from 60 to 100 m into the ABL. The microscale model validation focused on a 32-day period from 13 April 13 to 15 May 2017, characterized by mostly fair weather, but also periods with stronger synoptic forcing.

It is an open question what is the best way to obtain the most appropriate mesoscale tendencies to force the microscale model. The two main questions, that remains unanswered are:

- Based on physical characteristics of the site, What is the most appropriate grid spacing to use for the mesoscale model?
- How should the mesoscale tendencies be filtered to achieve the most appropriate, noise-free signals?

In this study, the answer to the first questions was to use the most fine-scaled domain available, that still does not resolve the characteristic scales of the topography surrounding the site. For Perdigão, this meant using the WRF domain with a horizontal grid spacing of 9 km to generate the microscale model input. At that spacing, one mesoscale grid cell covers most of the footprint of the Perdigão complex, including the two ridges, the central valley, and much of the surrounding area. As a result, the orographic forcing from the Perdigão site does not propagate into the tendencies, except for the general sloping of the terrain. The Perdigão site stands relatively separate from other major mountain-ranges, making the task of choosing the appropriate mesoscale grid spacing easier. Generalizing the methodology arbitrary complex

sites may be more challenging when the site in question is connected to topography made up of a larger range of characteristic scales. The answer to the second question above, in this study, has been to simply use (instantaneous) hourly averaged values, without any spatial averaging involved.

The sensitivities of the mesoscale tendencies to the mesoscale model configuration in complex terrain are largely unknown. Olsen et al. (2018) showed only small sensitivities to planetary boundary layer (PBL) and surface layer (SL) scheme in simple terrain without further coupling, but further analysis of the impact of different PBL schemes, SL schemes, and land surface models, is needed.

The tendency-driven microscale simulations were shown to capture the general flow patterns at the site, but with a clear sensitivity to the grid resolution. The microscale model is operated at the scales within the *terra incognita*, which means the model permits development of energetic ABL eddies, especially during CBL conditions. This can be a problem because the RANS assumption of scale-separation may be violated and a grid-dependency of the solution can occur. To study the influence of effective flow-resolution, the first-order accurate upwind (UDS) discretization scheme was compared to the third-order accurate QUICK scheme. The UDS scheme has many undesirable properties: it is dampening and much less numerically accurate than typical methods used, but as a result it has a decreased effective flow-resolution, i.e. it may maintain scale separation at finer grid resolution than high-order schemes does, reducing eddy formation. As expected, significant differences were observed from using the two numerical methods. The simulations using the third-order accurate scheme was more prone to grid-dependent flow structures, while the first-order scheme produced less variance and generally lower wind speeds, but resolved less eddy structures, even when run at finer grid spacing than the high-order scheme (80 m UDS vs 120 m QUICK, Fig. 5.16).

With the dependencies of the grid and numerical methods in mind, three different microscale setups were chosen and evaluated qualitatively and quantitatively for a longer period of 32 days. One setup used a grid of  $80 \times 80$  m grid spacing and the UDS scheme (G02-U), one used  $120 \times 120$  m and UDS (G03-U), and one a grid of  $120 \times 120$  m grid spacing and the QUICK scheme (G03-Q). Results for G02-U and G03-U were very similar, while larger differences were seen for G03-Q compared to the two others.

Qualitatively, the microscale model captured many of the features that characterize the flow around the Perdigão site, including some of the wave-like features observed in the nocturnal low level jets (LLJ), such as the lee-side standing wave behind the southwest ridge during northeasterly flow conditions. However, the fine details of the LLJ were not

quite captured, probably in large part due to how well, or poorly, the LLJ is resolved in the mesoscale tendencies. Eddy-structures were observed in all three simulations, but more variance and a stronger tendency to develop eddy-structures was seen for G03-Q. Quantitatively, G02-U and G03-U was shown to capture the flow around Perdigão quite accurately both at the ridge tops and in the central valley. For the four masts on the ridge tops (masts 20, 29, 34, 37), the mean wind speed errors of G02-U for the 32 days were less than 3% and root-mean-square errors were low compared to the WRF domains, and G03-Q. In the central valley of the site, the mean flow characteristics were also well captured by G02-U, including the turning of the wind towards southeasterly and northwesterly flow (along the ridges). G03-Q also captured the valley flow, but showed larger mean wind speeds for all of the masts, and at the ridge tops the overestimation of the mean wind speed was larger than the mean error of the mesoscale domains and the two other microscale simulations.

During situations of rapid surface cooling and weak winds, runaway cooling, where the heat flux and friction velocity dropped to near-zero, was observed causing a detachment of the flow near surface and the upper air above. Lower limits were put on the turbulent kinetic energy and its dissipation to reduce this phenomena, but limiting the friction velocity may prove useful as well, similar to e.g. some SL schemes in WRF (Jiménez and Dudhia, 2012).

The coupling methodology has previously been shown to work well in simple terrain (Olsen et al., 2018; Sanz Rodrigo et al., 2017b). This study shows promising results, that indicate that it could work well in complex terrain as well. The microscale model captures the slowly varying (weather) patterns fed to it by the mesoscale tendencies, while also adding local orographic and surface effects. As such, the mesoscale model tendencies seems to provide the appropriate large-scale forcing. However, the tendencies used for coupling are difficult to validate, especially in complex terrain. Therefore, it is difficult to judge whether they represent actual physical tendencies in the atmosphere. Validation of the coupling technique, and related sensitivity studies, must be done indirectly by, for example, studying the final microscale model results.

One major disadvantage of the coupling methodology, is that a large jump in spatial scales is needed. In this study, the 9-km mesoscale domain is coupled directly to microscale grids with a grid spacing of order  $\approx 100$  m; an effective grid-refinement ratio of around 100. This ratio is much greater than what is typically used with LBCs, where small grid-refinement ratios are desirable. It is also much greater than the ratio of 3 or 5 recommended when e.g. running WRF Skamarock et al. (2008). It is likely that this spatial jump can result in

under-resolving important flow features taking place in-between the resolved scales of the WRF domain and the microscale domain.

Using dynamical downscaling for wind resource assessment is computationally expensive, so one positive side-effect of the needed scale-jump is the reduced cost of computations. If the mesoscale share of dynamical downscaling can be limited to scales of order 10 km, rather than order 1 km, a significant reduction in computations is achieved. In fact, it may not be required to use limited area models (LAMs) at all, instead tendencies and surface temperatures from global circulation models (GCM) could be used, as they are already operated at the mesoscales, and higher resolution is gradually achieved. However, these types of fields are typically not available from reanalysis datasets.

In the microscale domain, the methodology relies on strong temperature nudging towards the horizontally homogeneous mesoscale temperature of the grid column covering the site. The influence of nudging is not fully understood, especially not when it comes to the impact on the flow in complex terrain, where differential heating and advection are prevalent. Because the temperature in the microscale model is otherwise limited to the heat fluxes from the surface and temperature advection tendencies from the mesoscale model, to evolve the state of the temperature nudging is important to account for many physical phenomena that are otherwise not captured by the microscale model. Additionally, the nudging helps to keep microscale temperature in line with the mesoscale grid-column, reducing problems that could arise from adding temperature advection tendencies that are out-of-sync with the microscale model state. On the other hand, the strong nudging also limits the degrees of freedom of the microscale model, potentially suppressing the development of desirable/physical states. Ultimately, a better understanding of the relative magnitudes and interactions of temperature advection, temperature nudging, and heat-fluxes throughout the microscale domain, and during the diurnal-cycle, is needed.

A homogeneous surface roughness of  $\approx 5$  cm was used in the microscale simulations. It was derived via the USGS vegetation table from the CORINE-derived land-use class in the WRF grid cell at the site. Up-scaling of the fine-scale CORINE land use classification was done via the dominant class of the individual CORINE cells inside the larger WRF cell. There are many indications that 5 cm is a vast underestimation of the true frictions of the terrain in the area, including LIDAR scans of the vegetation (not shown), and private communication. The CORINE land use class in the grid cell corresponds to “Mixed Shrubland/Grassland”, but much of the area is covered by Eucalyptus and Pine trees. Hence, it is very likely that a major source of the overestimation of the mean wind speed seen for G03-Q is caused by the

low surface roughness. Likewise, the skillfulness observed for G02-U and G03-U may be due to a canceling-of-errors scenario, where errors due to low surface roughness are canceled by errors caused by the diffusive discretization scheme. In addition, large parts of the Perdigão site are forested, which is ignored in this study. However, treating the forest via adjustment of the surface roughness, using displacement heights, or via adding roughness elements to the domain, may improve upon the results, near the surface and in the valley in the particular. Further analysis of the impact of the surface roughness is needed.

The resolution of the microscale domains is high-enough that the largest turbulent eddies, of typical length scale  $\approx 1$  km, are well within the resolved scales, permitting the development of eddy structures in the modelled ABL. Atmospheric modelling at these scales has been discussed by Wyngaard (2004), Hong and Dudhia (2012), Zhou et al. (2014), and others, and remains a range of scales where the RANS assumption of scale separation comes into question, and hence whether the risk of “double-counting” turbulent-effects should be considered. However, (Arnold et al., 2012; Hong and Dudhia, 2012) suggests that the double-counting problem may be negligible because both the explicit and modelled turbulence feed on the same available energy. If the modelled turbulence is stronger, i.e. mixes more/earlier, it could suppress explicit mixing. At this point it is not clear whether the combined dynamical and parameterized turbulence effects are correct in the *terra incognita*, so further research is needed to quantify this. The added eddy viscosity resulting from the turbulence closure cause additional diffusion that helps to suppress small scale (turbulent) structures from developing, but larger eddy structures did form in the microscale solutions, especially when buoyant forcing favoured vertical motion. Grid-dependent solutions are obviously undesirable, but it remains to be determined how much, if at all, it affects the long-term wind climate. If, on the long-term the grid-dependant solutions converges to correct statistics, it may still be useful for resource assessment.

The large differences in the simulations using the G03-U and G03-Q configurations, which differed only by discretization scheme, must be caused by differences in: numerical diffusion or interactions between explicit and modelled turbulence, or (most likely) a combination of the two. This should also be investigated further.

Ultimately, using a first-order accurate discretization of the governing equations is undesirable due to its low accuracy and non-parameterized diffusiveness across scales. Instead, if double-counting of turbulence is deemed a problem, diffusiveness could be increased explicitly via increased eddy viscosity, or other similar ways to lower the effective flow-resolution, while maintaining a high resolution of the topography. Alternatively, novel approaches that circumvent the potential double-counting issues could be implemented. For example hybrid

methodologies that filter the governing equations by turbulence-content instead of averaging across all turbulent scales. One example of such a methodology is the partially-averaged Navier-Stokes equations (Girimaji and Abdol-Hamid, 2005), which defaults to using the turbulence closure model when the characteristic turbulent length scales are smaller than the implicit grid-scale filter, and that gradually reduces the influence of the turbulence closure, moving towards a DNS solution, when the turbulent length scales are greater than the grid-scale filter.

All in all, the study shows promising results for flow modeling around complex sites by coupling CFD-type microscale models with mesoscale tendencies. Future studies can, hopefully, generalize the methodology further, study the sensitivities, and expand the validation to many other complex sites with different characteristics. For wind resource assessment, another aspect to study is how to best utilize dynamical model-chains, such as this, to, in the most computationally inexpensive way, capture the long-term, 5+ years, wind climate at the site.



# Chapter 6

## Conclusions

### 6.1 Summary

This thesis presents the development and results of a technique for meso- to microscale model coupling via momentum and temperature tendencies; a largely untested way of coupling atmospheric models for downscaling wind. It presents sensitivity studies and validation against observed tall mast measurements from both simple and complex sites, which cover long-enough periods to be relevant for wind climate estimation applications.

The coupling technique, based on ideas from e.g. Bosveld et al. (2014) and Sanz Rodrigo et al. (2017b), adds momentum and temperature tendencies terms extracted from a mesoscale model as source terms in the governing equations to force the microscale model, rather than the common approach based on lateral boundary conditions. The tendency terms correspond to the large-scale pressure and advective tendencies to the flow at the site from scales larger than the characteristic scales of the microscale model domain. The *Weather Research and Forecasting* (WRF) and the *EllipSys3D* RANS-type CFD model with a  $k-\varepsilon$  two-equation turbulence closure is used. EllipSys3D is modified to include buoyancy and Coriolis forces and was the starting point for the investigation of model coupling for downscaling of the wind.

The meso-microscale coupling methodology was first studied in simple terrain at the Cabauw and FINO3 meteorological masts, which are located offshore and inland, respectively. These sites of relative simple and homogeneous terrain allowed for the use of a Single-Column Model version of the microscale model at a fraction of the computational costs of the 3D model. This study showed that a combination of the time- and height-varying sum of the pressure-gradient force and advection tendencies as a source for the momentum equation and advective tendencies for temperature as source for the temperature equation gave the most accurate long-term statistics. The impact of including the temperature advection was



small in comparison to that of the momentum advection. Similar findings were shown in Sanz Rodrigo et al. (2017b) for the ability of a similar SCM to capture the flow for a real single day LLJ test case.

The study at simple sites included an investigation of the impact of using different planetary boundary layer and surface layer schemes in the WRF model used to generate the tendencies for the microscale model. The results showed that although the surface response was statistically similar in the different SCM results, the long-term wind statistics of the SCM largely followed the results of the mesoscale simulation used to generate forcing.

A separate aim of the study in simple terrain was to study the ability of the  $k-\varepsilon$  turbulence closure used in the microscale model to work well in a range of different weather conditions. Generally the SCM showed comparable results to those of the different WRF simulations, but the results from the microscale model had a tendency to exaggerate the surface cooling and overestimate the wind shear at turbine heights. This indicates that further improvements can be made to the surface boundary condition methodology and the to the treatment of unstable stability conditions in the turbulence closure itself.

The encouraging results seen for the simple terrain sites led to applying the coupling methodology at a site with more complex terrain to explore the feasibility of using the technique for downscaling in a challenging site with highly heterogeneous terrain characteristics. The Perdigão double hill experiment site was chosen, which was the subject of an intensive measurement campaign during the spring and summer months of 2017. For that case, the tendencies extracted from the WRF model were used to force the 3D microscale model.

The computational grids used for the microscale model at Perdigão were of high enough resolution to permit the formation of eddy structures of turbulent nature to form in the flow solution, indicating a potential violation of the RANS assumption of scale-separation. Due to the possibility of double-counting the influence of turbulence, special consideration was given to the study of the influence of grid-spacing and the numerical discretisations used, the latter used as a switch to decrease the effective resolution of the flow. The diffusiveness of low-order advection schemes suppresses more of the small-scale features from developing in the flow than high-order methods. Using numerical discretisation to increase diffusion is a crude way of suppressing turbulence. It is perhaps more appropriate to increase diffusion by increasing the eddy viscosity via the turbulence closure.

The study showed that the solutions are dependant on both grid spacing and numerical methods, showing more small-scale (turbulent) fluctuations in the fine grid and with a high-order advection scheme. These findings motivated the use of three different microscale setups for an extensive 32-day study period. The first setup (G02-U) used 80 m grid spacing near the area of interest and the upwind (first-order accurate) discretisation scheme and the second

setup (G03-U) used 120 m grid spacing and the same scheme, the last setup (G03-Q) used 120 m grid spacing and the QUICK (third-order accurate) discretisation scheme. Results for G02-U and G03-U did differ, but the largest differences were seen between the those two and G03-Q showing big variations at different times during the simulations. Three snap-shots of the long simulation highlighted some key differences of the G02-U and G03-Q solutions and how they compare to the (LIDAR) observed flow pattern around the site. A low level jet formed on many nights, and regularly this LLJ developed into a wave on the lee side of the southwest ridge. Both the G02-U and G03-Q setups captured some characteristics of this LLJ wave, but the modeled LLJ was too deep, owing most likely to limitations imposed by the structure of the mesoscale tendencies. The results from the WRF model simulations failed to develop these wave structures, owing probably to the coarse grid spacing.

Generally for the 32-day period, the G03-U, and especially the G02-U simulation showed very accurate results at all nine of the meteorological masts at the Perdigão site, compared to both a naive WRF model simulation with an innermost grid of 333 m grid spacing and the G03-Q simulation. The mean wind speed biases for G02-U were less than 3% for the top anemometer height of the four masts located on one of the two ridge tops at the site, while it was less than 5% for G03-U. The G03-Q setup showed an overestimation of 15–17% and the results from the 1 km and 333 m WRF domains showed overestimation of the wind speed by 8–12% and 17–25%, respectively. Likewise, the results from the G02-U and G03-U setups had the smallest RMSEs at the four masts.

Strong temperature nudging was used in both the simple and complex terrain cases. The vertical temperature profile of the microscale model was nudged towards the vertical temperature profile of WRF at the corresponding time. The motivation for using this technique was to capture effects in the WRF model, e.g. radiative cooling during the night and maintenance of the capping inversion, that microscale model can not capture by itself. Furthermore, it was presumed that inconsistencies between the microscale and WRF models can cause issues when both nudging and temperature advection are included. It is largely unknown how these three temperature components interact, requiring further analysis.

In summary, the coupling methodology of using momentum and temperature tendencies to drive a microscale model for downscaling the wind in complex terrain shows encouraging results. Tendencies extracted from a WRF domain, using 9 km grid spacing, were shown to be adequate forcing for the microscale model to achieve a large improvement of estimated wind statistics in complex terrain. This is promising results that may lead to an accurate model-chain for statistical-dynamical downscaling of wind climates, and other purposes in complex terrain. Because the mesoscale domain can be relatively coarse, the method may also be computationally cheaper than methods that rely on LBCs and a small grid-refinement

ratio. However, further studies are needed to investigate remaining uncertainties, and how the method may be generalized to many different sites.

## 6.2 Implications and future perspectives

One of the major challenges in determining site conditions for wind energy applications is developing computationally downscaling methodologies that are computationally feasible and work well in complex terrain. The coupling methodology studied in this thesis illustrates a possible path towards this end.

The traditional approach of coupling meso- and microscale models via LBCs suffers from several issues that the use of tendency terms may resolve. There are inconsistencies between the two coupled models, related to both the grids and the formulation: inconsistencies of the resolved topography and surface friction, incompressibility versus compressibility, dry vs. cloud-permitting formulation, treatment of the surface layer, etc. These contribute to an adjusted flow in the inflow region near the boundary. These inconsistencies require the addition of a relatively large fetch zone around the area of interest. Using source terms instead eliminates that problem, although it requires using periodic boundary conditions and a smoothed-out boundary region. It remains to be shown how the two coupling methodologies compare, this issue should be further investigated, perhaps with an intercomparison of the various current methods.

The issue of model coupling across the *gray scales*, from *mesoscale* flow with no resolved turbulence to *microscale* flow at turbulence-resolving scales, should be better handled by using tendencies. The tendencies approach avoids the issues related to feeding in a smooth inflow with no turbulent structures inside, requiring perturbation techniques or similar techniques to spin up the correct turbulent structures. Forcing the flow via source terms and having cyclic boundaries should cause a more rapid development of, and better maintained, turbulent structures.

Besides the possible benefits of coupling via tendencies from a scientific standpoint, there are additional technical benefits of using source terms. For many CFD modelers, a background pressure gradient is already used to force the flow for idealized simulations, so adaption to implementing varying tendencies may be simpler than implementing appropriate LBCs. The coupling methodology used in this study for RANS-type microscale models, should also work well for LES, or even DNS, simulations.

Further validation of the coupling methodology should be carried out with the focus on several different aspects. For the methodology to be widely useful, some degree of generality of the methodology should exist, so it should be investigated if the method be generalized to multiple complex sites, by e.g. determining a universal rule/strategy for generating tendencies from the mesoscale model.

Another concern about the methodology that should be further studied is the need for a relatively large jump in scales from the parent, mesoscale domain, to the microscale domain, because of the desire to avoid resolving microscale effects in the parent domain. It may become an issue for particular sites where phenomena at the intermediate scales are important for the flow at the site.

Another key aspect to study is how the potential double-counting of turbulence at the gray scales impact the results, and how it can be avoided without using LES and the limitations that come with that. For example, it may be that using hybrid filtering techniques, like *Partially-Averaged Navier-Stokes*, provide the necessary balance between using a turbulence closure, and sometimes explicitly solving turbulence.

There is also a need for further improvement of the use of surface boundary conditions, including the development of techniques to reduce runaway cooling and surface detachment effects, and the use of more detailed heterogeneous surface roughness in the microscale model.

For the Perdigão case specially, to improve modelling of the flow additional surface friction and forest parameterization in the microscale model should be investigated.

While the methodology showed promising results for dynamical downscaling in a (single) complex terrain case for a one-month period, it remains to be shown the relative benefit of using the model-chain for long-term wind climate estimation. Future studies focusing on this particular problem would be highly interesting. Especially, if the studies focus on the comparison to the state-of-the-art methodologies to highlight benefits and flaws. This should also include a study of the relative feasibility of using statistical-dynamical downscaling techniques, e.g. Rife et al. (2013), to reduce the computational costs, and its impact on the predicted wind climate.



# Appendix A

## Additional resources for thesis chapters

### A.1 Chapter 4

#### A.1.1 WRF namelist.input sample

Listing A.1 namelist.input sample (one chunk) of WRF simulations used in Chapter 4.

```
&time_control
run_days              = 3
run_hours             = 0
run_minutes           = 0
run_seconds           = 0
start_year            = 2006, 2006,
start_month           = 10, 10,
start_day             = 04, 04,
start_hour            = 12, 12,
start_minute          = 00, 00,
start_second          = 00, 00,
end_year              = 2006, 2006,
end_month             = 10, 10,
end_day              = 07, 07,
end_hour              = 12, 12,
end_minute            = 00, 00,
end_second            = 00, 00,
interval_seconds      = 21600
input_from_file       = .true., .true.,
history_interval      = 10, 10
frames_per_outfile    = 6, 6
restart               = .false.
restart_interval       = 5000
io_form_history        = 2
io_form_restart       = 2
io_form_input         = 2
io_form_boundary       = 2
debug_level           = 0
iofields_filename     = 'WAfields.txt', \
```

```

                                'WAfields.txt', \
                                'WAfields.txt', \
                                'WAfields.txt', \
                                'WAfields.txt'

ignore_iofields_warning      = .true.
/

&domains
time_step                   = 90
time_step_fract_num         = 0
time_step_fract_den         = 22
use_adaptive_time_step      = .true.
step_to_output_time         = .true.
target_cfl                   = 1.15, 1.15,
target_hcfl                  = 0.85, 0.85,
max_step_increase_pct       = 5, 51,
starting_time_step           = 54, -1,
max_time_step                = 108, -1,
min_time_step                = 27, -1,
adaptation_domain           = 1
max_dom                      = 2
e_we                        = 124, 142
e_sn                        = 100, 142
e_vert                      = 61, 61
p_top_requested              = 5000
num_metgrid_levels           = 33
num_metgrid_soil_levels      = 4
dx                          = 27000, 9000
dy                          = 27000, 9000
grid_id                     = 1, 2,
parent_id                   = 0, 1,
i_parent_start               = 1, 42,
j_parent_start               = 1, 33,
parent_grid_ratio             = 1, 3,
parent_time_step_ratio       = 1, 3,
feedback                    = 0
smooth_option                = 0
eta_levels                   = 1.000000, 0.998600, 0.996000, 0.994000, \
                                0.992000, 0.990000, 0.987592, 0.984486, \
                                0.980977, 0.977016, 0.972544, 0.967500, \
                                0.961813, 0.955403, 0.948185, 0.940062, \
                                0.930929, 0.920670, 0.909158, 0.896257, \
                                0.881820, 0.859633, 0.830162, 0.794019, \
                                0.751945, 0.704330, 0.659043, 0.615990, \
                                0.575078, 0.536219, 0.499329, 0.464324, \
                                0.431126, 0.399657, 0.369845, 0.341616, \
                                0.314904, 0.289641, 0.265763, 0.243210, \
                                0.221922, 0.201841, 0.182641, 0.164410, \
                                0.148206, 0.132526, 0.117709, 0.104002, \
                                0.091398, 0.079808, 0.069150, 0.059351, \
                                0.050340, 0.042054, 0.034434, 0.027428, \
                                0.020986, 0.015062, 0.009615, 0.004606, \
                                0.000000
/

```

```

&physics
mp_physics              = 3,      3,
ra_lw_physics           = 1,      1,
ra_sw_physics           = 1,      1,
radt                    = 30,     30,
sf_sfclay_physics       = 1,      1,
sf_surface_physics      = 2,      2,
bl_pbl_physics          = 1,      1,
bldt                    = 0,      0,
cu_physics              = 1,      1,
cudt                    = 5,      5,
isfflx                  = 1,
ifsnow                  = 1,
icloud                  = 1,
surface_input_source    = 3,
num_soil_layers         = 4,
num_land_cat            = 28,
sf_urban_physics        = 0,      0,
bl_mynn_edmf            = 0,      0,
bl_mynn_edmf_mom        = 0,      0,
bl_mynn_edmf_tke        = 0,      0,
/

&dynamics
w_damping               = 0
diff_opt                = 1,      1,
km_opt                  = 4,      4,
diff_6th_opt            = 0,      0,
diff_6th_factor         = 0.12,   0.12,
base_temp               = 290.0
damp_opt                = 0
zdamp                  = 5000.0, 5000.0,
dampcoef                = 0.2,    0.2,
khdif                   = 0,      0,
kvdif                   = 0,      0,
non_hydrostatic         = .true., .true.,
moist_adv_opt           = 1,      1,
scalar_adv_opt          = 1,      1,
/

&bdy_control
spec_bdy_width          = 5
spec_zone               = 1
relax_zone              = 4
specified                = .true., .false.,
nested                  = .false., .true.,
/

```

## A.1.2 EllipSys1D sample input file (input.dat)

Listing A.2 EllipSys1D sample input file (input.dat)

```

# -----
#   project grid

```



```

# -----
#           solver parameters
# -----
mstep 187200
subiterations 8 8
reslim 1.d-4
# -----
#           run parameters
# -----
transient  true 1.0
# -----
#           relaxation parameters
# -----
relaxu .7d0
# -----
#           fluid parameters
# -----
density  1.225d0
viscosity 1.78406d-5
# -----
#           farfield values
# -----
ufarfield  9.5
vfarfield  0.0
func-const teini 0.1
func-const edini 0.003d0
field u value 9.5
field v value 0.0
field w value 0.0
field tke value teini
field dtke value edini
# -----
#           temperature
# -----
gravitation -9.81
temperature air
prandtl 0.74 0.74
prandtl_var
inlet temp 100 151 file 1 Twall.dat
field temp value 289+(z+0.1)*3.5d-3
field temp min 289+(4000+0.1)*3.5d-3
field temp file 2 Tprof.dat
temp_inlet 276.7810552465451
temp_wall 276.7810552465451
temp_relaxation
temp_farfield 276.7810552465451
relaxtemp 0.6
# -----
#           Turbulence model
# -----
turbulence  kepsilon
ke_version  rough-abl
loglaw true
roughness 0.05128924344121879
lmaxmy 0.075

```

```

ambient_ke 1.0d-4 7.208d-8
kappa 0.4
cmu 0.03
ce1 1.52
ce2 1.833
pred_ke 2.95131
prtke_ke 2.95131
relaxturb 6.0d-1
te_inlet 1.0d-1
ed_inlet 0.003d0
te_farfield 1.0d-1
ed_farfield 0.003d0
turb_cori true 0.00011481912944662681
field u file 3 Uprof.dat
field v file 4 Vprof.dat

```

## A.2 Chapter 5

### A.2.1 WRF namelist.input sample

Listing A.3 namelist.input sample (one chunk) of WRF simulations used in Chapter 5.

```

&time_control
run_days = 3
run_hours = 0
run_minutes = 0
run_seconds = 0
start_year = 2017, 2017, 2017, 2017, 2017,
start_month = 04, 04, 04, 04, 04,
start_day = 12, 12, 12, 12, 12,
start_hour = 12, 12, 12, 12, 12,
start_minute = 00, 00, 00, 00, 00,
start_second = 00, 00, 00, 00, 00,
end_year = 2017, 2017, 2017, 2017, 2017,
end_month = 04, 04, 04, 04, 04,
end_day = 15, 15, 15, 15, 15,
end_hour = 12, 12, 12, 12, 12,
end_minute = 00, 00, 00, 00, 00,
end_second = 00, 00, 00, 00, 00,
interval_seconds = 21600
input_from_file = .true., .true., .true., .true., .true.
history_interval = 10, 10, 10, 10, 10,
frames_per_outfile = 6, 6, 6, 6, 6,
restart = .false.
restart_interval = 5000
io_form_history = 2
io_form_restart = 2
io_form_input = 2
io_form_boundary = 2
debug_level = 0
iofields_filename = 'WAfields.txt', 'WAfields.txt', \
                    'WAfields.txt', 'WAfields.txt', \
                    'WAfields.txt'

```

```

ignore_iofields_warning      = .true.
/

&domains
time_step                   = 90
time_step_fract_num         = 0
time_step_fract_den         = 22
use_adaptive_time_step      = .true.
step_to_output_time         = .true.
target_cfl                  = 1.15,    1.15,    1.15,    1.15,    1.15
target_hcfl                 = 0.85,    0.85,    0.85,    0.85,    0.85
max_step_increase_pct       = 5,       51,     51,     51,     51
starting_time_step          = 54,      -1,     -1,     -1,     -1
max_time_step               = 108,     -1,     -1,     -1,     -1
min_time_step               = 27,      -1,     -1,     -1,     -1
adaptation_domain           = 1
max_dom                     = 5
e_we                        = 100,    100,    100,    100,    100,
e_sn                        = 100,    100,    100,    100,    100,
e_vert                      = 61,     61,     61,     61,     61,
p_top_requested             = 5000
num_metgrid_levels          = 33
num_metgrid_soil_levels     = 4
dx                          = 27000.0000, 9000.0000, 3000.0000, \
                             1000.0000, 333.3333
dy                          = 27000.0000, 9000.0000, 3000.0000, \
                             1000.0000, 333.3333

grid_id                     = 1,       2,       3,       4,       5
parent_id                   = 0,       1,       2,       3,       4
i_parent_start              = 1,      34,      34,      34,      34,
j_parent_start              = 1,      34,      34,      34,      34,
parent_grid_ratio            = 1,       3,       3,       3,       3
parent_time_step_ratio      = 1,       3,       3,       3,       3
feedback                    = 0
smooth_option               = 0
eta_levels                  = 1.000000, 0.998600, 0.996000, 0.994000, \
                             0.992000, 0.990000, 0.987592, 0.984486, \
                             0.980977, 0.977016, 0.972544, 0.967500, \
                             0.961813, 0.955403, 0.948185, 0.940062, \
                             0.930929, 0.920670, 0.909158, 0.896257, \
                             0.881820, 0.859633, 0.830162, 0.794019, \
                             0.751945, 0.704330, 0.659043, 0.615990, \
                             0.575078, 0.536219, 0.499329, 0.464324, \
                             0.431126, 0.399657, 0.369845, 0.341616, \
                             0.314904, 0.289641, 0.265763, 0.243210, \
                             0.221922, 0.201841, 0.182641, 0.164410, \
                             0.148206, 0.132526, 0.117709, 0.104002, \
                             0.091398, 0.079808, 0.069150, 0.059351, \
                             0.050340, 0.042054, 0.034434, 0.027428, \
                             0.020986, 0.015062, 0.009615, 0.004606, \
                             0.000000
/

&physics
mp_physics                  = 3,       3,       3,       3,       3,

```

```

ra_lw_physics      = 1,      1,      1,      1,      1,
ra_sw_physics      = 1,      1,      1,      1,      1,
radt               = 30,     30,     30,     30,     30,
sf_sfclay_physics  = 1,      1,      1,      1,      1,
sf_surface_physics = 2,      2,      2,      2,      2,
bl_pbl_physics     = 1,      1,      1,      1,      1,
bldt               = 0,      0,      0,      0,      0,
cu_physics         = 1,      1,      0,      0,      0,
cudt               = 5,      5,      5,      5,      5,
isfflx             = 1,
ifsnow             = 1,
icloud            = 1,
surface_input_source = 3,
num_soil_layers    = 4,
num_land_cat       = 28,
sf_urban_physics   = 0,      0,      0,      0,      0,
bl_mynn_edmf       = 0,      0,      0,      0,      0,
bl_mynn_edmf_mom    = 0,      0,      0,      0,      0,
bl_mynn_edmf_tke    = 0,      0,      0,      0,      0,
/

&dynamics
w_damping          = 0
diff_opt           = 1,      1,      1,      1,      1
km_opt             = 4,      4,      4,      4,      4
diff_6th_opt       = 0,      0,      0,      0,      0
diff_6th_factor    = 0.12,   0.12,   0.12,   0.12,   0.12
base_temp          = 290.0
damp_opt           = 0
zdamp              = 5000.0, 5000.0, 5000.0, 5000.0, 5000.0
dampcoef           = 0.2,     0.2,     0.2,     0.2,     0.2
khdif              = 0,      0,      0,      0,      0
kvdif              = 0,      0,      0,      0,      0
non_hydrostatic    = .true., .true., .true., .true., .true.
moist_adv_opt      = 1,      1,      1,      1,      1
scalar_adv_opt     = 1,      1,      1,      1,      1
/

&bdy_control
spec_bdy_width     = 5
spec_zone          = 1
relax_zone         = 4
specified          = .true., .false., .false., .false., .false.
nested             = .false., .true., .true., .true., .true.
/

&namelist_quilt
nio_tasks_per_group = 0
nio_groups          = 1
/

```

## A.2.2 EllipSys3D input file sample (input.dat)

Listing A.4 capt

```

# -----
#       project name
# -----
#       project grid
# -----
#       solver parameters
# -----
#       grid_level 2
#       mstep 86400 10 10 10 10
#       mstepp 5
#       subiterations 5 5
#       reslim 1.d-4 1.d-4 1.d-4 1.d-4 1.d-3
#       reslimp 2.d-1
#       diff_scheme quick
#       pres_corr simplea 1.0 1.0
#       pres_levels 5
#       interpolationorder 2
#       nrrestart 10800
#       extension true
# -----
#       run parameters
# -----
#       transient true 2.0
# -----
#       relaxation parameters
# -----
#       relaxu .7d0
#       relaxp .2d0
# -----
#       fluid parameters
# -----
#       density 1.225d0
#       viscosity 1.78406d-5
# -----
#       inlet values
# -----
#       winlet 0.d0
#       uinlet 0.4d0
# -----
#       farfield values
# -----
#       wfarfield 0.d0
#       ufarfield 9.5d0
#       vfarfield 0.0d0
# -----
#       temperature
# -----
#       gravitation 0 0 -9.81
#       temperature air
#       prandtl 0.74 0.74
#       prandtl_var
#       inlet temp 100 151 file 1 Twall.dat
#       field temp file 2 Tprof.dat
#       temp_inlet 294.5594099702149
#       temp_wall 294.5594099702149

```

```
temp_relaxation
temp_farfield 294.5594099702149
relaxtemp 0.6
# -----
#   Turbulence model
# -----
turbulence      kepsilon
ke_version      rough-abl
turbcrossterms  false
loglaw          true
roughness       0.045489024525633255
transient_scalar_lmax  file 6 lmax.dat
ambient_ke      0.0001 7.208e-08
cmu             0.03
ce1             1.52
ce2             1.833
pred_ke         2.95131
prtke_ke        2.95131
relaxturb       6.0d-1
te_inlet        1.0d-1
ed_inlet        0.003d0
te_farfield     1.0d-1
ed_farfield     0.003d0
forceallocation
turb_cori       true 9.316919707069196e-05
field u         file 3 Uprof.dat
field v         file 4 Vprof.dat
field w         file 5 Wprof.dat
```

### A.2.3 Convergence of EllipSys3D results

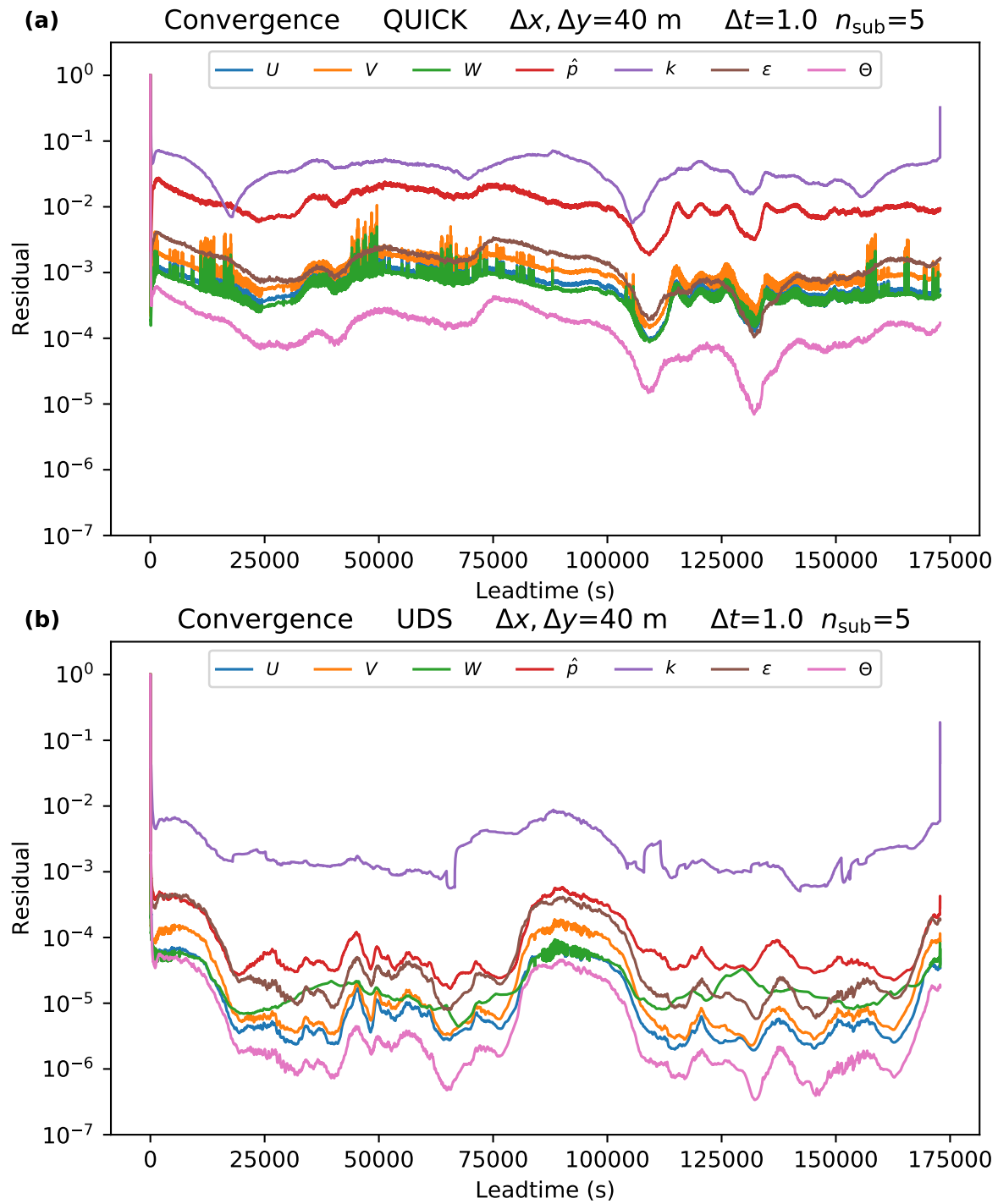


Fig. A.1 Residuals during the two-day sensitivity study (12:00 20 April to 12:00 22 April, 2017) for the G01-Q **(a)** and G01-U **(b)** simulations.

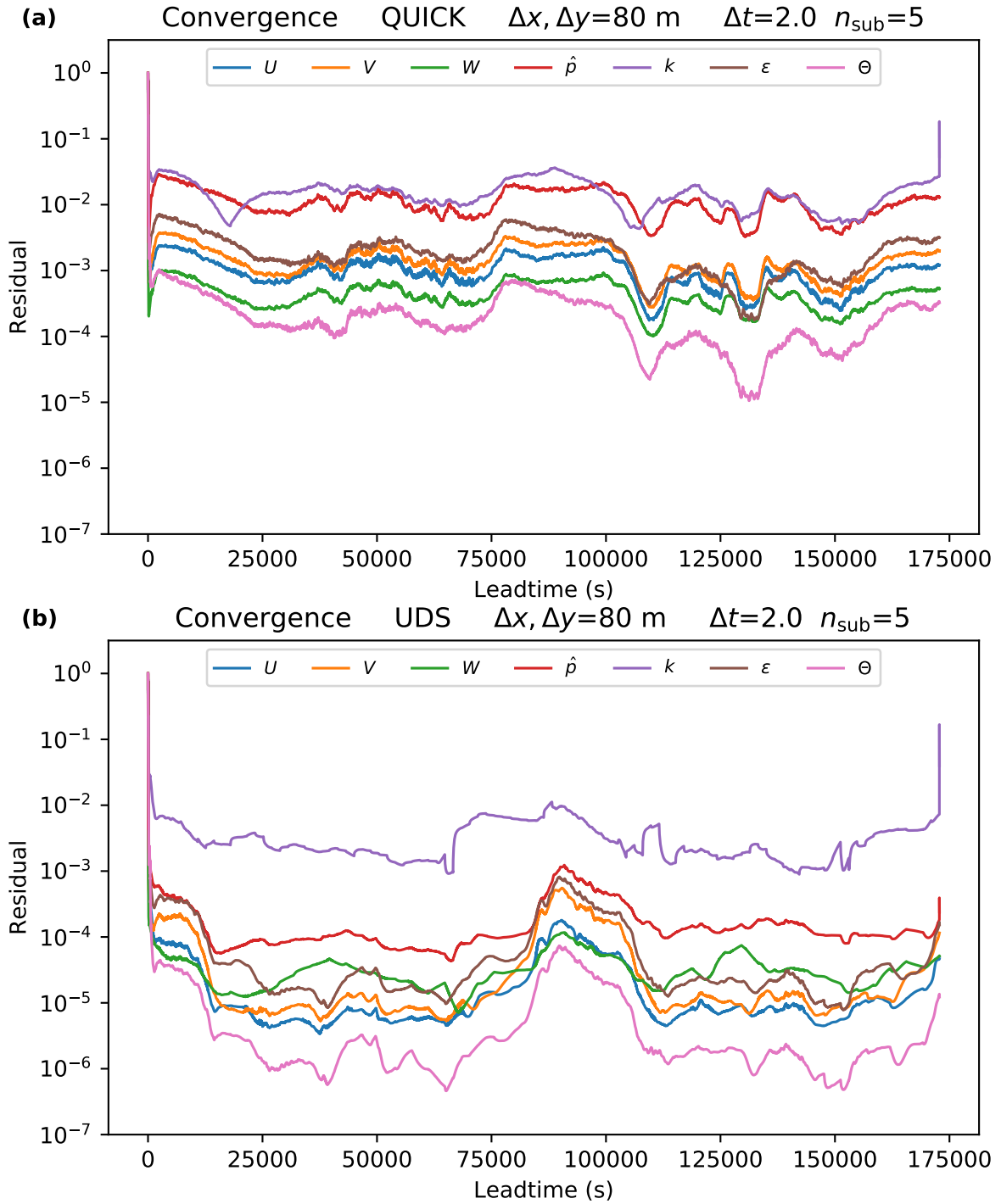


Fig. A.2 Residuals during the two-day sensitivity study (12:00 20 April to 12:00 22 April, 2017) for the G02-Q **(a)** and G02-U **(b)** simulations.



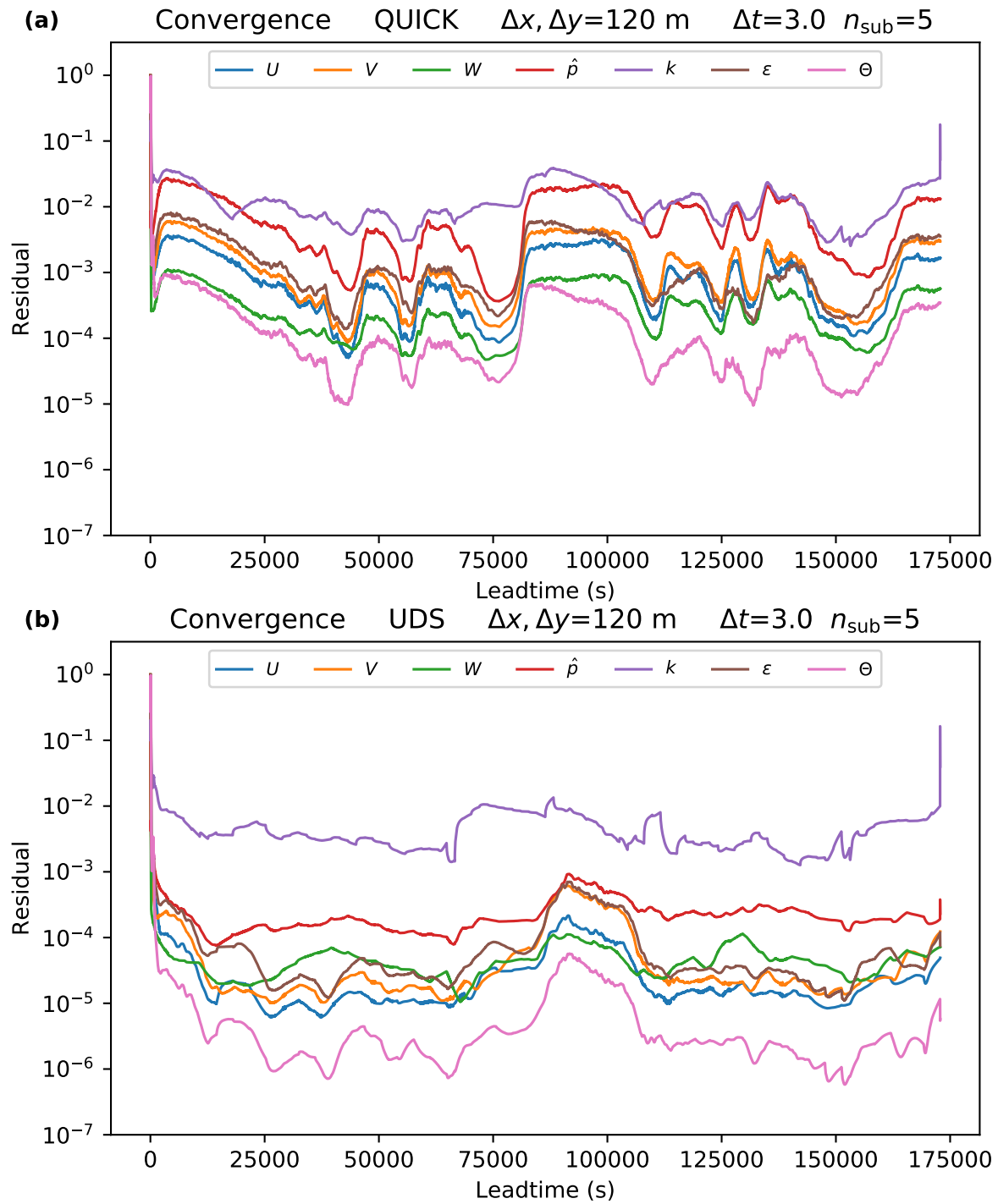


Fig. A.3 Residuals during the two-day sensitivity study (12:00 20 April to 12:00 22 April, 2017) for the G03-Q **(a)** and G03-U **(b)** simulations.

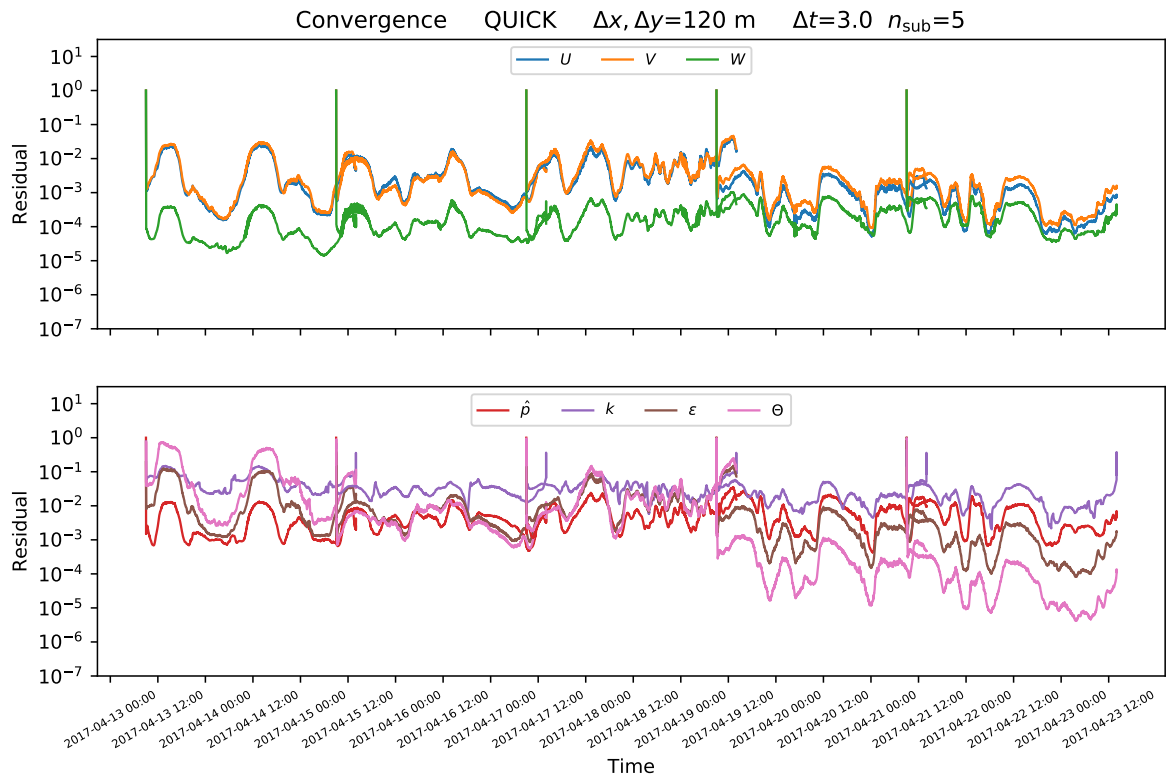


Fig. A.4  $U$ ,  $V$ , and  $W$  (a) and  $\hat{p}$ ,  $k$ ,  $\epsilon$ , and  $\Theta$  (b) residuals during the first 10 days of the long simulations (12:00 13 April to 12:00 15 May, 2017) for the G03-Q setup.

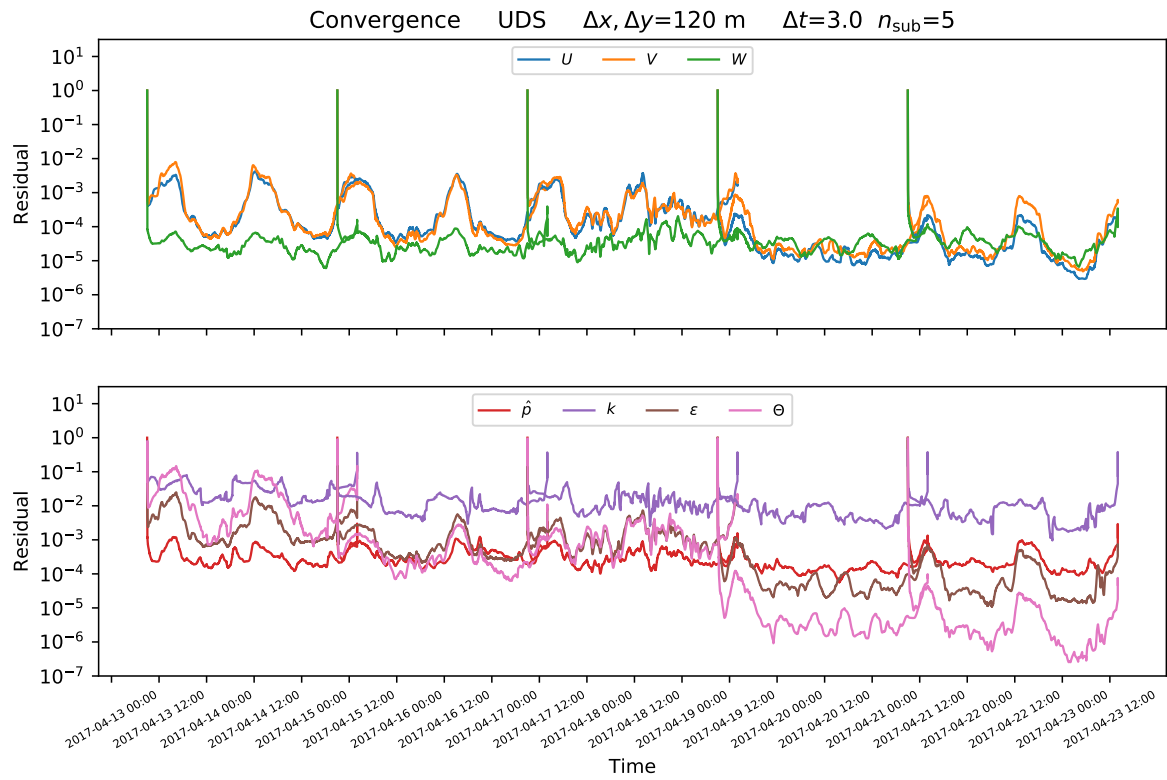


Fig. A.5  $U$ ,  $V$ , and  $W$  (a) and  $\hat{p}$ ,  $k$ ,  $\epsilon$ , and  $\Theta$  (b) residuals during the first 10 days of the long simulations (12:00 13 April to 12:00 15 May, 2017) for the G03-U setup.

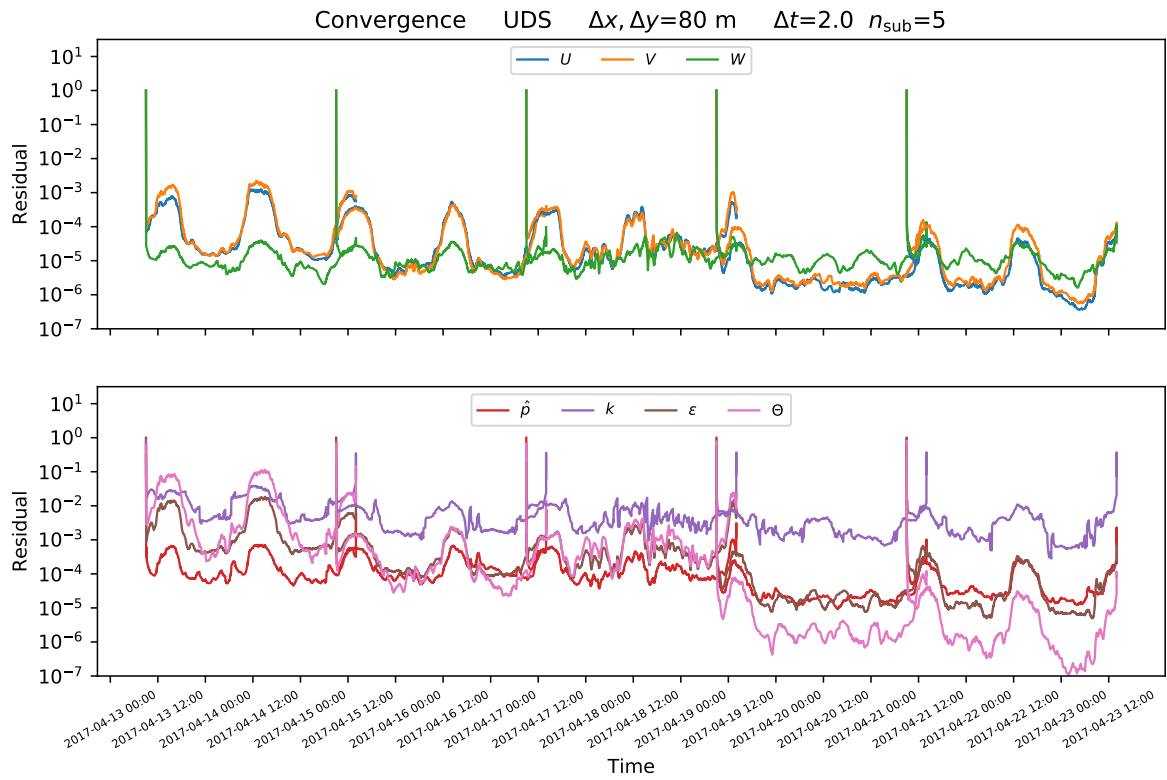


Fig. A.6  $U$ ,  $V$ , and  $W$  **(a)** and  $\hat{p}$ ,  $k$ ,  $\epsilon$ , and  $\Theta$  **(b)** residuals during the first 10 days of the long simulations (12:00 13 April to 12:00 15 May, 2017) for the G02-U setup.



## **Appendix B**

# **An intercomparison of mesoscale models at simple sites for wind energy applications**

Authors: Olsen, B.T., Hahmann A.N., Sempreviva, A.M., Badger, J., Jørgensen, H.E., (2017),  
*Wind Energy Science*, 2(1):211-228



# An intercomparison of mesoscale models at simple sites for wind energy applications

Bjarke T. Olsen, Andrea N. Hahmann, Anna Maria Sempreviva, Jake Badger, and Hans E. Jørgensen

DTU Wind Energy, Frederiksborgvej 399, 4000 Roskilde, Denmark

*Correspondence to:* Bjarke T. Olsen (btol@dtu.dk)

Received: 10 November 2016 – Discussion started: 1 December 2016

Revised: 31 March 2017 – Accepted: 31 March 2017 – Published: 4 May 2017

**Abstract.** Understanding uncertainties in wind resource assessment associated with the use of the output from numerical weather prediction (NWP) models is important for wind energy applications. A better understanding of the sources of error reduces risk and lowers costs. Here, an intercomparison of the output from 25 NWP models is presented for three sites in northern Europe characterized by simple terrain. The models are evaluated using a number of statistical properties relevant to wind energy and verified with observations. On average the models have small wind speed biases offshore and aloft ( $< 4\%$ ) and larger biases closer to the surface over land ( $> 7\%$ ). A similar pattern is detected for the inter-model spread. Strongly stable and strongly unstable atmospheric stability conditions are associated with larger wind speed errors. Strong indications are found that using a grid spacing larger than 3 km decreases the accuracy of the models, but we found no evidence that using a grid spacing smaller than 3 km is necessary for these simple sites. Applying the models to a simple wind energy offshore wind farm highlights the importance of capturing the correct distributions of wind speed and direction.

## 1 Introduction

Numerical weather prediction (NWP) models are increasingly being used in wind energy applications, e.g., wind power resource mapping and site assessment, for planning and developing wind farms, power forecasting, electricity scheduling, maintenance of wind farms, and energy trading on electricity markets. In site assessment, NWP models are commonly part of the model chain used to estimate the annual energy production (AEP) and are responsible for a large part of the uncertainty of this estimate.

The extensive use of NWP models, and the vast customization space of each model, means that a strong demand exists for quantification of (a) the overall model uncertainties and (b) the sensitivity of the uncertainties to the choice of sub-components and parameters. Understanding the sensitivities and uncertainties of the NWP model output can reduce their associated risks and improve decision making. Model users aware of the sensitivity of individual model components will be able to optimize the model setup for specific applications.

In the following, the NWP models will be referred to as mesoscale models, signifying that they partly resolve atmo-

spheric phenomena in the mesoscale range, defined as the range of horizontal length scales from about one to several hundreds of kilometers (Orlanski, 1975).

A common way to assess NWP model uncertainties is to use an ensemble approach, where a number of parallel model runs, referred to as ensemble members, are run with slightly perturbed initial conditions (Warner, 2010). The magnitude of the perturbations is typically limited by the uncertainty associated with the particular perturbed variable in the expectation that the ensemble of solutions will cover the solution space arising from the uncertainties of the input parameters. Ensemble-based techniques are used for many meteorological applications, including precipitation forecasting (Gebhardt et al., 2011; Bowler et al., 2006) and wind power production forecasting (Constantinescu et al., 2011). However, one would not expect that the ensembles of any particular modeling system fully represent the uncertainties of another modeling system. This was also demonstrated in the DEMETER project (Development of a European multi-model Ensemble for seasonal to inTERannual climate prediction) (Palmer et al., 2004), where a multi-model ensemble

approach, consisting of a number of different modeling systems, each split into a number of ensembles, provided a better representation of the overall uncertainties than any single model ensemble.

Mesoscale model uncertainties in wind speed near the ground are particularly sensitive to some model components, e.g., the choice of planetary boundary layer (PBL) scheme, the spin up and simulation time, and the grid spacing. In the last couple of decades these sensitivities have been studied in great detail. Vincent and Hahmann (2015), Draxl et al. (2014), and Hahmann et al. (2015b) studied the sensitivities of the Weather Research and Forecasting (WRF) model (Skamarock et al., 2008) in offshore and coastal areas in northern Europe. Vincent and Hahmann (2015) studied the effect of grid nudging, spin-up time, and simulation time on near-surface and upper-PBL wind speed variance. They showed that (1) spatial smoothing is observed when nudging is used, but the impact is small in the lower part of the atmosphere, and (2) longer nudged simulation times (11 days) only have slightly lower variance than short simulations (36 h), which makes longer simulations appropriate for climatological wind energy studies. Draxl et al. (2014) studied the ability of the WRF model to represent the wind speed and wind shear profiles at a coastal site in Denmark using seven different PBL schemes. They showed that the Yonsei University (YSU) (Hong et al., 2006) scheme represents the profiles best for unstable atmospheric stability conditions, while the Asymmetric Convective Model version 2 (ACM2) (Pleim, 2007b), and the Mellor–Yamada–Janjić (MYJ) (Janjić, 1994) PBL schemes had more realistic profiles for neutral and stable conditions respectively. Using the WRF model for wind resource assessment, Hahmann et al. (2015b) showed that the choice of PBL scheme and spin-up time has the greatest impact on the simulated mean wind speed for a number of offshore sites, while the number of vertical levels and the source of initial conditions had a smaller impact.

Several studies have investigated the WRF model sensitivities in regions of complex terrain. Carvalho et al. (2012) studied the sensitivities related to the choice of initialization frequency, grid nudging, suite of surface layer (SL) scheme, PBL scheme, and land surface model (LSM). They observe that using grid nudging and frequent starts (every second day) gives the best agreement for wind speed, with several masts located in complex terrain in Portugal. Carvalho et al. (2012) and García-Díez et al. (2013) found a seasonal dependency of the optimal suite of SL–PBL–LSM for simulating PBL winds and temperature. Carvalho et al. (2014b) investigated the sensitivities related to the SL and PBL schemes in the WRF model at both land and offshore sites in and near Portugal. They showed that the Pleim–Xiu SL scheme (Pleim, 2006) combined with the ACM2 PBL scheme (Pleim, 2007b) gave the smallest errors for wind speed and wind energy production estimates across the sites, while the quasi-normal scale elimination (QNSE) SL and PBL schemes (Sukoriansky et al., 2005) gave smaller errors

for offshore sites. In a similar study, Gómez-Navarro et al. (2015) analyzed the sensitivities of the WRF model to the choice of PBL scheme and grid spacing in complex terrain in Switzerland. They found that using a modified version of the YSU PBL scheme, which accounts for effects of unresolved topography (Jiménez and Dudhia, 2012), in combination with the smallest grid spacing (2 km) and analysis nudging gave the best agreements with measurements during a number of wind storms. Carvalho et al. (2014a) studied the sensitivities of simulating the local wind resource with the WRF model at several masts in Portugal to the choice of data set used for initial and boundary conditions. They show that using the ERA-Interim reanalysis data set (Simmons et al., 2007) gave the smallest errors compared to NCEP (National Centers for Environmental Prediction) R2 (Kanamitsu et al., 2002), CFSR (Saha et al., 2010), FNL, and GFS data sets, as well as the NASA MERRA data set (Rienecker et al., 2011).

Sensitivities to the choice of modeling system have also been studied for wind energy applications. Horvath et al. (2012) compared the MM5 (Grell et al., 1994) and WRF models for a site in west-central Nevada characterized by complex terrain. Both models were run in a grid nesting setup from 27 km to 333 m grid spacing, and the near surface wind was compared to wind observations from several 50 m tall towers. The study showed that the WRF-derived winds were in better agreement with mean wind speed observations, but thermally driven flows were overestimated in both intensity and frequency. Hahmann et al. (2015a) compared two downscaling methodologies: the KAMM-WAsP (Badger et al., 2014) and WRF Wind Atlas (Hahmann et al., 2015b) methods, both based on a model chain approach between a NWP model and a linearized flow microscale model, for a number of mast sites in South Africa. The study showed that the WRF-based method gave smaller biases than the KAMM-based approach, which underestimated the wind speeds.

Community-driven model intercomparison projects provide an opportunity to study both model uncertainties and sensitivities to model components. In the last decade, several intercomparison projects have been successfully carried out based on model output submitted by modelers from the wind energy community. The Bolund experiment (Bechmann et al., 2011) was an intercomparison of flow models, from simple linearized flow models to computational fluid dynamics (CFD) models. The models were compared to measurements around the small island of Bolund in Denmark. The Comparison of Resource and Energy Yield Assessment Procedures (CREYAP; Mortensen et al., 2015) was an intercomparison of energy yield assessment procedures based on four case studies. The study revealed a large spread amongst the different procedures and highlighted the need for further studies into the uncertainties associated with the models themselves. A similar intercomparison of NWP models is attractive for a number of reasons. First, it offers an opportunity for model developers, model users, and stake holders to get a better understanding of the model uncertainties. Sec-



ondly, a collaborative intercomparison project, which utilizes model data crowdsourced from the wind energy community, increases the scalability of the study compared to traditional sensitivity studies by distributing the workload and computational cost among participants. Finally, if sufficient meta-data are collected, they offer a unique insight into the common practices in mesoscale modeling within the wind energy community.

In this paper, a blind intercomparison of the output from 25 different NWP simulations is presented for three locations in northern Europe. The study is based on model output submitted by the modeling community to an open call for model data for a benchmarking exercise co-organized by the European Wind Energy Association (EWEA, now WindEurope) and the European Energy Research Alliance, Joint Programme Wind Energy (EERA JP WIND). The three chosen sites represent some of the simplest terrains: offshore, inland near the coast, and inland in flat terrain, where the smoothing of the terrain representation is not an issue. The three sites have quality observations from tall meteorological masts with many heights. The main objectives of this study are (1) to highlight and quantify the uncertainties of the models and serve as motivation for future analysis of model uncertainties and (2) to identify model setup decisions that have an impact on the model performance. The models are evaluated using simple metrics relevant to wind energy applications.

The structure of the paper is as follows. In Sect. 2 we present a detailed description of the methodology used, including a description of the three study sites and the models used by the participants. Section 3 presents the intercomparison results, and finally Sect. 4 contains the summary and conclusions of the study.

## 2 Methodology

### 2.1 Sites and observations

Three sites with quality measurements from tall meteorological masts with different terrain characteristics were chosen for this study: (1) FINO3, an offshore mast in the North Sea, (2) Høvsøre, a land mast near the Danish west coast, and (3) Cabauw, a land mast in the Netherlands. The mast locations are shown in Fig. 1, and the coordinates and characteristics of each site are provided in Table 1. Long-term measurements are available from each of the masts, but a single year (2011) was selected as the study period due to its excellent data availability.

FINO3 (Fabre et al., 2014) is a marine platform located in the North Sea 80 km off the coast of Denmark, with a meteorological mast reaching 120 m above mean sea level (a.m.s.l.). We used measurements at 40, 60, and 90 m a.m.s.l. in this study. The Høvsøre (Peña et al., 2014) mast is located about 2 km east of the coastline in western Jutland, Denmark. Apart from the sharp surface roughness change at the coast-

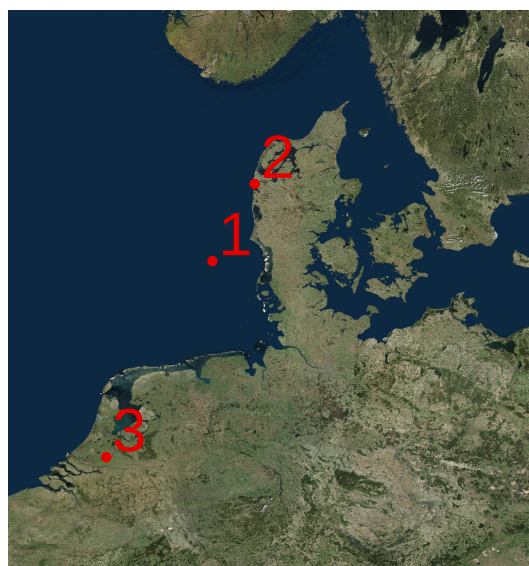


**Figure 1.** Map of northern Europe with the three site locations used in the model intercomparison: (1) FINO3, in the North Sea. (2) Høvsøre, Denmark. (3) Cabauw, the Netherlands.

line and the presence of a small coastal escarpment, the surrounding terrain is homogeneous and flat. We used measurements at 10, 40, 60, 80, 100 m at this site. The Cabauw mast (Ulden and Wieringa, 1995) is located 40 km inland near the small towns of Cabauw and Lopik in the Netherlands. The surroundings are flat and characterized by fairly homogeneous agricultural fields, but with patches of forest and buildings. Here we used measurements at 10, 20, 40, 80, 140, and 200 m.

Figure 2 shows availability of wind speed observations for 2011 at the three meteorological masts. At Cabauw, the data were gap-filled by simple interpolation as the missing values were few (less than 2 % missing data per month) and the gaps short. The time series from the two other sites were not gap-filled.

At FINO3, the wind speed measurements at three of the heights, 50, 70, 90 m, are a combination of the measurements from three anemometers at three separate booms 120° apart. This procedure minimizes the effects of the mast flow distortion. At the other two heights, 40 and 60 m, only one anemometer is available, and the wind measurements are therefore susceptible to flow distortion. Thus, instead of using the single-anemometer data from 40 and 60 m, the measurements from 50 and 70 m were vertically interpolated in log height to 40 and 60 m. This assumes that the errors due to interpolation and extrapolation are much smaller than those caused by mast flow distortion.

### 2.2 Submission procedure and models

EWEA issued an open call for data and the submission procedure consisted of a template spreadsheet and a question-

**Table 1.** Site description, including latitude and longitude coordinates, classification of the site, the height of the mast  $z_s$ , and the location terrain elevation relative to sea-level  $z_{asl}$  and prevailing wind direction.

No.	Name	Latitude (°)	Longitude (°)	Type	$z_s$ (m)	$z_{asl}$ (m)	Prev. wind direction
1	FINO3	55.195	7.158	Offshore	120	0	WSW
2	Høvsøre	56.441	8.151	Coastal	116	2	WSW
3	Cabauw	51.970	4.926	Land	213	−1	SW

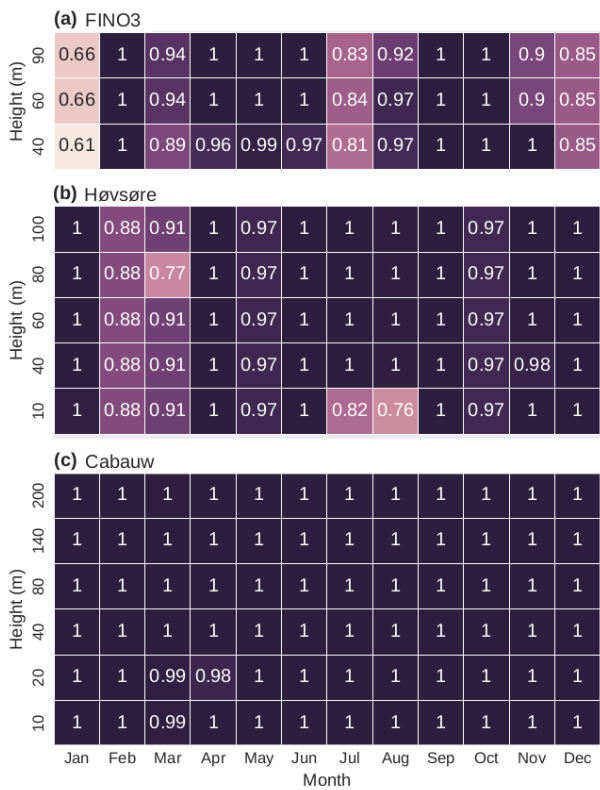


**Figure 2.** Availability of wind speed and direction observations for (a) FINO3, (b) Høvsøre, and (c) Cabauw given as the fraction of completeness for each month of the year 2011 for each height.

naire available for download from the EWEA website. The participants filled the spreadsheet with the time series of the required variables at each location and height. The questionnaire contained details about the setup of the modeling system used. The participants returned the spreadsheet to EWEA, who passed it on to the authors in an anonymous version.

The requested model variables were hourly wind speed and direction, air temperature, and atmospheric stability. The questionnaire asked about the modeling setup, i.e., the model code and version, the SL and PBL schemes, the LSM, the grid nest size(s) and spacing(s), the vertical levels, the land use data, the length of the simulation, the spin-up time, and the source of the initial and boundary conditions. The participants were also asked to comment on any additional modifi-

cations made to the model, including assimilation, ensemble, or other methods used.

Table 3 lists the various groups participating in the exercise. It includes representatives from private companies, universities, research centers, and meteorological institutes. Table 4 summarizes the models and the different model setup options used. The WRF model is by far the most commonly used model in the study, with 18 out of 25 models (Table 4). The Noah LSM was the most common LSM used, and the ERA-Interim reanalysis was the most common source of boundary and initial conditions. The PBL scheme used and the source of land cover data were more varied amongst the participants. Most models used a maximum simulation length of less than 100 h, including the spin-up time (most typically 12 h spin-up and 36 h of total simulation). The simulation and spin-up length ranged from 1 h spin-up and 7 h simulation to 24 h spin-up and continuously running for the full year.

For reference, wind time series from the ERA-Interim reanalysis (Dee et al., 2011) were included in the comparisons whenever possible. The ERA-Interim reanalysis data set is a global data set based on extensive assimilation of surface and upper-air observations. The data are available on a grid spacing of about 80 km in the horizontal with 60 vertical levels, with values at approximately 10, 34, 69, 118, 187, and 275 m above the model surface. We used bilinear interpolation to interpolate to the sites coordinates and linear interpolation in the vertical. The data set is available in 6 h intervals; thus, linear interpolation in time was used to obtain hourly samples.

2.3 Statistical methods

This study is based on direct comparison between the observations and model output at collocated positions, as well as intercomparison of the modeled output. The sampling frequency for the study was chosen to be 1 h. For the observation data this means hourly mean values; for the mesoscale models the inter-hourly variation is small; thus, instantaneous values were used. To ensure temporal consistency between observations and modeled output, instances of missing data from the observations were removed from the modeled output. Furthermore, to get consistent vertical profiles, only instances where all heights for a particular mast with available data were used. The model output submitted was

assumed to be quality checked by the submitter, but it was also checked by the authors for obvious nonphysical or inconsistent behavior and not used in that case. The number of models excluded was between two and four at each of the sites, but no model was excluded from all three sites.

### Inter-model mean and inter-model variations

The emphasis of this study is on the wind speed,  $u$ , and wind direction, as they are the most important variables for wind energy applications. In the following, a subscript “m” signifies the temporal mean of a variable, i.e.,  $u_m$  is the temporal mean wind speed. This is not to be confused with the mean value of the model ensemble, also referred to as the inter-model mean, which is denoted with a tilde. For example, the mean of the model ensemble for the temporal mean wind speed is denoted as  $\tilde{u}_m$  and calculated as

$$\tilde{u}_m = \frac{1}{N} \sum_i^N u_{m,i}. \quad (1)$$

Here  $i$  is the model index and  $N$  is the total number of models. Likewise, it is useful to define its standard deviation:

$$\tilde{\sigma}_{u_m} = \sqrt{\frac{1}{N} \sum_i^N (u_{m,i} - \tilde{u}_m)^2}, \quad (2)$$

which is the standard deviation of the inter-model variation between the temporal model means. Since  $\tilde{u}_m$  and  $\tilde{\sigma}_{u_m}$  are both sensitive to outliers, we used the following procedure:

1. Calculate  $\tilde{u}_m$  and  $\tilde{\sigma}_{u_m}$ .
2. Remove models whose mean  $|u_{m,i} - \tilde{u}_m| > 3.5 \tilde{\sigma}_{u_m}$ .
3. Recalculate  $\tilde{u}_m$  and  $\tilde{\sigma}_{u_m}$  with the new subset of models.

The value of  $3.5 \tilde{\sigma}_{u_m}$  was chosen somewhat arbitrarily to ensure that only extreme outliers were removed. The procedure included only models with output available at all the heights to ensure a vertically consistent profile of the mean and its variation. Typically, only one or two models were removed by this criteria.

### Coefficient of variation

Variations in wind speed often scale with the mean wind speed. Thus, to allow for intercomparison of wind speed variation intensity across vertical levels, we define the coefficient of variation,  $C_{v,u}$ . It is defined as the ratio of the standard deviation and the mean,  $\sigma_u/u_m$ , and is a unit-less measure of the relative variation at the sampling timescale. At timescales of seconds it is known as the turbulence intensity, but in this case, with a sampling frequency of 1 h, it represents the intensity of variations of synoptic- and mesoscale weather phenomena.

### Wind speed shear exponent

To diagnose the wind shear in the boundary layer, we use the wind shear exponent,  $\alpha$ , which uses the wind speed  $u_1$  and  $u_2$  at two heights  $z_1$  and  $z_2$ , given by the expression

$$u_2 = u_1 \left( \frac{z_2}{z_1} \right)^\alpha. \quad (3)$$

In the surface layer,  $\alpha$  is strongly influenced by the surface roughness and the atmospheric stability. By comparing the modeled to the measured  $\alpha$ , it is thus possible to gain insights into how the model captures these effects.

### Error metrics

The RMSE and the normalized RMSE (NRMSE) were used as error metrics to obtain single-value measures of the error across heights at a site. The RMSE and NRMSE are defined as

$$\text{RMSE} = \sqrt{\frac{1}{n} \sum_{j=1}^n (x_j^M - x_j^O)^2} \quad (4)$$

$$\text{NRMSE} = \sqrt{\frac{1}{n} \sum_{j=1}^n \left( \frac{x_j^M - x_j^O}{x_j^O} \right)^2} \quad (5)$$

for a set of  $n$  modeled values  $x_j^M$  and observed values  $x_j^O$ . The RMSE was used for variables that do not scale with height in the surface layer, e.g., wind speed shear exponent; the NRMSE was used for variables that do scale with height, e.g., wind speed.

### 2.4 Wind energy application

To investigate the errors associated with the use of each model in wind energy applications, we performed a simple wind resource assessment exercise, using both measurements and modeled time series at FINO3.

A typical approach to resource assessment is to run a mesoscale model for a number of years, followed by a down-scaling process where the wind climate statistics obtained from the mesoscale model are used as input to a microscale model (Badger et al., 2014; Hahmann et al., 2015a). In simple terrain, the microscale model usually consists of a flow model like the one used by the Wind Applications and Analysis Program (WASP). WASP uses a linearized flow model based on Jackson and Hunt (1975). The procedure in WASP consists first of an upscaling, where local effects from variations in orography, surface roughness, and obstacles are removed from the wind climate statistics. This is referred to as generalization of the wind climate, which makes it representative for a larger area than the site-specific wind climate. The size of this area depends on the complexity of the surface roughness and orographic variations in that area. To

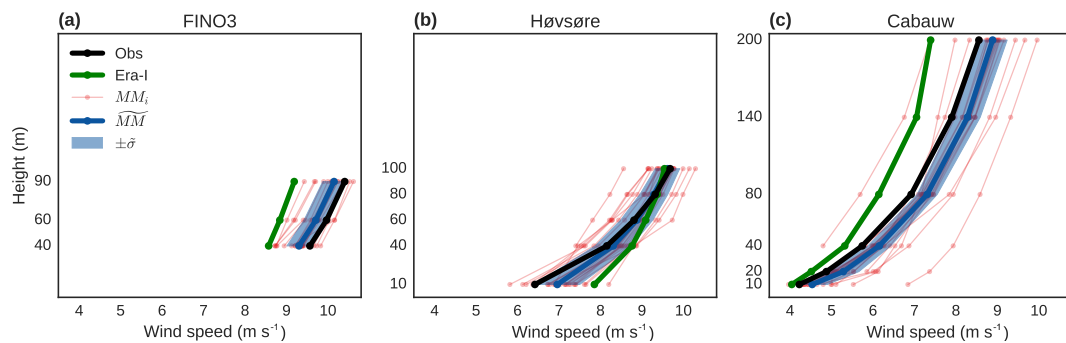


**Figure 3.** Vertical profiles of mean wind speed ( $u_m$ ) at the three sites for the observations (black), the ERA-Interim data set (green), the mesoscale models  $MM_i$  (red), and the inter-model mean  $\widetilde{MM}$  (blue line), and its standard deviation  $\pm\sigma$  (blue shade).

obtain a site-specific wind climate at a new site in this area, the generalized wind climate is downscaled by reversing the generalization process, i.e., by introducing the site-specific effects of orography, surface roughness, and obstacles of the new site.

Given the wind climate and the turbine power curve, the expected power output can be calculated for any site. Since the participants in this intercomparison were not requested to submit the model-specific orography and roughness maps near each site, it is not possible to go through the generalization procedure and subsequent downscaling process at the inland sites. However, for the offshore site FINO3 there are no effects of orography, and the differences in roughness between the models can be assumed to be negligible. Therefore, we can use the raw model output at this site to estimate the wind resources estimated by each of the models, without the generalization procedure.

We performed the wind resource exercise at 90 m at FINO3, assuming first a single Vestas V80 turbine at the site, and then repeated for the exercise for the wind farm of Horns Rev, which is an 80-turbine wind farm located near FINO3. The resource estimations for the wind farm include the simple wake parametrization present in the WAsP model, which was used to estimate the power losses.

### 3 Results

#### 3.1 Mean quantities and distributions

The following subsection is dedicated to the general performance of the models and their ability to capture the mean and the distributions of a number of wind-related quantities. As previously stated, the goal is to highlight the weaknesses of the models to encourage further analysis of model sensitivities.

##### 3.1.1 Annual mean wind speed

Figure 3 shows the vertical profiles of mean wind speed ( $u_m$ ) at the three sites. At FINO3 (Fig. 3a), most mesoscale mod-

els (MMs) underpredict  $u_m$  at all heights. However, the bias on average is less than  $0.27 \text{ m s}^{-1}$  ( $\sim 2.8\%$ ). This is a small bias compared to that of the ERA-Interim data, which show a larger bias than all the mesoscale models. The inter-model variance  $\tilde{\sigma}_{u_m}$  at FINO3 is 2.7–3.1 % of the inter-model mean, and decreases with height. That is the lowest combined inter-model variance of any of the three sites.

At Høvsøre (Fig. 3b), the MMs generally have small wind speed biases above 10 m. The error of the inter-model mean of the models is smaller than  $\pm 0.16 \text{ m s}^{-1}$  ( $\sim 1.9\%$ ), and the inter-model variance is 3.0–5.2 %, decreasing with height, which is low compared to the biases at the other site on land (Fig. 3c). At 10 m, most MMs overpredict the mean wind speed. The inter-model mean has a positive bias of  $0.54 \text{ m s}^{-1}$  ( $\sim 8.4\%$ ). The largest inter-model variance is also seen at 10 m (7.8 %). The ERA-Interim also overpredicts the mean wind speed at 10 m, with a larger bias than  $\tilde{u}_m$ . Above 10 m, ERA-Interim has smaller errors, but the shape of the profile is not well captured. Signs of a “kink” in both the observed and modeled profiles are present, which could indicate the transition from the low surface roughness of the sea to the higher surface roughness inland.

At Cabauw (Fig. 3c), most of the MMs overpredict  $u_m$ . Only one of the models and the ERA-Interim reanalysis show a significant underprediction, and in the case of the reanalysis, this underestimation increases with height. The overprediction by the rest of the MMs varies in magnitude, but the average of the models, excluding the outliers, is in the range of 4–9 % across the different heights. The largest relative errors are at the lowest levels. The inter-model variance ( $\tilde{\sigma}_{u_m}$ ) at Cabauw varies between 3.3 and 8.1 % across the different heights and is largest at the lowest levels. The decrease in wind speed bias with height was also observed by Jiménez et al. (2016), who associated this with excessive turbulent mixing, which may be caused by a misrepresentation of the surface roughness length.



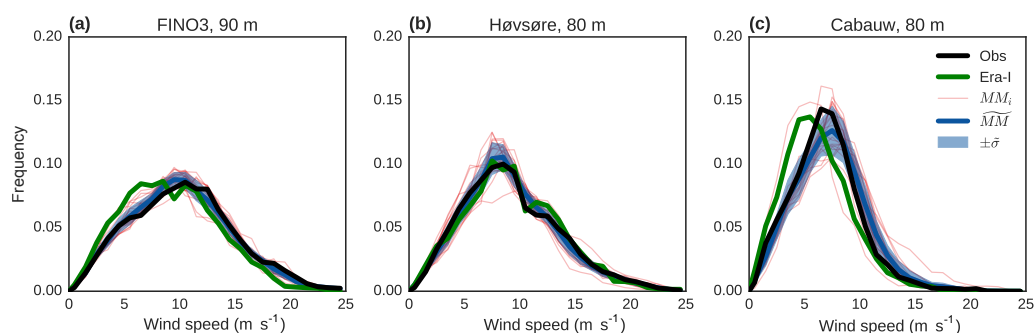


**Figure 4.** Wind speed distributions at the three sites (FINO3 at 90 m, Høvsøre at 80 m, and Cabauw at 80 m) for the observations (black), the ERA-Interim data set (green), the mesoscale models  $MM_i$  (red), and the inter-model mean  $\bar{MM}$  (blue line) and its standard deviation  $\pm\sigma$  (blue shade).

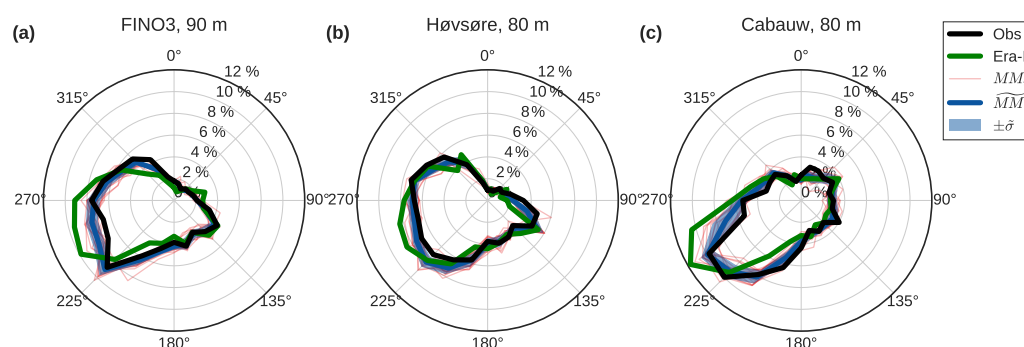


**Figure 5.** Wind direction distributions at the three sites (FINO3 at 90 m, Høvsøre at 80 m, and Cabauw at 80 m), based on 24 sectors, for the observations (black), the ERA-Interim data set (green), the mesoscale models  $MM_i$  (red), and the inter-model mean  $\bar{MM}$  (blue line) and its standard deviation  $\pm\sigma$  (blue shade).

### 3.1.2 Frequency distribution of wind speed

Figure 4 shows that, on average, the MMs capture the wind speed distributions well compared to the observations. The only exception is a slight shift towards higher wind speeds at Cabauw, corresponding to the positive bias in mean wind speed observed in Fig. 3. The ERA-Interim data set captures the distribution well at Høvsøre, but it has distributions that are shifted towards lower wind speeds at FINO3 and Cabauw, corresponding to the bias in Fig. 3.

### 3.1.3 Distribution of wind direction

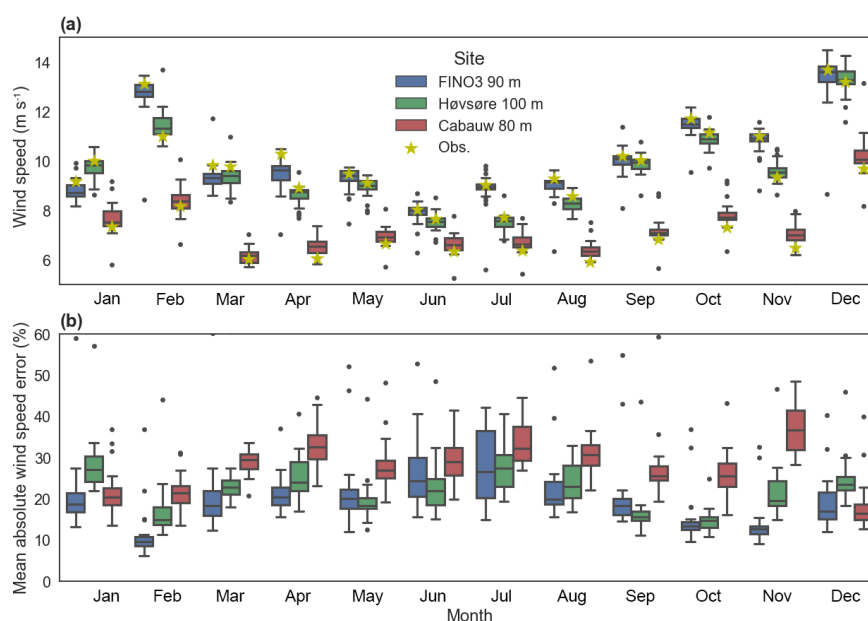
Figure 3 shows that the MMs generally capture the mean wind speed well. This is also true for the wind direction distributions, commonly called “wind roses”. The distributions are split into  $15^\circ$  sectors at heights of either 80 or 90 m. Figure 5 also shows that the models are in good agreement. At all three sites the MMs capture the distribution better than the reanalysis data. At all sites, but most markedly at Cabauw, the ERA-Interim distribution is rotated clockwise relative to the distribution from the observations and MMs. This rotation might result in a different wind farm layout if its power

is optimized according to the wind roses from MMs or the ERA-Interim.

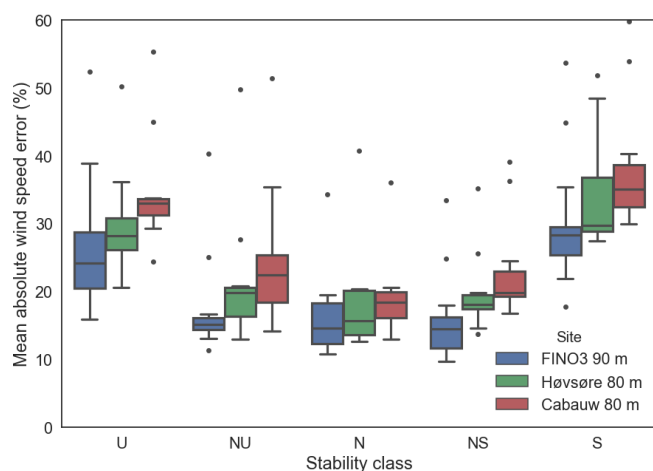
### 3.1.4 Annual wind speed cycle

Figure 6a shows the monthly distribution of the mean wind speed for the MMs and the measurements. Apart from a few models outside the  $3 \times$  quartile range, most models capture the diurnal cycle well. Interestingly, the figure also reveals that both the overestimation by the models at Cabauw and the underestimation at FINO3, seen in Fig. 3, are evenly distributed throughout the year. At Høvsøre, a mix of under- and overestimations are observed.

Figure 6b shows the monthly distribution of the mean absolute error (MAE) for wind speed for the MMs. Summer and spring are generally associated with larger deviations between the modeled and observed wind speeds. It is well established that fall and winter weather in northern Europe is governed by large-scale planetary and synoptic weather phenomena, which is well captured by mesoscale models. During spring and summer, meso- and thermally induced phenomena (e.g., sea breezes and convection) have a larger impact on the flow, which is more difficult for the models to correctly capture. The lowest MAE is observed at FINO3 in



**Figure 6.** (a) Monthly distributions of mean wind speed for the MMs (box plots) and observations (star) at each location (colors). (b) Monthly distributions of the models for the mean absolute error (MAE) for wind speed at each location (colors). The boxes represent the second and third quartiles. The whiskers extend to the smallest (bottom) or largest (top) value that is within 1.5 times the inter-quartile range. Samples outside this range are shown as outliers.



**Figure 7.** Distribution of mean absolute error (MAE) for wind speed at the three sites for five stability classes: unstable (U), near-unstable (NU), neutral (N), near-stable (NS), and stable (S). See definitions in Table 2. The boxes represent the second and third quartiles. The whiskers extend to the smallest (bottom) or largest (top) value that is within 1.5 times the inter-quartile range. Samples outside this range are shown as outliers.

February, October, and November, with most MAE values near 10 %. The largest MAEs are in November at Cabauw (values in the range of 30–45 %).

### 3.1.5 Effect of atmospheric stability

It is generally acknowledged that non-neutral atmospheric stability conditions pose one of the greatest challenges for MMs (Fernando and Weil, 2010). To study the performance of the models in different stability regimes, the stability parameters supplied for each model (inverse Obukhov length or bulk Richardson number) were used to group the hourly samples into five stability classes based on Gryning et al. (2007) and Mohan and Siddiqui (1998), shown in Table 2. Because the models represent atmospheric stability in different ways, the number of samples in each stability group varies for the different models. However, the number of samples in each group was never below 150 h (out of 8760 h), and it was more than 400 in most cases. The MAE for wind speed was calculated for each of groups and for all models. The results are shown in Fig. 7.

At all three sites, the smallest deviations between modeled and measured wind speeds are found when the models perceive the surface layer stability from unstable (U) to stable (S). The MAE in these cases typically range from 10 to 35 %, with just a few models outside of the  $3 \times$  quartile range. The largest deviations are found when the models estimated very stable conditions (VS) or very unstable conditions (VU) (typical values in the range 15–45 % MAE). The site where the largest errors are found is Cabauw, and the smallest is FINO3. This is in agreement with the results in Sect. 3.1.

**Table 2.** Ranges of inverse Obukhov length ( $1/L$ ) and bulk Richardson number ( $Ri_b$ ) used in the stability classification. The  $1/L$  classes were used in Gryning et al. (2007) and the  $Ri_b$  classes in Mohan and Siddiqui (1998). In both cases the original very unstable and the stable classes have been combined into the open-ended stable class. The same is true for the original very unstable and unstable classes, which have been combined into the open-ended unstable class.

Stability class	Class name	$1/L$ interval [ $m^{-1}$ ]	$Ri_b$
U	Unstable	$1/L < -0.005$	$Ri_b < -0.011$
NU	Near-unstable	$-0.005 \leq 1/L < -0.002$	$-0.011 \leq Ri_b < -0.0036$
N	Neutral	$-0.002 \leq 1/L < 0.002$	$-0.0036 \leq Ri_b < 0.0072$
NS	Near-stable	$0.002 \leq 1/L < 0.005$	$0.0072 \leq Ri_b < 0.42$
S	Stable	$0.005 \leq 1/L$	$0.42 \leq Ri_b$

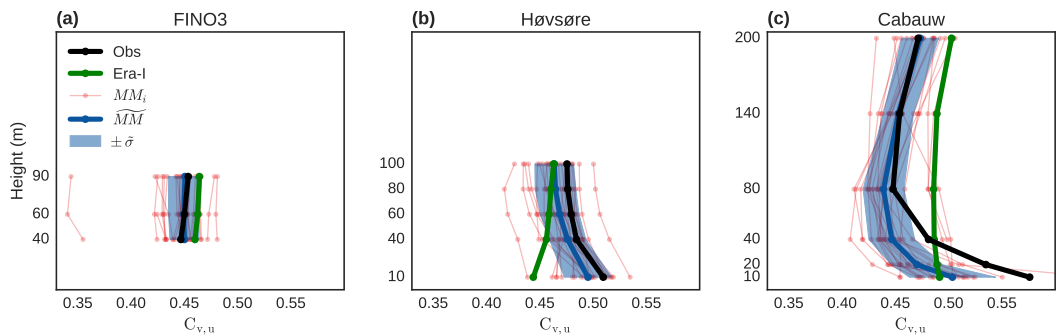


**Figure 8.** Vertical profiles of the coefficient of variation for wind speed  $C_{v,u}$  at the three sites for observations (black), ERA-Interim (green), the mesoscale models  $MM_i$  (red), and the mesoscale models mean and inter-model variance  $MM \pm \tilde{\sigma}$  (blue).

3.1.6 Coefficient of variation of wind speed

Figure 8 shows the mean coefficient of variation ( $C_{v,u}$ ) for wind speed at the three sites. At FINO3, the average of the MMs  $\tilde{C}_{v,u}$  is similar to the observations, with a bias of less than 1 % at all three heights. Ignoring one outlier, the inter-model variance ranges between 3.0 and 3.5 % at the three heights. The outlier, which shows much lower values, is a consequence of the low variance for that model compared to the other models. It was removed by the filtering method described in Sect. 2.3 when calculating the mean of the models ( $\tilde{C}_{v,u}$ ) and the inter-model variance ( $\tilde{\sigma}_{C_{v,u}}$ ). The ERA-Interim data set also captures the magnitude of  $C_{v,u}$  well.

At Høvsøre,  $C_{v,u}$  decreases with height for both the observations and most of the MMs. The inter-model mean of the models ( $\tilde{C}_{v,u}$ ) agrees well with the observations, but underestimates it by about 2 %. The ERA-Interim data set does not capture this behavior, and instead shows an increase with height. At the highest levels, however, it reaches the average of the models and the observed values. The spread of the MMs ( $\sigma_{C_{v,u}}$ ) is slightly higher than at FINO3 (3.6–4.4 %) and is highest at the lowest levels.

At Cabauw,  $C_{v,u}$  at 10 m is the largest value found across all sites. Above 10 m a sharp drop-off is found up to 80 m, where it starts to slowly increase up to 200 m. Most of the MMs capture this behavior, which is reflected in the mean of the models ( $\tilde{C}_{v,u}$ ). However, the models underestimate the magnitude and the drop-off of  $C_{v,u}$  at the lowest levels, with

**Table 3.** Participants in the study in alphabetical order.

Participant	Institution	Country
3E	Company	Belgium
Anemos GmbH	Company	Germany
ATM-PRO	Company	Belgium
CENER	Research center	Spain
CIEMAT	Research center	Spain
DEWI	Company	Germany
DTU Wind Energy	University	Denmark
DX Wind Technologies	Company	China
EMD International	Company	Denmark
ISAC-CNR	Research center	Italy
KNMI	Meteorological institute	The Netherlands
Met Office	Meteorological institute	United Kingdom
RES Ltd.	Company	United Kingdom
Statoil ASA	Company	Norway
University of Oldenburg	University	Germany
Vestas	Company	Denmark
Vortex	Company	Spain

a bias of up to 12 % at 10 and 20 m. Above 80 m the models agree with the observations. The ERA-Interim data set is nearly constant with height, underestimates  $C_{v,u}$  below 40 m, and overestimates it above. The inter-model variance ( $\tilde{\sigma}_{C_{v,u}}$ ) of the MMs is largest at the lowest levels, 8.0 % at 10 m, and gradually decreases to less than 4 % at 200 m.

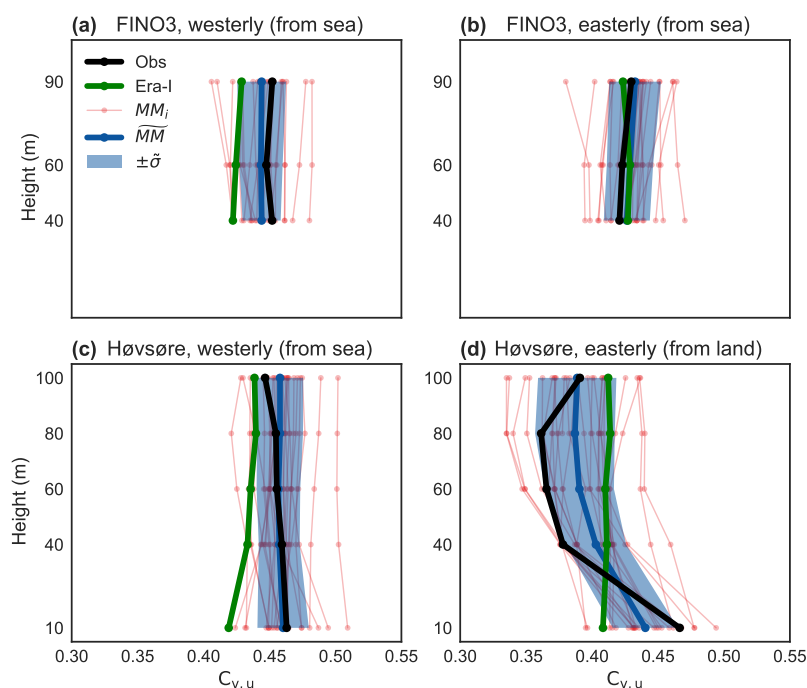


**Figure 9.** Coefficient of variation for wind speed  $C_{v,u}$  for westerly (a, c) and easterly (b, d) winds at FINO3 (a, b) and Høvsøre (c, d) for the observations (black), the ERA-Interim data set (green), the MMs  $MM_i$  (red), and the mesoscale models mean and inter-model variance  $MM \pm \tilde{\sigma}$  (blue).

#### Effect of upstream conditions on the variation of wind speed

The coastal site Høvsøre and the offshore site FINO3 is used to investigate whether there is a dependency of the coefficient of variation for wind speed (shown in Fig. 8) on upstream surface conditions. With a nearby coastline aligned north–south, Høvsøre represents the case with anisotropic surface roughness conditions: westerly winds come from the sea (on-shore flow) and easterly winds from land (offshore flow). In contrast, the offshore site FINO3 has isotropic upstream surface roughness. To study the differences, the coefficients of variation were binned according to four wind direction sectors, each spanning  $90^\circ$ : north, east, south, and west. The values for the east and west sectors were then extracted and analyzed. Figure 9 shows the profiles of  $C_{v,u}$  for the two wind directions at FINO3 and Høvsøre.

At FINO3, the coefficient of variance is almost constant with height and slightly lower for easterly winds than for westerly flow. This is true for both models and observations. The sample size for easterly winds is smaller, about half, than for westerly flow. However, both sample sizes are large ( $N > 1000$ ); thus, the influence from sample sizes is expected to be small. The average of the MMs captures the observed behavior well for both westerly and easterly winds, and the inter-model variance is similar for the two sectors. The ERA-Interim agrees better with the observations during easterly flow at FINO3.

At Høvsøre, the coefficient of variation is larger for westerly than for easterly winds. Easterly winds show larger coefficients of variation at 10 m than higher up. The reduction of  $C_{v,u}$  with height up to 40 m for easterly flow is underestimated by most of the mesoscale models and completely missed by the ERA-Interim data set. For westerly winds, the mean of the models and the observations agree but is underestimated by ERA-Interim.

The dependence on height of  $C_{v,u}$  is only present at Høvsøre for easterly winds and points to the influence of upstream surface conditions on the variation. The observed pattern is captured by the MMs, but the models show a more smoother vertical transition than the observations do. The ERA-Interim reanalysis does not capture the pattern.

#### 3.1.7 Distribution of wind speed shear exponent

Figure 10 shows the distributions of wind speed shear exponent ( $\alpha$ ) for each of the three sites calculated between 40 and 80 or 40 and 90 m. Under neutral atmospheric stability conditions and isotropic surface roughness, a sharp distribution centered around a single value is expected. This means that for offshore sites such as FINO3, the spread in shear exponent comes primarily from variations in atmospheric stability. With this in mind, the distributions show that most MMs capture the stability well at the site. The ERA-Interim data set does not capture the strongest shear situations well. This can be easily explained by the low data frequency (6 h).



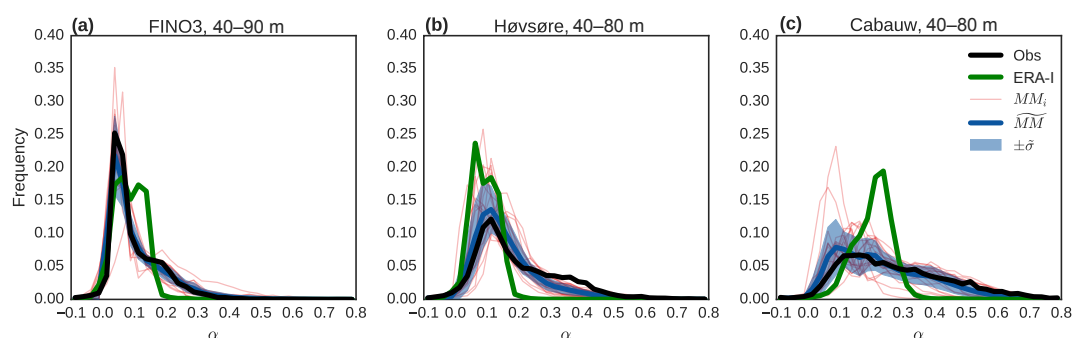


**Figure 10.** Frequency of occurrence of the shear exponent ( $\alpha$ ) at the three sites for the observations (black), the ERA-Interim data set (green), the mesoscale models  $MM_i$  (red), and the inter-model mean (blue line) and standard deviation  $\overline{MM} \pm \sigma$  (blue shade).

At Høvsøre and Cabauw, the distributions of  $\alpha$  reflect the combined effect of both the nonhomogenous upstream surface roughness and the variations in atmospheric stability. At the coastal site, the wind speed profile changes depending on whether the fetch is from land or from the sea, which is also reflected in the distribution of  $\alpha$  (Hahmann et al., 2015b). Figure 10 also shows that while the shear distributions are generally also well captured at Høvsøre and Cabauw, a slight shift towards lower values is observed at both sites. This points to an underestimation of the surface roughness, a misrepresentation of the atmospheric stability, or a combination of the two. Just like at FINO3, the ERA-Interim data set does not capture the weak and strong shear cases at Høvsøre and Cabauw.

### 3.2 Relating performance to model setup

To identify what model setup choices lead to better model performance, the statistics of each model across all heights are reduced to just two values at each site: NRMSE for wind speed ( $NRMSE_u$ ) and RMSE for wind speed shear exponent ( $RMSE_\alpha$ ). The shear exponent was calculated between pairs of nearby levels, e.g., at FINO3 two values were calculated, one between 40 and 70 m, and one between 70 and 90 m. The  $RMSE_\alpha$  was then calculated as described in Sect. 4 between modeled and observed values of the shear exponent across all height pairs.

Figure 11 shows  $NRMSE_u$  and  $RMSE_\alpha$  for all MMs at all three sites. It shows, similar to Sect. 3.1, that the models generally have smaller mean wind speed and mean shear exponent errors at the offshore site FINO3. However, as previously shown, errors are larger near the surface, and the three levels used at FINO3 are at 40 m and above, unlike Høvsøre and Cabauw where levels below 40 m are included.

The models were then grouped according to specific model components. Given the range of setup choices that influence the model performance, large groups were needed to obtain useful statistics. With this in mind, three setup options were chosen for analysis: PBL scheme, grid spacing, and simulation lead time; statistics of  $NRMSE_u$  and  $RMSE_\alpha$

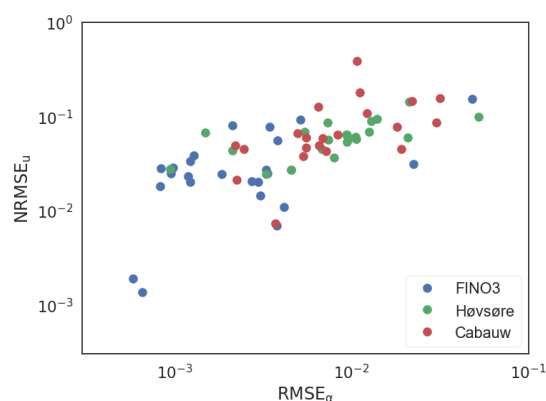


**Figure 11.** RMSE for wind speed shear exponent ( $RMSE_\alpha$ ) versus normalized RMSE for wind speed ( $NRMSE_u$ ) at the three sites.

were also computed for each group. The choice of groupings was based mainly on two criteria: (1) it was possible to form groups with at least six members in each group and (2) each of the options was highlighted in the literature as being important for model performance (Hahmann et al., 2015b; Gómez-Navarro et al., 2015; Carvalho et al., 2012; Draxl et al., 2014). Several other setup options were considered: MM, LSM, land cover, spin-up time, and data set used for initial and boundary conditions, but either it was not possible to group them in a meaningful way, or they were deemed of too little importance based on previous studies. Models missing information about particular setup options, or missing output at some heights, were excluded from this analysis.

#### 3.2.1 PBL scheme

The PBL scheme in a MM ensures an accurate representation of thermodynamic and kinematic structures of the lower troposphere (Cohen et al., 2015). Two important characteristics of the PBL schemes are their order of closure and whether mixing happens through a local or a nonlocal process. Equations

**Table 4.** Setup description of the 25 model setups ranked by horizontal grid spacing of the finest grid. The columns are the model name and version (model), the PBL scheme (PBL), the land surface model (LSM), whether nesting was used (Nest.), the horizontal grid spacing ( $\Delta$ ), the land cover source, simulation and spin-up time (Sim. time), and initial and boundary condition data (B.C.).

No.	Model	PBL	LSM	Nest.	$\Delta$ (km)	Land cover	Sim. time (h)	B.C.
1	WRF V3.6.1 <sup>a</sup>	Custom	–	yes	1	CORINE <sup>b</sup>	48–24	Era-I <sup>c</sup>
2	MAESTRO V15.01	–	–	no	1	CORINE	–	Era-I
3	WRF V3.6.1	MYJ <sup>d</sup>	Noah <sup>e</sup>	yes	2	USGS <sup>f</sup>	78–6	Era-I
4	WRF V3.3.1	MYJ	–	yes	2	GlobCover <sup>g</sup>	11 064–24	Era-I
5	WRF V3.5.1	YSU <sup>h</sup>	Noah	yes	2	CORINE	30–6	Era-I
6	WRF V3.5.1	YSU	Noah	yes	2	–	264–24	Era-I
7	HARMONIE V37h1.1 <sup>i</sup>	SURFEX <sup>j</sup>	ISBA <sup>k</sup>	yes	2.5	ECOCCLIMAP <sup>l</sup>	7–1	Era-I
8	WRF V3.6	ACM2 <sup>m</sup>	Noah	yes	3	USGS-MODIS	84–12	FNL <sup>n</sup>
9	WRF V3.4	MYJ	Noah	no	3	USGS	28–4	Era-I
10	WRF V3.6.1	YSU	Noah	yes	3	CORINE	672–96	CFSR <sup>o</sup>
11	WRF V3.0.1	MYJ	Noah	yes	3	GlobCover	36–6	CFSR
12	WRF V3.6.1	MYNN <sup>p</sup>	Noah	yes	3	USGS	816–72	Era-I
13	WRF V3.0.1	MYJ	Noah	yes	3	GlobCover	36–12	MERRA <sup>q</sup>
14	WRF V3.0.1	MYJ	Noah	yes	3	GlobCover	36–12	Era-I
15	WRF V3.1	MYJ	Noah	yes	3	MODIS <sup>r</sup>	54–6	FNL
16	WRF V3.6.1	YSU	Noah	yes	3	CORINE	336–96	CFSR
17	WRF V3.5.1	MYJ	Noah	yes	4	IGBP-MODIS <sup>s</sup>	264–24	Era-I
18	UM V8.4 <sup>t</sup>	Lock <sup>u</sup>	JULES <sup>v</sup>	yes	4	IGBP-MODIS	36–6	Era-I
19	WRF V3.5.1	YSU	Noah	yes	5	USGS	2424–24	Era-I
20	SKIRON V6.9 <sup>w</sup>	MYNN	OSU <sup>x</sup>	no	5	USGS	51–3	GFS <sup>y</sup>
21	WRF V3.5.1	YSU	Noah	yes	5	USGS	2424–24	Era-I
22	WRF V3.5.1	YSU	Noah	yes	6	IGBP-MODIS	264–24	Era-I
23	HIRLAM V6.4.2 <sup>z</sup>	CBR <sup>aa</sup>	ISBA	no	11	USGS	9–3	IFS <sup>ab</sup>
24	RAMS V6.0 <sup>ac</sup>	MYNN	LEAF <sup>ad</sup>	no	12	CORINE	36–12	IFS
25	MM5 V3 <sup>ae</sup>	YSU	–	no	20	CORINE	744–24	MERRA

<sup>a</sup> Skamarock et al. (2008). <sup>b</sup> Bossard et al. (2000). <sup>c</sup> Dee et al. (2011). <sup>d</sup> Janjić (2002). <sup>e</sup> Niu et al. (2011). <sup>f</sup> Garbarino et al. (2002). <sup>g</sup> Arino et al. (2008). <sup>h</sup> Hong et al. (2006). <sup>i</sup> Seity et al. (2011). <sup>j</sup> Masson et al. (2013) (Supplement). <sup>k</sup> Noilhan and Mahfouf (1996). <sup>l</sup> Champeaux et al. (2005). <sup>m</sup> Pleim (2007a). <sup>n</sup> NCEP final analysis. <sup>o</sup> Saha et al. (2010). <sup>p</sup> Nakanishi and Niino (2006). <sup>q</sup> Rienecker et al. (2011). <sup>r</sup> Friedl et al. (2010). <sup>s</sup> Loveland and Belward (1997). <sup>t</sup> Lean et al. (2008). <sup>u</sup> Lock et al. (2000). <sup>v</sup> Cox et al. (1999). <sup>w</sup> Kallos et al. (1997). <sup>x</sup> Pan and Mahrt (1987). <sup>y</sup> Global Forecast System. <sup>z</sup> Kallberg (1989). <sup>aa</sup> Cuxart et al. (2000). <sup>ab</sup> Integrated Forecasting System. <sup>ac</sup> Pielke et al. (1992). <sup>ad</sup> Walko and Tremback (2005). <sup>ae</sup> Grell et al. (1994).

tions describing turbulent motion of order  $n$  contain terms of order  $n + 1$ . The order of closure describes the highest order of equations included; higher orders are parametrized. In local schemes, variables are only affected by adjacent cells, while nonlocal schemes relate changes to gradients in the whole PBL column (Cohen et al., 2015).

To study the influence of the PBL schemes used, the MMs were split into three groups: YSU, MYJ, and Other. The statistics of NRMSE<sub>u</sub> and RMSE<sub>α</sub> for these groups are shown in Table 5. The YSU group consists of six models that used the YSU PBL scheme (Hong et al., 2006), which is a first-order nonlocal scheme. The models in this group span a range of grid spacings and lead times, but models with larger-than-average grid spacing and longer-than-average lead times dominate the group. The MYJ group contains six models that used the MYJ PBL scheme (Janjić, 1994), which is a 1.5 order local scheme. Most of the models use a short lead-time limit and a grid spacing that is close to the average for the MMs in this study. The last group, labeled Other, contains nine models that use a mix of different PBL

schemes (see Table 4), with different orders of closure and a mix of local and nonlocal formulations. These models have a wide representation of different grid spacings and lead times.

At FINO3, the group consisting of models not using either the YSU or MYJ PBL schemes generally has smaller wind speed errors; even though the group also contains the model with the largest NRMSE<sub>u</sub>. The models using the MYJ PBL scheme have smaller wind shear exponent errors, and also on average smaller wind speed errors than YSU. However, the median model in the YSU and MYJ groups has similar wind speed errors.

At Høvsøre, the three groups have very similar mean wind speed error statistics, with YSU showing only slightly smaller errors. However, for wind shear exponent, the models in the YSU group have the smallest errors, both on average and for the median model. Draxl et al. (2014) studied similar error statistics at Høvsøre for the WRF model run with a number of different PBL schemes during October 2009. They, unlike this study, found that MYJ gave slightly smaller errors than YSU. However, Draxl et al. (2014) used a version

**Table 5.** Statistics of NRMSE for wind speed ( $\text{NRMSE}_u$ ) and RMSE for wind speed shear exponent ( $\text{RMSE}_\alpha$ ) associated with the groups of PBL schemes across all heights at each site. There are six models in the YSU group, six in the MYJ group, and nine in the Other group. The smallest value for each metric is in bold.

FINO3						
Metric	PBL	Mean	Median	SD	Min	Max
$\text{NRMSE}_u$	YSU	0.047	0.029	0.028	0.018	0.091
	MYJ	0.032	0.029	<b>0.011</b>	0.020	<b>0.055</b>
	Other	<b>0.028</b>	<b>0.014</b>	0.045	<b>0.001</b>	0.154
$\text{RMSE}_\alpha$	YSU	0.029	0.019	0.034	0.004	0.116
	MYJ	<b>0.010</b>	<b>0.010</b>	<b>0.007</b>	0.004	<b>0.025</b>
	Other	0.057	0.019	0.120	<b>0.003</b>	0.396
Høvsøre						
Metric	PBL	Mean	Median	SD	Min	Max
$\text{NRMSE}_u$	YSU	<b>0.061</b>	<b>0.058</b>	0.037	<b>0.024</b>	0.144
	MYJ	0.063	0.064	<b>0.013</b>	0.045	<b>0.090</b>
	Other	0.062	0.059	0.026	0.027	0.100
$\text{RMSE}_\alpha$	YSU	<b>0.035</b>	<b>0.018</b>	0.029	<b>0.005</b>	0.087
	MYJ	0.049	0.044	<b>0.011</b>	0.030	<b>0.061</b>
	Other	0.086	0.051	0.100	0.027	0.365
Cabauw						
Metric	PBL	Mean	Median	SD	Min	Max
$\text{NRMSE}_u$	YSU	<b>0.058</b>	<b>0.049</b>	<b>0.033</b>	0.021	<b>0.127</b>
	MYJ	0.066	0.053	0.037	0.038	0.146
	Other	0.124	0.086	0.106	<b>0.007</b>	0.389
$\text{RMSE}_\alpha$	YSU	<b>0.025</b>	<b>0.022</b>	<b>0.007</b>	0.018	<b>0.036</b>
	MYJ	0.045	0.023	0.036	0.020	0.117
	Other	0.064	0.075	0.036	<b>0.015</b>	0.113

of the YSU scheme with a bug that was corrected in WRF version 3.4.1 (Hahmann et al., 2015b).

At Cabauw, the YSU group has smaller errors than the other groups for both wind speed and wind shear exponent, but the errors for the median model in the YSU and MYJ groups are quite similar. The single most accurate model is found in the Other group, but that group as a whole has larger errors.

### 3.2.2 Grid spacing

A mesoscale model should be able to explicitly resolve smaller and smaller phenomena as the grid spacing is decreased. Skamarock (2004) illustrated that the effective resolution of the WRF model is approximately 7 times the grid spacing used. However, mesoscale models, as the name suggests, have been developed to simulate the mesoscale, and they are often not capable of simulating weather at scales that lie between the micro- and mesoscales, i.e., between approximately 100 and 2000 m. To study the importance of the grid spacing, the models were ranked by grid spacing, similar to Table 4. The models were then split into three groups:

**Table 6.** Statistics of NRMSE for wind speed ( $\text{NRMSE}_u$ ) and RMSE for wind speed shear exponent ( $\text{RMSE}_\alpha$ ) associated with the group model grid spacing across all heights at each site. There are seven models in the fine group, eight in the moderate group, and six in the coarse group. The smallest value for each metric is in bold.

FINO3						
Metric	Grid spacing	Mean	Median	SD	Min	Max
$\text{NRMSE}_u$	Fine	<b>0.024</b>	<b>0.020</b>	<b>0.015</b>	<b>0.001</b>	<b>0.055</b>
	Moderate	0.037	0.027	0.025	0.007	0.080
	Coarse	0.044	0.025	0.046	0.002	0.154
$\text{RMSE}_\alpha$	Fine	<b>0.013</b>	0.013	<b>0.008</b>	0.005	<b>0.025</b>
	Moderate	0.015	<b>0.011</b>	<b>0.008</b>	0.004	0.028
	Coarse	0.067	0.019	0.121	<b>0.003</b>	0.396
Høvsøre						
Metric	Grid spacing	Mean	Median	SD	Min	Max
$\text{NRMSE}_u$	Fine	0.057	<b>0.057</b>	0.026	<b>0.024</b>	0.093
	Moderate	<b>0.054</b>	<b>0.057</b>	<b>0.012</b>	0.027	<b>0.064</b>
	Coarse	0.075	0.068	0.034	0.028	0.144
$\text{RMSE}_\alpha$	Fine	<b>0.040</b>	<b>0.040</b>	0.021	0.015	0.076
	Moderate	0.047	0.048	<b>0.010</b>	0.030	<b>0.060</b>
	Coarse	0.088	0.055	0.109	<b>0.005</b>	0.365
Cabauw						
Metric	Grid spacing	Mean	Median	SD	Min	Max
$\text{NRMSE}_u$	Fine	0.086	0.064	0.056	<b>0.007</b>	0.178
	Moderate	<b>0.048</b>	<b>0.046</b>	<b>0.015</b>	0.021	<b>0.078</b>
	Coarse	0.146	0.107	0.115	0.049	0.389
$\text{RMSE}_\alpha$	Fine	0.052	0.030	0.036	0.016	0.117
	Moderate	<b>0.031</b>	<b>0.021</b>	<b>0.017</b>	0.020	<b>0.066</b>
	Coarse	0.063	0.060	0.041	<b>0.015</b>	0.113

fine, moderate, and coarse. The fine group consists of seven models that all have a grid spacing below 3 km. The moderate group consists of eight models at exactly 3 km, and the coarse group consists of six models above 3 km. The fine group contains models that are well distributed in terms of PBL schemes and simulation lead time. The moderate models also have a good representation of different PBL schemes and lead-time limits, but the MYJ PBL scheme and short lead times are most common. The coarse group contains no models using the MYJ PBL scheme, and half of the models use a short lead time.

Table 6 shows the statistics for  $\text{NRMSE}_u$  and  $\text{RMSE}_\alpha$ . At FINO3, the fine group has the smallest wind speed errors. For the wind shear exponent, the smallest error is found in the coarse group, but on average the fine and moderate groups have smaller errors. At Høvsøre, the fine and moderate groups have similar errors for both wind speed and shear exponent. However, the model with the smallest shear exponent error is found in the coarse group. At Cabauw, the moderate group shows the smallest errors for both metrics, followed by the fine group. However, just as for Høvsøre, the model with the smallest  $\text{RMSE}_\alpha$  is found in the coarse group.

**Table 7.** Statistics of NRMSE for wind speed ( $\text{NRMSE}_u$ ) and RMSE for wind speed shear exponent ( $\text{RMSE}_\alpha$ ) associated with each group of simulation lead time across all heights at each site. There are nine models in the short group, eight in the medium group, and seven in the long group. The smallest value for each metric is in bold.

FINO3						
Metric	Sim. length	Mean	Median	SD	Min	Max
$\text{NRMSE}_u$	Short	0.032	<b>0.020</b>	0.044	<b>0.001</b>	0.154
	Medium	<b>0.028</b>	0.025	<b>0.014</b>	0.007	<b>0.055</b>
	Long	0.051	0.031	0.028	0.025	0.091
$\text{RMSE}_\alpha$	Short	0.052	<b>0.010</b>	0.122	<b>0.003</b>	0.396
	Medium	<b>0.016</b>	0.016	<b>0.006</b>	<b>0.003</b>	<b>0.025</b>
	Long	0.029	0.022	0.036	0.004	0.116
Høvsøre						
Metric	Sim. length	Mean	Median	SD	Min	Max
$\text{NRMSE}_u$	Short	<b>0.058</b>	0.059	0.023	<b>0.024</b>	0.100
	Medium	0.070	0.068	<b>0.016</b>	0.044	<b>0.093</b>
	Long	0.062	<b>0.057</b>	0.039	0.027	0.144
$\text{RMSE}_\alpha$	Short	0.081	<b>0.044</b>	0.102	0.018	0.365
	Medium	<b>0.044</b>	0.056	<b>0.023</b>	0.009	<b>0.076</b>
	Long	0.046	0.048	0.025	<b>0.005</b>	0.087
Cabauw						
Metric	Sim. length	Mean	Median	SD	Min	Max
$\text{NRMSE}_u$	Short	0.088	<b>0.058</b>	0.108	<b>0.007</b>	0.389
	Medium	0.103	0.097	0.058	0.043	0.178
	Long	<b>0.068</b>	0.064	<b>0.035</b>	0.021	<b>0.127</b>
$\text{RMSE}_\alpha$	Short	0.046	<b>0.021</b>	0.038	<b>0.015</b>	0.113
	Medium	0.058	0.054	0.038	0.018	0.117
	Long	<b>0.031</b>	0.025	<b>0.012</b>	0.020	<b>0.052</b>

3.2.3 Simulation time

As the solution in mesoscale models is integrated forward in time, the uncertainties associated with the errors in the initial conditions increase (Yoden, 2007). This can cause the model solution to drift away from the true solution. Furthermore, amplification errors can reduce the variance, which reduces the accuracy of the model in a statistical sense. To study the influence of the simulation time on the model performance, the models were ranked and split into three groups: short, medium, and long. The short group consists of nine models with a lead time below 48 h. Four models in the group use the MYJ scheme, and one uses the YSU scheme. The short group has a good representation of models with different grid spacings. The medium group includes eight models with a lead time between 48 and 335 h. The group has a good representation of different PBL schemes and grid spacing. The long group consists of seven models with a lead-time limit above 335 h. Five of the models use the YSU PBL scheme, and most of the models use a larger-than-average grid spacing.

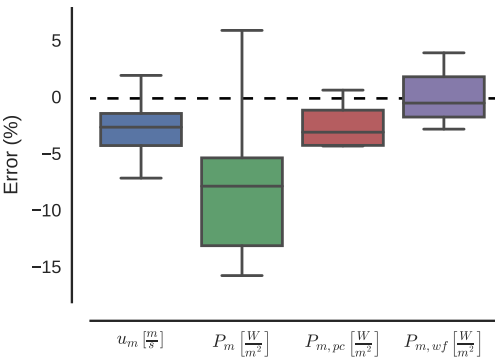


**Figure 12.** Distribution of errors from the model’s output at 90 m at FINO3 for the following errors: (1) the mean wind speed  $u_m$  (blue), (2) the power density  $P_m$  (green), (3) the power density with an implied power curve  $P_{m,pc}$  (red), and (4) the averaged power density of a wind farm, including the same implied power curve as (3) and the wake effects (purple). Outliers are not shown; the most extreme ones are  $-25\%$  for  $u_m$ ,  $-60\%$  for  $P_m$ ,  $-37\%$  for  $P_{m,wf}$ , and  $-35\%$  for  $P_{m,pc}$ .

Table 7 shows the errors statistics for the three simulation-time groups. At FINO3, the median model from the short group has the lowest  $\text{NRMSE}_u$  and  $\text{RMSE}_\alpha$ , but because one model has large errors, the lowest mean errors are found in the medium group. The medium group has smaller errors across all metrics compared to the long group.

At Høvsøre, the short and long groups have similar error statistics for wind speed, and both measures are lower than those for the medium group. For  $\text{RMSE}_\alpha$  the median model from the short group has the smallest error, while on average the errors are smallest in the medium group.

At Cabauw, the smallest errors for both wind speed and shear exponent are on average found in the long group, while the median model with the smallest errors is in the short group. It is worth noting that five of the seven models in the long group use the YSU PBL scheme, and in Sect. 3.2.1 the models using the YSU PBL scheme were shown to have smaller errors at Cabauw; thus, it cannot be ruled out that the small errors in the long group at Cabauw are related to the overrepresentation of the YSU scheme and not the simulation length.

3.3 Wind energy application

As described in Sect. 2.4, the output from the mesoscale models was applied to a simple wind energy exercise. The 90 m wind resource of a Horns Rev wind farm was estimated using the output from the various MMs at FINO3. Figure 12 shows the errors for four metrics: (1) error in mean wind speed  $u_m$ , (2) error in mean power density  $P_m$ , (3) error in mean power density using a single power curve  $P_{m,pc}$ , and (4) error in the mean power density of a wind farm of 80 turbines  $P_{m,wf}$ , including wake effects.



Figure 12 shows that the majority of the models have less than  $\pm 5\%$  error in mean wind speed. The errors are mostly underestimations, and in a few cases severe underestimation of more than 10 % (outside the scale of the figure). For the mean power density, the spread of the models is, as expected, much larger due to the third-power dependence on the wind speed. However, when the power density is calculated using a turbine power curve, where the highest wind speeds ( $> 14 \text{ m s}^{-1}$ ) are less important, the inter-model variance is comparable to that for mean wind speed. For the wind farm case, where the power density depends on the wind direction distribution, because of the wake losses, the variance is comparable in size to that of the mean wind speed and  $P_{\text{m,pc}}$ , and most models have errors smaller than  $\pm 2\%$ . The improvement seen for  $P_{\text{m,wr}}$  is caused by the underestimation of the wake effects by most models, leading to a relative increase in mean power density, offsetting the underprediction from the modeled wind speed distribution. However, the relative effect of over- or underpredicting the wake effects may just as well enhance the total power density errors, given slightly different wind direction distributions.

#### 4 Summary and conclusions

The mesoscale models in this study are able to reproduce the observed mean wind speed profiles and the distributions of wind speed well. At FINO3 and above 10 m at Høvsøre, the average of the models has a bias of 3 % or less. The largest mean wind speed biases (7–9 %) are found at the lowest levels at Høvsøre and Cabauw. Similarly, the MMs were able to reproduce the relative variations of wind speed well in most cases (Fig. 8), but they underestimated the relative variations at the lowest levels at Cabauw. A simple analysis of the impact of upstream surface roughness conditions on the relative wind speed variations suggested that the models may be misrepresenting the surface characteristics (Fig. 9), which could be a misrepresentation of either the land use classification, the conversion of land use classes into surface roughness lengths, or the PBL scheme. This problem highlights the need for (1) further analysis of the representativeness of the surface characteristics in mesoscale models and (2) downscaling of the mesoscale results using a coupled microscale model to capture subgrid-scale influence from variations in orography and surface roughness. The modeled distributions of the wind direction showed only minor differences compared to the observed ones.

For future benchmarking exercises, our study shows that the focus should be on the model representation of surface characteristics, such as orography and land use, and their associated surface roughness. An attempt was made here to include these details, but because only a subset of the participants supplied this information, it was not feasible. Further studies could also benefit from including more land masts with low to moderate complexity, where capturing the

surface characteristics is important, but still manageable by mesoscale models.

The impact of choosing specific model subcomponents was studied in some detail. To allow this, the output from the models was reduced to two metrics at each site, one related to the wind speed bias (NRMSE for wind speed) and one related to the shape of the wind speed profile (RMSE for wind speed shear exponent). The models were then separated into large groups according to their model setup for three setup choices: PBL scheme, grid spacing, and simulation lead time. At FINO3, the grouping revealed that the models using the MYJ PBL scheme had smaller wind speed and shear exponent errors than those that use the YSU scheme. At Høvsøre and Cabauw, the opposite was true. However, the differences between the two groups were not significant and the median model from the two groups had similar errors. Grouping the models according to grid spacing showed that the models with 3 km grid spacing or smaller had lower errors than the group with the largest grid spacings. For these sites, no conclusive evidence was found that reducing the grid spacing below 3 km results in smaller errors. For simulation lead time, the median model from the group with short lead times had the smallest errors at all sites, with the exception of the shear exponent error at Høvsøre. However, no significant difference between the mean of the groups was found, which suggests that the PBL scheme and grid spacing may be of greater importance for the performance at these sites. Future studies should include many more runs to provide more robust statistics, which can provide a basis for best-practice guidelines for wind energy applications using NWP models.

Last, we used the observed and modeled time series for a classical wind energy application, the estimation of power production at a hypothetical wind farm at FINO3. The power production, including wake losses, was estimated for both a single turbine and for a wind farm, using a standard power curve. The exercise showed that while a large spread exists between the modeled power density, it is reduced when the power is calculated using a power curve. It also showed the importance of accurately estimating the wind direction distribution since a small deviation in the distributions might induce large changes in the power production because of its sensitivity to the wind farm layout.

**Data availability.** The output data from the mesoscale models have been submitted to the European Wind Energy Association (EAWA) for the mesoscale benchmarking study under an agreement that ensures that individual participants are anonymous in the reported results, and that the model output was not publicly shared. The measurements from the meteorological masts FINO3, Høvsøre, and Cabauw are provided by the data owners under an agreement of not sharing the data with any third party.

**Competing interests.** The authors declare that they have no conflict of interest.

**Acknowledgements.** We would like to thank the three anonymous reviewers for constructive criticism. Their feedback elevated the level of the paper. Funding from the EU and the Danish Energy Agency through the project EUDP 14-II and ERA-NET Plus – New European Wind Atlas is greatly appreciated. The authors would also like to thank the European Wind Energy Association (EWEA) for organizing this mesoscale benchmarking study, the German Federal Ministry for the Environment, Nature Conservation, and Nuclear Safety (BMU), and the Project Management Jülich (PTJ) for sharing the FINO3 mast data. We would also like to thank the Cabauw Experimental Site for Atmospheric Research (CESAR) for making the measurements from the Cabauw mast freely available online (<http://www.cesar-observatory.nl>). Furthermore, we would like to thank the test and measurement section of DTU for providing the Høvsøre mast data. Finally, we would like to thank all the modeling groups that submitted output for this intercomparison. This study would not be possible without their contributions.

Edited by: J. Lundquist

Reviewed by: three anonymous referees

## References

- Arino, O., Bicheron, P., Achard, F., and Latham, J.: The most detailed portrait of Earth, *ESA Bull-Eur. Space*, available at: [https://www.esa.int/esapub/bulletin/bulletin136/bul136d\\_arino.pdf](https://www.esa.int/esapub/bulletin/bulletin136/bul136d_arino.pdf) (last access: 28 April 2017), 2008.
- Badger, J., Frank, H., Hahmann, A. N., and Giebel, G.: Wind-Climate Estimation Based on Mesoscale and Microscale Modeling: Statistical-Dynamical Downscaling for Wind Energy Applications, *J. Appl. Meteorol. Clim.*, 53, 1901–1919, doi:10.1175/JAMC-D-13-0147.1, 2014.
- Bechmann, A., Sørensen, N. N., Berg, J., Mann, J., and Réthoré, P. E.: The Bolund Experiment, Part II: Blind Comparison of Microscale Flow Models, *Bound-Lay. Meteorol.*, 141, 245–271, doi:10.1007/s10546-011-9637-x, 2011.
- Bossard, M., Feranec, J., and Otahel, J.: CORINE Land Cover Technical Guide – Addendum, European Environment Agency, 1–105, available at: <https://www.eea.europa.eu/publications/COR0-landcover> (last access: 28 April 2017), 2000.
- Bowler, N. E., Pierce, C. E., and Seed, A. W.: STEPS: A probabilistic precipitation forecasting scheme which merges an extrapolation nowcast with downscaled NWP, *Q. J. Roy. Meteor. Soc.*, 132, 2127–2155, doi:10.1256/qj.04.100, 2006.
- Carvalho, D., Rocha, A., Gómez-Gesteira, M., and Santos, C.: A sensitivity study of the WRF model in wind simulation for an area of high wind energy, *Environ. Modell. Softw.*, 33, 23–34, doi:10.1016/j.envsoft.2012.01.019, 2012.
- Carvalho, D., Rocha, A., Gómez-Gesteira, M., and Silva Santos, C.: WRF wind simulation and wind energy production estimates forced by different reanalyses: Comparison with observed data for Portugal, *Appl. Energ.*, 117, 116–126, doi:10.1016/j.apenergy.2013.12.001, 2014a.
- Carvalho, D., Rocha, A., Gómez-Gesteira, M., and Silva Santos, C.: Sensitivity of the WRF model wind simulation and wind energy production estimates to planetary boundary layer parameterizations for onshore and offshore areas in the Iberian Peninsula, *Appl. Energ.*, 135, 234–246, doi:10.1016/j.apenergy.2014.08.082, 2014b.
- Champeaux, J. L., Masson, V., and Chauvin, F.: ECOCLIMAP: a global database of land surface parameters at 1 km resolution, *Meteorol. Appl.*, 12, 29–32, doi:10.1017/S1350482705001519, 2005.
- Cohen, A. E., Cavallo, S. M., Coniglio, M. C., and Brooks, H. E.: A Review of Planetary Boundary Layer Parameterization Schemes and Their Sensitivity in Simulating Southeastern U.S. Cold Season Severe Weather Environments, *Weather Forecast.*, 30, 591–612, doi:10.1175/WAF-D-14-00105.1, 2015.
- Constantinescu, E. M., Zavala, V. M., Rocklin, M., Lee, S., and Anitescu, M.: A computational framework for uncertainty quantification and stochastic optimization in unit commitment with wind power generation, *IEEE T. Power Syst.*, 26, 431–441, doi:10.1109/TPWRS.2010.2048133, 2011.
- Cox, P. M., Betts, R. A., Bunton, C. B., Essery, R. L. H., Rowntree, P. R., and Smith, J.: The impact of new land surface physics on the GCM simulation of climate and climate sensitivity, *Clim. Dynam.*, 15, 183–203, doi:10.1007/s003820050276, 1999.
- Cuxart, J., Bougeault, P., and Redelsperger, J.-L.: A turbulence scheme allowing for mesoscale and large-eddy simulations, *Q. J. Roy. Meteor. Soc.*, 126, 1–30, doi:10.1002/qj.49712656202, 2000.
- Dee, D. P., Uppala, S. M., Simmons, A. J., Berrisford, P., Poli, P., Kobayashi, S., Andrae, U., Balmaseda, M. A., Balsamo, G., Bauer, P., Bechtold, P., Beljaars, A. C. M., van de Berg, L., Bidlot, J., Bormann, N., Delsol, C., Dragani, R., Fuentes, M., Geer, A. J., Haimberger, L., Healy, S. B., Hersbach, H., Hólm, E. V., Isaksen, I., Kållberg, P., Köhler, M., Matricardi, M., McNally, A. P., Monge-Sanz, B. M., Morcrette, J. J., Park, B. K., Peubey, C., de Rosnay, P., Tavolato, C., Thépaut, J. N., and Vitart, F.: The ERA-Interim reanalysis: Configuration and performance of the data assimilation system, *Q. J. Roy. Meteor. Soc.*, 137, 553–597, doi:10.1002/qj.828, 2011.
- Draxl, C., Hahmann, A. N., Peña, A., and Giebel, G.: Evaluating winds and vertical wind shear from Weather Research and Forecasting model forecasts using seven planetary boundary layer schemes, *Wind Energy*, 17, 39–55, doi:10.1002/we.1555, 2014.
- Fabre, S., Stickland, M., Scanlon, T., Oldroyd, A., Kindler, D., and Quail, F.: Measurement and simulation of the flow field around the FINO3 triangular lattice meteorological mast, *J. Wind Eng. Ind. Aerod.*, 130, 99–107, doi:10.1016/j.jweia.2014.04.002, 2014.
- Fernando, H. J. S. and Weil, J. C.: Whither the stable boundary layer?, *B. Am. Meteorol. Soc.*, 91, 1475–1484, doi:10.1175/2010BAMS2770.1, 2010.
- Friedl, M. A., Sulla-Menashe, D., Tan, B., Schneider, A., Ramankutty, N., Sibley, A., and Huang, X.: MODIS Collection 5 global land cover: Algorithm refinements and characterization of new datasets, *Remote Sens. Environ.*, 114, 168–182, doi:10.1016/j.rse.2009.08.016, 2010.

- Garbarino, R., Struzeski, T., and Casadevall, T.: US Geological Survey, available at: <http://citeseerx.ist.psu.edu/viewdoc/summary?doi=10.1.1.404.5834> (last access: 28 April 2017), 2002.
- García-Díez, M., Fernández, J., Fita, L., and Yagüe, C.: Seasonal dependence of WRF model biases and sensitivity to PBL schemes over Europe, *Q. J. Roy. Meteor. Soc.*, 139, 501–514, doi:10.1002/qj.1976, 2013.
- Gebhardt, C., Theis, S., Paulat, M., and Ben Bouallègue, Z.: Uncertainties in COSMO-DE precipitation forecasts introduced by model perturbations and variation of lateral boundaries, *Atmos. Res.*, 100, 168–177, doi:10.1016/j.atmosres.2010.12.008, 2011.
- Gómez-Navarro, J. J., Raible, C. C., and Dierer, S.: Sensitivity of the WRF model to PBL parametrisations and nesting techniques: evaluation of wind storms over complex terrain, *Geosci. Model Dev.*, 8, 3349–3363, doi:10.5194/gmd-8-3349-2015, 2015.
- Grell, G., Dudhia, J., and Stauffer, D.: A description of the fifth-generation Penn State/NCAR mesoscale model (MM5), NCAR Technical note, 1–121, 1994.
- Gryning, S. E., Batchvarova, E., Brümmner, B., Jørgensen, H., and Larsen, S.: On the extension of the wind profile over homogeneous terrain beyond the surface boundary layer, *Bound.-Lay. Meteorol.*, 124, 251–268, doi:10.1007/s10546-007-9166-9, 2007.
- Hahmann, A. N., Lennard, C., Badger, J., Vincent, C. L., Kelly, M. C., Volker, P. J. H., and Refslund, J.: Mesoscale modeling for the Wind Atlas of South Africa (WASA) project, DTU Wind Energy, No. 0050, 80 pp., doi:10.13140/RG.2.1.3735.6887, 2015a.
- Hahmann, A. N., Vincent, C. L., Peña, A., Lange, J., and Hasager, C. B.: Wind climate estimation using WRF model output: Method and model sensitivities over the sea, *Int. J. Climatol.*, 35, 3422–3439, doi:10.1002/joc.4217, 2015b.
- Hong, S.-Y., Noh, Y., and Dudhia, J.: A New Vertical Diffusion Package with an Explicit Treatment of Entrainment Processes, *Mon. Weather Rev.*, 134, 2318–2341, doi:10.1175/MWR3199.1, 2006.
- Horvath, K., Koracin, D., Vellore, R., Jiang, J., and Belu, R.: Sub-kilometer dynamical downscaling of near-surface winds in complex terrain using WRF and MM5 mesoscale models, *J. Geophys. Res.-Atmos.*, 117, 1–19, doi:10.1029/2012JD017432, 2012.
- Jackson, P. S. and Hunt, J. C. R.: Turbulent wind flow over a low hill, *Q. J. Roy. Meteor. Soc.*, 101, 929–955, doi:10.1002/qj.49710143015, 1975.
- Janjić, Z. I.: The Step-Mountain Eta Coordinate Model: Further Developments of the Convection, Viscous Sublayer, and Turbulence Closure Schemes, *Mon. Weather Rev.*, 122, 927–945, doi:10.1175/1520-0493(1994)122<0927:TSMECM>2.0.CO;2, 1994.
- Janjić, Z. I.: Nonsingular implementation of the Mellor–Yamada level 2.5 scheme in the NCEP Meso model, NCEP office note, NOAA Science Center, Camp Springs, MD, USA, 2002.
- Jiménez, P. A. and Dudhia, J.: Improving the representation of resolved and unresolved topographic effects on surface wind in the wrf model, *J. Appl. Meteorol. Clim.*, 51, 300–316, doi:10.1175/JAMC-D-11-084.1, 2012.
- Jiménez, P. A., de Arellano, J. V. G., Dudhia, J., and Bosveld, F. C.: Role of synoptic- and meso-scales on the evolution of the boundary-layer wind profile over a coastal region: the near-coast diurnal acceleration, *Meteorol. Atmos. Phys.*, 128, 39–56, doi:10.1007/s00703-015-0400-6, 2016.
- Kallberg, P.: The HIRLAM level 1 system, Documentation manual, SMHI, S-60176, Norrköping, Sweden, 1989.
- Kallos, G., Nickovic, S., and Papadopoulos, A.: The regional weather forecasting system SKIRON: An overview, Proceedings of the symposium on regional weather prediction on parallel computer environments, University of Athens, Athens, Greece, 1997.
- Kanamitsu, M., Ebisuzaki, W., Woollen, J., Yang, S. K., Hnilo, J. J., Fiorino, M., and Potter, G. L.: NCEP-DOE AMIP-II reanalysis (R-2), *B. Am. Meteorol. Soc.*, 83, 1631–1643, doi:10.1175/BAMS-83-11-1631, 2002.
- Lean, H. W., Clark, P. A., Dixon, M., Roberts, N. M., Fitch, A., Forbes, R., and Halliwell, C.: Characteristics of High-Resolution Versions of the Met Office Unified Model for Forecasting Convection over the United Kingdom, *Mon. Weather Rev.*, 136, 3408–3424, doi:10.1175/2008MWR2332.1, 2008.
- Lock, A. P., Brown, A. R., Bush, M. R., Martin, G. M., and Smith, R. N. B.: A New Boundary Layer Mixing Scheme. Part I: Scheme Description and Single-Column Model Tests, *Mon. Weather Rev.*, 128, 3187–3199, doi:10.1175/1520-0493(2000)128<3187:ANBLMS>2.0.CO;2, 2000.
- Loveland, T. R. and Belward, A. S.: The IGBP-DIS global 1 km land cover data set, DISCover: First results, *Int. J. Remote Sens.*, 18, 3289–3295, doi:10.1080/014311697217099, 1997.
- Masson, V., Le Moigne, P., Martin, E., Faroux, S., Alias, A., Alkama, R., Belamari, S., Barbu, A., Boone, A., Bouysse, F., Brousseau, P., Brun, E., Calvet, J.-C., Carrer, D., Decharme, B., Delire, C., Donier, S., Essaouini, K., Gibelin, A.-L., Giordani, H., Habets, F., Jidane, M., Kerdraon, G., Kourzeneva, E., Lafaysse, M., Lafont, S., Lebeaupin Brossier, C., Lemonsu, A., Mahfouf, J.-F., Marguinaud, P., Mokhtari, M., Morin, S., Pigeon, G., Salgado, R., Seity, Y., Taillefer, F., Tanguy, G., Tulet, P., Vincendon, B., Vionnet, V., and Voldoire, A.: The SURFEXv7.2 land and ocean surface platform for coupled or offline simulation of earth surface variables and fluxes, *Geosci. Model Dev.*, 6, 929–960, doi:10.5194/gmd-6-929-2013, 2013.
- Mohan, M. and Siddiqui, T. A.: Analysis of various schemes for the estimation of atmospheric stability classification, *Atmos. Environ.*, 32, 3775–3781, doi:10.1016/S1352-2310(98)00109-5, 1998.
- Mortensen, N. G., Nielsen, M., and Jørgensen, H. E.: Comparison of Resource and Energy Yield Assessment Procedures 2011–2015 : What have we learned and what needs to be done?, in: Proceedings of the EWEA Annual Event and Exhibition 2015 European Wind Energy Association (EWEA), 1–10, 2015.
- Nakanishi, M. and Niino, H.: An Improved Mellor–Yamada Level-3 Model: Its Numerical Stability and Application to a Regional Prediction of Advection Fog, *Bound.-Lay. Meteorol.*, 119, 397–407, doi:10.1007/s10546-005-9030-8, 2006.
- Niu, G.-Y., Yang, Z.-L., Mitchell, K. E., Chen, F., Ek, M. B., Barlage, M., Kumar, A., Manning, K., Niyogi, D., Rosero, E., Tewari, M., and Xia, Y.: The community Noah land surface model with multiparameterization options (Noah-MP): 1. Model description and evaluation with local-scale measurements, *J. Geophys. Res.*, 116, 1–19, doi:10.1029/2010JD015139, 2011.

- Noilhan, J. and Mahfouf, J. F.: The ISBA land surface parameterisation scheme, *Global Planet. Change*, 13, 145–159, doi:10.1016/0921-8181(95)00043-7, 1996.
- Orlanski, I.: A rational subdivision of scales for atmospheric processes, *B. Am. Meteorol. Soc.*, 56, 527–530, 1975.
- Palmer, T. N., Alessandri, A., Andersen, U., Cantelaube, P., Davey, M., Délecluse, P., Déqué, M., Díez, E., Doblas-Reyes, F. J., Feddersen, H., Graham, R., Gualdi, S., Guérémy, J. F., Hagedorn, R., Hoshen, M., Keenlyside, N., Latif, M., Lazar, A., Maisonnave, E., Marletto, V., Morse, A. P., Orfila, B., Rogel, P., Terres, J. M., and Thomson, M. C.: Development of a European multimodel ensemble system for seasonal-to-interannual prediction (DEMETER), *B. Am. Meteorol. Soc.*, 85, 853–872, doi:10.1175/BAMS-85-6-853, 2004.
- Pan, H. L. and Mahrt, L.: Interaction between soil hydrology and boundary-layer development, *Bound.-Lay. Meteorol.*, 38, 185–202, doi:10.1007/BF00121563, 1987.
- Peña, A., Floors, R., and Gryning, S. E.: The Høvsøre Tall Wind-Profile Experiment: A Description of Wind Profile Observations in the Atmospheric Boundary Layer, *Bound.-Lay. Meteorol.*, 150, 69–89, doi:10.1007/s10546-013-9856-4, 2014.
- Pielke, R. A., Cotton, W. R., Walko, R. L., Tremback, C. J., Lyons, W. A., Grasso, L. D., Nicholls, M. E., Moran, M. D., Wesley, D. A., Lee, T. J., and Copeland, J. H.: A comprehensive meteorological modeling system-RAMS, *Meteorol. Atmos. Phys.*, 49, 69–91, doi:10.1007/BF01025401, 1992.
- Pleim, J.: A Simple, Efficient Solution of Flux–Profile Relationships in the Atmospheric Surface Layer, *J. Appl. Meteorol. Clim.*, 45, 341–347, doi:10.1175/JAM2339.1, 2006.
- Pleim, J. E.: A combined local and nonlocal closure model for the atmospheric boundary layer. Part I: Model description and testing, *J. Appl. Meteorol. Clim.*, 46, 1383–1395, doi:10.1175/JAM2539.1, 2007a.
- Pleim, J. E.: A Combined Local and Nonlocal Closure Model for the Atmospheric Boundary Layer. Part II: Application and Evaluation in a Mesoscale Meteorological Model, *J. Appl. Meteorol. Clim.*, 46, 1396–1409, doi:10.1175/JAM2534.1, 2007b.
- Rienecker, M. M., Suarez, M. J., Gelaro, R., Todling, R., Bacmeister, J., Liu, E., Bosilovich, M. G., Schubert, S. D., Takacs, L., Kim, G. K., Bloom, S., Chen, J., Collins, D., Conaty, A., Da Silva, A., Gu, W., Joiner, J., Koster, R. D., Lucchesi, R., Molod, A., Owens, T., Pawson, S., Pegion, P., Redder, C. R., Reichle, R., Robertson, F. R., Ruddick, A. G., Sienkiewicz, M., and Woollen, J.: MERRA: NASA's modern-era retrospective analysis for research and applications, *J. Climate*, 24, 3624–3648, doi:10.1175/JCLI-D-11-00015.1, 2011.
- Saha, S., Moorthi, S., Pan, H. L., Wu, X., Wang, J., Nadiga, S., Tripp, P., Kistler, R., Woollen, J., Behringer, D., Liu, H., Stokes, D., Grubbin, R., Gayno, G., Wang, J., Hou, Y. T., Chuang, H. Y., Juang, H. M. H., Sela, J., Iredell, M., Treadon, R., Kleist, D., Van Delst, P., Keyser, D., Derber, J., Ek, M., Meng, J., Wei, H., Yang, R., Lord, S., Van Den Dool, H., Kumar, A., Wang, W., Long, C., Chelliah, M., Xue, Y., Huang, B., Schemm, J. K., Ebisuzaki, W., Lin, R., Xie, P., Chen, M., Zhou, S., Higgins, W., Zou, C. Z., Liu, Q., Chen, Y., Han, Y., Cucurull, L., Reynolds, R. W., Rutledge, G., and Goldberg, M.: The NCEP climate forecast system reanalysis, *B. Am. Meteorol. Soc.*, 91, 1015–1057, doi:10.1175/2010BAMS3001.1, 2010.
- Seity, Y., Brousseau, P., Malardel, S., Hello, G., Bénard, P., Bouttier, F., Lac, C., and Masson, V.: The AROME-France convective-scale operational model, *Mon. Weather Rev.*, 139, 976–991, doi:10.1175/2010MWR3425.1, 2011.
- Simmons, A., Uppala, S., Dee, D., and Kobayashi, S.: ERA-Interim: New ECMWF reanalysis products from 1989 onwards, ECMWF newsletter, 110, 25–35, 2007.
- Skamarock, W. C.: Evaluating Mesoscale NWP Models Using Kinetic Energy Spectra, *Mon. Weather Rev.*, 132, 3019–3032, doi:10.1175/MWR2830.1, 2004.
- Skamarock, W. C., Klemp, J. B., Dudhia, J., Gill, D. O., Barker, D. M., Duda, M. G., Huang, X.-Y., Wang, W., Powers, J. G.: A Description of the Advanced Research WRF Version 3, Tech. rep., National Center for Atmospheric Research, Boulder, CO, USA, 2008.
- Sukoriansky, S., Galperin, B., and Perov, V.: Application of a New Spectral Theory of Stably Stratified Turbulence to the Atmospheric Boundary Layer over Sea Ice, *Bound.-Lay. Meteorol.*, 117, 231–257, doi:10.1007/s10546-004-6848-4, 2005.
- Ulden, A. P. and Wieringa, J.: Atmospheric boundary layer research at Cabauw, *Bound.-Lay. Meteorol.*, 78, 39–69, doi:10.1007/BF00122486, 1995.
- Vincent, C. L. and Hahmann, A. N.: The impact of grid and spectral nudging on the variance of the near-surface wind speed, *J. Appl. Meteorol. Clim.*, 54, 1021–1038, doi:10.1175/JAMC-D-14-0047.1, 2015.
- Walko, R. and Tremback, C.: ATMET Technical Note 1, Modifications for the Transition from LEAF-2 to LEAF-3, ATMET, LLC, Boulder, Colorado 80308-2195, 2005.
- Warner, T. T.: Numerical Weather and Climate Prediction, Cambridge University Press, Cambridge, UK, 2010.
- Yoden, S.: Atmospheric Predictability, *J. Meteorol. Soc. Jpn.*, 85, 77–102, doi:10.2151/jmsj.85B.77, 2007.





# References

- Aarakawa, A. and Lamb, V. R. (1977). Computational Design of the Basic Dynamical Processes of the UCLA General Circulation Model. In *Methods in computational physics* 17, pages 173–265. Academic Press.
- Al-Yahyai, S., Charabi, Y., and Gastli, A. (2010). Review of the use of numerical weather prediction (NWP) models for wind energy assessment. *Renewable and Sustainable Energy Reviews*, 14(9):3192–3198.
- Apsley, D. D. and Castro, I. P. (1997). A limited-length-scale  $k$ - $\epsilon$  model for the neutral and stably-stratified atmospheric boundary layer. *Boundary-Layer Meteorology*, 83(1):75–98.
- Arnold, D., Morton, D., Schicker, I., Seibert, P., Rotach, M. W., Horvath, K., Dudhia, J., Satomura, T., Müller, M., Zängl, G., Takemi, T., Serafin, S., Schmidli, J., and Schneider, S. (2012). High Resolution Modelling in Complex Terrain . Report on the HiRCOT 2012 Workshop, Vienna, 21-23 February 2012.
- Baas, P., Bosveld, F. C., Lenderink, G., van Meijgaard, E., and Holtslag, A. A. M. (2010). How to design single-column model experiments for comparison with observed nocturnal low-level jets. *Quarterly Journal of the Royal Meteorological Society*, 136(648):671–684.
- Babic, N., Vecenaj, Z., and De Wekker, S. F. (2017). Spectral gap characteristics in a daytime valley boundary layer. *Quarterly Journal of the Royal Meteorological Society*, 143(707):2509–2523.
- Badger, J., Badger, M., Kelly, M., and Larsén, X. G. (2016). Global Wind Atlas.
- Badger, J., Frank, H., Hahmann, A. N., and Giebel, G. (2014). Wind-climate estimation based on mesoscale and microscale modeling: statistical–dynamical downscaling for wind energy applications. *Journal of Applied Meteorology and Climatology*, 53(8):1901–1919.
- Baklanov, A. A., Grisogono, B., Bornstein, R., Mahrt, L., Zilitinkevich, S. S., Taylor, P., Larsen, S. E., Rotach, M. W., and Fernando, H. J. (2011). The nature, theory, and modeling of atmospheric planetary boundary layers. *Bulletin of the American Meteorological Society*, 92(2):123–128.
- Baldauf, M., Seifert, A., Förstner, J., Majewski, D., Raschendorfer, M., and Reinhardt, T. (2011). Operational Convective-Scale Numerical Weather Prediction with the COSMO Model: Description and Sensitivities. *Monthly Weather Review*, 139(12):3887–3905.
- Balog, I., Ruti, P. M., Tobin, I., Armenio, V., and Vautard, R. (2016). A numerical approach for planning offshore wind farms from regional to local scales over the Mediterranean. *Renewable Energy*, 85:395–405.

- Basu, S., Holtslag, A. a. M., Van De Wiel, B. J. H., Moene, A. F., and Steeneveld, G.-J. J. (2008). An inconvenient "truth" about using sensible heat flux as a surface boundary condition in models under stably stratified regimes. *Acta Geophysica*, 56(1):88–99.
- Basu, S. and Porté-Agel, F. (2006). Large-Eddy Simulation of Stably Stratified Atmospheric Boundary Layer Turbulence: A Scale-Dependent Dynamic Modeling Approach. *Journal of the Atmospheric Sciences*, 63(1):2074–2091.
- Beare, R. J., Macvean, M. K., Holtslag, A. A. M., Cuxart, J., Esau, I., Golaz, J. C., Jimenez, M. A., Khairoutdinov, M., Kosovic, B., Lewellen, D., Lund, T. S., Lundquist, J. K., McCabe, A., Moene, A. F., Noh, Y., Raasch, S., and Sullivan, P. (2006). An intercomparison of large-eddy simulations of the stable boundary layer. *Boundary-Layer Meteorology*, 118(2):247–272.
- Bechmann, A. (2006). Large-Eddy Simulation of Atmospheric Flow over Complex Terrain.
- Bechmann, A. and Sørensen, N. N. (2011). Hybrid RANS/LES applied to complex terrain. *Wind Energy*, 14(1):225–237.
- Beljaars, B. A. C. M. (1994). The parametrization of surface fluxes in large-scale models under free convection. *Quarterly Journal of the Royal Meteorological Society*, 121(522):255–270.
- Blackadar, A. K. (1962). The vertical distribution of wind and turbulent exchange in a neutral atmosphere. *Journal of Geophysical Research*, 67(8):3095–3102.
- Blocken, B., Carmeliet, J., and Stathopoulos, T. (2007). CFD evaluation of wind speed conditions in passages between parallel buildings-effect of wall-function roughness modifications for the atmospheric boundary layer flow. *Journal of Wind Engineering and Industrial Aerodynamics*, 95(9-11):941–962.
- Blocken, B., Janssen, W. D., and van Hooff, T. (2012). CFD simulation for pedestrian wind comfort and wind safety in urban areas: General decision framework and case study for the Eindhoven University campus. *Environmental Modelling and Software*, 30:15–34.
- Bossard, M., Feranec, J., and Otahel, J. (2000). CORINE Land Cover Technical Guide - Addendum.
- Bosveld, F. C., Baas, P., van Meijgaard, E., de Bruijn, E. I. F., Steeneveld, G. J., and Holtslag, A. A. M. (2014). The Third GABLS Intercomparison Case for Evaluation Studies of Boundary-Layer Models. Part A: Case Selection and Set-Up. *Boundary-Layer Meteorology*, 152(2):133–156.
- Boussinesq, J. (1897). Théorie de l'écoulement tourbillonnant et tumultueux des liquides dans les lits rectilignes à grande section.. (Vol. 1). Gauthier-Villars.
- Brower, M. (1999). Validation of the WindMap program and development of MesoMap. *Proceeding from AWEA's WindPower conference. Washington, DC, USA*.
- Businger, J. A., Wyngaard, J. C., Izumi, Y., and Bradley, E. F. (1971). Flux-Profile Relationships in the Atmospheric Surface Layer. *Journal of the Atmospheric Sciences*, 28(2):181–189.

- Cabezón, D., Migoya, E., and Crespo, A. (2011). Comparison of turbulence models for the computational fluid dynamics simulation of wind turbine wakes in the atmospheric boundary layer. *Wind Energy*, 14(1):909–921.
- Calaf, M., Meneveau, C., and Meyers, J. (2010). Large eddy simulation study of fully developed wind-turbine array boundary layers. *Physics of Fluids*, 22(1):015110.
- Castro, F. A., Castro, M. P. S. S., and Palma, J. M. (2008). Parallelisation of the CFD code of a CFD-NWP coupled system for the simulation of atmospheric flows over complex terrain. *International Conference on High Performance Computing for Computational Science*, pages 27–38.
- Castro, F. A., Palma, J. M. L. M., and Lopes, a. S. (2003). Simulation of the Askervein flow. Part 1: Reynolds averaged Navier-Stokes equations ( $k - \epsilon$  turbulence model). *Boundary-Layer Meteorology*, 107(3):501–530.
- Castro, F. a., Santos, C. S., and Costa, J. C. L. (2010). Development of a meso-microscale coupling procedure for site assessment in complex terrain. *EWEC 2010-European Wind Energy Conference & Exhibition*, pages 1–10.
- Chang, C. Y., Schmidt, J., Dörenkämper, M., and Stoevesandt, B. (2018). A consistent steady state CFD simulation method for stratified atmospheric boundary layer flows. *Journal of Wind Engineering and Industrial Aerodynamics*, 172:55–67.
- Charney, J. G., Fjörtoft, R., and Neumann, J. V. (1950). Numerical Integration of the Barotropic Vorticity Equation. *Tellus*, 2(4):237–254.
- Chávez-Arroyo, R., Fernandes-Correia, P., Lozano-Galiana, S., Sanz-Rodrigo, J., Amezcua, J., and Probst, O. (2018). A novel approach to statistical-dynamical downscaling for long-term wind resource predictions. *Meteorological Applications*, 25(2):171–183.
- Chen, F. and Dudhia, J. (2001). Coupling an Advanced Land Surface-Hydrology Model with the Penn State-NCAR MM5 Modeling System. Part II: Preliminary Model Validation. *Monthly Weather Review*, 129(4):587–604.
- Cheng, Y. and Brutsaert, W. (2005). Flux-profile relationships for wind speed and temperature in the stable atmospheric boundary layer. *Boundary-Layer Meteorology*, 114(3):519–538.
- Cohen, A. E., Cavallo, S. M., Coniglio, M. C., Brooks, H. E., Cohen, A. E., Cavallo, S. M., Coniglio, M. C., and Brooks, H. E. (2015). A Review of Planetary Boundary Layer Parameterization Schemes and Their Sensitivity in Simulating Southeastern U.S. Cold Season Severe Weather Environments. *Weather and Forecasting*, 30(3):591–612.
- Collins, W. D., Bitz, C. M., Blackmon, M. L., Bonan, G. B., Bretherton, C. S., Carton, J. A., Chang, P., Doney, S. C., Hack, J. J., Henderson, T. B., Kiehl, J. T., Large, W. G., McKenna, D. S., Santer, B. D., and Smith, R. D. (2006). The Community Climate System Model Version 3 (CCSM3). *J. Climate*, 19(11):2122–2143.
- Courant, R., Isaacson, E., and Rees, M. (1952). On the solution of nonlinear hyperbolic differential equations by finite differences. *Communications in Applied Numerical Methods*, 5(3):243–255.

- Davidson, L. and Peng, S. H. (2003). Hybrid LES-RANS modelling: A one-equation SGS model combined with a  $k$ - $\omega$  model for predicting recirculating flows. *International Journal for Numerical Methods in Fluids*, 43(9):1003–1018.
- Deardorff, J. W. (1970). A numerical study of three-dimensional turbulent channel flow at large Reynolds numbers. *Journal of Fluid Mechanics*, 41(2):453–480.
- Dee, D. P., Uppala, S. M., Simmons, A. J., Berrisford, P., Poli, P., Kobayashi, S., Andrae, U., Balmaseda, M. A., Balsamo, G., Bauer, P., Bechtold, P., Beljaars, A. C. M., van de Berg, L., Bidlot, J., Bormann, N., Delsol, C., Dragani, R., Fuentes, M., Geer, A. J., Haimberger, L., Healy, S. B., Hersbach, H., Hólm, E. V., Isaksen, L., Kållberg, P., Köhler, M., Matricardi, M., McNally, A. P., Monge-Sanz, B. M., Morcrette, J. J., Park, B. K., Peubey, C., de Rosnay, P., Tavolato, C., Thépaut, J. N., and Vitart, F. (2011). The ERA-Interim reanalysis: Configuration and performance of the data assimilation system. *Quarterly Journal of the Royal Meteorological Society*, 137(656):553–597.
- Detering, H. W. and Etling, D. (1985). Application of the E-e turbulence model to the atmospheric boundary layer. *Boundary-Layer Meteorology*, 33(2):113–133.
- Dimitrova, R., Silver, Z., Zsedrovits, T., Hocut, C. M., Leo, L. S., Di Sabatino, S., and Fernando, H. J. (2016). Assessment of Planetary Boundary-Layer Schemes in the Weather Research and Forecasting Mesoscale Model Using MATERHORN Field Data. *Boundary-Layer Meteorology*, 159(3):589–609.
- Draxl, C., Hahmann, A. N., Peña, A., and Giebel, G. (2014). Evaluating winds and vertical wind shear from Weather Research and Forecasting model forecasts using seven planetary boundary layer schemes. *Wind Energy*, 17(1):39–55.
- Dudhia, J. (1989). Numerical Study of Convection Observed during the Winter Monsoon Experiment Using a Mesoscale Two-Dimensional Model. *Journal of the Atmospheric Sciences*, 46(20):3077–3107.
- Duraisamy, V. J., Dupont, E., Carissimo, B., and Duraisamy V. J., E. Dupont, B. C. (2014). Downscaling wind energy resource from mesoscale to microscale model and data assimilating field measurements. *Journal of Physics: Conference Series*, 555(1):1–13.
- Duynkerke, P. G. (1988). Application of the E- $\varepsilon$  turbulence closure model to the neutral and stable atmospheric boundary layer. *Journal of the atmospheric sciences*, 45(5):865–880.
- Dyer, A. J. (1974). A Review of Flux-Profile Relationships. *Boundary-Layer Meteorology*, 7(3):363–372.
- Dyer, A. J. and Hicks, B. B. (1970). Flux-gradient relationships in the constant flux layer. *Quarterly Journal of the Royal Meteorological Society*, 96(410):715–721.
- El Kasmi, A. and Masson, C. (2008). An extended  $k$  -  $\varepsilon$  model for turbulent flow through horizontal-axis wind turbines. *Journal of Wind Engineering and Industrial Aerodynamics*, 96(1):103–122.
- Ely, A., Stuart, P., Zhu, M., Palma, J. M. L. M. Veiga Rodrigues, C., and Chertovskih, R. (2012). Mesoscale and CFD coupling: an improved technique for predicting microscale wind. *Proceedings of the EWEA annual conference and exhibition*, 1:575–584.

- Fairall, C. W., Bradley, E. F., Rogers, D. P., Edson, J. B., and Young, G. S. (1996). Bulk parameterization of air-sea fluxes for Tropical Ocean-Global Atmosphere Coupled-Ocean Atmosphere Response Experiment. *Journal of Geophysical Research: Oceans*, 101(C2):3747–3764.
- Fernando, H., Mann, J., Palma, J., Lundquist, J., Barthelme, R., Belo-Pereira, M., Brown, W., Chow, F., Gerz, T., Hocut, C., Klein, P., Leo, L., Matos, J., Oncley, S., Pryor, S., Bariteau, L., Bell, T., Bodini, N., Carney, M., Courtney, M., Creegan, E., Dimitrova, R., Gomes, S., Hagen, M., Hyde, O., Kigle, S., Krishnamurthy, R., Lopes, J., Mazzaro, L., Neher, J., Menke, R., Murphy, P., Oswald, L., Otarola-Bustos, S., Pattantyus, A., Salvatore, J., Schady, A., Sirin, N., Spuler, S., Svensson, E., Tomaszewski, J., Turner, D., van Veen, L., Vasiljević, N., Vassalo, D., Voss, S., Wildmann, N., Wang, Y., and Wörl, P. (2018). Peering into Microscale Details of Mountain Winds. *Bulletin of the American Meteorological Society*.
- Finnigan, J. (2000). Turbulence in plant canopies. *Annual review of fluid mechanics*, 32(1):519–571.
- Foley, A. M., Leahy, P. G., Marvuglia, A., and McKeogh, E. J. (2012). Current methods and advances in forecasting of wind power generation. *Renewable Energy*, 37(1):1–8.
- Frank, H. P., Landberg, L., Rathmann, O., Mortensen, N. G., and Petersen, E. L. (2001). The Numerical Wind Atlas-the KAMM / WaSP Method. *Conference proceedings (on CD-ROM). Washington, DC: American Wind Energy Association (AWEA)*.
- Franke, J., Hellsten, A., Schlunzen, K. H., and Carissimo, B. (2011). The COST 732 Best Practice Guideline for CFD simulation of flows in the urban environment: a summary. *International Journal of Environment and Pollution*, 44(1-4):419–427.
- Galperin, B., Sukoriansky, S., and Perov, V. (2007). Implementation of the quasi-normal scale elimination (QNSE) turbulence model in WRF. *The 8th WRF Users' Workshop, Boulder CO*.
- García-Díez, M., Fernández, J., Fita, L., and Yagüe, C. (2013). Seasonal dependence of WRF model biases and sensitivity to PBL schemes over Europe. *Quarterly Journal of the Royal Meteorological Society*, 139(671):501–514.
- Gemmill, W., Katz, B., and Li, X. (2007). Daily real-time global sea surface temperature - high resolution analysis at NOAA/NCEP. Technical report, NOAA/NWS/NCEP/MMAB.
- Gevorgyan, A. (2018). A Case Study of Low-Level Jets in Yerevan Simulated by the WRF Model. *Journal of Geophysical Research: Atmospheres*, 123(1):300–314.
- Girimaji, S. and Abdol-Hamid, K. (2005). Partially-Averaged Navier Stokes Model for Turbulence: Implementation and Validation. *43rd AIAA Aerospace Sciences Meeting and Exhibit*.
- Girimaji, S. S. (2006). Partially-Averaged Navier-Stokes Model for Turbulence: A Reynolds-Averaged Navier-Stokes to Direct Numerical Simulation Bridging Method. *Journal of Applied Mechanics*, 73(3):413.

- Gjerstad, J., Aasen, S. E., Andersson, H. I., Brevik, I., and Lovseth, J. (1995). An Analysis of Low-Frequency Maritime Atmospheric-Turbulence. *Journal of the Atmospheric Sciences*, 52(15):2663–2669.
- Gopalan, H., Gundling, C., Brown, K., Roget, B., Sitaraman, J., Mirocha, J. D., and Miller, W. O. (2014). A coupled mesoscale–microscale framework for wind resource estimation and farm aerodynamics. *Journal of Wind Engineering and Industrial Aerodynamics*, 132:13–26.
- Grachev, A. A., Fairall, C. W., Persson, P. O. G., Andreas, E. L., and Guest, P. S. (2005). Stable boundary-layer scaling regimes: The SHEBA data. *Boundary-Layer Meteorology*, 116(2):201–235.
- Grell, G., Dudhia, J., and Stauffer, D. (1994). A description of the fifth-generation Penn State/NCAR mesoscale model (MM5).
- Guo Larsén, X., Petersen, E. L., and Larsen, S. (2018). Variation of boundary-layer wind spectra with height. *Quarterly Journal of the Royal Meteorological Society*.
- GWEC (2016). Global Wind Report.
- Hahmann, A. N., Lennard, C., Badger, J., Vincent, C. L., Kelly, M. C., Volker, P. J. H., Refslund, J., Lennard, C., Badger, J., Vincent, C. L., Kelly, M. C., Volker, P. J. H., and Refslund, J. (2014). Mesoscale modeling for the Wind Atlas of South Africa (WASA) project. Technical report, DTU Wind Energy.
- Hanna, S. R., Brown, M. J., Camelli, F. E., Chan, S. T., Coirier, W. J., Kim, S., Hansen, O. R., Huber, A. H., and Reynolds, R. M. (2006). Detailed Simulations of Atmospheric Flow and Dispersion in Downtown Manhattan: An Application of Five Computational Fluid Dynamics Models. *Bulletin of the American Meteorological Society*, 87(12):1713–1726.
- Hariprasad, K. B. R. R., Srinivas, C. V., Singh, A. B., Vijaya Bhaskara Rao, S., Baskaran, R., and Venkatraman, B. (2014). Numerical simulation and intercomparison of boundary layer structure with different PBL schemes in WRF using experimental observations at a tropical site. *Atmospheric Research*, 145-146:27–44.
- Holtstlag, A. and Svensson, G. (2013). Stable atmospheric boundary layers and diurnal cycles: challenges for weather and climate models. *Bulletin of the American Meteorological Society*, 94(11):1691–1706.
- Holtstlag, A. A. M. (2014). Introduction to the Third GEWEX Atmospheric Boundary Layer Study (GABLS3). *Boundary-Layer Meteorology*, 152(2):127–132.
- Holtstlag, A. A. M. and De Bruin, H. A. R. (1988). Applied Modeling of the Nighttime Surface Energy Balance over Land. *Journal of Applied Meteorology*, 27(6):689–704.
- Hong, S.-Y. and Dudhia, J. (2012). Next-Generation Numerical Weather Prediction: Bridging Parameterization, Explicit Clouds, and Large Eddies. *Bulletin of the American Meteorological Society*, 93(1):ES6–ES9.

- Hong, S.-Y., Dudhia, J., and Chen, S.-H. (2004). A Revised Approach to Ice Microphysical Processes for the Bulk Parameterization of Clouds and Precipitation. *Monthly Weather Review*, 132(1):103–120.
- Hong, S.-Y., Noh, Y., and Dudhia, J. (2006). A New Vertical Diffusion Package with an Explicit Treatment of Entrainment Processes. *Monthly Weather Review*, 134(9):2318–2341.
- Hong, S.-Y. and Pan, H.-L. (1996). Nonlocal Boundary Layer Vertical Diffusion in a Medium-Range Forecast Model. *Monthly Weather Review*, 124(10):2322–2339.
- Honnert, R., Masson, V., and Couvreux, F. (2011). A Diagnostic for Evaluating the Representation of Turbulence in Atmospheric Models at the Kilometric Scale. *Journal of the Atmospheric Sciences*, 68(12):3112–3131.
- Horvath, K., Koracin, D., Vellore, R., Jiang, J., and Belu, R. (2012). Sub-kilometer dynamical downscaling of near-surface winds in complex terrain using WRF and MM5 mesoscale models. *Journal of Geophysical Research Atmospheres*, 117(11):1–19.
- Hu, X. M., Klein, P. M., Xue, M., Lundquist, J. K., Zhang, F., and Qi, Y. (2013). Impact of low-level jets on the nocturnal urban heat island intensity in Oklahoma city. *Journal of Applied Meteorology and Climatology*, 52(8):1779–1802.
- Hu, X. M., Nielsen-Gammon, J. W., and Zhang, F. (2010). Evaluation of three planetary boundary layer schemes in the WRF model. *Journal of Applied Meteorology and Climatology*, 49(9):1831–1844.
- Huser, A., Jahre, P. N., and Skåtun, H. (1997). Application of k- $\epsilon$  model to the stable ABL: Pollution in complex terrain. *Journal of Wind Engineering*, 67:425–436.
- Israeli, M. and Orszag, S. A. (1981). Approximation of radiation boundary conditions. *Journal of Computational Physics*, 41(1):115–135.
- Jackson, P. S. and Hunt, J. C. R. (1975). Turbulent wind flow over a low hill. *Quarterly Journal of the Royal Meteorological Society*, 101(430):929–955.
- Janjić, Z. I. (1994). The Step-Mountain Eta Coordinate Model: Further Developments of the Convection, Viscous Sublayer, and Turbulence Closure Schemes. *Monthly Weather Review*, 122(5):927–945.
- Jimenez, B., Durante, F., Lange, B., Kreutzer, T., and Tambke, J. (2007). Offshore wind resource assessment with WAsP and MM5: Comparative study for the German bight. *Wind Energy*, 10(2):121–134.
- Jiménez, P. A. and Dudhia, J. (2012). Improving the representation of resolved and unresolved topographic effects on surface wind in the wrf model. *Journal of Applied Meteorology and Climatology*, 51(2):300–316.
- Jiménez, P. A., Dudhia, J., González-Rouco, J. F., Navarro, J., Montávez, J. P., and García-Bustamante, E. (2012). A Revised Scheme for the WRF Surface Layer Formulation. *Monthly Weather Review*, 140(3):898–918.



- Kaimal, J. C. and Finnigan, J. J. (1994). *Atmospheric boundary layer flows: their structure and measurement*. Oxford university press.
- Kain, J. S. (2004). The Kain-Fritsch Convective Parameterization: An Update. *Journal of Applied Meteorology*, 43(1):170–181.
- Kantha, L., Bao, J. W., and Carniel, S. (2005). A note on Tennekes hypothesis and its impact on second moment closure models. *Ocean Modelling*, 9(1):23–29.
- Katul, G. G., Mahrt, L., Poggi, D., and Sanz, C. (2004). One- and two-equation models for canopy turbulence. *Boundary-Layer Meteorology*, 113(1):81–109.
- Kelly, M., Larsen, G., Dimitrov, N. K., and Natarajan, A. (2014). Probabilistic meteorological characterization for turbine loads. *Journal of Physics: Conference Series*, 524(1).
- Kitamura, Y. (2016). Improving a Turbulence Scheme for the Terra Incognita in a Dry Convective Boundary Layer. *Journal of the Meteorological Society of Japan. Ser. II*, 94(6):491–506.
- Kleczek, M. A., Steeneveld, G. J., and Holtslag, A. A. M. (2014). Evaluation of the Weather Research and Forecasting Mesoscale Model for GABLS3: Impact of Boundary-Layer Schemes, Boundary Conditions and Spin-Up. *Boundary-Layer Meteorology*, 152(2):213–243.
- Klemp, J. B. and Durran, D. R. (1983). An Upper Boundary Condition Permitting Internal Gravity Wave Radiation in Numerical Mesoscale Models. *Monthly Weather Review*, 111(3):430–444.
- Koblitz, T. (2013). *CFD Modeling of Non-Neutral Atmospheric Boundary Layer Conditions*. PhD thesis, Technical University of Denmark.
- Koblitz, T., Bechmann, A., Sogachev, A., Sørensen, N., and Réthoré, P. E. (2015). Computational Fluid Dynamics Model of Stratified Atmospheric Boundary-Layer Flow. *Wind Energy*, 18(1):75–89.
- Kosović, B., Jimenez, P. A., Haupt, S. E., Martilli, A., Olson, J., and Bao, J. W. (2017). Recent developments and assessment of a three-dimensional PBL parameterization for improved wind forecasting over complex terrain. In. *Abstracts, AGU Fall Meeting*.
- Kumar, V., Kleissl, J., Meneveau, C., and Parlange, M. B. (2006). Large-eddy simulation of a diurnal cycle of the atmospheric boundary layer: Atmospheric stability and scaling issues. *Water Resources Research*, 42:1–18.
- Landahl, M. T. and Mollo-Christensen, E. (1992). *Turbulence and random processes in fluid mechanics*. Cambridge University Press.
- Landberg, L., Myllerup, L., Rathmann, O., Petersen, E. L., Jørgensen, B. H., Badger, J., and Mortensen, N. G. (2003). Wind resource estimation - An overview. *Wind Energy*, 6:261–271.
- Launder, B. E. and Spalding, D. B. (1974). The numerical computation of turbulent flows. *Computer Methods in Applied Mechanics and Engineering*, 3(2):269–289.

- Lauritzen, P. H., Jablonowski, C., Taylor, M. A., and Nair, R. D. (2011). *Numerical techniques for global atmospheric models*, volume 80. Springer Science & Business Media.
- Lehner, M. (2012). *Observations and Large-Eddy Simulations of the Thermally Driven Cross-Basin Circulation in a Small, Closed Basin*. PhD thesis, University of Utah.
- Leonard, B. (1979). A stable and accurate convective modelling procedure based on quadratic upstream interpolation. *Computer methods in applied mechanics and engineering*, 19:59–98.
- Lettau, H. (1950). A Re-examination of the “Leipzig Wind Profile” Considering some Relations between Wind and Turbulence in the Frictional Layer. *Tellus*, 2(2):125–129.
- Letzel, M. O., Krane, M., and Raasch, S. (2008). High resolution urban large-eddy simulation studies from street canyon to neighbourhood scale. *Atmospheric Environment*, 42(38):8770–8784.
- Lin, S.-J. (2004). A “Vertically Lagrangian” Finite-Volume Dynamical Core for Global Models. *Monthly Weather Review*, 132(10):2293–2307.
- Lindborg, E. (1999). Can the atmospheric kinetic energy spectrum be explained by two-dimensional turbulence? *Journal of Fluid Mechanics*, 388:259–288.
- Liu, G., Liu, Y., and Endo, S. (2013). Evaluation of Surface Flux Parameterizations with Long-Term ARM Observations. *Monthly Weather Review*, 141(2):773–797.
- Liu, Y., Warner, T., Liu, Y., Vincent, C., Wu, W., Mahoney, B., Swerdlin, S., Parks, K., and Boehnert, J. (2011). Simultaneous nested modeling from the synoptic scale to the LES scale for wind energy applications. *Journal of Wind Engineering and Industrial Aerodynamics*, 99(4):308–319.
- Louis, J. F. (1979). A parametric model of vertical eddy fluxes in the atmosphere. *Boundary-Layer Meteorology*, 17(2):187–202.
- Lovejoy, S., Tuck, A. F., Schertzer, D., and Hovde, S. J. (2009). Reinterpreting aircraft measurements in anisotropic scaling turbulence. *Atmospheric Chemistry and Physics*, 9(14):5007–5025.
- Lu, H. and Porté-Agel, F. (2011). Large-eddy simulation of a very large wind farm in a stable atmospheric boundary layer. *Physics of Fluids*, 23(6).
- Lundquist, J. K., Mirocha, J. D., and Kosović, B. (2010). Nesting large-eddy simulations within mesoscale simulations in WRF for wind energy applications. *5th International Symposium on Computational Wind Engineering (CWE2010)*, pages 23–27.
- Mahrt, L. (1998). Stratified Atmospheric Boundary Layers and Breakdown of Models. *Theoretical and Computational Fluid Dynamics*, 11(3-4):263–279.
- Mahrt, L. T. and Sun, J. (1995). The Subgrid Velocity Scale in the Bulk Aerodynamic Relationship for Spatially Averaged Scalar Fluxes. *Monthly Weather Review*, 123(10):3032–3041.

- Malhi, Y. S. (1995). The significance of the dual solutions for heat fluxes measured by the temperature fluctuation method in stable conditions. *Boundary-Layer Meteorology*, 74(4):389–396.
- Matheou, G., Chung, D., Nuijens, L., Stevens, B., and Teixeira, J. (2011). On the Fidelity of Large-Eddy Simulation of Shallow Precipitating Cumulus Convection. *Monthly Weather Review*, 139(9):2918–2939.
- Mazzaro, L. J., Muñoz-Esparza, D., Lundquist, J. K., and Linn, R. R. (2017). Nested mesoscale-to-LES modeling of the atmospheric boundary layer in the presence of under-resolved convective structures. *Journal of Advances in Modeling Earth Systems*, 9(4):1795–1810.
- Meissner, C., Gravdahl, A. R., and Steensen, B. (2009). Including thermal effects in CFD wind flow simulations. *Journal of the Environmental Sciences*, 18(8):833–839.
- Mellor, G. L. and Yamada, T. (1974). A hierarchy of turbulence closure models for planetary boundary layers. *Journal of the Atmospheric Sciences*, 31(7):1791–1806.
- Michelsen, J. A. (1992). Basis3D - a platform for development of multiblock PDE solvers. Technical report, Department of Fluid Mechanics, Technical University of Denmark.
- Michelsen, J. A. (1994). Block structured multigrid solution of 2D and 3D elliptic PDE's. Technical report, Department of Fluid Mechanics, Technical University of Denmark.
- Milovac, J., Warrach-Sagi, K., Behrendt, A., Späth, F., Ingwersen, J., and Wulfmeyer, V. (2016). Investigation of PBL schemes combining the WRF model simulations with scanning water vapor differential absorption lidar measurements. *Journal of Geophysical Research*, 121(2):624–649.
- Mirocha, J., Kosović, B., and Kirkil, G. (2014). Resolved Turbulence Characteristics in Large-Eddy Simulations Nested within Mesoscale Simulations Using the Weather Research and Forecasting Model. *Monthly Weather Review*, 142(2):806–831.
- Mirocha, J. D., Lundquist, J. K., and Kosović, B. (2010). Implementation of a Nonlinear Subfilter Turbulence Stress Model for Large-Eddy Simulation in the Advanced Research WRF Model. *Monthly Weather Review*, 138(11):4212–4228.
- Mirocha, J. D., Rajewski, D. A., Marjanovic, N., Lundquist, J. K., Kosović, B., Draxl, C., and Churchfield, M. J. (2015). Investigating wind turbine impacts on near-wake flow using profiling lidar data and large-eddy simulations with an actuator disk model. *Journal of Renewable and Sustainable Energy*, 7(4).
- Mlawer, E. J., Taubman, S. J., Brown, P. D., Iacono, M. J. I., and Clough, S. A. C. (1997). Radiative transfer for inhomogeneous atmospheres: RRTM, a validated correlated-k model for the longwave. *Journal of Geophysical Research: Atmospheres*, 102(D14):16663–16682.
- Moeng, C.-H., Dudhia, J., Klemp, J., and Sullivan, P. (2007). Examining Two-Way Grid Nesting for Large Eddy Simulation of the PBL Using the WRF Model. *Monthly Weather Review*, 135(6):2295–2311.

- Monin, A. S. and Obukhov, A. M. (1954). Basic laws of turbulent mixing in the surface layer of the atmosphere. *Contrib. Geophys. Inst. Acad. Sci. USSR*, 24(151):163–187.
- Monteiro, C., Bessa, R., Miranda, V., Botterud, A., Wang, J., Conzelmann, G., and INESC Porto (2009). Wind power forecasting : state-of-the-art.
- Mortensen, N. G., Bowen, A. J., and Antoniou, I. (2006). Improving WAsP predictions in (too) complex terrain. *Proceedings of the 2006 European Wind Energy Conference and Exhibition*, 28.
- Mortensen, N. G., Landberg, L., Troen, I., Petersen, E. L., Rathmann, O., Nielsen, M., and Erik, L. (2004). WAsP Utility Programs.
- Muñoz-Esparza, D., Kosović, B., García-Sánchez, C., and van Beeck, J. (2014a). Nesting Turbulence in an Offshore Convective Boundary Layer Using Large-Eddy Simulations. *Boundary-Layer Meteorology*, 151(3):453–478.
- Muñoz-Esparza, D., Kosović, B., Mirocha, J., and van Beeck, J. (2014b). Bridging the Transition from Mesoscale to Microscale Turbulence in Numerical Weather Prediction Models. *Boundary-Layer Meteorology*, 153(3):409–440.
- Muñoz-Esparza, D., Kosović, B., van Beeck, J., and Mirocha, J. (2015). A stochastic perturbation method to generate inflow turbulence in large-eddy simulation models: Application to neutrally stratified atmospheric boundary layers. *Physics of Fluids*, 27.
- Munoz-Esparza, D., Lundquist, J. K., Sauer, J. A., Kosovic, B., and Linn, R. R. (2017). Coupled mesoscale-LES modeling of a diurnal cycle during the CWEX-13 field campaign: From weather to boundary-layer eddies. *Journal of Advances in Modeling Earth Systems*, 6:513–526.
- Muñoz-Esparza, D., Sauer, J. A., Linn, R. R., and Kosović, B. (2016). Limitations of One-Dimensional Mesoscale PBL Parameterizations in Reproducing Mountain-Wave Flows. *Journal of the Atmospheric Sciences*, 73(7):2603–2614.
- Muñoz-Esparza, D., Sharman, R. D., and Lundquist, J. K. (2017). Turbulent dissipation rate in the atmospheric boundary layer: observations and WRF mesoscale modeling during the XPIA field campaign. *Monthly Weather Review*, 9:1572–1594.
- Nakanishi, M. and Niino, H. (2004). An improved Mellor-Yamada Level-3 model with condensation physics: Its design and verification. *Boundary-Layer Meteorology*, 112(1):1–31.
- Nakanishi, M. and Niino, H. (2006). An Improved Mellor-Yamada Level-3 Model: Its Numerical Stability and Application to a Regional Prediction of Advection Fog. *Boundary-Layer Meteorology*, 119(2):397–407.
- Nakayama, A. and Miyashita, K. (2001). URANS simulation of flow over smooth topography. *International Journal of Numerical Methods for Heat and Fluid Flow*, 11(8):723–743.
- Nastrom, G. D. and Gage, K. S. (1985). A Climatology of Atmospheric Wavenumber Spectra of Wind and Temperature Observed by Commercial Aircraft. *Journal of the Atmospheric Sciences*, 42(9):950–960.

- Olsen, B. T. and Cavar, D. (2018). Mesoscale to microscale coupling via momentum and temperature tendencies in complex terrain. *Wind Energy Science*, page [IN PREPARATION].
- Olsen, B. T., Cavar, D., Hahmann, A. N., and Kelly, M. (2018). Mesoscale to microscale coupling via momentum and temperature tendencies: validation in simple terrain. *Wind Energy Science*, page [IN PREPARATION].
- Olsen, B. T., Hahmann, A. N., Sempreviva, A. M., Badger, J., and Jørgensen, H. E. (2017). A comparison of mesoscale model output at simple sites for wind energy applications. *Wind Energy Science*, 2(1):211–228.
- Orlanski, I. (1975). A rational subdivision of scales for atmospheric processes. *Bulletin of the American Meteorological Society*, 56:527–530.
- Patankar, S. V. and Spalding, D. B. (1972). A calculation procedure for heat, mass and momentum transfer in three-dimensional parabolic flows. *International Journal of Heat and Mass Transfer*, 15(10):1787–1806.
- Paulson, C. A. (1970). The Mathematical Representation of Wind Speed and Temperature Profiles in the Unstable Atmospheric Surface Layer. *Journal of Applied Meteorology*, 9(6):857–861.
- Pleim, J. E. (2007). A Combined Local and Nonlocal Closure Model for the Atmospheric Boundary Layer. Part II: Application and Evaluation in a Mesoscale Meteorological Model. *Journal of Applied Meteorology and Climatology*, 46(9):1396–1409.
- Pleim, J. E. and Chang, J. S. (1992). A non-local closure model for vertical mixing in the convective boundary layer. *Atmospheric Environment Part A, General Topics*, 26(6):965–981.
- Poll, S., Shrestha, P., and Simmer, C. (2017). Modelling convectively induced secondary circulations in the terra incognita with TerrSysMP. *Quarterly Journal of the Royal Meteorological Society*, 143(707):2352–2361.
- Pope, S. B. (2001). *Turbulent flows*. Cambridge University Press.
- Porté-Agel, F., Wu, Y. T., and Chen, C. H. (2013). A numerical study of the effects of wind direction on turbine wakes and power losses in a largewind farm. *Energies*, 6(10):5297–5313.
- Porté-Agel, F., Wu, Y. T., Lu, H., and Conzemius, R. J. (2011). Large-eddy simulation of atmospheric boundary layer flow through wind turbines and wind farms. *Journal of Wind Engineering and Industrial Aerodynamics*, 99(4):154–168.
- Rai, R. K., Berg, L. K., Kosović, B., Mirocha, J. D., Pekour, M. S., and Shaw, W. J. (2017a). Comparison of Measured and Numerically Simulated Turbulence Statistics in a Convective Boundary Layer Over Complex Terrain. *Boundary-Layer Meteorology*, 163(1):69–89.
- Rai, R. K., Berg, L. K., Pekour, M., Shaw, W. J., Kosovic, B., Mirocha, J. D., and Ennis, B. L. (2017b). Spatiotemporal variability of turbulence kinetic energy budgets in the convective boundary layer over both simple and complex terrain. *Journal of Applied Meteorology and Climatology*, 56(12):3285–3302.

- Reyers, M., Pinto, J. G., and Moemken, J. (2015). Statistical-dynamical downscaling for wind energy potentials: evaluation and applications to decadal hindcasts and climate change projections. *International Journal of Climatology*, 35(2):229–244.
- Reynolds, O. (1895). On the Dynamical Theory of Incompressible Viscous Fluids and the Determination of the Criterion. *Philosophical Transactions of the Royal Society of London*, 186:123–164.
- Rhie, C. M. and Chow, W. L. (1983). Numerical Study of the Turbulent Flow Past an Airfoil with Trailing Edge Separation. *AIAA Journal* 21, 11(11):1525–1532.
- Rife, D. L., Vanvyve, E. V., Pinto, J. O., Monaghan, C. A. D., and Poulos, G. S. (2013). Selecting representative days for more efficient dynamical climate downscaling: application to wind energy. *Journal of Applied Meteorology and Climatology*, 52(1):47–63.
- Rodrigues, C. V., Palma, J. M. L. M., and Rodrigues, H. (2015). Atmospheric Flow over a Mountainous Region by a One-Way Coupled Approach Based on Reynolds-Averaged Turbulence Modelling. *Boundary-Layer Meteorology*, 159(2):1–31.
- Sanz Rodrigo, J., Allaerts, D., Avila, M., Barcons, J., Cavar, D., Chávez Arroyo, R. A., Churchfield, M., Kosovic, B., Lundquist, J. K., Meyers, J., Esparza, D. M., Palma, J., Tomaszewski, J. M., Troldborg, N., Van Der Laan, M. P., and Rodrigues, C. V. (2017a). Results of the GABLS3 diurnal-cycle benchmark for wind energy applications. *Journal of Physics: Conference Series*, 854(1).
- Sanz Rodrigo, J., Churchfield, M., and Kosovic, B. (2017b). A methodology for the design and testing of atmospheric boundary layer models for wind energy applications. *Wind Energy Science*, 2(1):35–54.
- Sathyanadh, A., Prabha, T. V., Balaji, B., Resmi, E. A., and Karipot, A. (2017). Evaluation of WRF PBL parameterization schemes against direct observations during a dry event over the Ganges valley. *Atmospheric Research*, 193(April):125–141.
- Schmitt, F. G. (2007). About Boussinesq’s turbulent viscosity hypothesis: historical remarks and a direct evaluation of its validity. *Comptes Rendus - Mécanique*, 335(9-10):617–627.
- Scire, J. S., Robe, F. R., Fernau, M. E., and Yamartino, R. J. (2000). A user’s guide for the CALMET meteorological model (Version 5).
- Seifert, A. and Heus, T. (2013). Large-eddy simulation of organized precipitating trade wind cumulus clouds. *Atmospheric Chemistry and Physics*, 13(11):5631–5645.
- Sescu, A. and Meneveau, C. (2014). A control algorithm for statistically stationary large-eddy simulations of thermally stratified boundary layers. *Quarterly Journal of the Royal Meteorological Society*, 140(683):2017–2022.
- Shin, H. H. and Dudhia, J. (2016). Evaluation of PBL Parameterizations in WRF at Sub-kilometer Grid Spacings: Turbulence Statistics in the Dry Convective Boundary Layer. *Monthly Weather Review*, 144(3):1161–1177.

- Siebesma, A. P., Bretherton, C. S., Brown, A., Chlond, A., Cuxart, J., Duynkerke, P. G., Jiang, H., Khairoutdinov, M., Lewellen, D., Moeng, C.-H., Sanchez, E., Stevens, B., and Stevens, D. E. (2003). A Large Eddy Simulation Intercomparison Study of Shallow Cumulus Convection. *Journal of the Atmospheric Sciences*, 60(10):1201–1219.
- Simmons, A., Uppala, S., Dee, D., and Kobayashi, S. (2007). ERA-Interim: New ECMWF reanalysis products from 1989 onwards. *ECMWF newsletter*, 110(110):25–35.
- Skamarock, W. C. (2004). Evaluating Mesoscale NWP Models Using Kinetic Energy Spectra. *Monthly Weather Review*, 132:3019–3032.
- Skamarock, W. C. and Klemp, J. B. (2008). A time-split nonhydrostatic atmospheric model for weather research and forecasting applications. *Journal of Computational Physics*, 227(7):3465–3485.
- Skamarock, W. C., Klemp, J. B., Dudhia, J., Gill, D. O., Barker, D. M., Duda, M. G., Huang, X.-Y., Wang, W., and Powers, J. G. (2008). A Description of the Advanced Research WRF Version 3. Technical report, National Center for Atmospheric Research, Boulder, CO, USA.
- Skamarock, W. C., Ringler, T., Klemp, J. B., Thuburn, J., Duda, M. G., Gunzburger, M., Ju, L., Park, S. H., and Fowler, L. (2010). Global Non-Hydrostatic Modeling Using Voronoi Meshes: The MPAS Model. *Proceedings of the ECMWF Workshop on Non-Hydrostatic Modelling*, pages 8–10.
- Smagorinsky, J. (1963). General Circulation Experiments With the Primitive Equations. *Monthly Weather Review*, 91(3):99–164.
- Sogachev, A., Kelly, M., and Leclerc, M. Y. (2012). Consistent two-equation closure modelling for atmospheric research: buoyancy and vegetation implementations. *Boundary-Layer Meteorology*, 145(2):307–327.
- Sogachev, A. and Panferov, O. (2006). Modification of two-equation models to account for plant drag. *Boundary-Layer Meteorology*, 121(2):229–266.
- Sørensen, N. N. (1995). *General purpose flow solver applied to flow over hills*. PhD thesis, Risø National Laboratory.
- Stoll, R. and Porté-Agel, F. (2008). Large-eddy simulation of the stable atmospheric boundary layer using dynamic models with different averaging schemes. *Boundary-Layer Meteorology*, 126(1):1–28.
- Storm, B., Dudhia, J., Basu, S., Swift, A., and Giammanco, I. (2009). Evaluation of the weather research and forecasting model on forecasting low-level jets: Implications for wind energy. *Wind Energy*, 12(1):81–90.
- Stull, R. (1988). *An Introduction to Boundary Layer Meteorology*. Springer Science & Business Media, vol. 13 edition.
- Sukoriansky, S., Galperin, B., and Perov, V. (2005). Application of a New Spectral Theory of Stably Stratified Turbulence to the Atmospheric Boundary Layer over Sea Ice. *Boundary-Layer Meteorology*, 117(2):231–257.

- Svensson, G., Holtslag, A. A. M., Kumar, V., Mauritsen, T., Steeneveld, G. J., Angevine, W. M., Bazile, E., Beljaars, A., de Bruijn, E. I. F., Cheng, A., Conangla, L., Cuxart, J., Ek, M., Falk, M. J., Freedman, F., Kitagawa, H., Larson, V. E., Lock, A., Mailhot, J., Masson, V., Park, S., Pleim, J., Söderberg, S., Weng, W., and Zampieri, M. (2011). Evaluation of the diurnal cycle in the Atmospheric Boundary Layer over land as Represented by a Variety of Single-Column models: The second GABLS EXperiment. *Boundary-Layer Meteorology*, 140(2):177–206.
- Talbot, C., Bou-Zeid, E., and Smith, J. (2012). Nested Mesoscale Large-Eddy Simulations with WRF: Performance in Real Test Cases. *Journal of Hydrometeorology*, 13(5):1421–1441.
- Taylor, K. E. (2001). Summarizing multiple aspects of model performance in a single diagram. *Journal of Geophysical Research*, 106:7183–7192.
- Troen, I., Bechmann, A., Kelly, M., Sørensen, N. N., Réthoré, P.-E., Cavar, D., and Jørgensen, H. E. (2014). Complex Terrain Wind Resource Estimation With the Wind-Atlas Method: Prediction Errors Using Linearized and Nonlinear CFD Micro-Scale Models. *Proceedings of EWEA 2014 European Wind Energy Association (EWEA)*.
- Troen, I. and Petersen, E. L. (1989). *European wind atlas*. Risø National Laboratory.
- Troen, I. B. and Mahrt, L. (1986). A simple model of the atmospheric boundary layer; sensitivity to surface evaporation. *Boundary-Layer Meteorology*, 37(1-2):129–148.
- Tseng, Y. H., Meneveau, C., and Parlange, M. B. (2006). Modeling flow around bluff bodies and predicting urban dispersion using large eddy simulation. *Environmental Science and Technology*, 40(8):2653–2662.
- Uchida, T. and Ohya, Y. (2003). Large-eddy simulation of turbulent airflow over complex terrain. *Journal of Wind Engineering and Industrial Aerodynamics*, 91(1-2):219–229.
- Udina, M., Sun, J., Kosović, B., and Soler, M. R. (2016). Exploring Vertical Turbulence Structure in Neutrally and Stably Stratified Flows Using the Weather Research and Forecasting–Large-Eddy Simulation (WRF–LES) Model. *Boundary-Layer Meteorology*, 161(2):355–374.
- Van de Wiel, B. J. H., Moene, A. F., Jonker, H. J. J., Baas, P., Basu, S., Donda, J. M. M., Sun, J., and Holtslag, A. A. M. (2012). The Minimum Wind Speed for Sustainable Turbulence in the Nocturnal Boundary Layer. *Journal of the Atmospheric Sciences*, 69(11):3116–3127.
- van der Laan, P. and Sørensen, N. N. (2017). A 1D version of EllipSys. Technical report, Department of Wind Energy, Technical University of Denmark.
- Van Ulden, A. P., Wieringa, J., Ulden, A. P., and Wieringa, J. (1996). Atmospheric boundary layer research at Cabauw. *Boundary-Layer Meteorology 25th Anniversary Volume. 1970-1995*, pages 39–69.
- Vanvyve, E., Delle Monache, L., Monaghan, A. J., and Pinto, J. O. (2015). Wind resource estimates with an analog ensemble approach. *Renewable Energy*, 74:761–773.



- Vasiljevia, N., Palma, J. M., Angelou, N., Matos, J. C., Menke, R., Lea, G., Mann, J., Courtney, M., Frölen Ribeiro, L., and Gomes, V. M. (2017). Perdigaõ 2015: Methodology for atmospheric multi-Doppler lidar experiments. *Atmospheric Measurement Techniques*, 10(9):3463–3483.
- Vasiljevic, N. (2014). *A time-space synchronization of coherent Doppler scanning lidars for 3D measurements of wind fields*. PhD thesis, Technical University of Denmark.
- Verkaik, J. W. and Holtslag, A. A. M. (2007). Wind profiles, momentum fluxes and roughness lengths at Cabauw revisited. *Boundary-Layer Meteorology*, 122(3):701–719.
- Vu, T. C., Ashie, Y., Asaeda, T., Ca, V. T., Ashie, Y., and Asaeda, T. (2002). A  $k$ - $\epsilon$  turbulence closure model for the atmospheric boundary layer including urban canopy. *Boundary-Layer Meteorology*, 102(3):459–490.
- Wallace, J. M. and Hobbs, P. V. (2006). *Atmospheric science: an introductory survey*. Elsevier, vol. 92 edition.
- Walmsley, J. L., Taylor, P. A., and Keith, T. (1986). A simple model of neutrally stratified boundary-layer flow over complex terrain with surface roughness modulations (MS3DJH/3R). *Boundary-Layer Meteorology*, 36(1-2):157–186.
- Walton, A., Cheng, A. Y. S., and Yeung, W. C. (2002). Large-eddy simulation of pollution dispersion in an urban street canyon - Part I: comparison with field data. *Atmospheric Environment*, 36(22):3601–3613.
- Wang, Y., Basu, S., and Manuel, L. (2013). Coupled Mesoscale-Large-Eddy Modeling of Realistic Stable Boundary Layer Turbulence. *arXiv preprint arXiv:1307.2484*.
- Warner, T. T. (2010). *Numerical Weather and Climate Prediction*. Cambridge University Press.
- Warner, T. T. (2011). Quality assurance in atmospheric modeling. *Bulletin of the American Meteorological Society*, 92(12):1601–1610.
- Webb, E. K. (1970). Profile relationships: The log-linear range, and extension to strong stability. *Quarterly Journal of the Royal Meteorological Society*, 96(407):67–90.
- Wilcox, D. C. (1998). *Turbulence modeling for CFD*. DCW Industries, 2nd edition.
- Windeurope (2017). Wind energy in Europe: Outlook to 2020.
- Wyngaard, J. C. (2004). Toward Numerical Modeling in the “Terra Incognita”. *Journal of the Atmospheric Sciences*, 61(2):1816–1826.
- Wyngaard, J. C. (2010). *Turbulence in the atmosphere*. Cambridge University Press.
- Xie, Z. T. and Castro, I. P. (2008). Efficient generation of inflow conditions for large eddy simulation of street-scale flows. *Flow, Turbulence and Combustion*, 81(3):449–470.
- Xie, Z. T. and Castro, I. P. (2009). Large-eddy simulation for flow and dispersion in urban streets. *Atmospheric Environment*, 43(13):2174–2185.

- Xie, Z. T., Coceal, O., and Castro, I. P. (2008). Large-Eddy simulation of flows over random urban-like obstacles. *Boundary-Layer Meteorology*, 129(1):1–23.
- Yair, Y., Lynn, B., Price, C., Kotroni, V., Lagouvardos, K., Morin, E., Mugnai, A., and Del Carmen Llasat, M. (2010). Predicting the potential for lightning activity in Mediterranean storms based on the Weather Research and Forecasting (WRF) model dynamic and microphysical fields. *Journal of Geophysical Research Atmospheres*, 115(4):1–13.
- Yamaguchi, T. and Feingold, G. (2012). Technical note: Large-eddy simulation of cloudy boundary layer with the Advanced Research WRF model. *Journal of Advances in Modeling Earth Systems*, 4(3).
- Yang, W., Quan, Y., Jin, X., Tamura, Y., and Gu, M. (2008). Influences of equilibrium atmosphere boundary layer and turbulence parameter on wind loads of low-rise buildings. *Journal of Wind Engineering and Industrial Aerodynamics*, 96(10-11):2080–2092.
- Zhang, D. and Anthes, R. A. (1982). A High-Resolution Model of the Planetary Boundary Layer—Sensitivity Tests and Comparisons with SESAME-79 Data. *Journal of Applied Meteorology*, 21(11):1594–1609.
- Zhang, J., Draxl, C., Hopson, T., Monache, L. D., Vanvyve, E., Hodge, B.-m. M., Delle, L., Vanvyve, E., Hodge, B.-m. M., Monache, L. D., Vanvyve, E., and Hodge, B.-m. M. (2015). Comparison of numerical weather prediction based deterministic and probabilistic wind resource assessment methods. *Applied Energy*, 156(October):528–541.
- Zhang, W., Markfort, C. D., and Porté-Agel, F. (2012). Near-wake flow structure downwind of a wind turbine in a turbulent boundary layer. *Experiments in Fluids*, 52(5):1219–1235.
- Zhou, B., Simon, J. S., and Chow, F. K. (2014). The Convective Boundary Layer in the Terra Incognita. *Journal of the Atmospheric Sciences*, 71(7):2545–2563.

This thesis was submitted in partial fulfillment of the requirements for obtaining the PhD degree at the Technical University of Denmark (DTU). The work was done at the Department of Wind Energy from December 2014 to June 2018. The PhD project was funded by the NEWA ERA-NET Plus project, topic FP7-ENERGY.2013.10.1.2, and by the Technical University of Denmark.

Principal supervisor: Head of Section, Senior Researcher, Ph.D. Jake Badger, DTU

Co-supervisor: Senior Researcher, Ph.D. Andrea N. Hahmann, DTU

Co-supervisor: Senior Researcher, Ph.D. Dalibor Cavar, DTU

Co-supervisor: Professor Jakob Mann, DTU

**DTU Wind Energy**  
**Technical University of Denmark**

Building 115  
Frederiksborgvej 399  
4000 Roskilde  
[www.vindenergi.dtu.dk](http://www.vindenergi.dtu.dk)